
SAPIENZA
UNIVERSITÀ DI ROMA

Ph.D. Thesis in Pharmaceutical Sciences
XXXI cycle

# Investigation on smart triggers and smart lipid vesicles as new tools for drug delivery applications

**Candidate**
Martina Nardoni
ID number 1385360

**Thesis Supervisor**
Prof. Stefania Petralito

**Thesis co-Supervisor**
Prof. Maria Antonietta Casadei
Prof. Patrizia Paolicelli

**A.Y. 2017/2018**

**Thesis Committee**
Prof. Alessia Ciogli
Prof. Patrizia Diana
Prof. Sonia Trombino

**Reviewers**
Prof. Calogero Fiorica
Prof. Delia Mandracchia

Author's address:
Martina Nardoni
Sapienza - University of Rome
Piazzale Aldo Moro 5, 00185 Rome, Italy
e-mail: **martina.nardoni@uniroma1.it**

Alla mia famiglia

La chimica è una cosa che serve a tutto.
Serve a coltivarsi, serve a crescere,
serve a inserirsi in qualche modo
nelle cose concrete.

Primo Levi

# Table of Contents

## Chapter 5

## Theoretical and experimental evaluation of the nanosecond electric pulses as triggers to permeabilize nano-lipid based drug delivery systems ..... 108

# List of Figures

## Chapter 1

### Introduction ..... 1

# List of Tables

## Chapter 1



## Chapter 3



## Chapter 4



## Chapter 5

# Chapter 1

# Introduction

Nanotechnology is defined as the understanding and control of matter at dimensions between 1 and 100 nm, where unique phenomena enable novel applications [1]. The concept of a ''nanometer'' was first proposed by the Nobel Prize for Chemistry Richard Zsigmondy, who used this term for characterizing particle size and who was the first to measure the size of particles such as gold colloids, using a microscope. Modern nanotechnology was the brain child of Richard Feynman that, during the 1959, in his talk ''There's Plenty of Room at the Bottom'', described the possibility of synthesis via direct manipulation of atoms. The golden era of nanotechnology began in the 1980s when Eric Drexler, inspired by Feynman's concepts, coined the term "nanotechnology", suggesting in his book, "Engines of Creation: The Coming Era of Nanotechnology", the idea of a nanoscale word where it is possible to place every atom where we want it to be placed [2]. From the 21st century to the present, nanotechnology turned out a radically new way of producing to obtain materials, structures and devices with greatly improved or entirely new properties and functions, offering resolution to problems considered previously unresolvable. Therefore, it took a leading role in all fields, pharmaceutical, cosmetic, food and engineering [3-6].

Recently, the fixed presence of nanotechnologies into the resolution of several diseases, originating from alteration of biological processes at nanoscale level, leaded to the birth of nanomedicine. The nanomedicine combines the innovation of drug delivery systems, characterized by shape and size of nanometer scale, to health care, providing new promising techniques to improve the efficacy of medical treatments and to prevent the patient safety.
In this regard, it is since 2005 that the European Technology Platform for Nanomedicine (ETPN) proposed an important iniziative to increase the competitiveness of Europe in the field of nanomedicine, both in the academia and industry panorama, publishing "The Strategic Research and Innovation Agenda" (SRIA). The SRIA document highlights the potential of the current and future nanomedical products in the areas of therapeutics,

diagnostics and regenerative medicine, to provide new and efficient solutions for health care [7].

Following the approach of nanotechnology reality with that of medicine, it was possible to design and develop several nanocarriers for the delivery of therapeutical molecules, as evidenced by the numerous examples of research aimed at producing nanosystems that can act as effective vectors for the transport and targeted distribution of drugs in the human body [8, 9].

Specific attention is dedicated to the development of selective nanocarriers, that could realize a targeted and controlled therapy. In fact, one of the most important challenges of medicine is actually the possibility to treat acute or chronic disorders like cancer, Alzheimer's, Parkinson's disease, cardiovascular or inflammatory problems, with systems able to deliver the drug at specific sites and times, at required concentrations, in order to avoid any damage to the surrounding healthy tissue and to improve the compliance of the patient. During the last decades, these purposes were achieved through the appropriate choice of nanomaterials and the processing of a variety of protocols and methods for the synthesis, functionalization and application of nanovectors.

Due to their unique properties [10, 11], nanosystems show favourable physico-chemical characteristics. For example, the reduction of volumes to the advantage of the exchange surfaces allows them not only greater interactions with living cells, but also the overcoming of the body barriers, such as blood-brain barrier or blood vessels. Therefore, when grows a tumor mass, that is a proliferating site and is characterized by leaky bloody vessels, nanovectors, thank to their smaller size, can easily arrive at the tumour site and release the therapeutic agents there [12]. In addition, nano-sized systems have the ability to modulate both the pharmacokinetic and pharmacodynamic profiles of drugs, thereby enhancing their therapeutic index.

According to studies on nanoscale technology, although many sophisticated and advanced nanocarriers for the delivery of drugs were investigated to date, liposomes remain one of

the most promising nanosystems for clinical applications and represent a great promise in the controlled drug delivery panorama [13-16].

Studied usually for the repackaging of traditional drugs, with the aim of obtaining an enhanced therapeutic efficacy and safety over the existing formulations, liposomes exhibit a wide range of recognized outstanding properties, such as good biocompatibility and safety profile, low antigenicity and ability to target bioactive molecules to their site of action. The liposomal structure also makes this type of nanocarrier particularly attractive and versatile for applications in drug delivery, since lends itself to be variously modified and engineered to respond to different endogenous and exogenous stimuli [17].

In light of this evidence, was possibile to realize multi-functional and multicomponent systems through the combination of two or more distinct biomaterials, organic or inorganic, into a structure that itself is still of nanoscale dimensions and whose medical effects are superior to those that could be realized from any simple mixture of the individual components [18]. Consequently, the combinatorial approach applied to the liposomes-based technology can determin the design of new hybrid nanocomposites, with enhanced release properties and stability [19], since the stability of carriers in the circulation is a desirable characteristic for successful drug delivery to diseased tissues.

Besides, it is also recognized that being able to trigger the release of liposomal contents once nanocarriers reached the target site, would lead to improvements in therapeutic outcomes. Indeed, new strategies in liposomal research are gaining interest and some clinical trials, based on the combination of different chemotherapeutic agents and stimuli-responsive release approaches, were started [20, 21]. Due to this, liposomes can be used as triggered nanocarriers through internal (e.g. pH variation, enzyme action) or external (e.g. temperature, electric or magnetic field) stimuli. In this way, the release of loaded drugs can be controlled and concentrated at the target desired [22].

## 1.1 Liposomes

Discovered first, by chance, in the course of research on lecithin dispersions, as reagents in blood coagulation [23], and become later prominent elements in the therapeutic field, liposomes, among colloidal vectors of lipid origin, are the most versatile and studied nanosystems for their potential benefits, not only in the medical but also in the cosmetic and food sectors [24]. Already observed before of 1854 and subjects of the micrograph contained in the volume of Otto Lehmann in 1911, that depicted a homogeneous dispersion of multilamellar liposomes as "artificial cells", liposomes were first described in 1965 by Alec Bangham and his coworkers [25]. The use of liposomes as drug delivery systems started only in the '70s, when it was clear their ability to encapsulate and transport biologically active compounds to the different districts of the human organism.

From the greek words "λίπος" and "σῶμα", that mean literally "fat body", liposomes are spherical self-closed structures, consisting of phospholipids which in water arranged spontaneously in double concentric layers of 4 nm of thickness, ordered and separated by aqueous compartments (Figure 1.1).

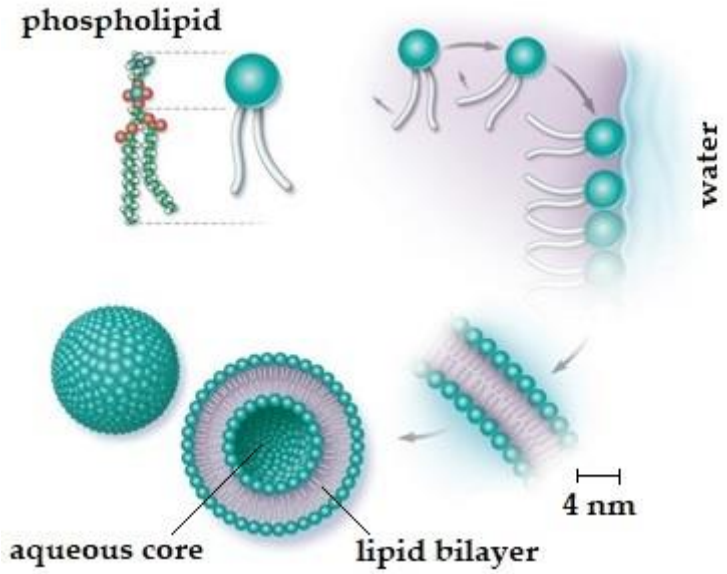


**Figure 1.1. Scheme of unilamellar liposomes, with the hydrophilic head groups (green) of phospholipids facing the water, and the hydrophobic tail groups (purple) buried within the bilayer.**

Depending on the number of lipid bilayers, which composes the vesicles, and on the base of their size, liposomes can be classified into the one of two categories: multilamellar vesicles (MLV) and unilamellar vesicles (Figure 1.2). Multilamellar vesicles (MLV) have an onion structure, characterized by five or more concentric layer, with a final diameter from 0.4 to 3.5 μm. In unilamellar liposomes, the vesicles have a single phospholipid bilayer sphere enclosing the aqueous solution. Among unilamellar liposomes, it is possible also to distinguish some kinds of vesicles for their diameter:

- small unilamellar vesicles (SUV), diameter range from 25 to 100 nm
- large unilamellar vesicles (LUV), diameter range from 0.1 to 1 μm
- giant unilamellar vesicles (GUV), diameters equal to/or bigger than 1 μm

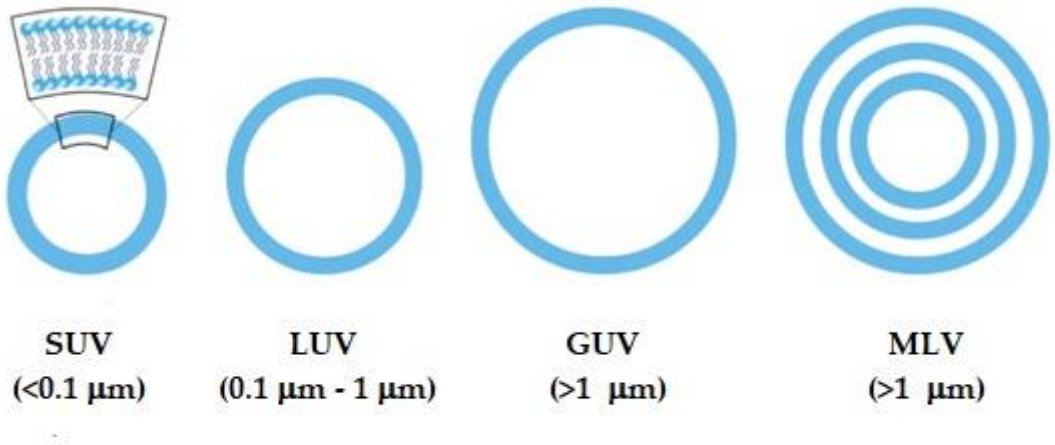


**Figure 1.2. Liposomes classification by their structural properties.**

The vesicle size is an acute parameter in determining the circulation half-life of liposomes, and both size and number of bilayers affect the amount of drug encapsulated in the liposomes [26]. The membrane composition and rearrangement determine their versatility in the ability of carrying both hydrophilic and hydrophobic drugs in the aqueous lumen and lipid bilayer, respectively, as well as in the possibility of protecting, as masking systems,

the different incorporated therapeutic molecules from the surrounding environment or tuning membrane permeability, with the application of opportune external stimuli [13, 27]. The remarkable structural analogy with the lipid bilayer characteristic of biological membranes awards them the role of the simplest cellular model (Figure 1.3), besides a high biocompatibility and biodegradability, as reported previously.

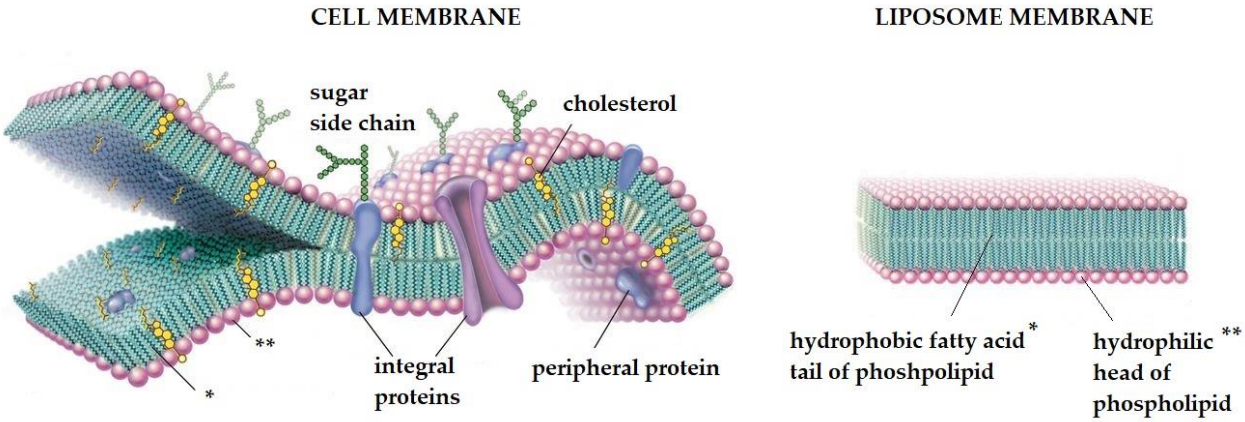


**Figure 1.3. Representation of the structure of cellular and liposomal membrane.**

Thanks to their innumerable properties and benefits, liposomes find wide use in the various fields of science and technology, from the study of the cells membrane to the design of complex drug delivery systems.

### 1.1.1 Chemical composition

A clear advantage is the fact that the liposomal membrane is made of physiological components, which decreases the danger of acute and chronic toxicity. Liposomes, indeed, are generally constituted of naturally occuring polar lipid, such as glycerolipids, sphingolipids and sterols. The net physicochemical properties of the lipids composing the liposomes, such as membrane fluidity, charge density, steric hindrance and permeability, determine liposomes' interactions with blood components and other tissues, after systemic administration. Thus, liposomes composition should be carefully designed, in order to maximize chemical and physical properties of liposomes formulations [28].

### 1.1.2 Phospholipids

As main components of cellular membrane, phospholipids have the characteristics of excellent biocompatibility and are renowned for their amphiphilic structures. The amphiphilicity confers self-assembly, emulsifying and wetting characteristics upon phospholipids. Those are lipids containing phosphorus, a polar and non-polar portion in their structures. According to the alcohols contained in the phospholipids, they can be divided into glycerophospholipids and sphingomyelins. In particular, the backbone of sphingomyelins, main components of animal cell membranes, is a sphingosine, while that of glycerophospholipids, which are the main phospholipids in eukaryotic cells, is made of glycerol [29]. Except for this main difference, glycerophospholipids and sphingomyelins are very similar in molecular structure.

The polar head of a glycerophospholipid it consists of glycerol esters in which a hydroxyl residue is esterified by a phosphoric group, while the other two “O-H” groups are bound to various types of fatty acids. The phosphoric part, in turn, is esterified with hydroxyl groups belonging to strongly hydrophilic molecules, such as amines, carbohydrates and amino acids (Figure 1.4).

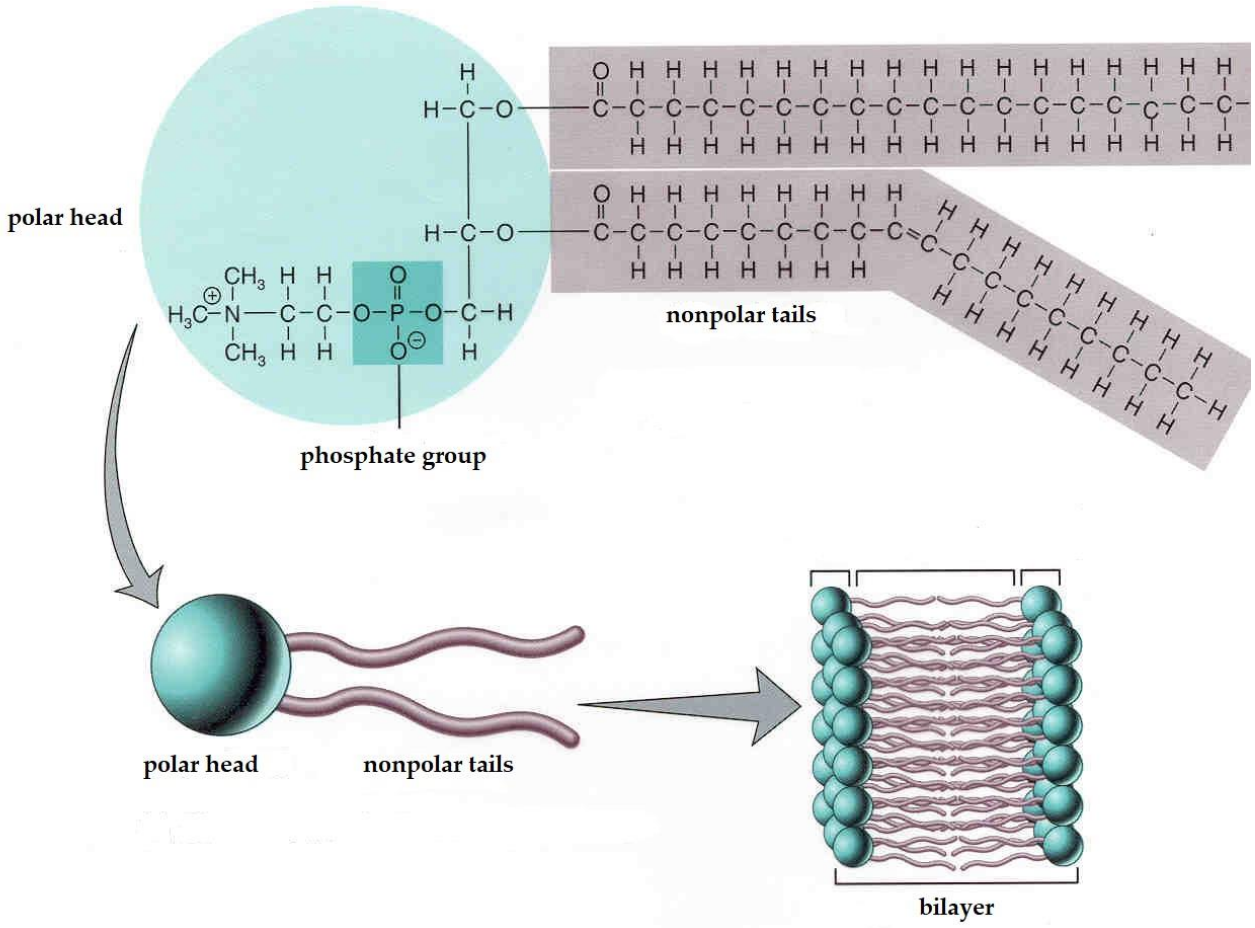


**Figure 1.4. Chemical structure of a glycerophospholipid.**

Variation in the head group, such as the zwitterionic (at most pH ranges), cationic or anionic character, leads to different glycerophospholipids: phosphatidylcholine (PC), phosphatidylethanolamine (PE), phosphatidylserine (PS), phosphatidic acid (PA), phosphatidylinositol (PI), phosphatidylglycerol (PG), cardiolipin (CL).

Furthermore, the characteristics of the apolar part is used for the classification of glycerophospholipids. The length and the saturation of hydrophobic side chains, the type of bonding between the aliphatic moieties and glycerol backbone and the number of aliphatic chains leads to dipalmitoyl, dimyristoyl, dioleoyl, distearoyl PC (Figure 1.5).

These aspects affect the overall lipophilia of the molecules.

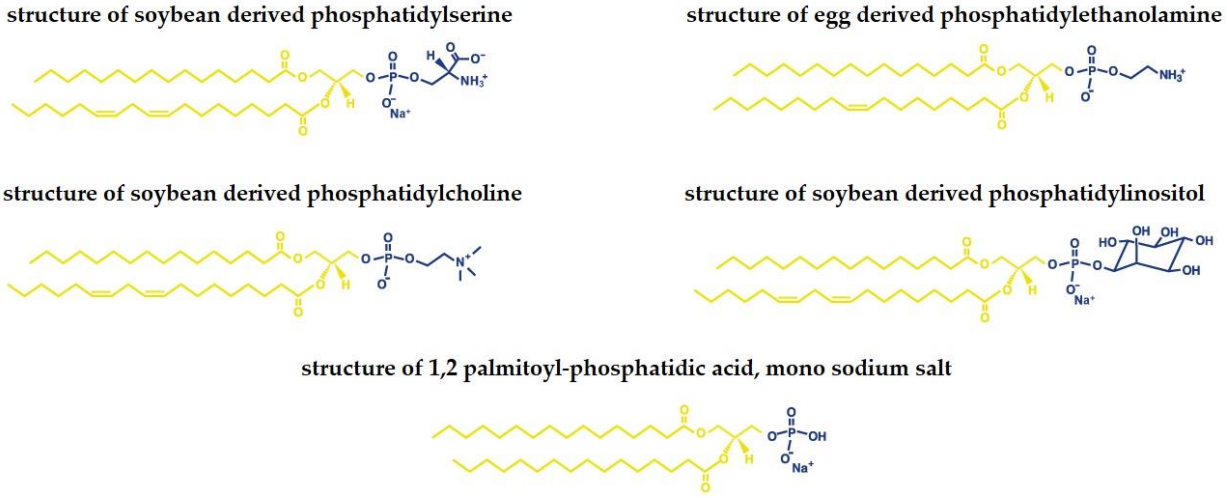


**Figure 1.5. Chemical structures of selected lipids used in liposome preparation.**

Various phospholipids are employed as important pharmaceutical excipients in different types of formulations. For example, phosphatidylcholine is the most commonly used phospholipid for liposome production and its main source is the chicken egg yolk or the cheapest soy beans.

### 1.1.3 Cholesterol

In addition to the phospholipids, liposome bilayers may also contain other constituents such as cholesterol. As a member of the steroid class, it has a carbon skeleton consisting of three six-point rings and one of five, essentially a rigid structure that can bind several substituents. The incorporation of cholesterol in the membranes induces different changes in the bilayer properties. For example, cholesterol can reduces molecular surface area [30-32] and membrane permeabilities [33, 34], varies lateral diffusion rates for both proteins and lipids [35, 36] and widens gel to liquid-crystalline phase transition.

Also, in liposomes strucuture, one of the primary roles of cholesterol is to modulate the physical properties of double lipid layer. Thanks to its ability of regulating membranes fluidity, it reduces the permeability to water-soluble molecules and increases the stability of the bilayer in the presence of biological fluids, such as blood or plasma. The capability to

modify membrane plasticity can be explained by its placement within the bilayer (Figure 1.6).

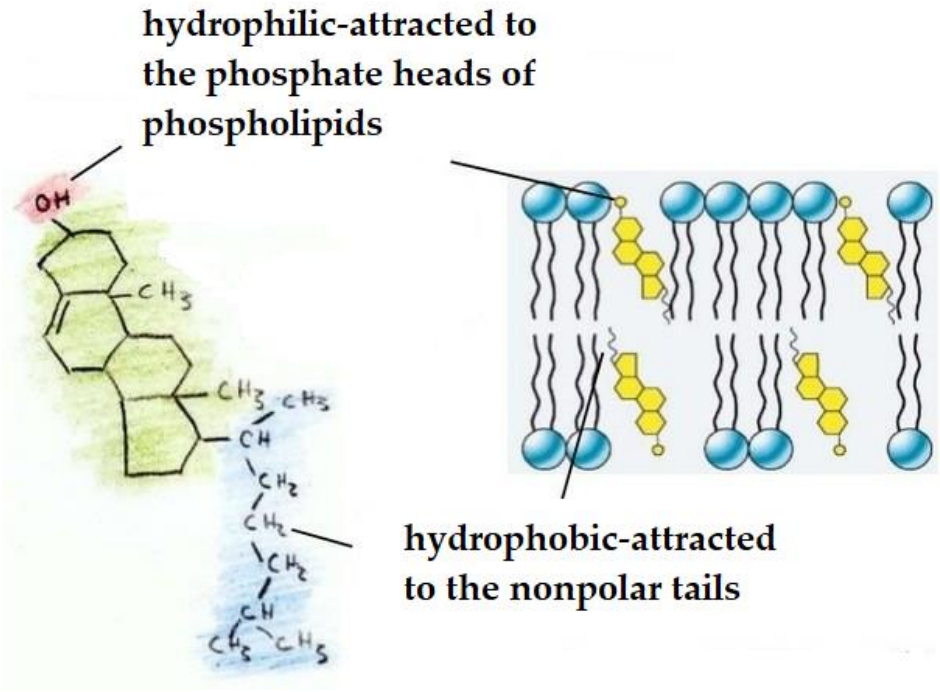


**Figure 1.6. Arrangement of cholesterol molecules in the phospholipid bilayer.**

The hydroxyl group is positioned in such a way as to be at the level of the bonds, which join the fatty acid chains to glycerol. The hydrophobic part, instead, extends towards the internal and apolar zone of the bilayer.

### 1.1.4 Bilayer fluidity and permeability

Physicochemical parameters as temperature, pH, ionic strength and other factors, such as the chemical structure of the lipid constituents and the presence of cholesterol, strongly influence the physical state of the phospholipid bilayer. Liposomal membrane may exist in different physical states, which are characterized by the lateral organization, the molecular order as well as the mobility of the lipid molecules. This, in turn, affects the permeability of the bilayer, which is a critical parameter when applying liposomes as drug delivery systems as permeability influences the leakage of the delivered compounds. In liposomes there are two extreme lipid phases, the so-called gel and fluid phases. In the gel phase (Lβ), also called solid-ordered phase, the lipids usually arranged on a two-dimensional triangular lattice in the plane of the membrane [37]. The hydrocarbon lipid chains display an all-trans configuration and are elongated at the maximum, giving rise to an extremely compact lipid network. Consequently, the lateral diffusion of lipids is reduced. Parameters such as the nature of the polar head group and the presence of counterions, which affect the head group conformation, may also influence the tilt of the lipid alkyl chains in the gel phase. For example, while the hydrocarbon chains of hydrated phosphatidylcholines are tilted with respect to the bilayers, the alkyl chains of hydrated phosphatidylethanolamines are approximately normal to the plane of the bilayers [38]. In the fluid phase, also called liquid-disordered (L$\alpha$) phase, trans-gauche isomerisation occurs giving rise to much less extended lipid chains. Moreover, the two-dimensional triangular lattice is completely lost. As a result, both the lateral and the rotational diffusion of lipids are favored.

The transition between the gel and fluid phases occurs at a specific temperature, called thermotropic phase transition temperature (Tm). The phase transition temperature of a membrane lipid, that is the temperature required for inducing the lipid melting from the Lβ to the L$\alpha$ phase, is depending on the nature of its hydrophobic moiety (acyl chain length, structure and degree of unsaturation of the hydrocarbon chains and presence of a methyl branch) and can be determined by using the differential scanning calorimetry technique.

The presence of double bonds in acyl chain results to Tm decrement and fluidity increment. The effect of the double bond on the temperature of the gel-to-liquid-crystal phase transition was greatest when it was situated in the middle of the chain. The Tm of saturated phospholipid bilayers is known to be proportional to the length of the alkyl chains, as by increasing the length of acyl chain, the Tm increases.

The crystalline gel-liquid heat-reversing transition is a parameter of fundamental importance for the assessment of lipid vesicles stability [39]. The transition from one phase to another involves a series of micro and macroscopic effects; for example, from gel to crystalline liquid phase the thickness of the membrane decreases. Consequently, the vesicles are slightly smaller than those in the crystalline liquid phase, due to both the disorder of the chains that can interdigitate, and the ingress of water molecules during the transition. In fact, in the gel phase the chains are rigidly packed, in the crystalline liquid phase the latter are free to rotate around the "C-C" bonds causing a high degree of conformational disorder. For some membrane lipids, such as phosphatidylcholines, the lipid disordering occurs in two steps when increasing temperature. A first transition is observed a few degrees below the main transition temperature (Figure 1.7).

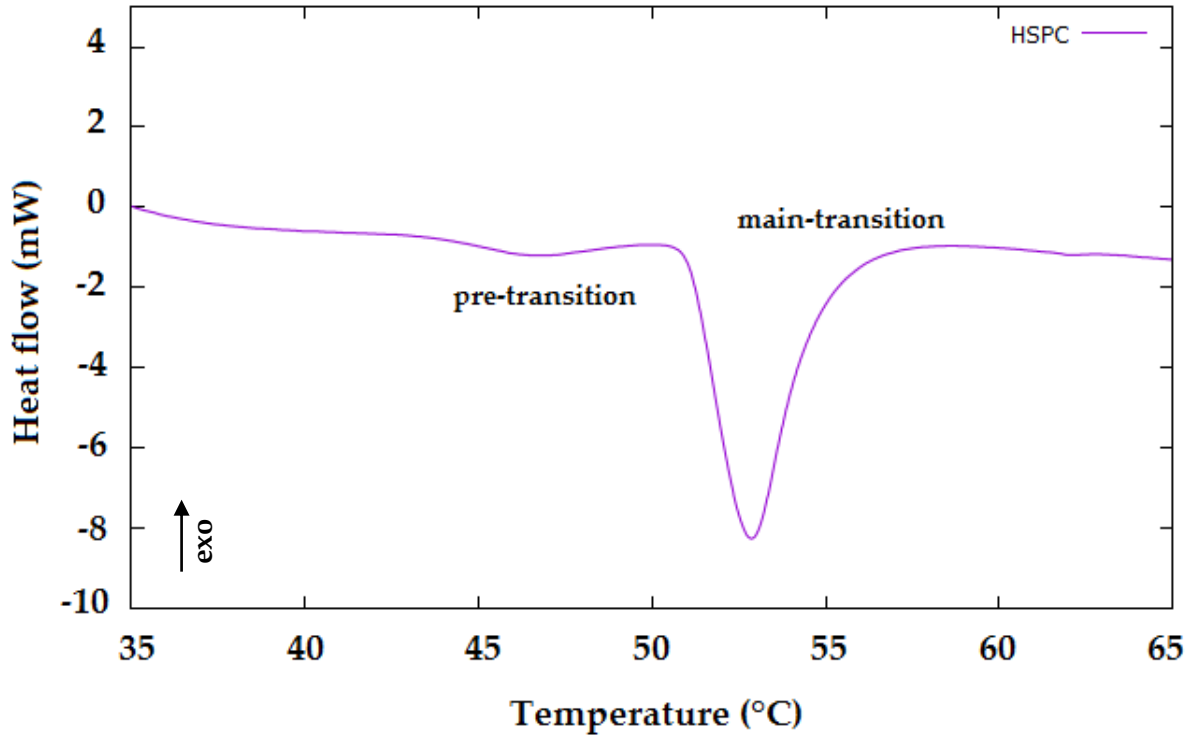


**Figure 1.7. Thermogram of hydrated film of hydrogenated phosphatidylcholine soybean (HSPC), recorded at scan rate 5 °C/min, in the temperature range 30-70 °C.**

This pre-transition may be due to changes in the proximity of the polar head group, such as an increase of the interaction of the lipid head groups with the solvent. The lipids that exhibit a pre-transition temperature, that is called ripple phase (Pβ), are characterized by periodic one-dimensional undulations on the surface of the lipid bilayer (Figure 1.8).

As this phase appears prior to the main chain melting, it must correspond to a partially disordered lipid phase. For this reason, it was supposed that the undulations, observed on the top of the lipid bilayers, arise from periodic arrangements of linear ordered and disordered lipid domains [40].

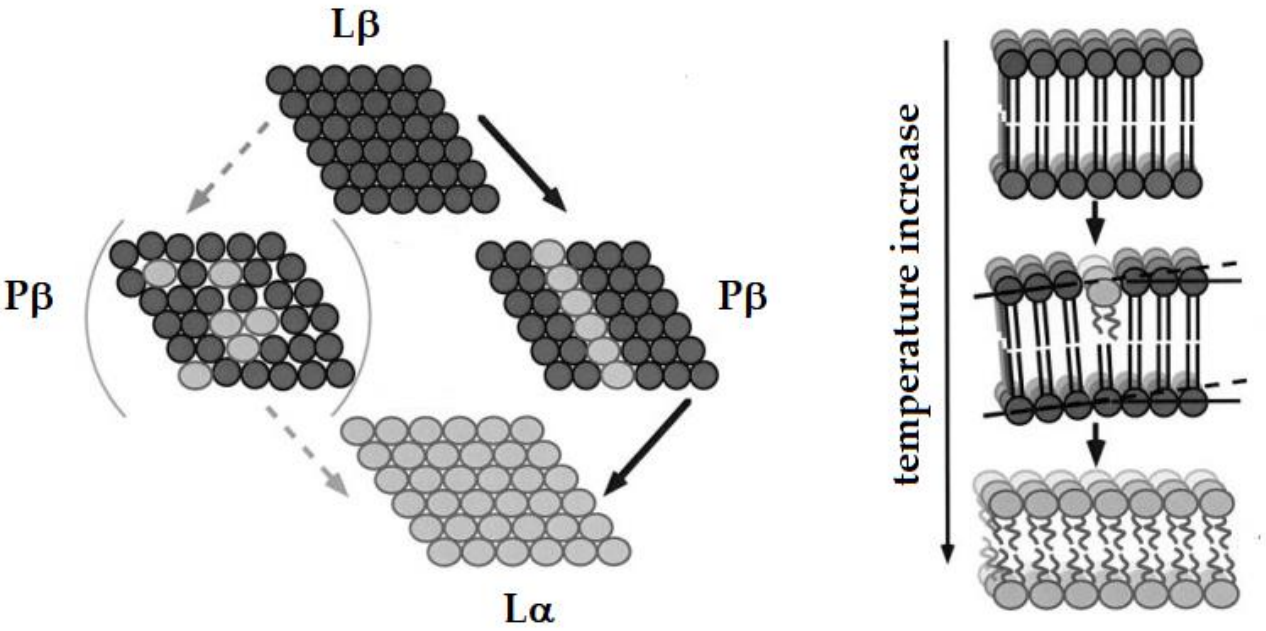


**Figure 1.8. Schematic view on a triangular lattice during the melting process. Gel and fluid lipids have different cross-sectional areas. Top: all lipids are in the gel state placed on an undistorted lattice. Center left: some fluid lipids are randomly arranged in a gel matrix, resulting in lattice distortion. Center right: the same number of fluid lipids is arranged in a line defect, which is possible without lattice distortion. Bottom: all lipids are in the fluid state and are situated on an undistorted lattice [41].**

When the gel-to-liquid-crystal phase transition occurs, the membrane permeability reaches a maximum. This increased permeability could be attributed to the following possibilities:

- defects caused by mismatched Lβ and L$\alpha$ phase hydrocarbon chain domains
- strong density and thermal fluctuations resulting in increased lateral membrane compressibility, which lowers the energy barrier for molecules to pass through the membrane, or to create defects.

This sharp increase in membrane permeability and Tm provides the possibility of controlling the release of the liposome contents.

All lipids have a characteristic Tm, so they exist in different physical states above and below the Tm. Therefore, the fluidity of liposome bilayers can be altered by using phospholipids with different Tm, which in turn can vary from -20 to 90 °C, depending upon the length and nature (saturated or unsaturated) of the fatty acid chains (Table 1.1). In particular, the longer

the hydrocarbon chains are long and saturated, the higher it will be their melting temperature.

**Table 1.1. Phase transition temperature of commonly used phospholipids [39, 42-44].**

| **Phospholipids** | **Abbreviation** | **Tm (°C)** |
|---|---|---|
| Soybean phosphatidylcholine | SPC | −20 to −30 |
| Hydrogenated soybean phosphatidylcholine | HSPC | 52 |
| Egg sphingomyelin | ESM | 40 |
| Egg phosphatidylcholine | EPC | −5 to −15 |
| Dimyristoyl phosphatidylcholine | DMPC | 23 |
| Dipalmitoyl phosphatidylcholine | DPPC | 41 |
| Dioleoyl phosphatidylcholine | DOPC | −22 |
| Distearoyl phosphatidylcholine | DSPC | 55 |
| Dimyristoyl phosphatidylglycerol | DMPG | 23 |
| Dipalmitoyl phosphatidylglycerol | DPPG | 41 |
| Dioleoyl phosphatidylglycerol | DOPG | −18 |
| Distearoyl phosphatidylglycerol | DSPG | 55 |
| Dimyristoyl phosphatidylethanolamine | DMPE | 50 |
| Dipalmitoyl phosphatidylethanolamine | DPPE | 60 |
| Dioleoyl phosphatidylethanolamine | DOPE | −16 |
| Dimyristoyl phosphatidylserine | DMPS | 38 |
| Dipalmitoyl phosphatidylserine | DPPS | 51 |
| Dioleoyl phosphatidylserine | DOPS | −10 |

Presence of high-Tm lipids (Tm >37 °C) makes the liposome bilayer membrane less fluid at the physiological temperature and less leaky. In contrast, liposomes composed of low-Tm lipids (Tm <37 °C) are more susceptible to spontaneous leakage of drugs encapsulated in aqueous phase, at physiological temperatures.

The fluidity of bilayers may also influence the *in vivo* performance of liposome formulations, in particular, the interaction of liposomes with cells: liposomes composed of high-Tm lipids appear to have a lower extent of uptake by the cells of reticuloendothelial system (RES), compared to those containing low-Tm lipid.

As mentioned above, the presence of cholesterol exerts a profound influence on the properties of the lipid bilayers. In presence of cholesterol, liposome membrane can adopt an

extra lamellar phase, called the liquid-ordered (L0) phase, which shares the characteristics of both gel and fluid phases [45]. This phase resembles to the gel phase with less lateral packing order and, at the same time, to the fluid phase with more packing order. The incorporation of cholesterol into a solid-ordered lamellar phase disturbs the lateral triangular lattice and, consequently, reduces the ordering of the lipid chains. Therefore, the liquid-ordered phase displays both a lateral and a rotational diffusion that are close to the ones of the liquid-disordered phase [46, 47], but a conformational order similar to the one of the solid-ordered phase [48]. Concerning membrane permeability, liposomes in gel phase are leak-proof in the absence of the cholesterol (Figure 1.9). At the opposite, in a liquid-disordered lamellar phase, the rigid hydrophobic moiety of cholesterol is intercalated between the lipid chains and favors a trans chain conformation [49], therefore liquid-disordered and liquid-ordered phases can coexist in a same lipid bilayer [50]. For example, a phase-coexistence between a cholesterol-poor liquid-disordered phase and a cholesterol-rich liquid-ordered phase was experimentally observed for lipid bilayers composed of phosphatidylcholine/cholesterol [51] and sphingomyelin/cholesterol [52] mixtures. In addition, the existence of phase-separated zones in the lipid bilayers has a major role to play in the engineering of "trigger release liposomes".

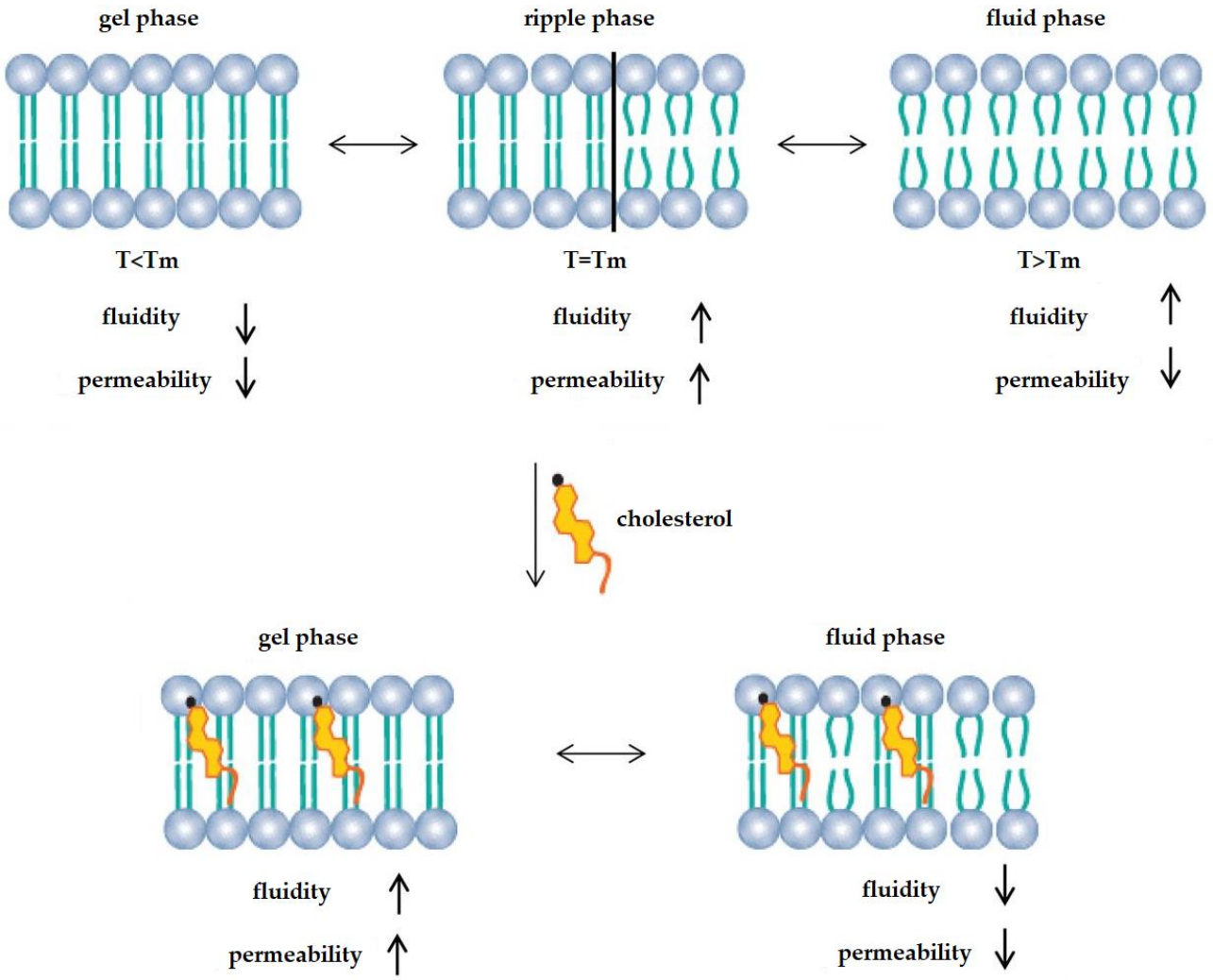


**Figure 1.9. Modification of the membrane properties after the integration of cholesterol molecules in the phospholipid bilayer.**

Because of this type of interactions, the presence of adequate amounts of cholesterol can come to suppress the phase transition and the membrane can exist in the ordered liquid phase over a wide temperature range [53].

## 1.2 Evolution and applications of liposomes in drug delivery

Described for the first time in 1965 by Alec Bangham and his students, liposomes are spherical vesicles known for their unique structure and properties. As a result, they became one of the most used delivery systems in the pharmaceutical market. Nowadays, liposomes represent versatile and advanced nanodelivery systems, for the packaging of a wide range of novel biologically active molecules and for the rearrangement of traditional drugs, aiming to enhance therapeutic efficacy and safety over the existing formulations. For demonstration, in the Table 1.2 is reported a list of many approved liposomal products for clinical applications and many others (e.g. ThermoDox, Stimuvax, Nyotran, Aroplatin, Liprostin) are in preclinical developments or in clinical trials.

**Table 1.2. Approved liposomes products on the market and associated clinical indications [54].**

| Year Approved | Brand Name | Drug | Approved Indication |
|---|---|---|---|
| 1986 | Diprivan | Propofol | Anesthesia |
| 1995 | Abelcet | Amphotericin B | Aspergillosis |
| 1995 | Doxil | Doxorubicin | Kaposi's sarcoma |
| 1995 | Epaxal | Inactivated hepatitis A virus | Hepatitis A |
| 1996 | Amphotec | Amphotericin B | Aspergillosis |
| 1997 | AmBisome | Amphotericin B | Leishmaniasis |
| 1997 | Inflexal V | Inactivated hemagglutinin | Influenza |
| 2000 | Visudyne | Verteporphin | Wet macular degeneration |
| 2000 | Myocet | Doxorubicin | Metastatic breast cancer |
| 2003 | Estrasorb | Estrogen | Menopause |
| 2003 | DepoDur | Morphine sulfate | Pain management |
| 2011 | Exparel | Bupivacaine | Anesthetic |
| 2013 | Marqibo | Vincristine | Lymphoblastic leukemia |

To reach this condition, numerous modifications were made on the initial liposomal structures, also known as "conventional" liposomes.

Indeed, despite their advantage of biocompatibility, biodegradability, versatility, relatively easy preparation and a rich selection of physicochemical properties, conventional liposomes performance [e.g. Ambisome, Amphotec and Albecet, commercialized for the therapy of fungal infections (55, 56)] proved to be limited. In general, the first generation of liposomes showed the difficulty in retaining some types of entrapped compounds in the inner core, the inclination to fuse with other close vesicles (because of the unprotected lipid surface) and moreover a profile release affected by the exposure to serum proteins. Hence, soon after their discovery, liposomes became the protagonists of a continuous evolutionary process aimed at overcoming these issues and developing optimized liposomal formulations as vehicles in drug delivery but also for imaging agents, thus in their ability to perform therapeutic and diagnostic functions. To overcome these issues, different strategies were evaluated (Figure 1.10). First, to slow the liposomes fusion rate and to increase vesicles stability and *in vivo* circulation time, the external surface area was functionalized [57-59] and, as a result, PEGylation process led to the approvation of many therapeutic drug formulations, including Myocet and Doxil for the cancer treatment [60-62]. Nevertheless, polymer-lipid stabilized vesicles were further engineered to target their specific location, improving in this way their selectivity for diseased tissues. Thus, different biomarkers and ligands were chosen to decorate externally the bilayer [63-66]. The idea of combining components of a different nature in the same system, as in the case of PEGylated liposomes, involved the use not only of polymers such as polyethylene-glycol, but also of organic or inorganic agents, resulting in promising hybrid liposomal carriers [67-70]. In particular, the production of nanosystems that respond to different types of stimuli, internal and external, turned out to be a successful strategy to control the properties and behaviour of liposomes.

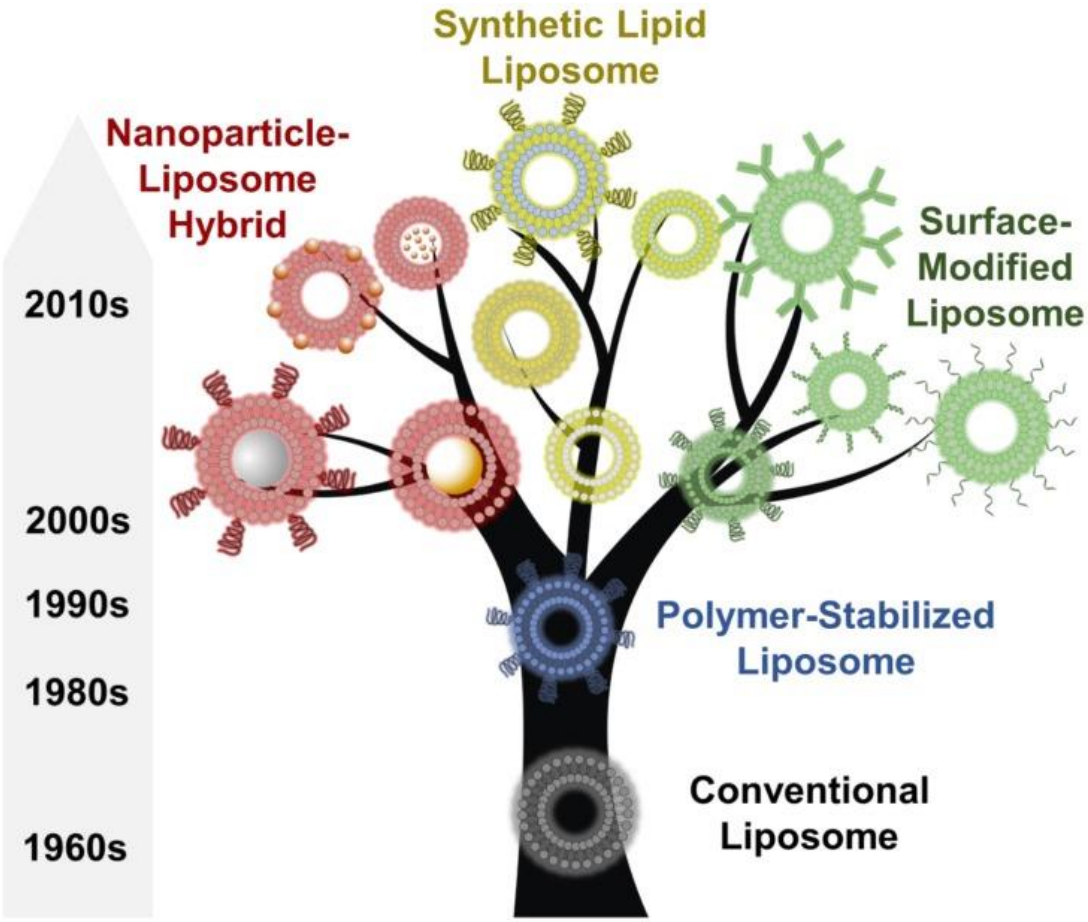


**Figure 1.10. An overview of the discovery, development and evolution of liposomes since their first report in 1965 [54].**

The background and development of liposomes demonstrated, over the years, in different fields such as medicine, immunology, diagnostics, cosmetics, ecology, cleansing and the food industry, however did not soften the interest of research for these structures. The statistical data obtained through the Scopus search engine (Figure 1.11) show indeed that the number of pubblications in the last ten years are constantly growing.

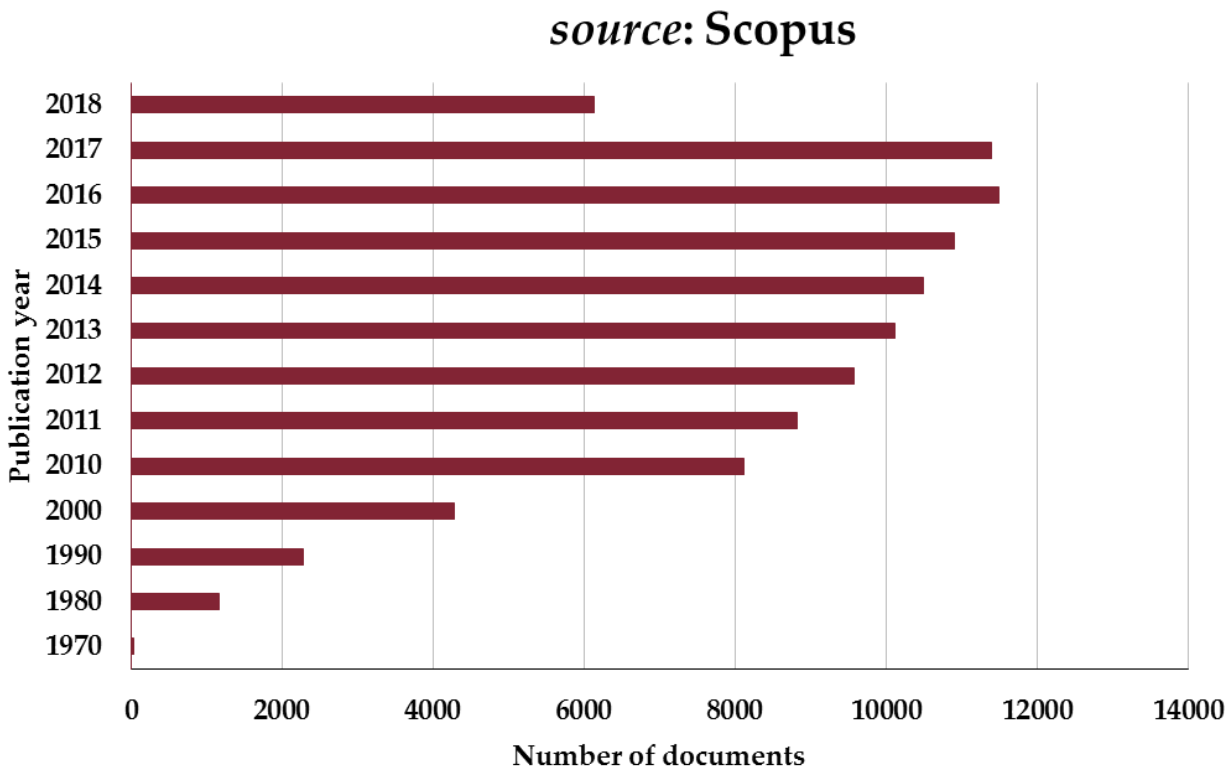


**Figure 1.11. Graphical representation of the constant growth in number of publications related to liposome technology, from 1970 to September 2018.**

In this regard, this Ph.D. thesis aims to contribute to the bright future employment of liposomes systems and to speculate optimistically about their spread in various disciplines, manipulating the liposomal structure in a novel way, as reported in detail in the following chapters.

### 1.2.1 Triggered release

Nanomedicine mainly acts improving the efficiency of drugs to pathological sites with a local release on the diseased tissues, reducing systemic secondary side effects for the healthy tissues [13, 71, 72]. This process takes the name of targeted drug delivery and basically can be achieved through three kind of way, as reported in the Figure 1.12:

- passive targeting
- active targeting
- triggered targeting

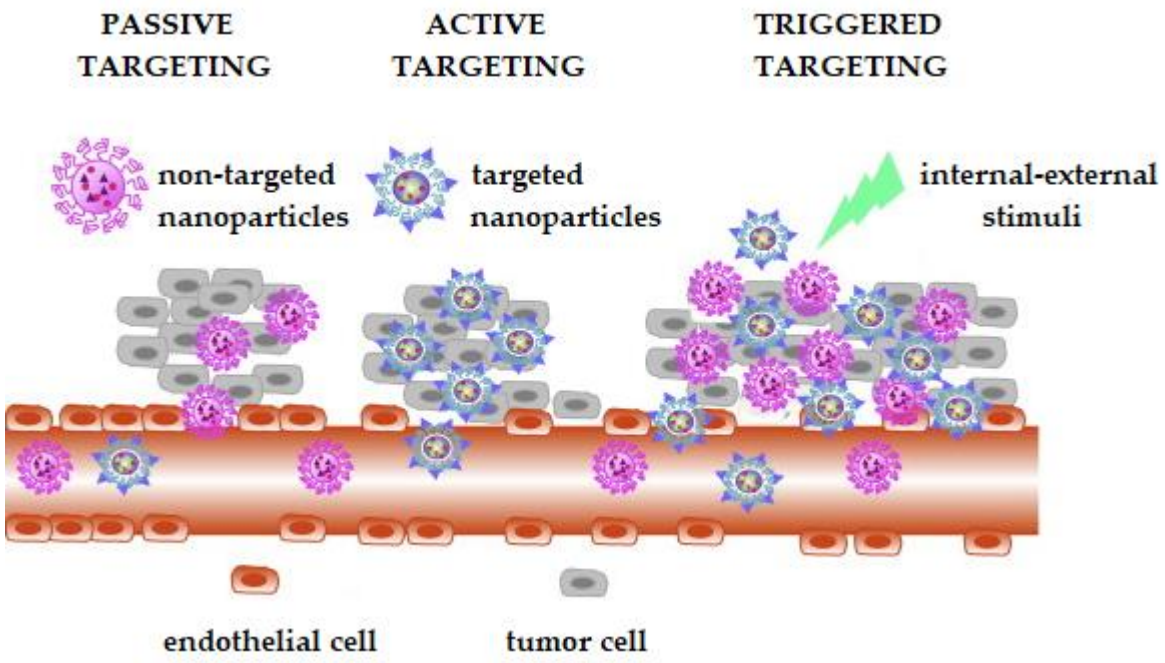


**Figure 1.12. Illustration of the targeted strategies: passive targeting, active targeting and triggered targeting.**

Passive targeting is based on the release of the drugs by the recognition of the diseased tissue, based on the morphological differences between the healthy and the ailing tissues. In the case of tumor cells, pathophysiological characteristics of cancers and their

environment were exploited for passive targeting. In particular, the permeability and retention (EPR) effect promotes the accumulation of nanomedicine drugs in the tumor site, based on the presence of leaky intratumoral blood vessels. For example, Kaposi sarcoma is a tumor type with fenestrated vasculatures [73] and, by convection and diffusion processes, the passive directing of nanomedicine therapeutics into tumors can occur, without any specific ligand attached to the surface of the nanocarrier. However, the passive targeting is not sufficient to control the side effects of cytotoxic drugs and fully exploit the benefits of targeted delivery, because of the heterogeneity of the diseased tissues [74] and the increased interstitial fluid pressure of tumor cells [75]. Instead, the active targeting is based on the functionalization of nanoparticles surface, using appropriate receptor ligands that react with specific site of the disease (for instance, the antigen for an overexpressed receptor on the tumour cell membrane). A wide range of ligands can be used, including small molecules such as folic acid and carbohydrates, or macromolecules such as peptides, proteins or antibodies. The ligand must allow binding to the target diseased cells, while minimizing binding to healthy cells. Moreover, a prolonged circulation of the drug is vital to avoid unwanted interactions with serum proteins or the immune system [76]. However, actively targeted nanoparticles delivery can enhance drug retention in the tumor, due to increased cellular binding, minimize non-specific uptake and, also, circumvent mechanisms of resistance from biological barriers [77].

The last method to achieve a drug release consists in the use of an endogenous or exogenous stimulus to trigger the release of the drug in a determined target site. Stimuli-responsive systems act in response to physical, chemical or biological triggers, that promote release of drugs by modifying the structure or conformation of the nanocarrier. The advantage of using stimuli-responsive systems is that the drug, previously loaded into the nanocarrier, is released through a trigger, thus it is minimized the exposure of the surrounding healthy tissues to the pharmaceutic molecules. Liposomes are particularly suitable for this type of drug delivery [78-80]. Generally, successful examples of stimulus-responsive drug delivery approaches include changes in environmental conditions, as redox potential, pH, osmolality

and temperature, conditions that are found in some diseases. For example, solid tumor tissues exhibit some peculiar pathophysiological characteristics that can be appropriately exploited for the selective delivery and release of drugs [81, 82]. Tumor cells, in fact, express or overexpress often specific membrane receptors and have an altered redox potential. Moreover, due to the high metabolism, solid tumors resemble an inflamed tissue with a higher temperature and a lower pH than those of healthy tissues. Modified liposomes can therefore take advantage of these characteristics to specifically release the drug into the tumor mass. In this regard, a micro-environment, that serves as a trigger for drug release, is the hypoxic area of tumors, exhibiting low oxygen pressure and poor nutrient levels. The low oxygen level can be used for promoting release from redox-responsive nanocarriers [83-85]. pH-sensitive liposomes, instead, stable in physiological condition (pH= 7.4), but destabilized in acid environment such as tumor tissues [86], exploit pH variation for specific site delivery [87, 88]. In detail, at the cellular level, the pH of intracellular organelles (pH= 6.5 - 7.2) differs from that of the cytoplasm or blood; hence pH sensitivity can either induce the release of the transported drug into late endosomes or lysosomes, or promote the escape of the nanocarriers from the lysosomes to the cell cytoplasm (Figure 1.13).

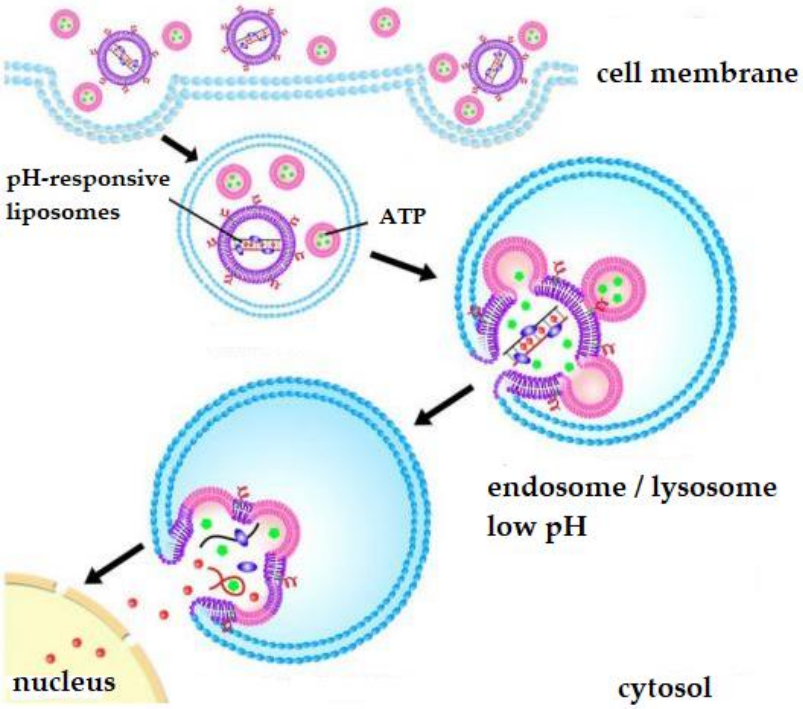


**Figure 1.13. Liposomal drug delivery system mediated by a pH variation of the cell, respect to the physiological level.**

Another kind of destabilization is the temperature increase (at temperatures higher than 37 °C), which can provide a phase transition of the constituent lipids and the associated conformational variations in the lipid bilayers, enhancing the release of the transported compounds (Figure 1.14).

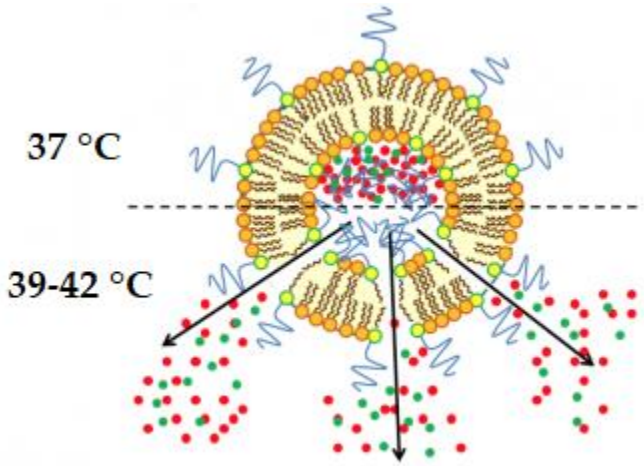


**Figure 1.14. Activation of the liposomal drug delivery system mediated by the temperature increase.**

These kinds of nanocarriers are called thermosensitive liposomes [89, 90] and they can be fabricated not only with phospholipids, but also with polymers as N-isopropylacrylamide (NIPAM), that are able to contribute to the content release depending on the temperature. Thermoresponsive drug delivery is among the most investigated stimuli-responsive strategies, widely explored in oncology. Ideally, thermosensitive liposomes retain their payload at the body temperature (37 °C) and rapidly deliver the drug within a locally heated tumor (40-42 °C), to counteract rapid blood-passage time and washout from the tumor [90, 91]. Also, in the case of thermosensitive liposomes, the increase in temperature can be pursued at the loco-regional level thanks to external stimuli mediated by microwave or magnetic heating [92, 93]. Nevertheless, the slow response time to these stimuli and inability to control drug release dosage, moved to prefer the application of extracorporeal physical stimuli such ultrasounds [94, 95], magnetic [96] or electric field [97, 98]. The advantage of these exogenous stimulations is that the stimuli are generated by machines protocols that can be easily standardized to achieve regulated release [99].

### 1.2.2 Magnetic field stimulus

Magnetic stimulus represents a potential trigger for the remote-controlled release of compounds, thanks to the fact that has the major advantage of penetrating easily in the human tissue without loosing any transmission power. Due to this, recently with the technological progress, the use of magnetic fields to treat inflammatory and neuronal diseases, of therapies and drug delivery systems for nanomedicine considerably increased [100, 101]. The progresses in nanomedicine ranges from nanoparticles for molecular diagnostics, imaging and therapy, to integrated medical nanosystems [102, 103] in order to act at the cellular level inside the body. The advantage of using a magnetic field relies on the different nature that the magnetic response can take, which can be a magnetic guidance under a permanent magnetic field, a temperature increase when an alternating magnetic field is applied, or both of them. Furthermore, in medicine there is the possibility of performing magnetic resonance imaging and hence to associate diagnostics and therapy within a single system, the so-called theranostic approach [104].

In the recent years, a great number of investigations were reported on exploiting the combination of magnetic material with tunable physical properties and liposomes to achieve the synthesis of systems triggerable by the magnetic field. Magnetic nanoparticles (MNPs), based on iron oxide (maghemite $\gamma$–$Fe_2O_3$ or magnetite $Fe_3O_4$), are widely used in nanomedicine, both for their biocompatibility and superparamagnetic properties. The selection of appropriate materials to produce magnetic particles is a very important subject. Ferromagnetic materials, iron oxide (magnetite) for example, are magnetized strongly in the direction of an external magnetic field and tend to retain their magnetization after the external magnetic field remotion. This leads to aggregation of particles and increases the risk of blood vessel thrombosis. But sufficiently small particles, less than 150-200 nm, undergo drastic thermal fluctuations and loose magnetization and tendency to aggregate, immediately after removing the external magnetic field. This phenomenon is called superparamagnetism. This type of nanoparticles is currently being studied for diagnostic and therapeutic applications. The MNPs, in fact, allowed to increase the ability to discern

normal from the diseased tissue if used in magnetic resonance imaging (MRI). Imaging of the liver, lymph nodes, bone marrow, spleen to finish with cardiovascular system, represent some of the main clinical applications of MNPs, given their capacity to accumulate at different sites of the human body, closely linked to their small size. In oncology, MNPs, guided where the neoplasm is present, can oscillate under the action of a variable magnetic field of appropriate intensity, thus generating heat until the critical temperature for survival of the tumor cells. With this type of treatment, known as intracellular hyperthermia, following repeated exposure to the alternating magnetic field, it is possible to obtain the complete tumor regression [105]. The main advantage of this minimally invasive technique is the ability to prevent unwanted heating in healthy tissues, because only MNPs absorb and locate the energy supplied by the magnetic field. Though large-scale studies of pharmacokinetics and toxicity of superparamagnetic particles of magnetite did not reveal any acute or subacute damaging effect and their favorable properties, MNPs show some undesidered effects such as: oxidative stress, unpredictable cellular responses and signal response induction, alteration of gene expression and potential instability of iron homeostasis. Due to their high specific surface area, nanoparticles have low energy barriers, causing them to aggregate and achieve a stabilized state. Aggregation decreases the free surface area of the nanoparticles, thereby reducing their adsorption capacity. Brownian motion of particles further contributes to reducing their effectiveness. To overcome the problems associated with aggregation, it becames extremely important to modify the surface of MNPs for good balancing of high adsorption capacity and nanoparticle stability. To this end, different surface modification approaches were attempted [106]. In this sense, the inclusion of MNPs within phospholipid vesicles could represent a different and interesting approach for improving, at the same time, their stability and reactivity [107].

Liposome-magnetic nanoparticle assemblies represent a promising route for designing multifunctional therapeutic constructs. To prepare magnetoliposomes (MLs), the superparamagnetic particles should be enclosed into lipid vesicles. The first magnetoliposomes and the term itself were suggested by Margolis and colleagues in 1983

[108]. Later, two different types of magnetic liposomes were studied, according to the MNPs locationing in their structure. The first classical type [109] is represented by magnetic spheres occupying the whole space inside of bilayer vesicles, thanks to a hydrophobic coating (Figure 1.15, A). In this type of liposomes, the ratio of magnetic material to lipid is very high. When large quantities of paramagnetic material are endocytosed into the cytoplasm, the lipids can minimize the toxic effect [110]. However, these liposomes do not have a space for drugs. Only compounds dissolved in the lipid bilayer or attached to the surface of the bilayer can be loaded using this type of liposomes. The second type of magnetoliposomes are vesicles of 100-500 nm, containing a suspension of very small superparamagnetic particles with hydrophilic coating in the internal space filled with water [111], (Figure 1.15, B). The advantage of this type of liposomes is the possibility to introduce water soluble compounds inside the internal space of the vesicles, although their magnetizability is not high because the magnetic moment of small particles is decreased [112].

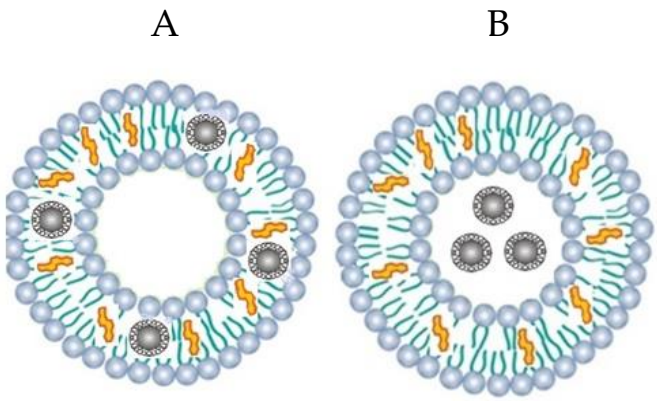


**Figure 1.15. Schematic representation of magnetoliposomes with hydrophobic (A) and hydrophilic (B) MNPs, respectively in the bilayer and in the aqueous core.**

Both types of magnetic hybrid systems, when composed of thermosensitive phospholipids and magneto-heating mediators, show enhanced release of a model drug when exposed to an external alternating current magnetic field (AMF) and negligible release without exposure to the AMF [113, 114]. The release was essentially attributed to the magnetocaloric

effect resulting in the liposome phase transition [96]. The heat generation efficiency of MNPs heavily depends on the particle size and frequency of the external AMF, in particular, when exposed to appropriate magnetic fields of proper strength (1-10 kA/m) and frequency (10-100 kHz), MNPs embedded into liposomes are able to convert magnetic stimulus into heat, either from hysteresis losses or from Neel or Brownian relaxation processes [115], (Figure 1.16).

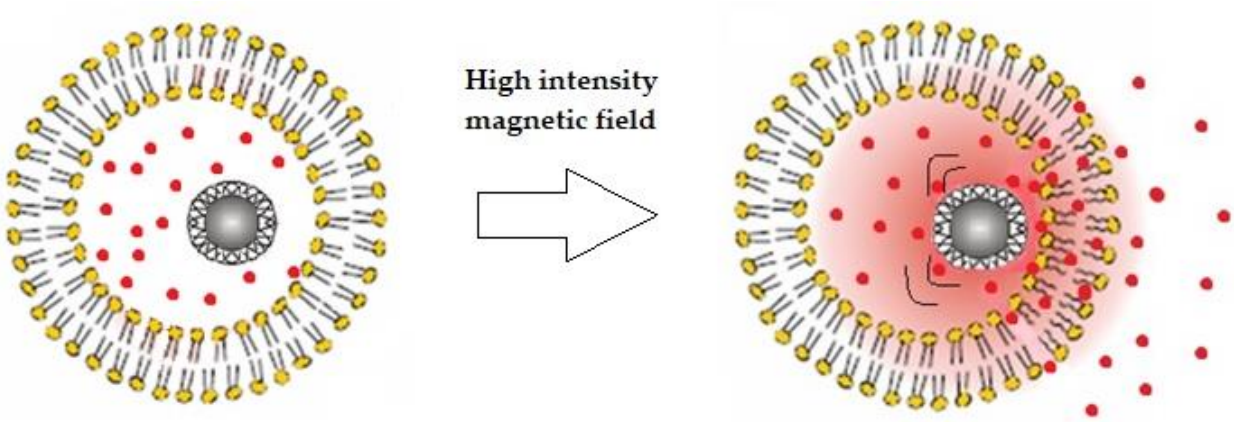


**Figure 1.16. Release from magnetoliposomes induced by an external magnetic field of high intensity.**

The magnetically induced heat is transferred to the entire magneto-carrier, causing temperature increases since tolerable hyperthermia (41-46 °C), with structural changes in the lipid bilayer (from Lβ to Lα phase), which may act as a smart trigger for the drug release [116]. Despite the heat generation is the main pattern of AMF energy consumption, a magnetic field can also induce vibration or rotation of iron oxide particles, hence the oscillating MNPs can mechanically damage membrane of nanoscale actuators (e.g. liposomes).

In particular, was proposed an alternative "magneto-mechanical" explanation to comprehend magnetic controlled release: MNPs motions and oscillations induced by external AMF could improve the bilayer permeability and it could contribute to the magnetocaloric effect, allowing for cargo release. This hypothesis arises from the finding that AMF-induced oscillation of MNPs was proved to be able to mechanically damage

cancer cells *in vitro* [117]. The magneto-mechanical effect produced by the oscillation of the MNPs was extensively addressed to find efficacy for triggering a mechanical disturbance to the cells and therefore for inducing cell death in a non-chemotoxic way. It could find application also for the control of drug release. In order to support this purpose, were deliberately selected field frequencies and strength that are of several orders of magnitude lower than those needed for the magnetic thermal approach. It will allow to reduce the heating contribution of the MNPs in the AMF to negligible levels, with the objective to evaluate the peculiarities and advantages of a non-heating action of MNPs in inducing the release from the carrier. Via the application of an external magnetic field, the idea is to induce a mechanical stress on the liposome membrane (Figure 1.17), thanks to MNPs oscillations, at the same time avoiding the thermal-magnetic stimuli with such temperature increases and magnetically induced eddy currents that can cause undesirable effects to the surrounding tissues, limiting their clinical applicability [118].

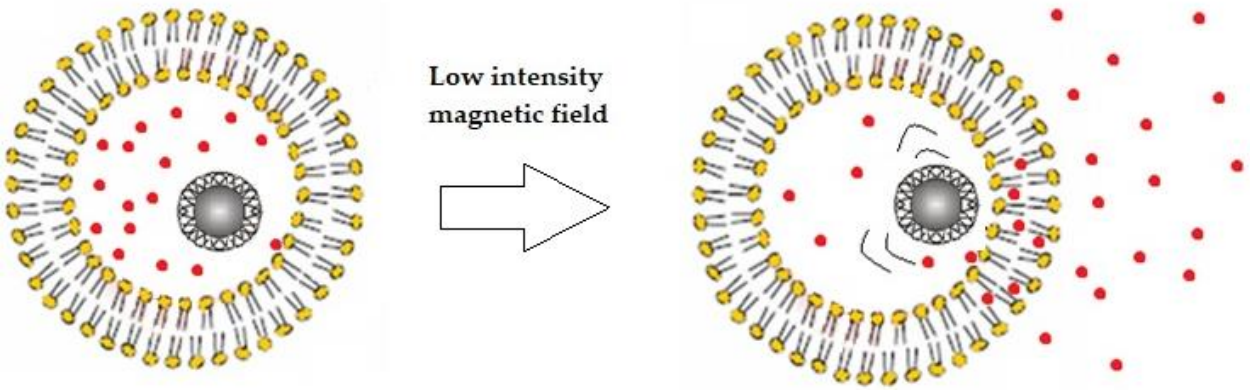


**Figure 1.17. Release from magnetoliposomes induced by an external magnetic field of low intensity.**

In this regard, some studies suggested that, actually, after the application of magnetic fields of low intensities (A/m), the magnetic-impelled motions drive to the destabilization of the bilayer rather than the liposome phase transition or the destruction of the liposome structure [119, 120]. The efficiency of this type of magneto-mechanical approach was further

evaluated using structures defined high-transition temperature liposomes (high-Tm MLs), therefore characterized by membrane that can exist only in the ordered state within the physiological temperature interval and by neither spontaneous leakage nor thermal responsiveness occuring up to 50 °C. In summary, was showed that high-Tm MLs, including in the aqueous core MNPs, respond to a low amplitude magnetic field at temperatures well below the Tm of the bilayer and that the content released from the high-Tm MLs could be triggered repetitively by switching on and off the AMF until almost completely depleting the carrier. The low-intensity AMF triggered release properties hence demonstrated that the drug release from liposomes was due to reversible and controllable permeability change of the bilayer, inducing by the MNPs mechanical stress on the liposomes membrane, in the absence of heating [121].

### 1.2.3 Electric field stimulus

Another challenging way to activate release from liposomes vesicles is the use of pulsed electric fields, which can be considered a useful external stimulus to trigger drug delivery from the carrier and, simultaneously, to achieve the uptake from permeabilized cell membranes as target [122]. Low electric fields (typically about 1 V) can be used to achieve pulsed or sustained drug release through a variety of actuation mechanisms [98, 123].

One of these mechanisms can be an oxidizing voltage activated by the splitting of a vesicle membrane into smaller organelles, like micelles, releasing the cargo and then reassembling on the application of a reductive voltage [124]. For example, iontophoresis, which uses an electric field to enhance the transdermal delivery of charged compounds, is a particularly versatile approach [125, 126] and was recently applied to various types of nanoscaled systems, including liposomes containing insulin [127].

Recently the research on electropulsation technique, which causes the formation of pores in cells membrane, increasing its permeability to molecules that otherwise can not cross them (Figure 1.18), significantly improved the practice of medicine by the use of electric pulses of shorter duration (nanosecond) and higher intensity (in the order of MV/m), which allows to directly interact with internal cell organelles (nucleus, endoplasmic reticulum, mitochondria) [128-132] and, also, with the plasma membrane [133, 134].

The *in vitro* applications on eukaryotic cells, exposed to nanosecond pulsed electric fields (nsPEFs), highlighted how the plasma membrane is more affected with longer pulses than with short pulses, leading to the best uptake of dye molecules after applying single pulses [135].

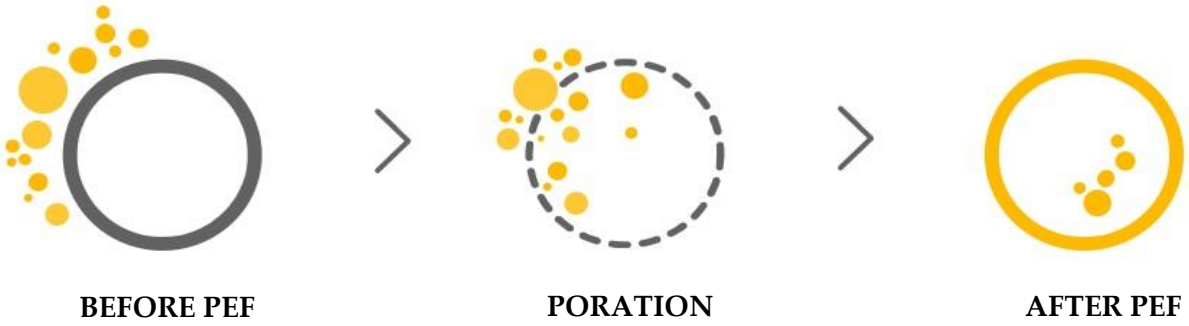


**Figure 1.18. Schematization of drug cellular uptake mediated by electropermeabilization of the cell membrane next to the application of the electric field.**

Other works showed a release of calcium independently of intra-cytoplasmic membrane calcium channels, which was directly linked to the destabilization of organelles envelopes by pulses shorter than 100 ns [136]. One important aspect is the cell viability after the application of nsPEF. Because of their very short duration, nsPEFs do not transfer a large energy to the sample and, thus, the observed effects are probably non-thermal. Anyhow, the destabilization of the cell membrane could cause, depending on the duration and pulse intensity, the cell death. It was demonstrated that for very high intensities of 300 kV/cm and duration of 300 ns, apoptotic phenomena were observed on up to 90% of cell population in less than 10 min following the application of the pulses [137]. Despite of this, reducing the pulse duration to 10 ns or less with intensity in the order of kV/cm, cell membrane could be destabilized without causing cell death [134]. At this regard, was investigated the effects of 4 ns electric pulses duration with intensity of 10 MV/m at 1 kHz of repetition rate and a loss of the mitochondrial membrane potential and a plasma membrane permeabilization was observed, possibly due to the permeabilization of the inner mitochondrial membrane by the nsPEF application [133]. The ability of nsPEF to interact with small internal structures and the similarity of the cell and liposome membrane were the starting points for investigations of nsPEF applicability in drug delivery, using liposomes of small dimensions respect to the cells [13, 138]. Due to the present research activity on the use of electroporation of cells for

different medical applications, the use of nsPEF for potential drug delivery applications can be a promising technique, because it might allow the on-demand release of drugs encapsulated in a nanocarrier (e.g. liposomes), by the application of an appropriate electrical stimulus. In turn, the electric signal allows controlled release and uptake of drugs from liposome to the cell, thanks to the accumulation of charges on both sides of the plasma membrane and consequently the formation of an induced transmembrane voltage (*TMP*), which causes the pore formation and the drug uptake. Previous works analysed the effect of nsPEFs on liposomes characterized by giant dimension [139, 140]. Unfortunately, this kind of liposomes can not be used for drug delivery applications, because they could be recognized as external agent by the immune system with a consequent systemic reaction from the body [141]. In fact, in order to realize a succesfull on-demand drug delivery and to determine a controlled interaction with the biological tissue [136], not only the choice of nsPEF characteristics is important, but also is essential to consider the dimensions of the drug delivery systems. In this regard, a previous study focalized on numerically applying nsPEFs on a biological cell, containing a nucleus and small internalized liposomes, demonstrated the selective electropermeabilization of liposomal and plasma membrane [142]. Lipid vesicles, characterized by different hydrodynamic diameters (from 50 to 500 nm), were placed in different positions into the cell, with different conductivities inside the liposomes. Several durations (4, 10, 20 and 50 ns) of the applied nsPEFs were considered.
Another important issue to be considered is the simultaneous permabilization of liposomes and cell membranes, in order to let the chemical load internalized in the vesicles to be released inside the cells. A recent paper [135] numerically showed the possibility to achieve simultaneous liposomes and cells electropermeabilization, placing liposomal vesicles outside the cell. This arrangement can be promised for a potential liposomal drug delivery system, because it is not necessary to wait for the penetration of liposomes into the cell to obtain a targeted controlled release. Moreover, the analysis evaluated the influence of liposomes diameter, which represents a critical parameter as a compromise between the amplitude of the field and the immune system response. In fact, the dimensional difference

between cells and liposomes is one of the main concerns to achieve a simultaneous permeabilization of the two targets. According to Schwan's equation at steady-state, which is reported below, liposomes are permeabilized by higher intense fields, with respect to the cells, due to the direct proportionality between the transmembrane potential (*TMP*) and the radius (Equation 1.1).

$$TMP = f_s ERcos(\theta) \tag{1.1}$$

In this Equation 1.1, $f_s$ is a function which depends on membrane and extracellular medium properties and $f_s = \frac{3}{2}$ for a spherical structure and physiological conditions; *E* is the external electric field applied; *R* is the radius of cell or liposome structure and $\theta$ is the angle formed with the electric field direction. According to this *TMP* relation, the ratio between cell and liposome radii $R_{cell}/R_{lip}$ (which is typically around 100) determines the ratio between the intensity of the electric fields able to porate the two structures. Schwan's relation is valid in static conditions and at low frequency values, for spherical structures. But the dimension differences between cells and liposomes provide a variation of validity limits of the static approximation in the frequency range. In particular, for cells the validity of static conditions is for frequency values up to hundreds of kHz, while for liposomes is up to tens of MHz. This difference is caused by phenomena occurring in cell, in the range of frequency from hundreds of kHz to tens of MHz.

According to these results, is important to consider a second order model for the *TMP* expression, that is related to the frequency value, as reported in Equation (1.2):

$$TMP(\omega) = f_s(\omega) ERcos(\theta) \tag{1.2}$$

So, the $f_s \neq \frac{3}{2}$ and where other parameters become important [143, 144], such as membrane and extracellular medium properties, so and it can be written as the equation below (Equation 1.3), depending on the frequency value:

$$f_s(\omega) = \frac{3\sigma_{ext}^*[3d_m R^2\sigma_{int}^* + (3d_m^2 R - d_m^3)(\sigma_m^* - \sigma_{int}^*)]}{2R^3(\sigma_m^* + 2\sigma_{ext}^*)\left(\sigma_m^* + \frac{1}{2}\sigma_{int}^*\right) - 2(R - d_m)^3(\sigma_{ext}^* - \sigma_m^*)(\sigma_{int}^* - \sigma_m^*)} \quad (1.3)$$

where $\sigma_i^* = \sigma_i + j\omega\varepsilon_i$, with $i$ which refers to extracellular medium (ext), internal medium (int) and membrane (m).

In this way, the transmembrane potential behaviour in frequency domain is characterized by two poles and two zeros, that depend on the exposed structures parameters (Figure 1.19, B). For electric fields that have a frequency content up to GHz, is important to take into account the dielectric dispersion of the cell/liposome compartments, while for electric field characterized by a duration around 10 ns, the frequency content related has a first lobe at 100 MHz, so the β-relaxation phenomena are just occurred both for cell and liposome, as it is represented in the Figure 1.19 (A).

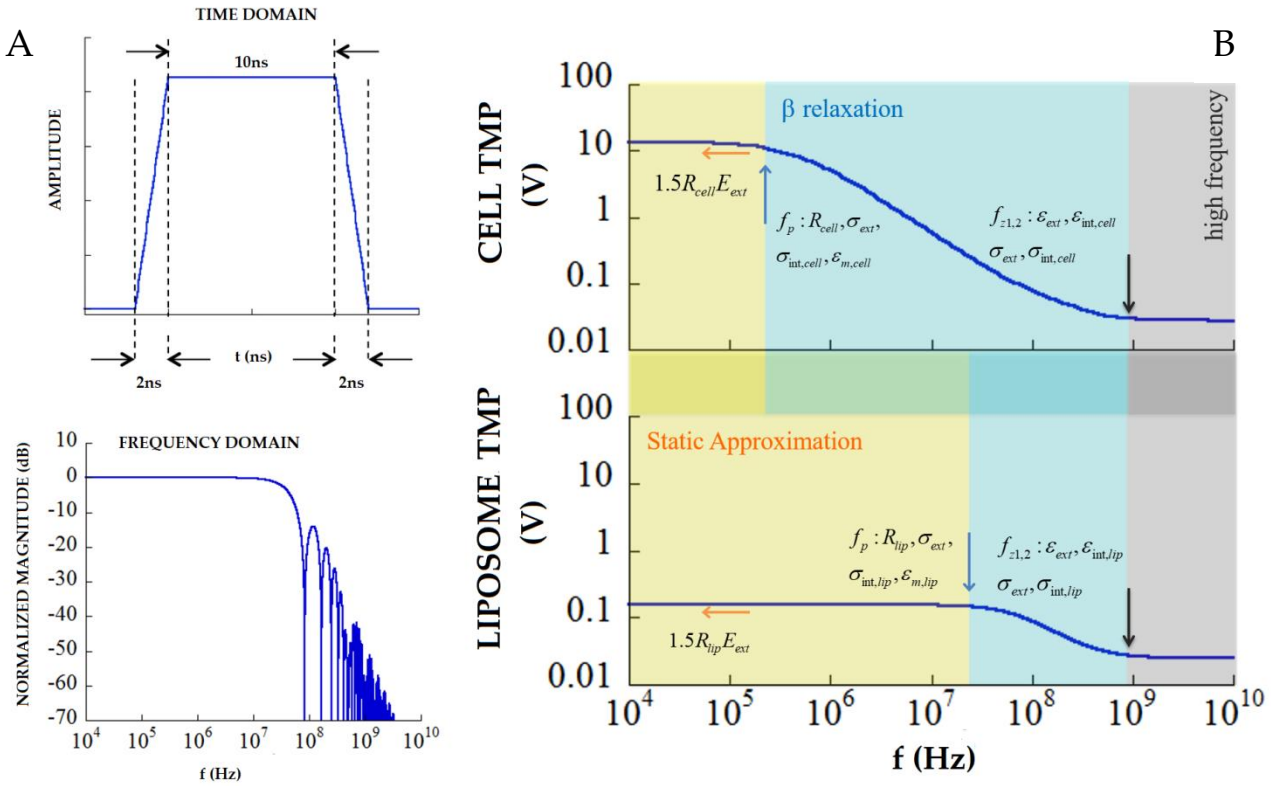


**Figure 1.19. In (A) is shown the applied electric field characterized by a duration of about 10 ns, with rise and fall time of 2ns and the spectrum content of the 10 nsPEF, with the first lobe at 100 MHz. In (B) is illustrated the different TMP as a function of frequency for cell and liposome structure [145].**

In these cases, *TMP* values for cells and liposomes become comparable, leading to a simultaneous electropermeabilization of the two targets.

The paper [145] focalizes the attention on the study of the dimension of liposomes (comparing 100, 200 and 400 nm of diameter) providing a 200 nm diameter as the right compromise, using a 12 nsPEF.

Moreover, through a microdosimetric model, in which are represented a cell and some liposomes around it, the simultaneous poration of cell and vesicles membranes is achieved, as it is shown in the scheme of the Figure 1.20.

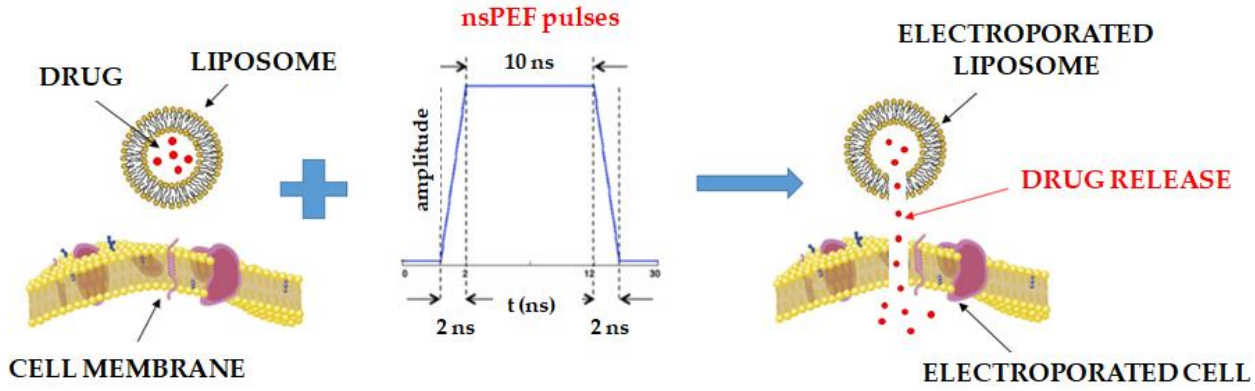


**Figure 1.20. Concept of liposomal drug delivery system mediated by the nano-electroporation.**

From these literature results, the conclusion is that, due to the frequency content of the nsPEF characterized by a duration around 10ns, it is necessary to consider the influence of sample parameters, such as conductivity and permeability of membrane, intracellular and extracellular medium, in order to achieve an efficient electropermeabilization, consequent delivery of compounds from liposomes and uptake through the cell membrane.

### 1.2.4 Methods of liposomes stabilization

Besides liposomes great advantages, as high biocompatibility, biodegradability, toxicity and antigenicity, due to the particular structure and composition of the phospholipid bilayer, one of the major drawbacks in their use, as drug delivery systems, is the instability. Therefore, to satisfy different therapeutic needs and aspects related to the formulation, after their discovery, several generations of liposomes succeeded over time, as a result of multiple manipulations of their composition and structure. The choice of the lipid as well as the structural modifications, together with the optimization of the preparation methods, allowed to obtain products with specific chemical-physical and biopharmaceutical characteristics.

For example, since neutral liposomes tend to easily aggregate and sediment, the use of charged phospholipids permitted to increase the stability of the formulation [146-148]. The presence of a superficial charge determines, in fact, a strong electrostatic repulsion between the phospholipid vesicles, which is opposed to their natural tendency to aggregate and their subsequent sedimentation. A negative surface charge may also reduce the interaction of liposomes with plasma proteins, since the latter generally carries a negative charge. The choice of the charge of liposomes must be made based on the nature of the active substance to be incorporated, on the possible interactions with the components of the biological fluids and on the probable pharmacokinetic implications [149-151]. The changes in the lipid and surface composition led, over the years, to the creation of increasingly stable and particularly selective systems for specific tissues [152-155]. Indeed, changing parameters such as size [156] and type of lipid, or introducing ligands as proteins, polysaccharides, monoclonal antibodies [15, 157-161] with selective activity, able to recognize the pharmacological targets, were strengthened important characteristics for the therapeutic potential of biologically active molecules through the targeted distribution of the carrier system. Moreover, liposomes structure favoured the possibility of making changes to the external surface of the bilayer, bringing to the “stealth” or “long-circulation” liposomes, in order to bypass the rapid elimination from the bloodstream of uncoated systems and to

enhance their stability. In particular, polymers such as polyethylene glycol (PEG), characterized by flexible hydrophilic chains, were grafted on the liposomes surface, forming a protective shell able to prevent, due to steric obstruction, the access and binding of the plasma opsonins on the vesicles surface [162]. In this way, the identification by the endothelial reticular system (RES) is avoided, resulting in a prolonged stability of the liposomes in the bloodstream, after the *in vivo* administration, with the possibility of passive accumulation in other tissues and organs [163, 164]. A multiplicity of synthetic and natural polymers, such as poly (amino acids), heparin, dextran and chitosan, were proposed to replace the PEG [165-167]. Thanks to this approach, numerous formulations of sterically stabilized liposomes were described for the delivery of one or more active ingredients [168-170]. Despite the unquestionable benefits obtained in terms of drug delivery, passing from uncoated liposomes to those characterized by the transformed external surface area, some limitations prevent to fully exploit the potential of these carriers in the field of drug delivery. Sterically stabilized liposomes, considered non-immunogenic initially, were subsequently assessed able to provoke the immune response [171]. Furthermore, they may are linked to the degradation under mechanical stress of the structure and to the increase in blood clearance or unwanted side effects. Therefore, to be able to still consider the liposomes a valid choice for the drug delivery, it is necessary to design and investigate new strategies that allow to make chemical-physical changes on the system and to exceed the limits, further extending the applicability in clinic. More recently, interesting results, in terms of physical stability of the bilayer, were obtained following modifications of the internal liposomes compartment, which aim, in particular, to convert the fluid core of the vesicle into a viscoelastic hydrogel. Based on this assumption, were born novel hybrid nanosystems that possess, at the same time, the characteristics of conventional liposomes, such as biocompatibility and biodegradability and the viscoelasticity typical of the hydrogels. Different terminologies, like supramolecular biovectors (SMBV) [172], lipid-coated microgels [173, 174], lipobeads [175-181], gel-filled vesicles [182], lipogels [183, 184], gel-core liposomes [185], microgel-in-liposomes [186], hydrogel-supported lipid bilayer [187],

nanolipogels particles (nLG) [188], are known in the literature to refer to these hybrid nanostructures, defined in this Ph.D. thesis Gel-in-Liposomes (GiL). This type of formulation resulted from the possibility of inserting hydrophilic polymers also into the aqueous core of liposomes, obtaining, after appropriate cross-linking, the structuring of the polymer in a nanohydrogel of dimensions compatible with those of the vesicular core. It is not difficult to understand how a polymeric network, physically and chemically stable, can provide a valid internal mechanical support to the liposomal membrane, without altering the vesicles structure in dimensions and morphology, mimicking the elastic protein network of the cell cytoskeleton. The ideation of gelled core liposomes helps to improve the mechanical properties and physical stability of the vesicles and, at the same time, to obtain a variation of the release properties of conventional systems, thus increasing the therapeutic potential of these carriers [19]. In fact, the implementation of the mechanical properties of gelled liposomes results in the improvement of the stability system profile in terms of loss of the trapped drug. A necessary condition for avoiding the premature release of the vesicular content, is that the carrier must be stable and able to maintain its structure over time and finally to resist, as a consequence, to the destabilizing action of any surfactants and physiological proteins *in vivo*. The gelled liposomal vesicle may potentially remain intact for longer, preserving the payload from undesirable leakage phenomena. In these structures, not only the stability, but also the permeability can undergo variations. The presence of the polymer could alter the thermotropic properties of the bilayer; the polymer, in fact, according to its characteristics, could be interposed between the phospholipid molecules of one or both layers, modifying the fluidity and permeability of the membranes and/or increasing their stability *in vivo*. The useful combination of lipid and polymeric biomaterials contributes hence to the development of versatile nanostructures, capable of carrying both lipophilic and hydrophilic molecules, for which the release can also be slowed down by diffusion through the hydrogel meshes. Through the gelation of the liposomal core and alterations in the permeability of phospholipid bilayers it is possible, indeed, to obtain nanostructures particularly attractive for applications in the drug delivery field, able to

allow different release profiles. By using polymeric networks responsive to environmental stimuli, it could be exploited the possibility to obtain innovative release modalities from hybrid nanometer vesicles, as the "sponge-like", "poration" and "burst" type [189], potentially useful for the controlled release of drugs.

GiL nanosystems can be realized through two different synthetic strategies:

- polymerization within liposomal nano/microreactor:
  - thermal cross-linking;
  - ionotropic cross-linking;
  - chemical cross-linking;
- hydrogel / liposome mixing.

The first strategy is to use the internal core of the liposome as a chemical reactor for the formation of hydrogel, after the polymerization process (Figure 1.21).

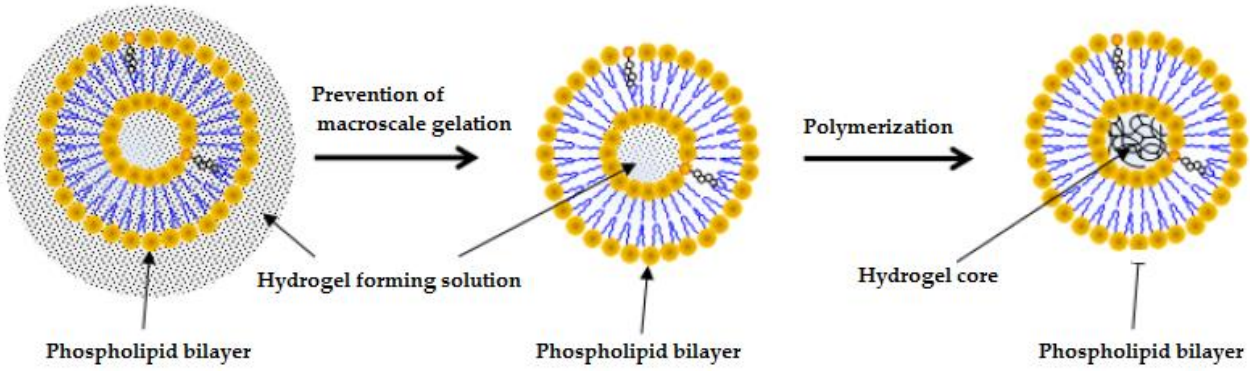


**Figure 1.21. Scheme of synthetic strategy polymerization within liposomal nano/microreactors.**

The components necessary for the formation of the hydrogel are encapsulated within the aqueous core of the liposome during the preparation of vesicles. Prior to crosslinking, to avoid the polymerization reaction outside the liposome, the excess components are removed by purification methods (gel filtration, centrifugation or dialysis) or by the introduction of polymerization scavengers (ascorbic acid) into the extravesicles space. The cross-linking of the polymer precursors is carried out. Finally, to remove the chemical

species that did not take part in the reaction, the formulation is further purified by centrifugation and/or dialysis.

The most common gelation mechanisms include both physical and chemical cross-linking reactions. Some heat-sensitive polysaccharides, such as agarose [190] and k-carrageenan [191], and some heat-sensitive proteins form a reversible gelled-core below a characteristic temperature, which liquefies after heating. Moreover, charged portions of hydrophilic polymers, previously encapsulated in the aqueous core of the liposome, can interact with ions of opposite charge capable of diffusing through the phospholipid bilayer in the fluid state, by means of an electrostatic attraction causing a cross-linking. This type of reaction allowed to obtain GiL structures with hydrogel $Ca^{2+}$-alginate by gelation of the alginate in the liposomal core, using a weak concentration gradient of $Ca^{2+}$ ions [192]. Finally, monomers of hydrophilic polymers, encapsulated in the aqueous core of the liposome, form a strongly crosslinked hydrogel following polymerization, by UV irradiation in the presence of radical photoinitiators [193, 194]. This type of reaction is the most used for the formation of liposomal structures with hydrogel in the inner core [195-197]. The second strategy consists in the formation of the double phospholipid layer on the surface of hydrogel particles, previously prepared, following the mixing of hydrogel particles and liposomal vesicles. In this case, the adsorption of the phospholipid bilayer is promoted through "coulombian attractions" between hydrogels and lipids with opposite charges [198]; hydration of lipid films with a hydrogel suspension [199]; introduction on the surface of the hydrogel of anchors which facilitate the assembly of adsorbed lipids [200]; centrifugation [173]; microfluidic flow [201]; emulsion [186]. Finally, any free liposomes are removed by centrifugation, ultrafiltration or dialysis (Figure 1.22).

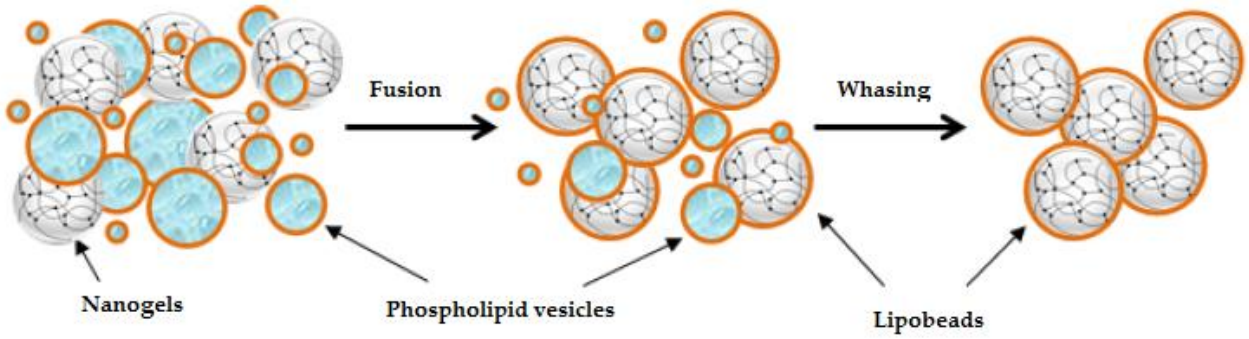


**Figure 1.22. Scheme of the synthetic strategy hydrogel/liposome mixing.**

This method is supported by the high compatibility of hydrogel and phospholipid bilayer, which underlines the spontaneously energetic formation of the gelled structures. Respect to the polymerization within liposomal nano/microreactor, this synthetic strategy does not allow to obtain hydrogels of nanometric dimensions.

## 1.3 References

[1] National Nanotechnology Initiative (NNI). National Science and Technology Council. *Committee on Technology, Subcommittee on Nanoscale Science, National Technology Initiative Strategic Plan*. 25 August 2015, www.nano.gov.

[2] Hulla, J.E.; Sahu, S.C.; Hayes, A.W. *Nanotechnology: History and future. Human and Experimental Toxicology*. 2015, 34(12), 1318–1321.

[3] Nie, S.; Xing, Y.; Kim, G.J.; Simons, J.W. *Nanotechnology applications in cancer*. Annu Rev Biomed Eng. 2007, 9, 257–288.

[4] Jin, T.; Sun, D.; Zhang, H.; Sue, H.J. *Antimicrobial efficacy of zinc oxide quantum dots against Listeria monocytogenes, Salmonella enteritidis and Escherichia coli*. J. Food Sci. 2009, 74, 46–52.

[5] Weiss, J.; Takhistov, P.; McClements, D.J. *Functional materials in food nanotechnology*. J Food Sci. 2006, 71, 107–116.

[6] Moraru, C.I.; Panchapakesan, C.P.; Huang, Q. *Nanotechnology: a new frontier in food science*. Food Technol. 2003, 57, 24–20.

[7] Weltring, G.N.K.M.; Martin, Gramatica Pereira, F.; Baanante, I. *Strategic research and innovation agenda for nano medicine*. ETP Nanomedicine. 2016, 2030.

[8] Kim, K.; Lee, W.G. *Electroporation for nanomedicine: a review*. Journal of Materials Chemistry B. 2017, 5(15), 2726-2738.

[9] Lu, H.; Wang, J.; Wang, T.; Zhong, J.; Bao, Y.; Hao, H. *Recent Progress on Nanostructures for Drug Delivery Applications*. Journal of Nanomaterials. 2016, 1-12.

[10] Murty, B.S.; Shankar, P.; Raj, B.; Rath, B.B. Murday, J. *Unique properties of nanomaterials*. In Textbook of Nanoscience and Nanotechnology. 2012, 29-65.

[11] Xia, Y.; Xiong, Y.; Lim, B.; Skrabalak, S.E. *Shape-controlled synthesis of metal nanocrystals: Simple chemistry meets complex physics?* Angew Chemie International Edition. 2009, 48(1), 60-103.

[12] Kanapathipillai, M.; Brock, A.; Ingber; D.E. *Nanoparticle targeting of anti-cancer drugs that alter intracellular signaling or influence the tumor microenvironment*. Advanced Drug Delivery Reviews. 2014, 79–80, 107–118.

[13] Allen, T.M.; Cullis, P.R. *Liposomal drug delivery systems: from concept to clinical applications*. Adv. Drug Deliver. Rev. 2013, 65(1), 36-48**.**

[14] Al-Jamal, W.T.; Kostarelos, K. *Liposomes: from a clinically established drug delivery system to a nanoparticle platform for theranostic nanomedicine*. Acc Chem Res. 2011, 44(10), 1094-1104.

[15] Torchilin, V.P. *Recent avdances with liposomes as pharmaceutical carriers*. Nat Rev Drug Discov. 2005, 4(2), 145-60.

[16] Vahed, S.Z.; Salehi, R.; Davaran, S.; Shari, S. *Liposome-based drug co-delivery systems in cancer cells.* Materials Science and Engineering: C. 2017, 71, 1327-1341.

[17] Perrier, D.L.; Rems, L.; Boukany, P.E. *Lipid vesicles in pulsed electric fields: Fundamental principles of the membrane response and its biomedical applications*. Advances in Colloid and Interface Science. 2017, 249, 248–271.

[18] Sailor, M.J.; Park, J.H. *Hybrid Nanoparticles for Detection and Treatment of Cancer*. Advanced Materials. 2012, 24, 3779–3802.

[19] Petralito, S.; Spera, R.; Pacelli, S.; Relucenti, M.; Familiari, G.; Vitalone, A.; Paolicelli, P.; Casadei, M.A. *Design and development of PEG-DMA gel-in-liposomes as a new tool for drug delivery*. Reactive and functional polymers. 2014, 77, 30-38.

[20] Dicko, A.; Mayer, L.D.; Tardi, P.G. *Use of nanoscale delivery systems to maintain synergistic drug ratios in vivo*. Expert opinion on drug delivery. 2010, 7(12), 1329-1341.

[21] Malekigorji, M.; Curtis, A.D.M.; Hoskins, C. *The use of iron oxide nanoparticles for pancreatic cancer therapy*. J. Nanomed. Res. 2014, 1(1), 1-12.

[22] Zhu, L.; Torchilin, V.P. *Stimulus-responsive nanopreparations for tumor targeting*. Integrative Biology. 2013, 5(1), 96-107.

[23] Lasic, D.D. *Liposomes from Physics to Applications*. Biphysical Jourmal Volume. 1993, 67, 1358-1362.

[24] Pattni, B.S.; Chupin, V.V.; Torchilin, V.P. *New Developments in Liposomal Drug Delivery*. Chemical Reviews. 2015, 115 (19), 10938-10966.

[25] Bangham, D.; Standish, M.M.; Watkins, J.C. *Diffusion of univalent ions across the lamellae of swollen phospholipids*. Journal of Molecular Biology. 1965, 13(1), 238-252.

[26] Abolfazl, A.; Rogaie, R.S.; Soodabeh, D.; Sang, W.J.; Nosratollah, Z.; Younes, H.; Mohammad, S.; Mohammad, K.; Kazem, N.K. *Liposome: classification, preparation, and applications*. Nanoscale Research Letters 2013, 8, 102.

[27] Elbayoumi, T.A.; Torchilin, V.P. *Current trends in liposome research*. Methods in Molecular Biology. 2010, 605, 1-27.

[28] Sharma, A.; Uma, S. *Liposomes in drug delivery: progress and limitations*. International Journal of Pharmaceutics. 1997, 154(2), 123- 140.

[29] Li,J.; Wang, X.; Zhang, T.; Wang, C.; Huang, Z.; Luo, X.; Deng, Y. *A review on phospholipids and their main applications in drug delivery systems*. Asian Journal of Pharmaceutical Sciences. 2015, 10(2), 81-98.

[30] Demel, R.A.; van Deenen, L.L.; Pethica, B.A. Biochim. Biophys. Acta. 1967, 135, 11.

[31] Joos, P.; Demel, R.A. *The interaction energies of cholesterol and lecithin in spread mixed monolayers at the air-water interface*. Biochim. Biophys. Acta.1969, 183(3), 447-457.

[32] Bush, S.F.; Levin, H.; Levin, I.W. *Cholesterol-lipid interactions: An infrared and raman spectroscopic study of the carbonyl stretching mode region of 1,2-dipalmitoyl phosphatidylcholine bilayers*. Chem. Phys. Lipids. 1980, 27(2), 101-111.

[33] Clejan, S.; Bittman, R.; Deroo, P.W.; Isaacson, Y.A.; Rosenthal, A.F. *Permeability properties of sterol-containing liposomes from analogues of phosphatidylcholine lacking acyl groups*. Biochemistry. 1979, 18(10), 2118-2125.

[34] Demel, R.A. De Kruyff, B. *The function of sterols in membranes*. Biochim. Biophys. Acta. 1976, 457, 109-132.

[35J Rubenstein, L.R.; Smith, B.A.; McConnell, H.M. *Lateral diffusion in binary mixtures of cholesterol and phosphatidylcholines.* Proc. Natl. Acad. Sci. 1979, 76(1), 15-18.

[36] Kuo, A.L.; Wade, C.G. *Lipid lateral diffusion by pulsed nuclear magnetic resonance*. Biochemistry. 1979, 18(11), 2300-2308.

[37] Chang, H.; Yeh, M. *Clinical development of liposome-based drugs: formulation, characterization, and therapeutic efficacy*. International Journal of Nanomedicine. 2012, 7, 49–60.

[38] McIntosh T.J. *Differences in hydrocarbon chain tilt between hydrated phosphatidylethanolamine and phosphatidylcholine bilayers. A molecular packing model*. Biophysical Journal. 1980, 29, 237–245.

[39] Taylor, K.M.G.; Morris, R. M. *Thermal analysis of phase transition behaviour in liposomes*. Thermochimica Acta. 1995, 248, 289-301.

[40] de Vries, A.H.; Yefimov, S.; Mark, A.E.; Marrink, S.J. *Molecular structure of the lecithin ripple phase*. Proceedings of the National Academy of Science USA. 2005, 102, 5392-5396.

[41] Heimburg, T. *A Model for the Lipid Pretransition: Coupling of Ripple Formation with the Chain-Melting Transition*. Biophysical Journal. 2000, 78(3), 1154-1165.

[42] Samad, A.; Sultana, Y.; Aqil, M. *Liposomal drug delivery systems: an update review*. Curr Drug Deliv. 2007, 4(4), 297-305.

[43] Ikeda, A.; Kawai, Y.; Kikuchi, J.; Akiyama, M.; Nakata, E.; Uto, Y.; Hori, H. *Formation and regulation of fullerene-incorporation in liposomes under the phase transition temperature*. Org Biomol Chem. 2011, 9(8), 2622-2627.

[44] Contreras, F.X.; Sot, J.; Ruiz-Argu¨ ello, M.B.; Alonso, A.; Goñi, F.M. *Cholesterol modulation of sphingomyelinase activity at physiological temperatures*. Chem Phys Lipids. 2004, 130(2), 127-134.

[45] Ipsen, J.H.; Karlstrom, G.; Mouritsen, O.G.; Wennerstrom, H.; Zuckermann, M.J. *Phase equilibria in the phosphatidylcholine-cholesterol system*. Biochimica et Biophysica Acta. 1987, 905, 162-172.

[46] Almeida, P.F.; Vaz, W.L.; Thompson, T.E. *Percolation and diffusion in three-component lipid bilayers: effect of cholesterol on an equimolar mixture of two phosphatidylcholines*. Biophysical Journal. 1993, 64, 399-412.

[47] Filippov, A.; Orädd, G.; Lindblom, G. *The effect of cholesterol on the lateral diffusion of phospholipids in oriented bilayers*. Biophysical Journal. 2003, 84, 3079-3086.

[48] Gally, H.U.; Seelig, A.; Seelig, J. *Cholesterol-induced rod-like motion of fatty acyl chains in lipid bilayers: a deuterium magnetic resonance study*. Hopp-Seyler's Z. Physiol. Chem. 1976, 357, 1447-1450.

[49] Sankaram, M.B.; Thompson, T.E. *Modulation of phospholipid acyl chain order by cholesterol. A solid-state 2H nuclear magnetic resonance study*. Biochemistry. 1990, 29, 10676-10684.

[50] Vist, M.E.; Davis, J.H. *Phase equilibria of cholesterol/dipalmitoylphosphatidylcholine mixtures: 2H nuclear magnetic resonance and differential scanning calorimetry*. Biochemistry. 1990, 29, 451-464.

[51] Sankaram, M.B.; Thompson, T.E. *Cholesterol-induced fluid-phase immiscibility in membranes*. Proceedings of the National Academy of Science USA. 1991, 88, 8686-8690.

[52] Ahmed, S.N.; Brown, D.A.; London, E. *On the origin of sphingolipid/cholesterol-rich detergent-insoluble cell membranes: physiological concentrations of cholesterol and sphingolipid induce formation of a detergent-insoluble, liquid-ordered lipid phase in model membranes*. Biochemistry. 1997, 36, 10944-10953.

[53] Genz, A.; Holzwarth, J. F.; Tsong, T. Y. *The influence of unilamellar dipalmytoylphosphatidylcholine vescicles*. Biophysical Journal. 1986, 50, 1043-1051.

[54] Xing, H.; Hwang, K.; Lu, Y. *Recent developments of liposomes as nanocarriers for theranostic applications*. Theranostics. 2016, 6(9), 1336-1352.

[55] Plotnick, A.N. *Lipid-based formulations of amphotericin B*. J Am Vet Med Assoc. 2000, 216, 838-841.

[56] Svenson, S. *Clinical translation of nanomedicines*. Curr Opin Solid St M. 2012, 16, 287-294.

[57] Maeda, H.; Sawa, T.; Konno, T. *Mechanism of tumor-targeted delivery of macromolecular drugs, including the EPR effect in solid tumor and clinical overview of the prototype polymeric drug SMANCS*. J Control Release. 2001, 74, 47-61.

[58] Allen. C.; Dos Santos, N.; Gallagher, R.; Chiu, G.N.C.; Shu, Y.; Li, W.M. Johnstone, S.A.; Janoff, A.S.; Mayer, L.D.; Webb, M.S.; Bally, M.B. *Controlling the physical behaviour and biological performance of liposome formulations through use of surface grafted poly(ethylene glycol)*. Bioscience Rep. 2002, 22, 225-250.

[59] Caliceti, P.; Veronese, F.M. *Pharmacokinetic and biodistribution properties of poly(ethylene glycol)-protein conjugates*. Adv Drug Deliver Rev. 2003, 55, 1261-1277.

[60] Barenholz, Y. *Doxil(R)--the first FDA-approved nano-drug: lessons learned*. J Control Release. 2012, 160, 117-34.

[61] Gabizon, A.; Shmeeda, H.; Barenholz, Y. *Pharmacokinetics of pegylated liposomal Doxorubicin: review of animal and human studies*. Clin Pharmacokinet. 2003, 42, 419-436.

[62] Muthu, M.S.; Singh, S. *Targeted nanomedicines: Effective treatment modalities for cancer, aids and brain disorders*. Nanomedicine (Lond). 2009, 4(1), 105–118.

[63] Malam, Y.; Loizidou, M.; Seifalian, A.M. *Liposomes and nanoparticles: nanosized vehicles for drug delivery in cancer*. Trends Pharmacol Sci. 2009, 30(11), 592-599.

[64] Lian, T.; Ho, R.J. *Trends and developments in liposome drug delivery systems*. J Pharm Sci. 2001, 90, 667-680.

[65] Bertrand, N.; Wu, J.; Xu, X.; Kamaly, N.; Farokhzad, O.C. *Cancer nanotechnology: the impact of passive and active targeting in the era of modern cancer biology*. Adv Drug Deliver Rev. 2014, 66, 2-25.

[66] Çağdaş, M.; Demir Sezer, A.; Bucak S. *Liposomes as Potential Drug Carrier Systems for Drug Delivery, Application of Nanotechnology in Drug Delivery*. PhD. Ali Demir Sezer (Ed.). 2014, ISBN: 978-953-51-1628-8, InTech, DOI: 10.5772/58459.

[67] Zhang, L.F.; Granick, S. *How to stabilize phospholipid liposomes (using nanoparticles)*. Nano Lett. 2006, 6, 694-698.

[68] Michel, R.; Plostica, T.; Abezgauz, L.; Danino, D.; Gradzielski, M. *Control of the stability and structure of liposomes by means of nanoparticles*. Soft Matter. 2013, 9, 4167-4177.

[69] Liu, J.W.; Jiang, X.M.; Ashley, C.; Brinker, C.J. *Electrostatically Mediated Liposome Fusion and Lipid Exchange with a Nanoparticle-Supported Bilayer for Control of Surface Charge, Drug Containment, and Delivery*. J Am Chem Soc. 2009, 131, 7567-7569.

[70] Liu, J.W.; Stace-Naughton, A. Jiang, X.M.; Brinker, C.J. *Porous Nanoparticle Supported Lipid Bilayers (Protocells) as Delivery Vehicles*. J Am Chem Soc. 2009, 131, 1354-1355.

[71] Mirza, A.Z.; Siddiqui, F.A. *Nanomedicine and drug delivery: a mini review*. International Nano Letters. 2014, 4(1), 94.

[72] Yatoo, M.I.; Saxena, A.; Malik, M.H.; Kumar, M.K.; Dimri, U. *Nanotechnology based drug delivery at cellular level: a review*. J Anim Sci Adv. 2014, 4(2), 705-709.

[73] Jain, R.K.; Stylianopoulos, T. *Delivering nanomedicine to solid tumors*. Nature reviews Clinical oncology. 2010, 7(11), 653-664.

[74] Prabhakar, U.; Maeda, H.; Jain, R.K.; Sevick-Muraca, E.M.; Zamboni, W.; Farokhzad, O.C.; Barry, S.T.; Gabizon, A.; Grodzinski, P. *Considerations of the enhanced permeability and retention effect for nanomedicine drug delivery in oncology*. Cancer Research. 2013, 73(8), 2412-2417.

[75] Lammers, T.; Kiessling, F.; Hennink, W.E.; Storm, G. *Drug targeting to tumors: principles, pitfalls and (pre-) clinical progress*. Journal of controlled release. 2012, 161(2), 175-187.

[76] Detampel, P.; Witzigmann, D.; Krahenbuhl, S.; Huwyler, J. *Hepatocyte targeting using pegylated asialofetuin-conjugated liposomes*. Journal of drug targeting. 2014, 22(3), 232-241.

[77] Xiang, T.; Anderson, B.D. *Liposomal drug transport: a molecular perspective from molecular dynamics simulations in lipid bilayers*. Advanced drug delivery reviews. 2006, 58(12), 1357-1378.

[78] Seigneuric, R.; Markey, L.; Nuyten, D.S.A.; Dubernet, C.; Evelo, C.T.A.; Finot, E.; Garrido, C. *From nanotechnology to nanomedicine: applications to cancer research*. Current Molecular Medicine. 2010, 10(7), 640-652.

[79] Stuart, M.A.C.; Huck, W.T.S.; Genzer, J.; Muller, M.; Ober, C.; Stamm, M.; Sukhorukov, G.B.; Szleifer, I.; Tsukruk, V.V.; Urban, M.; Winnik, F.; Zauscher, S.; Luzinov, I.; Minko, S. *Emerging applications of stimuli-responsive polymer materials*. Nature materials. 2010, 9(2), 101-113.

[80] van der Meel, R.; Vehmeijer, L.J.C.; Kok, R.J.; Storm, G.; van Gaal, E.V.B. *Ligand-targeted particulate nanomedicines undergoing clinical evaluation: current status*. Advanced drug delivery reviews. 2013, 65(10), 1284-1298.

[81] Andresen, T.L.; Jensen, S.S.; Jørgensen, K. *Advanced strategies in liposomal cancer therapy: Problems and prospects of active and tumor specific drug release*. Progress in Lipid Research. 2005, 44 (1), 68-97.

[82] Blenke, O. E.; Mastrobattista, E.; Schiffelers, R. M. *Strategies for triggered drug release from tumor targeted liposomes*. Expert Opinion on Drug Delivery. 2013, 10 (10), 1399-1410.

[83] Fleige, E.; Quadir, M.A.; Haag, R. *Stimuli-responsive polymeric nanocarriers for the controlled transport of active compounds: concepts and applications*. Advanced drug delivery reviews. 2012, 64(9), 866-884.

[84] Koo, A.N.; Lee, H.J.; Kim, S.E.; Chang, J.H.; Park, C.; Kim, C.; Park, J.H.; Lee, S.C. *Disulfide-cross-linked peg-poly (amino acid) s copolymer micelles for glutathione-mediated intracellular drug delivery*. Chemical Communications. 2008, (48), 6570-6572.

[85] Li, Y.; Xiao, K.; Luo, J.; Xiao, W.; Lee, J.S.; Gonik, A.M.; Kato, J.; Dong, T.A.; Lam, K.S. *Well-defined, reversible disulfide cross-linked micelles for on-demand paclitaxel delivery*. Biomaterials. 2011, 32(27), 6633-6645.

[86] Gao, G.H.; Park, M.J.; Li, Y.; Im, G.H.; Kim, J.H.; Kim, H.N.; Lee, J.W.; Jeon, P.; Bang, O.Y.; Lee, J.H.; Lee, D.S. *The use of ph-sensitive positively charged polymeric micelles for protein delivery*. Biomaterials. 2012, 33(35), 9157-9164.

[87] Chiang, Y.T.; Lo, C.L. *pH-Responsive polymer-liposomes for intracellular drug delivery and tumor extracellular matrix switched-on targeted cancer therapy*. Biomaterials. 2014, 35(20), 5414-5424.

[88] Li, T.; Amari, T.; Semba, K.; Yamamoto, T.; Takeoka, S. *Construction and evaluation of pH-sensitive immunoliposomes for enhanced delivery of anticancer drug to ErbB2 over-expressing breast cancer cells*. Nanomedicine: Nanotechnology, Biology and Medicine. 2017, 13 (3), 1219-1227.

[89] Lee, S.H.; Choi, S.H.; Kim, S.H.; Park, T.G. *Thermally sensitive cationic polymer nanocapsules for specific cytosolic delivery and efficient gene silencing of sirna: swelling induced physical disruption of endosome by cold shock*. Journal of Controlled Release. 2008, 125(1), 25-32.

[90] Al-Ahmady, Z.S.; Al-Jamal, W.T.; Bossche, J.V.; Bui, T.T.; Drake, A.F.; Mason, A.J.; Kostarelos, K. *Lipid peptide vesicle nanoscale hybrids for triggered drug release by mild hyperthermia in vitro and in vivo*. ACS nano. 2012, 6(10), 9335-9346.

[91] Tagami, T.; Foltz, W.D.; Ernsting, M.J.; Lee, C.M.; Tannock, I.F.; May, J.P.; Li, S.D. *Mri monitoring of intratumoral drug delivery and prediction of the therapeutic effect with a multifunctional thermosensitive liposome.* Biomaterials. 2011, 32(27), 6570-6578.

[92] Lu, T.; Lokerse, W.J.; Seynhaeve, A. L.; Koning, G. A.; ten Hagen, T. L. *Formulation and optimization of idarubicin thermosensitive liposomes provides ultrafast triggered release at mild hyperthermia and improves tumor response*. Journal of Controlled Release. 2015, 220(A), 425-437.

[93] Al-Ahmady, Z.; Lozano, N.; Mei, K.C.; Al-Jamal, W. T.; Kostarelos, K. *Engineering thermosensitive liposome-nanoparticle hybrids loaded with doxorubicin for heat-triggered drug release*. International Journal oh Pharmaceutics. 2016, 514 (1), 133-141.

[94] Schroeder, A.; Honen, R.; Turjeman, K.; Gabizon, A.; Kost, J.; Barenholz, Y. *Ultrasound triggered release of cisplatin from liposomes in murine tumors*. Journal of controlled release. 2009 137(1), 63-68.

[95] Kheirolomoom, A.; Mahakian, L.M.; Lai, C.Y.; Lindfors H.A.; Seo, J.W.; Paoli, E.E.; Watson, K.D.; Haynam, E.M.; Ingham, E.S.; Xing, L.; Cheng, R.H.; Borowsky, A.D.; Cardiff, R.D.; Ferrara, K.W. *Copper-doxorubicin as a nanoparticle cargo retains efficacy with minimal toxicity*. Molecular Pharmaceutics. 2010, 7(6), 1948-1958.

[96] Plassat, V.; Wilhelm, C.; Marsaud, V.; Menager, C.; Gazeau, F.; Renoir, J.M.; Lesieur, S. Anti-*estrogen-loaded superparamagnetic liposomes for intracellular magnetic targeting and treatment of breast cancer tumors*. Advanced Functional Materials. 2011, 21(1), 83-92.

[97] Lu, Y.; Sun, W.; Gu, Z. *Stimuli-responsive nanomaterials for therapeutic protein delivery*. Journal of controlled release. 2014, 194, 1-19.

[98] Liu, K.H.; Liu, T.Y.; Chen, S.Y.; Liu, D.M. *Drug release behavior of chitosan-montmorillonite nanocomposite hydrogels following electrostimulation*. Acta Biomaterialia. 2008, 4(4), 1038-1045.

[99] Mura, S.; Nicolas, J.; Couvreur, P. *Stimuli-responsive nanocarriers for drug delivery*. Nature materials. 2013, 12(11), 991-1003.

[100] Ross, C.L. *The use of magnetic field for the reduction of inammation: a review of the history and therapeutic results*. Alternative therapies in health and medicine. 2013, 19(2), 47-54.

[101] Rodzinski, A.; Guduru, R.; Stimphil, E.; Stewart, T.; Liang, P.; Runowicz, C.; Khizroev, S. *Targeted, controlled anticancer drug delivery and release with magnetoelectric nanoparticles*. Sci Rep. 2016, 6, 20867.

[102] Nune, S.K.; Gunda, P.; Thallapally, P.K.; Lin, Y.Y.; Forrest, M.L.; Berkland, C.J. *Nanoparticles for biomedical imaging*. Expert opinion on drug delivery. 2009, 6(11), 1175-1194.

[103] Shi, C.; Kendall, S.C.; Grote, E.; Kaminskyj, S.; Loewen, M.C. *N-terminal residues of the yeast pheromone receptor, Ste2p, mediate mating events independently of G1-arrest signaling*. J Cell Biochem. 2009, 107(4), 630-638.

[104] Yang, H.W.; Hua, M.Y.; Liu, H.L.; Huang, C.Y.; Tsai, R.Y.; Lu, Y.J.; Chen, J.Y.; Tang, H.J.; Hsien, H.Y.; Chang, Y.S.; Yen, T.C.; Chen, P.Y.; Wei, K.C. *Self-protecting core-shell*

*magnetic nanoparticles for targeted, traceable, long half-life delivery of bcnu to gliomas*. Biomaterials. 2011, 32(27), 6523-6532.

[105] Handy, B. C. *Clinical applications of nanotechnologies to the diagnosis and therapy of tumors*. Journal of Clinical Ligand Assay (Italian Ed.). 2006, 29(3).

[106] Hu, Z.; Potthoff, B.; Hollenberg, C.P.; Ramezani-Rad M. *Mdy2, a ubiquitin-like (UBL)-domain protein, is required for efficient mating in Saccharomyces cerevisiae*. J Cell Sci. 2006, 119, 326-338.

[107] Petralito, S.; Spera, R.; Memoli, A.; D'Inzeo, G.; Liberti, M.; Apollonio, F. *Preparation and characterization of lipid vesicles entrapping iron oxide nanoparticles*. Asia-Pacific J. Chem. Eng. 2012, 7, 335–341.

[108] Margolis, L.B.; Namiot, V.A.; Kljukin, L.M. *Magnetoliposomes: Another principle of cell sorting*. Biochim. Biophys. Acta. 1983, 735, 193-195.

[109] De Cuyper, M.; Joniau, M. *Magnetoliposomes. Formation and structural characterization*. Eur. Biophys. J. 1988, 15, 311-319.

[110] Soenen, S.J.; Baert, J.; de Cuyper, M. *Optimal conditions for labelling of 3T3 fibroblasts with magnetoliposomes without affecting cellular viability*. Chembiochem. 2007, 8(17), 2067-2077.

[111] Martina, M.S.; Fortin, J.P.; Menager, C.; Clement, O.; Barratt, G.; Grabielle-Madelmont, C.; Gazeau, F.; Cabuil, V.; Lesieur, S. *Generation of superparamagnetic liposomes revealed as highly efficient MRI contrast agents for in vivo imaging*. J. Am. Chem. Soc. 2005, 127(30), 10676-10685.

[112] Tarahovsky, Y.S. *"Smart" Liposomal Nanocontainers in Biology and Medicine*. Biochemistry (Mosc). 2010, 75, 811-824.

[113] Pradhan, P.; Giri, J.; Rieken, F.; Koch, C.; Mykhaylyk, O.; Doblinger, M.; Banerjee, R.; Bahadur, D.; Plank, C. *Targeted temperature sensitive magnetic liposomes for thermo-chemotherapy*. Journal of Controlled Release. 2010, 142(1), 108-112.

[114] Preiss, M.R.; Bothun, G.D. *Stimuli-responsive liposome-nanoparticle assemblies.* Expert opinion on drug delivery. 2011, 8(8), 1025-1040.

[115] Guardia, P.; Di Corato, R.; Lartigue, L.; Wilhelm, C.; Espinosa, A.; Garcia-Hernandez, M.; Gazeau, F.; Manna, L.; Pellegrino, T. *Water-soluble iron oxide nanocubes with high values of specific absorption rate for cancer cell hyperthermia treatment*. ACS nano. 2012, 6(4), 3080-3091.

[116] Yatvin, M.B.; Weinstein, J.N.; Dennis, W.H.; Blumenthal, R. *Design of liposomes for enhanced local release of drugs by hyperthermia*. Science. 1978, 202(4374),1290-1293.

[117] Cheng, D.; Li, X.; Zhang, G.; Shi, H. *Morphological effect of oscillating magnetic nanoparticles in killing tumor cells*. Nanoscale research letters. 2014, 9(1), 195.

[118] Gupta, A.K.; Naregalkar, R.R.; Vaidya, V.D.; Gupta, M. *Recent advances on surface engineering of magnetic iron oxide nanoparticles and their biomedical applications*. Nanomedicine. 2010, 2, 23–39.

[119] Nappini, S.; Baldelli Bombelli, F.; Bonini, M.; Norden, B.; Baglioni, P. *Magnetoliposomes for controlled drug release in the presence of low-frequency magnetic field*. Soft Matter. 2010, 6(1), 154-162.

[120] Spera, R.; Petralito, S.; Liberti, M.; Merla, C.; d'Inzeo, G.; Pinto, R.; Apollonio, F. *Controlled release from magnetoliposomes aqueous suspensions exposed to a low intensity magnetic field*. Bioelectromagnetics. 2014, 35(4), 309-312.

[121] Spera, R.; Apollonio, F.; Liberti, M.; Paffi, A.; Merla, C.; Pinto, R.; Petralito, S. *Controllable release from high-transition temperature magnetoliposomes by low-level magnetic stimulation*. Colloids and Surfaces B: Biointerfaces. 2015, 131,136-140.

[122] Napotnik, T.B.; Rebersek, M.; Vernier, P.T.; Mali, B. Miklavčič, D. *Effects of high voltage nanosecond electric pulses on eukaryotic cells (in vitro): a systematic review*. Bioelectrochemistry. 2016, 110, 1-12.

[123] Im et al. 2010.

[124] Kim, W.; Brooks, D.M.; Wei, G.Y. *A fully-integrated 3-level DC/DC converter for nanosecond-scale DVS with fast shunt regulation*. In Solid-State Circuits Conference Digest of Technical Papers (ISSCC). IEEE International. IEEE. 2011. 268–270.

[125] Ita, K. *Transdermal iontophoretic drug delivery: advances and challenges*. Journal of Drug Targeting. 2016, 24(5), 386-391.

[126] Malinovskaja-Gomez, K.; Espuelas, S.; Garrido, M.J.; Hirvonen, J.; Laaksonen, T. *Comparison of liposomal drug formulations for transdermal iontophoretic drug delivery*. European Journal of Pharmaceutical Sciences. 2017, 106, 294-301.

[127] Chen, H.; Zhua, H.; Zheng, J.;Mou D.; Wan J.; Zhang, J.;Shi T.;Zhao, Y.; Xu, H.;Yang, X. *Iontophoresis-driven penetration of nanovesicles through microneedle-induced skin microchannels for enhancing transdermal delivery of insulin*. Journal of Controlled Release. 2009, 139(1), 63-72.

[128] Denzi, A.; Merla, C.; Camilleri, P.; Paffi, A.; d'Inzeo, G.; Apollonio, F.; Liberti, M. *Microdosimetric study for nanosecond pulsed electric fields on a cell circuit model with nucleus*. The Journal of membrane biology. 2013, 246(10), 761-767.

[129] Beebe, S.J.; White, J.; Blackmore, P.F.; Deng, Y.; Somers, K.; Schoenbach, K.H. *Diverse effects of nanosecond pulsed electric fields on cells and tissues*. DNA and cell biology. 2003, 22(12), 785-796.

[130] Scarlett, S.S.; White, J.A.; Blackmore, P.F.; Schoenbach, K.H.; Kolb, J.F. *Regulation of intracellular calcium concentration by nanosecond pulsed electric fields*. Biochimica et Biophysica Acta (BBA)-Biomembranes. 2009, 1788(5), 1168-1175.

[131] Breton, M.; Mir, L.M. *Microsecond and nanosecond electric pulses in cancer treatments*. Bioelectromagnetics. 2012, 33(2), 106-123.

[132] Weaver, J.C.; Smith, K.C.; Esser, A.T.; Son, R.S.; Gowrishankar, T.R. *A brief overview of electroporation pulse strength-duration space: a region where additional intracellular effects are expected*. Bioelectrochemistry. 2012, 87, 236-243.

[133] Napotnik, T.B.; Wu, Y.H.; Gundersen, M.A.; Miklavcic, D.; Vernier, P.T. *Nanosecond electric pulses cause mitochondrial membrane permeabilization in jurkat cells*. Bioelectromagnetics. 2012, 33(3), 257-264.

[134] Chopinet, L.; Rols, M.P. *Nanosecond electric pulses: A mini-review of the present state of the art*. Bioelectrochemistry. 2015, 103, 2-6.

[135] Denzi, A.; Della Valle, E.; Esposito, G.; Mir, L.M.; Apollonio, F.; Liberti, M. *Technological and Theoretical Aspects for Testing Electroporation on Liposomes*. Biomed Res Int. 2017. Article ID 5092704, 10 pages.

[136] Vernier, P.T.; Sun, Y.; Marcu, L.; Salemi, S.; Craft, C.M.; Gundersen, M.A. *Calcium bursts induced by nanosecond electric pulses*. Biochemical and biophysical research communications. 2003, 310(2), 286-295.

[137] Beebe, S.J.; Fox, P.M.; Rec, L.J.; Willis, E.L.K.; Schoenbach, K.H. *Nanosecond, high-intensity pulsed electric fields induce apoptosis in human cells*. The FASEB journal. 2003, 17(11), 1493-1495.

[138] Tekle, E.; Oubrahim, H.; Dzekunov, S.M.; Kolb, J.F.; Schoenbach, K.H.; Chock, P.B. *Selective field effects on intracellular vacuoles and vesicle membranes with nanosecond electric pulses*. Biophysical journal. 2005, 89(1), 274-284.

[139] Breton, M.; Amirkavei, M., Mir, L.M. *Optimization of the electroformation of giant unilamellar vesicles (guvs) with unsaturated phospholipids*. The Journal of membrane biology. 2015, 248(5), 827-835.

[140] Portet, T.; Mauroy, C.; Démery, V.; Houles, T.; Escoffre, J.M.; Dean, D.S.; Rols, M.P. *Destabilizing giant vesicles with electric fields: an overview of current applications*. The Journal of membrane biology. 2012, 245(9), 555-564.

[141] Miyata, K.; Christie, R.J.; Kataoka, K. *Polymeric micelles for nano-scale drug delivery.* Reactive and Functional Polymers. 2011, 71(3), 227-234.

[142] Retelj, L.; Pucihar, G.; Miklavčič, D. *Electroporation of intracellular liposomes using nanosecond electric pulsesa theoretical study*. IEEE Transactions on Biomedical Engineering. 2013, 60(9), 2624-2635.

[143] Kotnik, T.; Miklavcic, D. *Theoretical evaluation of the distributed power dissipation in biological cells exposed to electric fields*. Bioelectromagnetics. 2000, 21(5), 385-394.

[144] Merla, C.; Denzi, A.; Paffi, A.; Casciola, M.; d'Inzeo, G.; Apollonio, F.; Liberti. M. *Novel passive element circuits for microdosimetry of nanosecond pulsed electric fields*. IEEE Transactions on Biomedical Engineering. 2012, 59(8), 2302-2311.

[145] Denzi, A.; della Valle, E.; Apollonio, F.; Breton, M.; Mir, L.M.; Liberti, M. *Exploring the applicability of nano-poration for remote control in smart drug delivery systems*. The Journal of Membrane Biology. 2017, 250(1), 31–40.

[146] Juliano, R. L.; Stamp, D. *The effect of particle size and charge on the clearance rates of liposomes and liposome encapsulated drugs*. Biochemical and Biophysical Research Communications. 1975, 63(3), 651-658.

[147] Gabizon, A.; Papahadjopoulos, D. *The role of surface charge and hydrophilic groups on liposome clearance in vivo*. Biochimica et Biophysica Acta (BBA) – Biomembranes. 1992, 1103(1), 94-100.

[148] Levchenko, T.S.; Rammohan, R.; Lukyanov, A.N.; Whiteman, K.R.; Torchilin, V.P. *Liposome clearance in mice: the effect of a separate and combined presence of surface charge and polymer coating*. International Journal of Pharmaceutics. 2002, 240 (1-2), 95-102.

[149] Johnson, S.M. *The effect of charge and cholesterol on the size and thickness of sonicated phospholipid vesicles*. Biochimica et Biophysica Acta (BBA) – Biomembranes. 1973, 307(1), 27-41.

[150] Miller, C.R.; Bondurant, B.; McLean, S.D.; McGovern, K.A.; Brien, D.F.O'. *Liposome-cell interactions in vitro: effect of liposome surface charge on the binding and endocytosis of conventional and sterically stabilized liposomes*. Biochemistry. 1998, 37(37), 12875-12883.

[151] Campbell, R.B.; Fukumura, D.; Brown, E.B.; Mazzola, L.M.; Izumi, Y.; Jain, R.K.; Torchilin, V.P.; Munn, L.L. *Cationic Charge Determines the Distribution of Liposomes between the Vascular and Extravascular Compartments of Tumors*. Cancer Research. 2002, 62(23), 6831-6836.

[152] Kelly, C.; Jefferies, C.; Cryan, S.A. *Targeted Liposomal Drug Delivery to Monocytes and Macrophages*. Journal of Drug Delivery. 2011, 2011, 727241.

[153] Crielaard, B. J.; Lammers, T.; Schiffelers, R.M.; Storm, G. *Drug targeting systems for inflammatory disease: one for all, all for one*. Journal of Controlled Release. 2012, 161(2), 225-234.

[154] Liu, C.; Liu, X.N.; Wang, G.L.; Hei, Y.; Meng, S.; Yang, L.F.; Yuan, L.; Xie, Y. *A dual-mediated liposomal drug delivery system targeting the brain: rational construction, integrity evaluation across the blood–brain barrier, and the transporting mechanism to glioma cells*. International Journal of Nanomedicine. 2017, 12, 2407-2425.

[155] Chen, Y.Y.; Lu, Y.H.; Ma, C.H.; Tao, W.W.; Zhu, J.J.; Zhang, X. *A novel elastic liposome for skin delivery of papain and its application on hypertrophic scar*. Biomedicine & Pharmacotherapy. 2017, 87, 82-91.

[156] Nagayasu, A.; Uchiyama, K.; Kiwada, H. *The size of liposomes: a factor which affects their targeting efficiency to tumors and therapeutic activity of liposomal antitumor drugs*. Advanced Drug Delivery Reviews. 1999, 40(1-2), 75-87.

[157] Erdogan, S.; Medarova, Z.O.; Roby, A.; Moore, A.; Torchilin, V.P. *Enhanced Tumor MR Imaging with Gadolinium-Loaded Polychelating Polymer-Containing Tumor-Targeted Liposomes*. Journal of Magnetic Resonance Imaging. 2008, 27, 574-580.

[158] Li, H.; Guo, K.; Wu, C.; Shu, L.; Guo, S.; Hou, J.; Zhao, N.; Wei, L.; Man, X.; Zhang, L. *Controlled and Targeted Drug Delivery by a UV-responsive Liposome for Overcoming Chemo-resistance in Non-Hodgkin Lymphoma*. Chemical Biology & Drug Design. 2015, 86, 783-794.

[159] Kangarlou, S.; Ramezanpour, S.; Balalaie, S.; Mohammadi, S.R.; Haririan, I. *Curcumin-loaded nanoliposomes linked to homing peptides for integrin targeting and neuropilin-1-mediated internalization*. Pharmaceutical Biology. 2017, 55(1), 277-285.

[160] Lu, X.F.; Zhou, Y.; Zhang, J.; Wang, G. Q. *Pharmacokinetics and tissue distribution of larotaxel in rats: comparison of larotaxel solution with larotaxel-loaded folate receptor-targeting amphiphilic copolymer-modified liposomes*. Xenobiotica. 2017, 47(5), 416-422.

[161] Tan, G.; Yu, S.; Pan, H.; Li, H.J.; Liu, D.; Yuan, K.; Yang, X.; Pan, W. *Bioadhesive chitosan-loaded liposomes: A more efficient and higher permeable ocular delivery platform for timolol maleate*. International Journal of Biological Macromolecules. 2017, 94(A), 355-363.

[162] Yan, X.; Scherphof, G.L.; Kamps, J.A.A.M. *Liposome opsonization*. Journal of Liposome Research. 2005, 15(1-2), 109-139.

[163] Klibanov, A.L.; Maruyama, K.; Torchilin, V.P.; Huang, L. *Amphipathic polyethyleneglycols effectively prolong the circulation time of liposome*. FEBS Letters. 1990, 268(1), 235-237.

[164] Torchilin, V.P.; Shtilman, M.I.; Trubetskoy, V.S.; Whiteman, K.; Milstein, A.M. *Amphiphilic vinyl polymers effectively prolong liposome circulation time in vivo*. Biochimica et Biophysica Acta (BBA) – Biomembranes. 1994, 1195(1), 181-184.

[165] Salmaso, S.; Caliceti, P. *Stealth Properties to Improve Therapeutic Efficacy of Drug Nanocarriers*. Journal of Drug Delivery. 2013. Article ID 374252, 19 pages.

[166] Peng, S.; Zou, L.; Liu, W.; Li, Z.; Liu, W.; Hu, X.; Chen, X.; Liu, C. *Hybrid liposomes composed of amphiphilic chitosan and phospholipid: Preparation, stability and bioavailability as a carrier for curcumin*. Carbohydrate Polymers. 2017, 156, 322-332.

[167] Simões, M.G.; Alves, P.; Carvalheiro, M.; Simões, P.N. *Stability effect of cholesterol-poly(acrylic acid) in a stimuli-responsive polymer-liposome complex obtained from soybean lecithin for controlled drug delivery*. Colloids and Surfaces B: Biointerfaces. 2017, 152, 103-113.

[168] Li, M.; Fei, X.; Shi, F.; Dou, J.; Wu, S.; Wu, D.; Zhang, Y.; Pan, M.; Luo, S.; Gu, N. *Homoharringtonine delivered by high proportion PEG of long-circulating liposomes inhibits RPMI8226 multiple myeloma cells in vitro and in vivo*. American Journal of Translational Research. 2016, 8(3), 1355-1368.

[169] Sylvester, B.; Porfire, A.; Muntean, D.M.; Vlase, L.; Tomuță, I. *Formulation optimization of pravastatin loaded long-circulating liposomes using a design of experiments*. Farmacia. 2016, 64(3), 449-458.

[170] Achim, M.; Tomuță, I.; Muntean, D.; Porfire, A.; Tefas, L.R.; Patras, L.; Licarete, E.; Alupei, M.C.; Vlase, L.; Banciu, M. *Optimization and in vitro evaluation of 5-fluorouracil-loaded long-circulating liposomes*. Farmacia. 2017, 65(1), 82-91.

[171] Utkhede, D.R.; Tilcock, C.P. *Studies Upon the Toxicity of Polyethylene Glycol Coated Lipid Vesicles: Acute Hemodynamic Effects, Pyrogenicity and Complement Activation*. Journal of Liposome Research. 1998, 8(4), 537-550.

[172] von Hoegen, P. *Synthesis biomimetic supra molecular Biovector™ (SMBV™) particles for nasal vaccine delivery*. Advanced Drug Delivery Reviews. 2001, 51, 113-125.

[173] Kiser, P.F.; Wilson, G.; Needham, D. *A synthetic mimic of the secretory granule for drug delivery*. Nature. 1998, 394, 459-462.

[174] Kiser, P.F.; Wilson, G.; Needham, D. *Lipid-coated microgels for the triggered release of doxorubicin*. Journal of Controlled Release. 2000, 68(1), 9-22.

[175] Jin, T.; Pennefather, P.; Lee, P.I. *Lipobeads: a hydrogel anchored lipid vesicle system*. FEBS Letters. 1996, 397(1), 70-74.

[176] Ng, C.C.; Cheng, Y.L.; Pennefather, P.S. *One-Step Synthesis of a Fluorescent Phospholipid-Hydrogel Conjugate for Driving Self-Assembly of Supported Lipid Membranes*. Macromolecules. 2001, 34(17), 5759-5765.

[177] Ng, C.C.; Cheng, Y.L.; Pennefather, P.S. *Properties of a Self-Assembled Phospholipid Membrane Supported on Lipobeads*. Biophysical Journal. 2004, 87(1), 323-331.

[178] Buck, S.; Pennefather, P.S.; Xue, H.Y.; Grant, J.; Cheng, Y.L.; Allen, C.J. *Engineering lipobeads: Properties of the Hydrogel Core and the Lipid Bilayer Shell*. Biomacromolecules. 2004, 5(6), 2230-2237.

[179] Kazakov, S.; Levon, K. *Liposome-nanogel structures for future pharmaceutical applications*. Current Pharmaceutical Design. 2006, 12(36), 4713-4728.

[180] Kazakov, S.; Levon, K. *Lipobeads as Drug Delivery Systems*. NSTI-Nanotech 1. 2006, 467-470.

[181] Kazakov, S.; Kaholek, M.; Levon, K. *Lipobeads and their production*. 2009. US Patent 7618565 B2.

[182] Campillo, C.C.; Schroder, A.P.; Marques, C.M.; Pépin-Donat, B. *Composite gel-filled giant vesicles: Membrane homogeneity and mechanical properties*. Materials Science and Engineering C. 2009, 29(2), 393-397.

[183] Saleem, Q.; Liu, B.; Gradinaru, C.C.; Macdonald, P.M. *Lipogels: Single-Lipid-Bilayer-Enclosed Hydrogel Spheres*. Biomacromolecules. 2011, 12(6), 2364-2374.

[184] Liu, J.; Lu, N.; Li, J.; Weng, Y.; Yuan, B.; Yang, K.; Ma, Y. *Influence of Surface Chemistry on Particle Internalization into Giant Unilamellar Vesicles*. Langmuir. 2013, 29(25), 8039-8045.

[185] Tiwari, S.; Goyal, A.K.; Khatri, K.; Mishra, N.; Vyas, S.P. *Gel core liposomes: An advanced carrier for improved vaccine deliver*. Journal of Microencapsulation. 2009, 26(1), 75-82.

[186] An, E.; Jeong, C.B.; Cha, C.; Kim, D.H.; Lee, H.; Kong, H.; Kim, J.; Kim, J.W. *Fabrication of Microgel-in-Liposome Particles with Improved Water Retention*. Langmuir. 2012, 28(9), 4095-4101.

[187] Helwa, Y.; Dave, N.; Liu, J. *Electrostatically directed liposome adsorption, internalization and fusion on hydrogel microparticles*. Soft Matter. 2013, 9(26), 6151-6158.

[188] Park, J.; Wrzesinski, S.H.; Stern, E.; Look, M.; Criscione, J.; Ragheb, R.; Jay, S.M.; Demento, S.L.; Agawu, A.; Limon, P.L.; Ferrandino, A.F.; Gonzalez, D.; Habermann, A.; Flavell, R.A.; Fahmy, T.M. *Combination delivery of TGF-inhibitor and IL-2 by nanoscale liposomal polymeric gels enhances tumour immunotherapy*. Nature Materials. 2012, 11(10), 895-905.

[189] Kazakov, S. *Technological Challenges and Potential Advantages of Lipobeads as Drug Delivery Systems*. Biotech, Biomaterials and Biomedical. 2016, 101-104.

[190] Monshpouri, M.; Rudolph, A.S. *Method of forming hydrogel particles having a controlled size using liposomes*. 1995. US patent 5464629.

[191] Campbell, A.; Taylor, P.; Cayre, O. J.; Paunov, V. N. *Preparation of aqueous gel beads coated by lipid bilayers*. Chemical Communications. 2004, 21, 2378-2379.

[192] Hong, J. S.; Vreeland, W. N.; DePaoli Lacerda, S. H.; Locascio, L. E.; Gaitan, M.; Raghavan, S. R. *Liposome-Template Supramolecular Assembly of Responsive Alginate Nanogels*. Langmuir. 2008, 24, 4092-4096.

[193] Torchilin, V.P.; Klibanov, A.L.; Ivanov, N.N.; Ringsdorf, H.; Schlarb, B. *Polymerization of liposome-encapsulated hydrophilic monomers*. Macromolecular Rapid Communications. 1987, 8(9), 457-460.

[194] Kazakov, S.; Kaholek, M.; Teraoka, I.; Levon, K. *UV-Induced Gelation on Nanometer Scale Using Liposome Reactor*. Macromolecules. 2002, 35(5), 1911-1920.

[195] Stauch, O.; Uhlmann, T.; Fröhlich, M.; Thomann, R.; El-Badry, M.; Kim, Y. K.; Schubert, R. *Mimicking a Cytoskeleton by Coupling Poly(N-isopropylacrylamide) to the Inner Leaflet of Liposomal Membranes: Effects of Photopolymerization on Vesicle Shape and Polymer Architecture*. Biomacromolecules. 2002, 3(2), 324-332.

[196] Wang, Y.; Tu, S.; Pinchuk, A. N.; Xiong, M. P. *Active drug encapsulation and release kinetics from hydrogel-in-liposome nanoparticles*. Journal of Colloid and Interface Science. 2013, 406, 247-255.

[197] Thet, N. T.; Jamieson, W. D.; Laabei, M; Mercer-Chalmers, J. D.; Jenkins, A.T.A. *Photopolymerization of Polydiacetylene in Hybrid Liposomes: Effect of Polymerization on Stability and Response to Pathogenic Bacterial*. The Journal of Physical Chemistry B. 2014, 118(20), 5418-5427.

[198] Helwa, Y.; Dave, N.; Liu, J. *Electrostatically directed liposome adsorption, internalization and fusion on hydrogel microparticles*. Soft Matter. 2013, 9(26), 6151-6158.

[199] Gao, K.; Huang, L. *Solid core liposomes with encapsulated colloidal gold particles*. Biochimica et Biophysica Acta, Biomembranes. 1987, 897(3), 377-383.

[200] MacKinnon, N.; Guerin, G.; Liu, B.; Gradinaru, C.C.; Rubinstein, J. L.; Macdonald, P. M. *Triggered Instability of Liposomes Bound to Hydrophobically Modified Core-Shell PNIPAM Hydrogel Beads*. Langmuir. 2010, 26(2), 1081-1089.

[201] Hong, J. S.; Stavis, S. M.; DePaoli Lacerda, S. H.; Locascio, L. E.; Raghavan, S. R.; Gaitan, M. *Microfluidic Directed Self-Assembly of Liposome-Hydrogel Hybrid Nanoparticles.* Langmuir. 2010, 26(13), 11581-11588.

# Chapter 2

## Purpose of the research

The rational design of systems for controlled drug delivery is an important area of research for advancing new therapies for many diseases. Nanomaterial based controllable drug delivery platforms would overcome many of the major drawbacks in pharmacological therapy, because they would store the therapeutic molecules during transportation within the body and provide triggered and finely controlled release of the agent at the target site. In this context, lipid vesicles as liposomes attracted, since their discovery, growing interest for their potential applications as drug delivery vectors. They are now considered clinically established nanometer-scaled systems for the delivery of cytotoxic drugs or agents for biomedical applications. However, liposomes can be further engineered to improve their performance in terms of stability and controlled delivery, since the rapid degradation, due to the reticuloendothelial system (RES), and inability to achieve sustained drug delivery, over a prolonged period, limit their biological efficacy and use in pharmaceutics.

Interesting results were obtained in terms of physical stability through the approach that provides the combination of different biomaterials within the same delivery lipid system. Following this concept, it was possibile to change the surface properties of the bilayer, by coating it with water-soluble polymers, like polyethylene glycol, leading to "stealth liposomes". More recently, satisfying achievements resulted from the modification of the internal structure of liposomes, with the aim to convert the aqueous inner core into a soft and elastic hydrogel, obtaining structures able to retain the cargo for longer time, without unwanted burst release of the delivered compound.

An ideal drug delivery platform should encompass not only the carrier stability, but also controllable timing, dosage and site specificity of drug release, and permit remote, non-invasive and reliable switching of the therapeutic agent, in order to prevent deleterious side effects of cytotoxic drugs toward normal and healthy tissue. Much of innovations in materials design, for drug delivery, manifest in producing "smart liposomes" that are able

to respond to "smart triggers", in order to realize on-demand processes, allowing for tailored release profiles with excellent temporal and dosage control. In principle, the on-demand drug delivery is becoming feasible through the design of stimuli-responsive systems that recognize their microenvironment and react in a dynamic way. Specifically, it is possible to engineere the liposomal structure making it capable of responding to physical, chemical or biological triggers.

Among the endogenous or exsogenous stimuli that can be applied, magnetic stimulus represents a potential trigger for the remotely-on demand release, evaluating that normal biological tissues are essentially transparent to low-frequency magnetic fields. Through the encapsulation of superparamagnetic nanoparticles, giving rise to the Magneto-Liposomes (MLs), it is possibile to modulate the transmembranal drug diffusion by using an external magnetic field with intensity significantly lower that no heat generation, harmful to healthy tissues, is observed.

Another challenging way to activate release from liposomes is the use of pulsed electric fields. In particular, since it was demonstrated that electric pulses of shorter duration (nanosecond) and higher intensity (in the order of MV/m) directly interact not only with cell membrane, but also with internal cell organelles of nanometer dimensions, nanosecond electric pulses are proposed as sufficient signals to generate an alteration of the liposomal transmembrane voltage, which is followed by the formation of temporary hydrophilic pores. Without implying the phenomenon of irreversible poration, the nanosecond pulses therefore can be considered useful external stimuli to trigger the simultaneous permabilization of liposomes and cells membranes, in order to let that the chemical load internalized in the vesicles to be released inside the cells.

In this scenario is placed the main activity of this Ph.D. thesis, whose aim is to provide a multiscale and multidisciplinary approach to demonstrate the capability of liposomes to prove effective smart systems for the on-demand and modified drug delivery, able to minimize off-target effects and maximize programmability of therapy.

Following a briefly overview of this Ph.D. thesis is given.

In **Chapter 3** is reported the study which highlights the utility in trapping MNPs within phospholipid vesicles, generating hybrid magneto-responsive constructs. Particularly, in this work the inclusion of hydrophilic $Fe_3O_4$ nanoparticles (MNPs) within phospholipid vesicles, characterized by different rigidity and stiffness, was investigated as novel strategy for improving stability and reactivity of these MNPs, since the integration in liposomes may prevent MNPs from aggregation and extend their potential use in the environmental remediation. The stability of these hybrid systems was indirectly investigated evaluating the ability of retaining a fluorescent marker in their structure, under both mechanical and thermal stress conditions. In particular, for the mechanical stress test, a low intensity non-thermal alternating magnetic field (AMF) was applyed to magnetic liposomes. The AMF could, in fact, cause a mechanical destabilization of the vesicle membrane, due to MNPs oscillation within the liposomes, which may induce the release of the dye.

In **Chapter 4**, according to the results obtained in the previous work, shown in **Chapter 3**, is presented the research project which combines engineering skills, specifically focused on electromagnetic fields, with competences in synthesis and characterization of hybrid magnetic nanocarriers, to assess a remotely on-demand drug delivery. Specifically, here is refiled the possibility to trigger drug release from high-transition temperature magnetoliposomes (high-Tm MLs) entrapping MNPs, through a magneto-nanomechanical approach, where the mechanical actuation of the MNPs is used to enhance the membrane permeability, avoiding temperature rise. Since the AMF, as an external magnetic signal, found rare application in clinic, in this case, the ability of the non-thermal pulsed electromagnetic fields (PEMFs), that are already employed in theraphy, due to their anti-inflammatory effects, was tested, in order to verify if, once applied to high-Tm MLs, PEMFs could be able to efficiently trigger the transmembranal drug diffusion.

In the **Chapter 5** and **6** is illustrated another sophisticated and innovative drug delivery strategy to activate an efficient on-demand release. Specifically, in **Chapter 5** is reported the theoretical work and the experimental proof-of-concept of the possibility of applying ultra-short (ns) and intense (MV/m) external pulsed electric fields (nsPEFs), to remotely trigger the release from liposomes of nanometer-sizing. The nanoelectropermeabilization, that probably occurs with the formation of transient pores in the bilayer, because of the external pulsed electric field enforcement, was evaluated in relation to the diffusion across the bilayer of a probe, previously trapped in the core of liposomes. To support the experimental data, a numerical model of liposomes suspension, exposed to nsPEF by means a standard electroporation cuvette, was carried out according with the experimental conditions. In **Chapter 6** was demonstrated, once again, the possibility of permeabilizing the liposomal membrane, applying the same type of pulses, described in **Chapter 5**, but, in this case, delivered to the nanometer-sized lipid vesicles by a coplanar exposure system. Furthermore, the electropermeabilization mechanism in liposomes membrane was investigated through the Raman Coherent anti-Stokes spectroscopy (CARS), highlighting, for the first time, the experimental proof of the role of water molecules of the interstitial phase in the electropermeabilization of vesicles bilayer.

Finally, in **Chapter 7** is described the project who leaded to the development of a novel hybrid lipid-polymer nanocostructs, designed to merge the beneficial properties of both polymeric drug delivery systems and liposomes in a single nanocarrier and at the same time take care of liposomes limitations, such as the physical and chemical stability issues. Starting from previous studies on the use of liposomes as template to create nanohydrogel, this research brought to the novel Gel-in-Liposome (GiL) systems, relying from the combination of lipid vesicles and the polymer polyethylene glycol-dimethacrylate (PEG-DMA) at two different molecular weight. These hybrid systems are characterized by the presence of a chemically crosslinked polymeric network within the aqueous compartment of liposomes. The effect of PEG-DMA, on the properties of the new lipid-polymer nanosystems and on

the related changes of the membrane permeability and stability, against different stresses, were evaluated to understand GiL potential use as drug carriers in clinics.

# Chapter 3

# Magnetoliposomes: envisioning new strategies for water decontamination

Stefania Petralito[1], Patrizia Paolicelli[1], Martina Nardoni[1], Francesca Apollonio[2], Micaela Liberti[2], Caterina Merla[4], Rosanna Pinto[4], Maria Antonietta Casadei[1], Maria Cristina Annesini[3]

[1]*Department of Drug Chemistry and Technologies, "Sapienza" University of Rome, Piazzale Aldo Moro 5, 00185 Rome, Italy*

[2]*Department of Information Engineering, Electronics and Telecommunications (DIET), "Sapienza" University of Rome, Via Eudossiana 18, 00184 Rome, Italy*

[3]*Department of Chemical, Material and Environmental Engineering, "Sapienza" University of Rome, Via Eudossiana 18, 00184 Rome, Italy*

[4]*Unit of Radiation Biology and Human Health, Enea Research Center, Rome, Italy*

**Chemical engineering transactions 2016, 47; ISBN 978-88-95608-38-9; ISSN 2283-9216**

***3.1 Abstract.*** *In this work the inclusion of magnetic nanoparticles (MNPs) within phospholipid vesicles were investigated as novel strategy for improving stability and reactivity of these nanoparticles and extending their potential use in the environmental field. Two phospholipids, able to form liposomes characterized by different rigidity and stiffness, were used as potential carriers of MNPs. The magneto-responsive liposomes were investigated for their physicochemical and stability properties. In particular, the stability of the two systems was indirectly investigated evaluating the ability of the hybrid constructs to retain a fluorescent marker in their structure. Alterations in the permeability of the membranes were determined by the rate of the marker release from the liposomes, under both mechanical and thermal stress conditions.*

***Keywords:*** *magneto mechanical trigger; magneto-responsive liposomes; stability; magnetic nanoparticles; AMF; non-thermal magnetic field; permeability.*

## 3.2 Introduction

Over the last decades, nanotechnologies have received growing attention in different fields of fundamental and applied sciences [1]. The reasons behind the wide interest raised by nanoparticles have to be find in the appealing and unique characteristics exhibited by nanostructured materials. In fact, both physical and chemical properties of materials change significantly, sometimes abruptly, as their size approaches the nanoscale [2-4]. These attractive characteristics of nanostructured materials are helping to considerably improve, even revolutionize, several research areas, finding applications in different fields from medicine to energy and environment. In the last case, nanotechnologies have been proposed as valid systems for environmental sensing and monitoring, as well as chemical degradation and remediation, among others. In this context, magnetic nanoparticles (MNPs) have proved to be effective sorbents for removal of toxic pollutants, such as heavy metals, in contaminated water [5, 6]. Due to their high surface-to-volume ratio and magnetic properties, MNPs can adsorb on their surface various pollutants enabling their easy separation from aqueous solutions by the application of external magnetic fields [5]. However, due to their high specific surface area, nanoparticles have low energy barriers, causing them to aggregate and achieve a stabilized state. Aggregation decreases the free surface area of the nanoparticles, thereby reducing their adsorption capacity. Brownian motion of particles further contributes to reducing their effectiveness. To overcome the problems associated with aggregation, it becames extremely important to modify the surface of MNPs for good balancing of high adsorption capacity and nanoparticle stability. To this end, different surface modification approaches have been attempted [7]. In this sense, the inclusion of MNPs within phospholipid vesicles, also known as liposomes, could represent a different and interesting approach for improving, at the same time, their stability and reactivity [8]. The entrapment of MNPs within phospholipid vesicles generate hybrid magneto-responsive constructs (magneto-liposomes, MLs) [9, 10], which may widen the potential use of MNPs within the environmental field. In fact, on the one hand, the inclusion in liposomes may prevent nanoparticles form aggregation; on the other hand, the various

types of phospholipids (e.g. saturated and unsaturated) available for MLs production, offer the opportunity for novel surface modifications leading to functionalized MLs, which may open new perspectives in the use of MNPs for environmental remediation. Magnetoliposomes have been extensively investigated in the pharmaceutical and biomedical fields, as tools for both therapy and diagnosis [11].

Having in mind these informations, in this work, potential application of MLs for water decontamination, has been investigated. To this end, MNPs have been entrapped within phospholipid vesicles and the resulting hybrid magnetic structures have been characterized for dimensions, surface charge, morphology and entrapment efficiency. Moreover, the mechanical and physical stability of MLs have been studied as these hybrid structures could result more fragile than classical liposomes. In fact, phospholipids are in very close contact with the iron oxide surface in MLs, consequently any mechanical stress on the liposome membrane, due to nanoparticles oscillations in proximity of phospholipid membrane, could change the permeability of the bilayer leading to MNPs escape or even rupture of the MLs structure. Therefore, MLs should be able to preserve their physical integrity over time when exposed to a magnetic field or when subjected to a temperature increase, as fluidity and permeability of membranes increase with increasing temperature [9, 10].

For these reasons, two lipid compositions, soybean phosphatidylcholine (SPC) and hydrogenated soybean phosphatidylcholine (HSPC), with different degree of unsaturation, were used in order to obtain vesicles displaying a main transition temperature (Tm) lower or higher than room temperature, respectively. In fact, the thermotropic behaviour and structural properties of liposomal dispersions strongly depend on the chemical properties of the fatty acids of phospholipids, which compose the bilayer membrane: the high amount of unsaturated acyl chains in SPC lecithin (predominantly oleic (18:1) and linoleic (18:2) acid) imparts a very low Tm value to the mixture. The presence of double bonds in the acyl chains led to less compact structures. For this reason, the resulting SPC liposomal membrane can be more susceptible to external perturbations, due to its liquid-phase state at room temperature. Instead, liposomal membranes formulated with saturated lipids (high purity

hydrogenated soybean phosphatidylcholine, HSPC) have modest permeability due to their gel phase state at room temperature, which potentially make them less vulnerable to external perturbations. The stability of the two different hybrid constructs was investigated evaluating their ability to retain a fluorescent marker in their structure, under mechanical and thermal stress conditions.

## 3.3 Experimental section

### 3.3.1 Materials

Hydrogenated soybean phosphatidylcholine (HSPC), Phospholipon 90H, from Lipoid GmbH and soybean phosphatidylcholine (SPC), Phospholipon 90, from Lipoid GmbH were kindly gifted by AVG Srl. Cholesterol (Chol), 4-(2-hydroxyethyl) piperazine-1-ethanesulfonic acid (HEPES), 5-(6) carboxyfluorescein [5-(6) CF], Triton X-100 (TX-100), Sephadex G-50, thiocyanatoiron, iron (III) nitrate and hydrochloric acid were purchased from Sigma-Aldrich. Chloroform was obtained from Merck. Bidistilled water, 1,2-dichloroethane and ethanol were supplied by Carlo Erba Reagents. Aqueous dispersion of 50 nm carboxymethyl-dextran coated magnetite ($Fe_3O_4$) nanoparticles, fluidMAG-CMX (MNPs), was obtained from Chemicell GmbH.

### 3.3.2 Preparation and physicochemical characterization of liposomes

Unilamellar magnetoliposomes (MLs) were prepared using the thin lipid film hydration method followed by sequential extrusion as reported in [8]. Briefly, MNPs were entrapped within the aqueous core of liposomes. Two different lipid compositions were used in order to obtain vesicles displaying a Tm lower or higher than 25 °C. In particular, soybean phosphatidylcholine (PC-MLs) or mixture of hydrogenated soybean phosphatidylcholine with 20% mol/mol of cholesterol (HSPC/Chol-MLs) were selected to obtain Tm <4 °C or Tm >50 °C, respectively. The thin film of SPC or HSPC and cholesterol was hydrated with 10

mM HEPES buffer solution (pH= 7.4) containing MNPs and 20 mM 5-(6) CF used as a fluorescent marker for stability experiments. Plain liposomes, without MNPs, were also prepared and used as a control. Repeated extrusion through membrane filters, having 0.4 μm and 0.2 μm pore sizes, yielded unilamellar liposomes with a narrow size distribution. Following extrusion, the unentrapped marker and MNPs were removed by size exclusion chromatography (SEC) carried out on a Sephadex G-50 column eluted with HEPES buffer (10 mM, pH= 7.4). All liposome formulations were stored in the dark at 4 °C and used within 1 week from their preparation. The hydrodynamic diameter and polydispersity index (PdI) were evaluated by dynamic light scattering (DLS) experiments. All measurements were carried out with Zetasizer Nano ZS90 (Malvern Instruments Ltd., UK) thermostatically controlled at 25 °C. Phospholipid concentration was determined using the phosphorus colorimetric assay [12], using a double beam UV–Vis spectrophotometer Lambda 25 (Perkin Elmer, USA). The measurements were repeated before and after SEC purification of extruded samples.

MNPs content in MLs was determined using the 8.5% w/v hydrochloric acid assay [13]. The calibration curve was performed with standards solutions of magnetite. Measurements were repeated before and after SEC purification of extruded MLs. All data collected were used to determine the magnetite/phospholipid ratio.

The amount of 5-(6) CF entrapped in the inner aqueous compartment of liposomes was determined measuring the fluorescence emitted at 512 nm, after excitation at 492 nm, by purified samples pre-incubated with 10% non-ionic surfactant Triton X-100 for vesicles lysis. The measurements were carried out using a spectrofluorometer LS 50B (Perkin Elmer, USA).

### 3.3.3 AMF exposure set-up

The AMF exposure system used was the same described in detail in previous works [9, 10]. Briefly, it consists of two coaxial magnetic coils of square shape with a side length of 21 cm and placed 11 cm apart; coil section is square with a diameter of 2 cm and is composed of

25 cable turns. A high H field homogeneity of 99% is achieved in a volume of 10 × 10 × 6 $cm^3$ around center of the system where the samples were placed. The coils are connected to a signal generator (HP 3314A; Agilent Technologies, Santa Clara, CA) through a wide band amplifier (Krohn-Hite 7500; Krohn-Hite, Brockton, MA). AMF treatments were carried out with frequency of 20 kHz and intensity of 60 A/m. Both MLs and plain liposomes were exposed to AMF in continuous up to 9 h. During the AMF treatments samples were placed in a thermostatic bath at 37.0±0.5 °C, placed directly inside the coil system.

MLs were also treated without AMF (sham conditions) using currents flowing in opposite directions in the two wires, in order to null the resulting H field, as described in [14]. Sham samples were placed in the thermostatic bath at 37.0±0.5 °C within the same coil system and located in the same position of the AMF-exposed ones.

The release of 5-(6) CF was calculated by monitoring the fluorescence intensity of the marker. The percentage of 5-(6) CF, released from the different liposome suspensions, was calculated using the Equation 3.1.

$$5-(6)\ CF\ released\ (\%) = \frac{(I_t - I_0)}{(I_{max} - I_0)} \cdot 100 \qquad (3.1)$$

where: $I_0$ is the initial fluorescence intensity of 5-(6) CF loaded; $I_t$ is the fluorescence intensity measured at time *t*; $I_{max}$ is the fluorescence intensity after the complete lysis of the liposomal vesicles with TX-100.

### 3.3.4 Measurement of 5-(6) CF released from liposomes

In order to have data about MLs stability, 5-(6) CF, which is a self-quenching hydrophilic dye, was loaded into the core of MLs. The membrane permeation and release behaviour of MLs were determined fluorimetrically by monitoring 5-(6) CF fluorescence de-quenching at excitation and emission wavelengths of 492 and 512 nm, respectively. The release was measured both due to an applied low intensity AMF stimulation (20kHz, 60 A/m) under

controlled temperature conditions (37.0±0.5 °C) by the use of a thermal bath and measured by means of a thermocouple after 1-3-6-9 h of continuous heating, at selected temperature (37.0±0.5 °C) in the absence of AMF.

## 3.4 Results and Discussion

Phospholipid vesicles embedding MNPs were prepared by the classic thin film hydration method. Table 3.1 reports the results of the physicochemical characterization of plain liposomes and MNPs-loaded liposomes with two different phospholipid compositions, which are schematically depicted in Figure 3.1. Data for magnetoliposomes refer to vesicles obtained with 2:1 NPs/Ls ratio. Indeed, different ratios between magnetic nanoparticles and lipids were attempted in order to reach optimal vesicles formation; working at a 2:1 NPs/Ls ratio, no significant interference with the vesicles formation was observed, as suggested by the percentages of phospholipids forming vesicles, which are very similar for plain and MNPs-loaded liposomes irrespective of the type of phospholipid used. In fact, the percentage of the lipid molecules recovered from the high-Tm MLs is only partially decreased respect to plain vesicles, suggesting that the hydration step of liposome preparation was only slightly influenced by the presence of the MNPs. In a similar way, no differences in hydrodynamic diameter were evidenced between the two lipid compositions containing or not MNPs. In both cases, the hybrid systems are arranged in a monomodal distribution with PdI values lower than 0.200. Finally, the 5-(6) CF entrapment reaches satisfactory values for both SPC and HSPC MLs, showing that the loading capacity of the hybrid nanostructures is not limited by the co-presence of MNPs inside the vesicles (Table 3.1).

**Table 3.1. Physicochemical characteristics of liposomes entrapping magnetic nanoparticles and plain liposomes. Values (±S.D.) are the mean of three determinations.**

| Sample | SPC-MLs | SPC-Ls | HSPC/Chol-MLs | HSPC/Chol-Ls |
|---|---|---|---|---|
| **Hydrodynamic diameter (nm)[a]** | 207.6±2.3 | 166.7±2.0 | 235.5±6.4 | 242.7±9.7 |
| **$Fe_3O_4$ loading efficiency (%)[b]** | 98.6±0.6 | - | 70.2±3.4 | - |
| **$Fe_3O_4$ loading efficiency (mg/mmol phospholipid)[c]** | 71.6±2.6 | - | 115.0±4.2 | - |
| **5-(6) CF loading efficiency (μl/mg phospholipid)[d]** | 2.54±0.22 | 2.66±0.24 | 1.47±0.18 | 2.10±0.22 |
| **Phospholipid (%)[e]** | 93.4±1.2 | 98.2±0.5 | 78.1±2.3 | 90.1±1.5 |

[a]Hydrodynamic diameter and size distribution of liposomes and MLs were determined by dynamic light scattering; [b]$Fe_3O_4$ loading efficiency (mean concentration after purification/mean concentration before purification) x 100 determined by colorimetric assay [c]$Fe_3O_4$ amount (mg/mmol phospholipid) determined by Belikov assay; [d]fluorimetric determination of 5-(6) CF (μl/mg phospholipid) in the final formulation; [e]phospholipid concentration as determined by Yoshida assay.

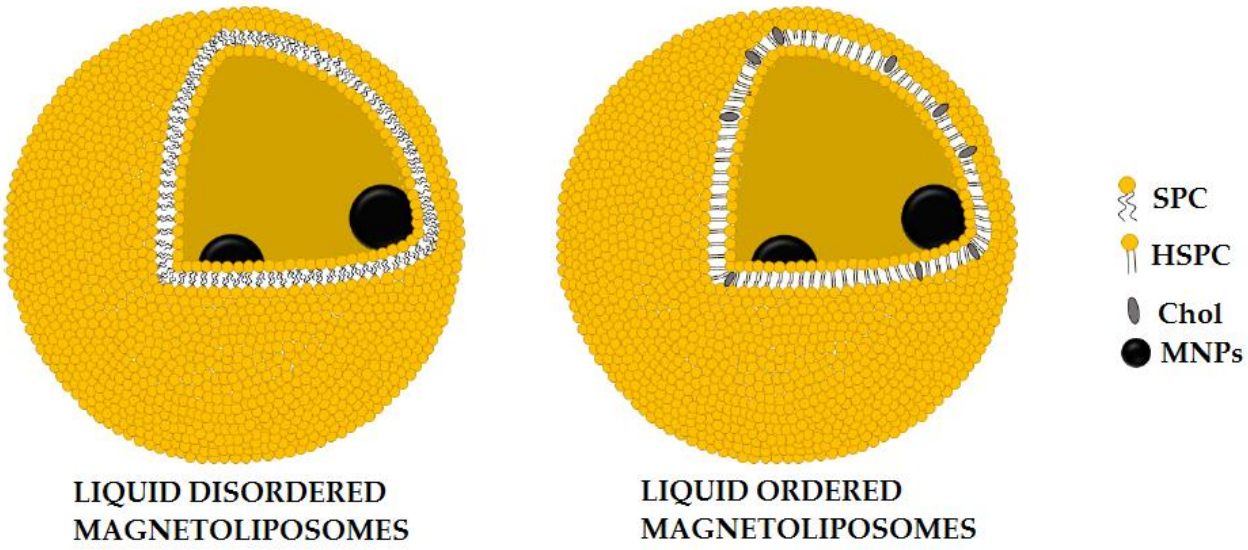


**Figure 3.1. Schematic representation of SPC and HSPC/Chol magnetoliposomes showing the different fluidity properties of the bilayers of the two hybrid constructs investigated.**

In order to provide insight on the influence of the magnetic nanoparticles on the stability and permeability properties of the two liposomal constructs produced, the release behaviour of the encapsulated hydrophilic marker 5-(6) CF was investigated under mechanical and thermal stress conditions. The application of AMF external stimulus to MLs could cause a mechanical destabilization of the vesicle membrane due to MNPs oscillation within the liposomes, which may induce the release of the dye. Therefore, the release rate of 5-(6) CF was used to have indirect informations about the ability of the different hybrid nanocostructs to resist to mechanical stress and avoid undesired leakage of their content.

Results reported in Figure 3.2 (A-B) show that, upon exposure to a magnetic field at 37.0 °C, release from magnetoliposomes having membrane in liquid disordered (SPC)-phase is more pronounced than the leakage obtained from vesicles in liquid ordered (HSPC)-phase. The release profiles are the combination of dual effects: magnetic and thermal, which affected the release kinetics of 5-(6) CF in a different way. In specific, it was observed that, in conditions of null magnetic field and 37.0±0.5 °C (sham conditions), the extent of 5-(6) CF release is much higher from MLs characterized by disordered-state membranes, compared to the more ordered HSPC bilayer.

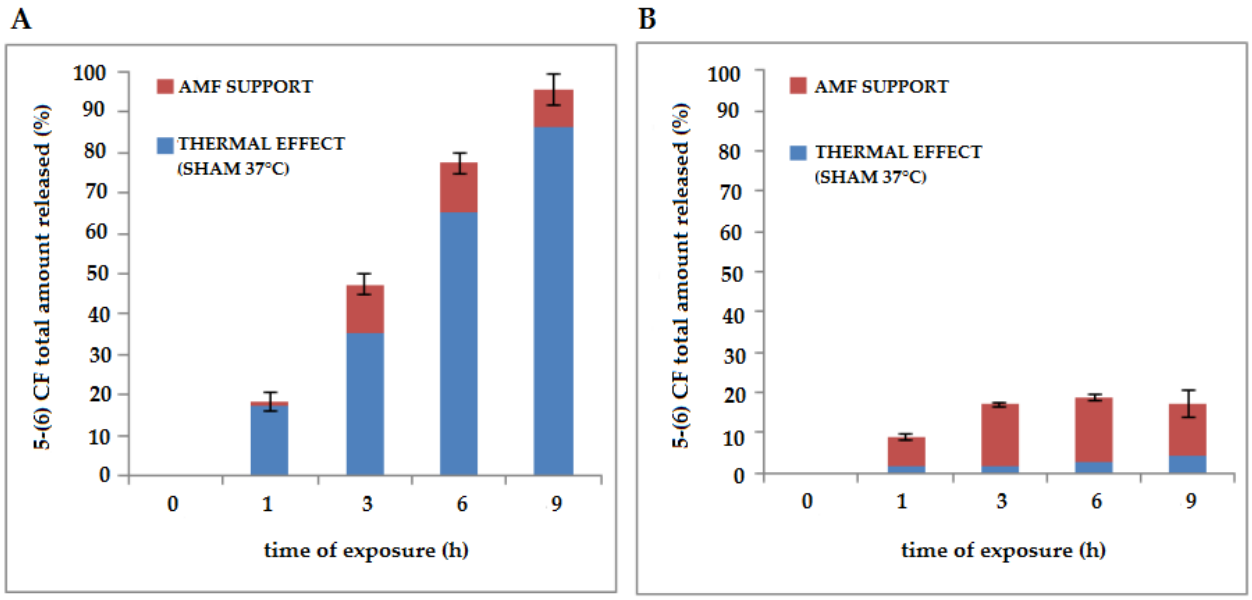


**Figure 3.2. Extent of thermal and AMF-induced release from MLs characterized by (A) disordered-(SPC) or (B) ordered (HSPC)-state membranes.**

These results can be explained considering that bilayers containing short or cis-unsaturated hydrocarbon chains are characterized by low Tm (e.g. soy phosphatidylcholine), as the double bounds hamper tight package of the hydrophobic tails, making the system more leaky than bilayers formed by saturated lipids, like HSPC. Therefore, at the same temperature, the unsaturated system will be more fluid than the respective saturated one. Consequently, when in disordered fluid state, the lateral motion of lipid molecules within the plane is much more freely, compared to liquid-ordered membrane, which results less leaky at the same temperature.

A loosely packed liquid-disordered system is obtained when low Tm lipids are used to prepare liposomes; instead, liquid-ordered domains are formed when cholesterol is included within gel-phase bilayers. The addition of cholesterol disrupts local packing orders of the saturated lipids, with a consequent increase in their diffusion coefficient and modulation of vesicle permeability. Nevertheless, results reported in Figure 3.2 (B) show that, even with the inclusion of cholesterol, HSPC liposomes did not become permeable and leaky under the experimental temperature conditions investigated.

External magnetic stimulation caused only a modest increase in the 5-(6) CF leakage compared to release occurring in sham conditions. The extent of AMF-induced release was quite low and almost independent from the fluidity characteristics of the bilayers. In fact, the increase in the percentage of 5-(6) CF released fall in the range 10-20%, with almost no differences between MLs characterized by liquid-disordered (SPC) state membrane, compared to liquid-ordered (HSPC) one.

Hence, if only magneto-mechanical effects on membrane permeability are taken into account, the stability of ordered or disordered bilayers against magnetically induced leakage suggests that both liposome structures could potentially be used as sorbents for water pollutants. The same consideration does not apply to temperature. In fact, the stability and integrity of SPC liposomes may be impaired if used in warm water. On the contrary, HSPC vesicles seems capable of withstanding both magnetic and thermal induced perturbations of the membrane. Overall, these results evidence promising and interesting

features of HSPC–based magnetoliposomes for application as effective sorbents of toxic pollutants.

## 3.5 Conclusions

Phosphatidylcholine liposomes may represent a promising alternative for application of magnetic nanoparticles in water decontamination. In particular, lipids composed of saturated fatty acids seem to represent a rational choice for the formation of vesicles able to withstand both mechanical a thermal destabilization effects, thus avoiding any escape of the magnetic payload from the hybrid systems and consequent loss of effectiveness.

***Acknowledgments.*** *This work was carried out with financial support from Sapienza University of Rome (Research project: "Magnetic-responsive drug delivery systems controlled by low intensity magnetic stimuli").*

## 3.6 References

[1] Daniel, M.C.; Astruc, D. *Gold nanoparticles: assembly, supramolecular chemistry, quantum-size-related properties, and applications toward biology, catalysis, and nanotechnology*. Chemical Reviews. 2004, 104(1), 293–346.

[2] Liu, J.; Qiao, S.Z.; Hu, Q.H.; Lu, G.Q. *Magnetic nanocomposites with mesoporous structures: synthesis and applications*. Small. 2011, 7(4), 425–443.

[3] Luechinger, N.A.; Grass, R.N.; Athanassiou, E.K.; Stark W.J. *Bottom-up fabrication of metal/metal nanocomposites from nanoparticles of immiscible metals*. Chemistry of Materials. 2010, 22(1), 155–160.

[4] Tiwari, D.K.; Behari, J.; Sen, P. *Time and dose-dependent antimicrobial potential of Ag nanoparticles synthesized by top-down approach*. Current Science. 2008, 95(5), 647–655.

[5] Zhang, X.; Qian, J.; Pan, B. *Fabrication of Novel Magnetic Nanoparticles of Multifunctionality for Water Decontamination*. Environ. Sci. Technol. 2016, 50, 881−889.

[6] Kaur, R.; Hasan, A.; Iqbal, N.; Alam, S.; Saini, M.K.; Raza, S.K. *Synthesis and surface engineering of magnetic nanoparticles for environmental cleanup and pesticide residue analysis: A review*. J. Sep. Sci. 2014, 37, 1805–1825.

[7] Hu, J.; Chen, G.; Lo, I. *Selective removal of heavy metals from industrial wastewater using maghemite nanoparticle: performance and mechanisms*. J. Environ. Eng. 2006, 132(7), 709–715.

[8] Petralito, S.; Spera, R.; Memoli, A.; D'Inzeo, G.; Liberti, M.; Apollonio, F. *Preparation and characterization of lipid vesicles entrapping iron oxide nanoparticles*. Asia-Pacific J. Chem. Eng. 2012, 7, 335–341.

[9] Spera, R.; Petralito, S.; Liberti, M.; Merla, C.; D'Inzeo, G.; Pinto, R.; Apollonio, F. *Controlled release from magnetoliposomes aqueous suspensions exposed to a low intensity magnetic field*. Bioelectromagnetics. 2014, 35(4), 309-312.

[10] Spera, R.; Apollonio, F.; Liberti, M.; Paffi, A.; Merla, C.; Pinto, R.; Petralito, S. *Controllable release from high-transition temperature magnetoliposomes by low-level magnetic stimulation*. Colloids and Surfaces B: Biointerfaces. 2015, 131, 136-140.

[11] Soenen, S.J.H.; Hodenius, M.; De Cuyper, M. *Magnetoliposomes: versatile innovative nanocolloids for use in biotechnology and biomedicine*. Nanomedicine. 2015, 4(2), 177-191.

[12] Yoshida, Y.; Furuya, E.; Tagawa, K. *A direct colorimetric method for the determination of phospholipids with dithiocyanatoiron reagent*. J. Biochem. 1980, 88, 463–468.

[13] Belikov, V.G.; Kuregyan, A.G.; Ismailova, G.K. *Standardization of magnetite*. Pharm. Chem. J. 2002, 36, 333–336.

[14] Schuderer, J.; Oesch, W.; Felber, N.; Spät, D.; Kuster, N. *In vitro exposure apparatus for ELF magnetic fields*. Bioelectromagnetics. 2004, 25, 582–591.

# Chapter 4

# Can pulsed electromagnetic fields trigger on-demand drug release from high-Tm magnetoliposomes?

Martina Nardoni[1], Elena della Valle[2], Micaela Liberti[2], Michela Relucenti[3], Maria Antonietta Casadei[1], Patrizia Paolicelli[1], Francesca Apollonio[2], Stefania Petralito[1]

[1]*Department of Drug Chemistry and Technologies, "Sapienza" University of Rome, Piazzale Aldo Moro 5, 00185 Rome, Italy*

[2]*Department of Information Engineering, Electronics and Telecommunications (DIET), "Sapienza" University of Rome, Via Eudossiana 18, 00184 Rome, Italy*

[3]*Department of Anatomical, Histological, Forensic Medicine and Orthopedic Science, "Sapienza" University of Rome, Via A. Borelli 50, 00161 Rome, Italy*

**Nanomaterials 2018, 8, 196; doi: 10.3390/nano804019**

***4.1 Abstract.*** *Recently, magnetic nanoparticles (MNPs) were used to trigger drug release from magnetoliposomes through a magneto-nanomechanical approach, where the mechanical actuation of the MNPs is used to enhance the membrane permeability. This result can be effectively achieved with low intensity non-thermal alternating magnetic fields (AMFs), which, however, found rare clinic application. Therefore, a different modality of generating non-thermal magnetic fields was now investigated. Specifically, the ability of the intermittent signals generated by non-thermal pulsed electromagnetic fields (PEMFs) were used to verify if, once applied to high-transition temperature magnetoliposomes (high-Tm MLs), they could be able to efficiently trigger the release of a hydrophilic model drug. To this end, hydrophilic MNPs were combined with hydrogenated soybean phosphatidylcholine and cholesterol to design high-Tm MLs. The release of a dye was evaluated under the effect of PEMF for different times. The MNPs motions produced by PEMF could effectively increase the bilayer permeability, without affecting the liposomes integrity and resulted in nearly 20% of release after 3 h exposure. Therefore, the current contribution provides an exciting proof-of-concept for the ability of PEMFs to trigger drug release, considering that PEMFs find already application in therapy due to their anti-inflammatory effects.*

***Keywords:*** *magneto mechanical trigger; magnetoliposomes; on-demand drug release; magnetic nanoparticles; PEMF; non-thermal magnetic field.*

## 4.2 Introduction

Lipid vesicles are considered clinically established systems for the delivery of drugs for nanomedicine applications, due to their biocompatibility and ability to encapsulate both hydrophilic and hydrophobic agents. Using a stimulus to release drugs from carriers at a specific time and location is one of the most sought results of drug delivery research. Typically, such a control is gained by changing the environmental conditions (e.g. ultrasound, UV–vis light, temperature or pH of the bulk medium) [1–5]. Among these stimuli, electromagnetic fields can offer substantial benefits for nanomedicine and controlled drug delivery as a remote actuation tool [6–8]. Most typically, high-frequency alternating magnetic fields (HF-AMF, 50–400 kHz) are used to promote local heating within lipid vesicles encapsulating magnetic nanoparticles (MNPs) either in the membrane or inside the water pool using them as devices for magnetic-controlled delivery of drugs [9, 10]. However, the application of these magnetic stimuli may determine damage and secondary effects to the surrounding tissues due to both the temperature increase and to magnetically induced eddy currents, limiting their clinical applicability [11]. Therefore, more recently, the attention has begun shifting to very distinct magnetic field effects exerted on MNPs, namely a magneto-mechanical action, which can be observed with an AMF of much lower intensity and in the absence of heating [12–15]. Aimed to investigate only the mechanical actuation of magnetic nanoparticles by non-heating AMF, in a previous work, authors demonstrated the possibility to gain a controlled release from high-transition temperature magnetoliposomes (high-Tm MLs) by low-level magnetic stimulation [16, 17]. The carrier payload was repetitively released by switching on and off a 20 kHz, 60 A/m magnetic field. The results indicated high reproducibility of cycle-by-cycle release induced by the magnetic-impelled motions driving to the destabilization of the bilayer rather than the phospholipid phase transition or the destruction of the vesicle structure. Therefore, mechanical actuation of magnetic nanoparticles by non-heating magnetic field provides an opportunity to overcome the drawback of heating-magnetic field actuation, creating conditions to consider MNPs and low amplitude magnetic fields prospective powerful

therapeutic tools. By the way, AMF are mainly used in laboratory conditions and rarely applied in clinic, nevertheless non-thermal pulsed electromagnetic fields (PEMFs) are already employed in therapy because of their ability to down-regulate specific cytokines in an inflame environment [18–20]. The main goal of this paper is to comprehend if the intermittent signals generated by PEMFs are able to enhance the permeability of high-Tm MLs (Tm=52 °C) as it occurs with low intensity AMF. The current contribution provides a proof-of-concept for the ability of PEMFs of similar intensity of those used in [16] to trigger on-demand drug release opening a new scenario of synergic dual effect for concrete application in clinics.

## 4.3 Experimental section

### 4.3.1 Materials

Hydrogenated soybean phosphatidylcholine (HSPC) Phospholipon 90H, from Lipoid GmbH (Germany), was kindly gifted by AVG Srl (Italy). Cholesterol (Chol), 4-(2-hydroxyethyl) piperazine-1-ethanesulfonic acid (HEPES), 5-(6) carboxyfluorescein [5-(6) CF], Triton X-100 (TX-100), Sephadex G-50 medium grade, thiocyanatoiron, iron (III) nitrate and hydrochloric acid (HCl) were purchased from Sigma Aldrich (Italy). Chloroform was obtained fromMerck (Italy). Bidistilled water, 1,2-dichloroethane and ethanol were supplied by CarloErba Reagents (Italy). Aqueous dispersion of 50 nm carboxymethyl-dextran coated magnetite ($Fe_3O_4$) nanoparticles (MNPs), fuidMAG-CMX, were obtained from Chemicell GmbH (Germany).

### 4.3.2 Magnetoliposomes preparation

The samples were prepared and characterized as previously reported [16] and here briefly described. We have combined hydrophilic $Fe_3O_4$ MNPs with HSPC and Chol to design a suitable carrier model. The obtained liposomes are referred to as high-temperature sensitive

magnetovesicles (high-Tm MLs) since their membrane can exist only in the ordered state within the experimental temperature interval and neither spontaneous leakage nor thermal responsiveness can occur up to 52 °C. Since the liposome membrane does not undergo transition in the experimental temperature conditions, they represent a suitable carrier model to put in evidence the non-thermal effect of the magnetic field on drug delivery. High-Tm MLs were prepared by means of incorporating commercially available carboxymethyl-dextran coated magnetite nanoparticles within the aqueous core of vesicles, according to the classical film re-hydration method followed by extrusion method, as reported in [21].

HSPC and Chol (5:1 molar ratio) were dissolved in the minimum volume of chloroform and the organic solution was poured into a round bottom flask. The organic solvent was evaporated under reduced pressure at 60 °C until a thin lipid film was formed on the bottom of the flask. The dry lipid film was then hydrated at 60 °C with 10 ml of HEPES buffer solution (10 mM, pH = 7.4) containing MNPs and 5-(6) CF sodium salt (20 mM). Final lipid concentration was 10 mM and magnetite to phospholipid ratio was 0.2 g $Fe_3O_4$/mmol HSPC. Control liposomes (CLs), without MNPs, were prepared by adding 5-(6) CF to the buffer used during the hydration step. The obtained multilamellar vesicles were downsized by sequential extrusion at T>Tm to form unilamellar liposomes in a Lipex extruder (Lipex Biomembranes, Vancouver, BC, Canada). This step was performed through polycarbonate membrane filters (Whatman Cyclopore membranes, Whatman International Ltd., Florham Park, NJ, USA) of decreasing pore size (0.8–0.4–0.2 μm) upon ten times to obtain a narrow size distribution. The unencapsulated fluorescent dye and the non-entrapped ferrofluid nanoparticles were removed by size exclusion chromatography (SEC) with a Sephadex G-50 column. The eluent was HEPES buffer. Alla liposomes formulation were stored in dark at 4 °C and used within 1 week.

### 4.3.3 Physicochemical characterization of liposomes

Hydrodynamic diameter, size distribution and ζ-potential of both CLs and high-Tm MLs were measured with a Zetasizer Nano ZS90 (Malvern Instruments Ltd., Malvern, UK). Hydrodynamic diameter and polydispersity index (PdI) were evaluated by dynamic light scattering (DLS) experiments, whereas ζ-potential was measured by electrophoretic light scattering (ELS) experiments. The DLS and ELS techniques used a photon correlator spectrometer equipped with a 4 mW He/Ne laser source operating at 633 nm. The particle size diameter was determined by Stokes-Einstein relationship. All experiments were performed at a scattering angle of 90°, after diluting 10 times the samples with HEPES buffer solution pH=7.4 to obtain a count-rate of approximately 200 kcps, avoiding interference phenomena of multiple scattering. The analysis were repeated in triplicate and were thermostatically controlled at 25 °C. The HEPES buffer solution used for DLS and ELS experiments was previously filtered through 0.2 μm polycarbonate filters to remove any interfering dust particles.

### 4.3.4 Transmission electron microscopy

The morphology of the nanosystems was examined by transmission electron microscopy (TEM), using a Transmission Electron Microscope operating at an acceleration voltage of 60 kV (TEM Zeiss EM 10, Germany). For the analysis, 20 μl of the suspension, previously diluted with HEPES buffer, were placed on a copper grid coated with a polymeric film (Formavar/Carbon 300 mesh Cu, Agar Scientific Ltd). The excess of water was removed letting the grid drying on a filter paper. Then, a drop of a contrast agent (an aqueous solution of uranyl acetate at 1% w/v) was deposited on the surface of the screen and left in contact with the sample for 5 min. After this time, the excess of the uranyl acetate solution was removed with a filter paper and the samples were dried, at room temperature, before the vesicles were imaged.

### 4.3.5 Phospholipid assay

Phospholipid concentration was determined using the phosphorus colorimetric assay [22]. Briefly, aliquots (0.4 ml) of phospholipids in 50% v/v ethanol were added to a mixture of 1 ml of thiocyanatoiron reagent (previously prepared by solubilizing 0.97 g of ferric nitrate and 15.2 g of ammonium thiocyanate in 100 ml of water) and 0.6 ml of 0.17 N HCl. The solution was incubated for 5 min at 37 °C and then the thiocyanatoiron–phospholipid complex formed was extracted with 3 ml of 1,2-dichloroethane by vigorous shaking for 2 min in a vortex-type mixer. The mixture was centrifuged for 5 min at 2000 rpm to separate the aqueous phase from the organic one containing the complex. The absorbance of the organic phase was measured at 470 nm against a blank without substrate, using a double beam Lambda 25 (Perkin Elmer, USA) UV–Vis spectrophotometer. The amount of lipid was obtained through an appropriate calibration curve, previously constructed. The measurements were repeated both before and after SEC purification of extruded samples.

### 4.3.6 8.5% hydrochloride acid assay

The magnetite content in magnetoliposomes was determined using the method described by Belikov et al. [23]. The method involves the formation, by the addition of 8.5% HCl, of the Iron (II, III) chlorides. To allow solubilization of the magnetite, the liposomal samples were added with 50 μl of TX-100 (30% w/v) that facilitates the breaking of the liposomes and the passage in solution of the chlorides. The mixture thus obtained was vigorously stirred, using a vortex-type mixer (ZX3). The absorbance of the obtained solutions was measured at 320 nm in a Lambda 25 spectrophotometer (Perkin Elmer, USA). The amount of magnetite was obtained through an appropiate calibration line performed with standards solution of magnetite. The measurements were repeated both before and after SEC purification of extruded MLs. All the data collected were used to calculate magnetite/phospholipid ratio.

### 4.3.7 Differential scanning calorimetry

Differential scanning calorimetry (DSC) was used to characterize the influence of cholesterol and MNPs on the thermotropic phase behaviour of HSPC membrane. The measurements were carried out with a DSC131 (Setaram, Caluire-et-Cuire, France), calibrated using the Indio standard (Tf = 157 °C) with a scan rate of 5 °C/min. The samples were obtained by solubilizing the constituents in the minimum amount of chloroform in a round-bottom flask and drying the solution obtained under vacuum at the Tm of the phospholipid (53 °C), until obtaining a thin phospholipid film stratified on the walls of the balloon. Aliquots of 5 mg of each dried film were placed in sealable aluminum pans, then 20 µl of distilled water was added and finally the pans were hermetically sealed. At least three heating/cooling cycles were performed under nitrogen flow (20 ml/min) by setting an initial isotherm at 30 °C for 300 s, a heating ramp from 30 to 70 °C and a second isotherm at 70 °C for 300 s. The thermograms were recorded at a rate of 5 °C/min. An empty aluminium pan was used as reference.

### 4.3.8 Loading efficiency of 5-(6) CF

The 5-(6) CF sodium salt stock solution was obtained dissolving 5-(6) CF powder with few drops of 1M NaOH solution, followed by the addition of HEPES buffered solution up to the appropriate molarity. The fluorescent marker 5-(6) CF was loaded into the aqueous core of the liposomal vesicles during the hydration phase of the thin film. To this end, the probe was added to the HEPES buffer used to hydrate the film, resulting in a marker concentration of 20 mM. Subsequently, the suspensions were purified by SEC to eliminate the non-trapped probe within the vesicles. The purified liposomal suspensions were appropriately diluted in order to have marker concentrations in the range from $1 \cdot 10^{-8}$ to $5 \cdot 10^{-7}$ mol/l. These dilutions were prepared both in the absence and in the presence of lithic concentrations of the TX-100 non-ionic detergent (at 52 °C for 30 min), in order to obtain the equations of the lines respectively of the integral liposomal vesicles and of the destroyed liposomal vesicles. Thus, according to the linear regression method, the entrapment capacity of the studied

nanosystems was estimated as μl of entrapped volume for mg of lipid. The fluorescence of all the samples was determined fluorimetrically by means of the spectrofluorometer LS 50B (Perkin Elmer, USA) at $\lambda_{ex}$= 492 nm and $\lambda_{em}$= 512 nm. The probe concentration was obtained through an appropriate calibration line, previously constructed (as reported in S.I.).
All experiments were performed in triplicate and the results reported as mean ± standard deviation.

### 4.3.9 Measurement of 5-(6) CF released from liposomes

The membrane permeation of the obtained high-Tm MLs was evaluated measuring the release behaviour of the self-quenching and membrane impermeable 5-(6) CF, used as a model hydrophilic drug. Specifically, in vitro release of 5-(6) CF from high-Tm MLs and from CLs samples was determined by monitoring marker fluorescence de-quenching through spectrofluorimetry at excitation and emission wavelengths of 492 and 512 nm, respectively. The release was measured both due to an applied PEMF stimulation and under sham-conditions [high-Tm MLs positioned as in Figure 4.2 (a) but without coil feeding]. The release of 5-(6) CF from high-Tm MLs and CLs was evaluated as a function of the PEMF application time, for different time durations: 15, 30, 60 and 180 min. In addition, the effect of the magnetic field on the sample was evaluated by switching on (3 h) and off (21 h) PEMF, for a total of 6 h of exposure. At the end of each series of measurements, all the liposomal vesicles were completely destroyed with addition of a non-ionic detergent (TX-100, 30% w/v) in order to evaluate the residual amount of 5-(6) CF still contained in the samples. A water bath was used to control the environmental temperature (37.0±0.1 °C). The percent release of 5-(6) CF was determined as follows:

$$5-(6)\ CF\ released\ (\%) = \frac{(I_t - I_0)}{(I_{max} - I_0)} \cdot 100 \qquad (4.1)$$

where: $I_t$ and $I_0$ are the intensities of fluorescence at each time and a $t_0$, respectively; $I_{max}$ is the total fluorescence after adding TX-100 (30% w/v).

### 4.3.10 PEMF exposure set-up

For the PEMF exposure, the medical device I-ONE (IGEA, Carpi, Italy), a product that is already CE certified, was used. In Figure 4.1 it is shown the system that is composed of:

- generator
- power supply
- solenoid

**Figure 4.1. I-ONE coil exposure set-up with the generator, the power supply and the solenoid.**

Battery-operated device I-ONE, generating a peak magnetic field of 1.5 mT at the coil, with a repetition frequency of 75 Hz, was tested in our experiments. The device is constituted by a current pulse generator feeding an external coil, which produces the PEMF. The pulsed signal has the following temporal characteristics (see Figure 4.2, b): duration of the active phase of the signal is 1.3±0.1 ms; repetition frequency is 75 Hz (which is equivalent to a repetition time period between two successive pulses of 13.3 ms); amplitude of the current peak value is 1.05 A.

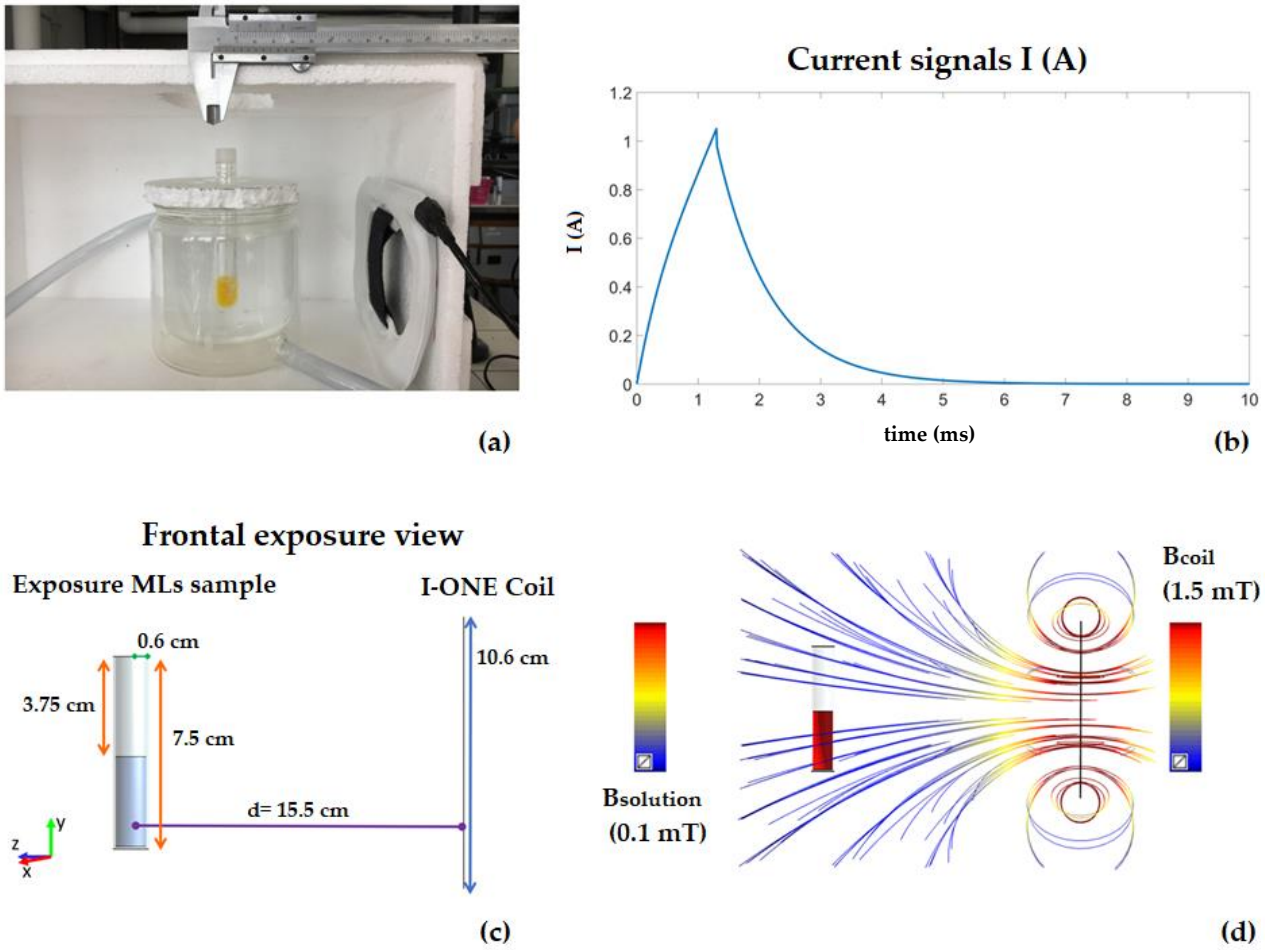


**Figure 4.2. (a) PEMF exposure setup; (b) current signal feeding the coil; (c) model of the high-Tm MLs exposure system in the frontal exposure view; (d) magnetic field distribution in the high-Tm MLs sample given by the magnetic field intensity of the coil (streamlines).**

The high-Tm MLs sample was placed at a distance of 13 cm from the coil (15.5 cm considering the thickness of both the coil and the thermal bath recipient), as shown in Figure 4.2 (a), obtaining a magnetic field of 100 mT. Such a distance was chosen with numerical Magneto Quasi-static simulations, performed with the Software Sim4Life (V. 3.4, ZMT Zurich MedTech AG, Zurich, Switzerland) at frequency of 250 Hz (the first lobe of the spectral of the signal). The model geometry is reported in Figure 4.2 (c). The cuvette was simulated as a cylinder with 7.5 cm of height and a radius of 0.6 cm, half-filled with a conductive solution (0.049 S/m), which represents the experimentally measured conductivity of the high-Tm MLs suspension (N=28, std.=0.005). A fine grid mesh (0.6 mm of resolution) was adopted for the coil and a more accurate resolution was chosen for the

cuvette discretization (0.4 mm). In Figure 4.2 (d), the magnetic field streamlines and the B field distribution inside the cuvette are reported, showing a B field of 100 mT inside the solution, when 1.5 mT is applied at the coil. The magnetic field appears to be homogeneous inside the sample ensuring a good exposure for the high-Tm MLs suspension.

## 4.4 Results

TEM images of CLs and high-Tm MLs structures are shown in Figure 4.3 (a–c). CLs and high-Tm MLs exhibited similar size and morphology, which indicates that MNPs interaction, at the lipid/MNPs ratio employed, did not affect vesicles formation and the overall bilayer integrity. TEM images also suggest that interaction between MNPs and HSPC lipids leads to magnetoliposomes with hybrid colloidal structure: the iron oxide nanoparticle can either decorate the liposomal surface (Figure 4.3, c) or be internalized inside the vesicles, as individual entities or MNPs aggregates (Figure 4.3, b). Free nanoparticles were not observed outside the liposome vesicles throughout the TEM grid, thus indicating the efficacy of the SEC purification step.

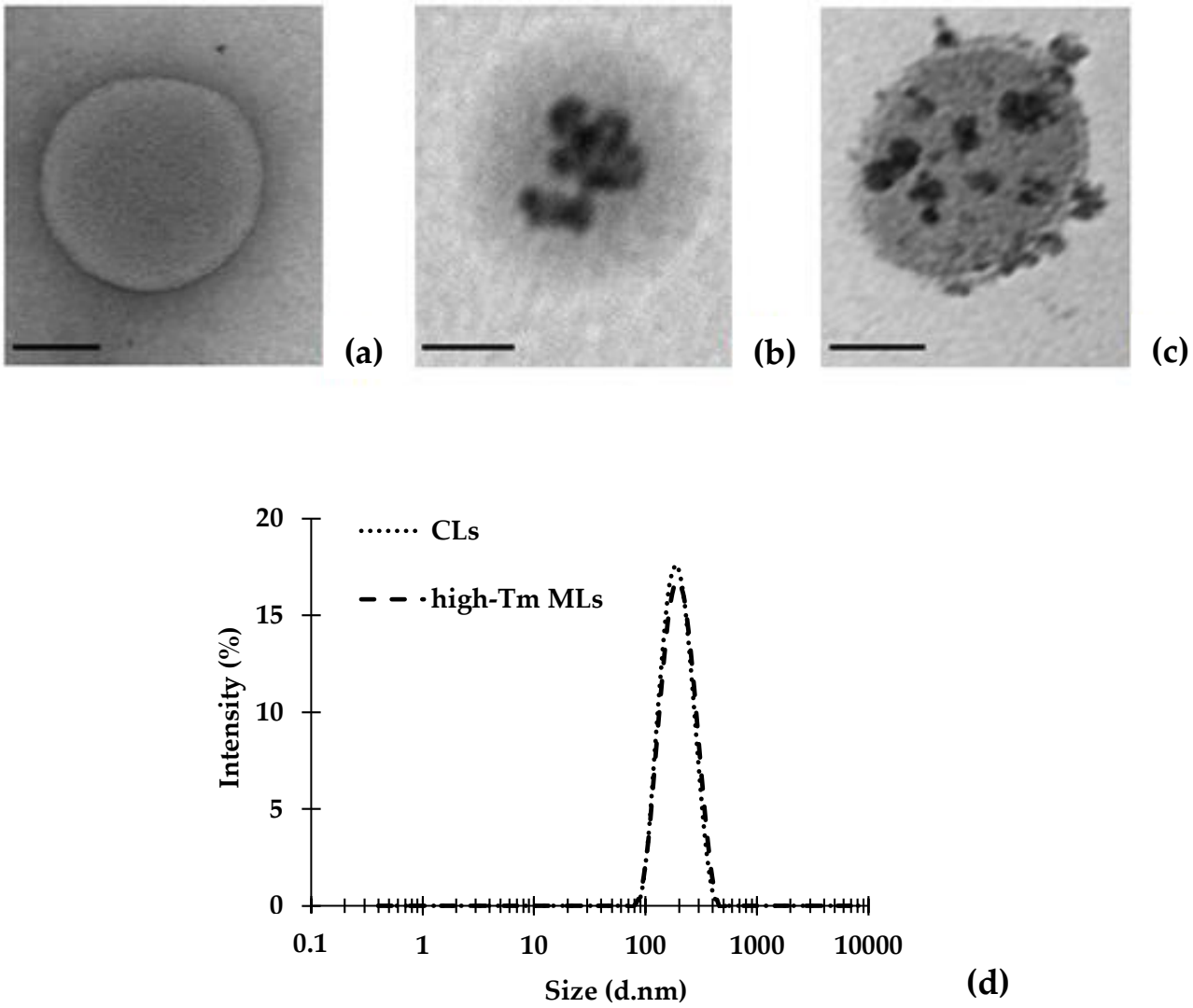


**Figure 4.3. TEM images showing HSPC liposomes (a) conventional and (b, c) high-Tm MLs (scale bar: 100 nm); (d) DLS measurements of liposomes size.**

No differences were observed in vesicles size between CLs and high-Tm MLs, as shown in Figure 4.3 (d). Both nanocarriers were arranged in a monomodal distribution with PdI values <0.200, as reported in Table 4.1. ζ-potential value of CLs and high-Tm MLs in the buffer medium is, in both cases, negative but the high-Tm MLs show more electronegative character, which suggests the presence of some negatively charged MNPs absorbed onto the external leaflet of the phospholipid bilayer.

Hydration step of the dry lipid film during liposome preparation was not influenced by the presence of MNPs in the hydrating medium. In fact, the percentage of lipid molecules found

in the self-closing bilayer of high-Tm MLs only partially decreased respect to CLs (>80%). Finally, to probe the membrane permeation and release behaviour of high-Tm MLs, 5-(6) CF was used as a model hydrophilic drug, with satisfactory values of marker loading efficiency, expressed as captured volume of marker bulk solution (20 mM) to lipid ratio (μl/mg structured HSPC), which was not limited by the co-loading of MNPs inside vesicles (Table 4.1). After SEC purification, the lipid and the magnetite content were determined and the encapsulation efficiency was calculated as g of iron oxide for mmol of lipid. The results are reported in Table 4.1 below.

**Table 4.1. Physical characterization of liposomes: the hydrodynamic diameter (Z-average), PdI values and ζ-potential values for CLs and high-Tm MLs were determined immediately after SEC purification. Loading efficiency of 5-(6) CF and of $Fe_3O_4$ are also reported.**

| Sample | CLs | MLs |
|---|---|---|
| **Hydrodynamic diameter (nm)** | 220.9±22.4 | 240.9±26.6 |
| **PdI** | 0.046±0.028 | 0.131±0.031 |
| **ζ-potential (mV)** | -10.28±1.43 | -15.42±1.51 |
| **5-(6) CF loading efficiency (μl/mg HSPC)** | 2.29±0.26 | 1.84±0.13 |
| **$Fe_3O_4$ loading efficiency (g/mmol HSPC)** | - | 0.2±0.1 |

In the thermogram reported in Figure 4.4, pure HSPC membranes exhibit two endothermic peaks at 46.6 °C and 52.8 °C, corresponding to the "pre" and "main" transition temperature (Tm), respectively. When Chol was added to HSPC (HSPC/Chol 5:1 mol ratio), the endothermic peak, corresponding to the main transition of the phospholipid, became smaller and broader, while the peak corresponding to the pre-transition disappeared. The position of the main transition peak of the mixture shifted toward lower temperatures, anyway liposomes with Chol can be still considered as high-Tm membrane vesicles, since within our experimental conditions, they can exist only in the ordered state. Neither spontaneous leakage nor thermal effects can occur up to 50 °C. Our results are in agreement with those reported by Kitayama and co-workers in [24]. We have also investigated the effect of the MNPs on the phase behaviour of HSPC/Chol 5:1 mol ratio mixture. As evident in the Figure 4.4, MNPs did not hinder the lipid ordering and phase behaviour of the

investigated bilayer. Moreover, the MNPs did not influence the thermal leakage behaviour of high-Tm MLs compared to CLs. 5-(6) CF leakage from high-Tm MLs and CLs was examined as a function of temperature from 25 to 52 °C. As evident from the results reported, both the high-Tm MLs and CLs exhibited maximum changes in 5-(6) CF leakage, at temperatures corresponding to the melting transition. These results confirm the agreement between the leakage and phase transition peaks.

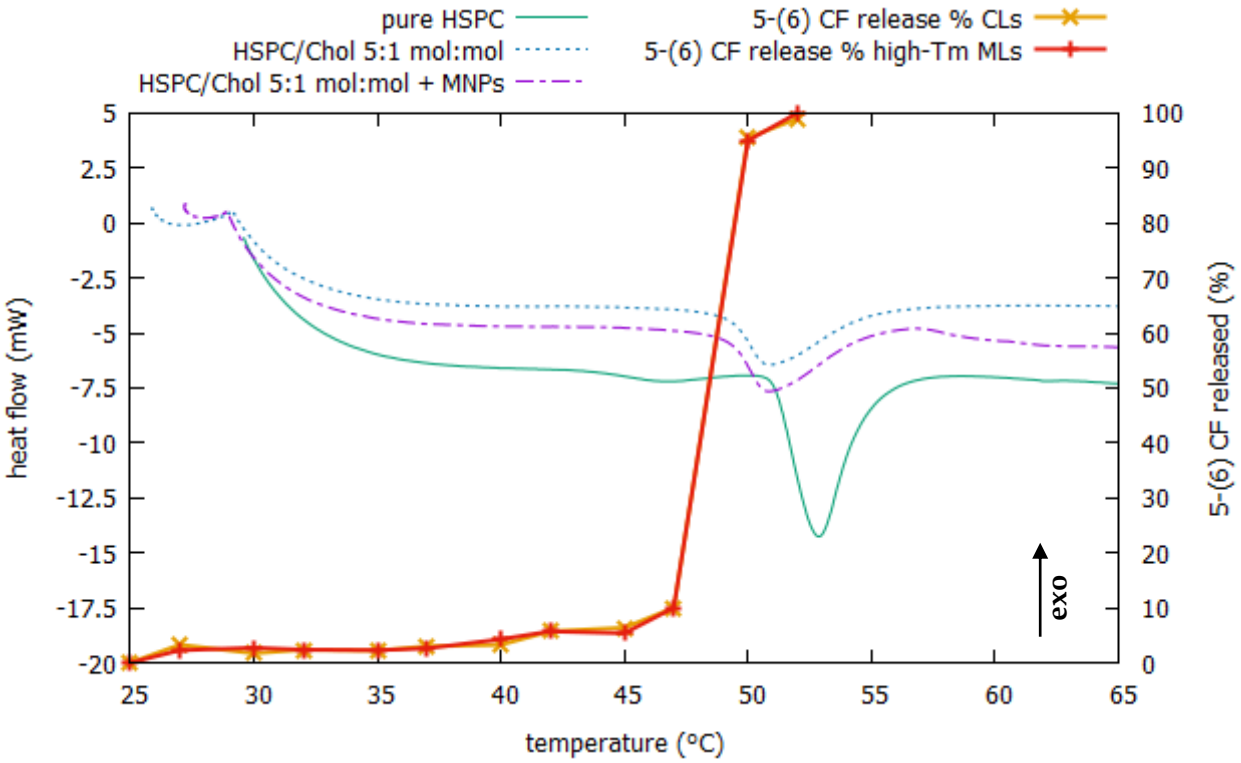


**Figure 4.4. 5-(6) CF cumulative release from high-Tm MLs (red points-lines) and CLs (orange points-line) as a function of temperature from 25 to 52 °C and DSC scanning profile of the melting process of HSPC/Chol 5:1 mol ratio mixture, with or without MNPs.**

The release of 5-(6) CF from high-Tm MLs was evaluated as a function of the PEMF application time. Figure 4.5 displays the release behaviour of high-Tm MLs, reported as concentration of 5-(6) CF released for different lipid concentrations before and after 180 min of continuous PEMF exposure.

At the end of each series of measurements, all the liposomal vesicles were completely destroyed with the addition of a non-ionic detergent in order to evaluate the residual amount of 5-(6) CF. According to the results, PEMF stimulation modify the membrane permeability, as indicated by the marker leakage, which reaches about 17% after 180 min.

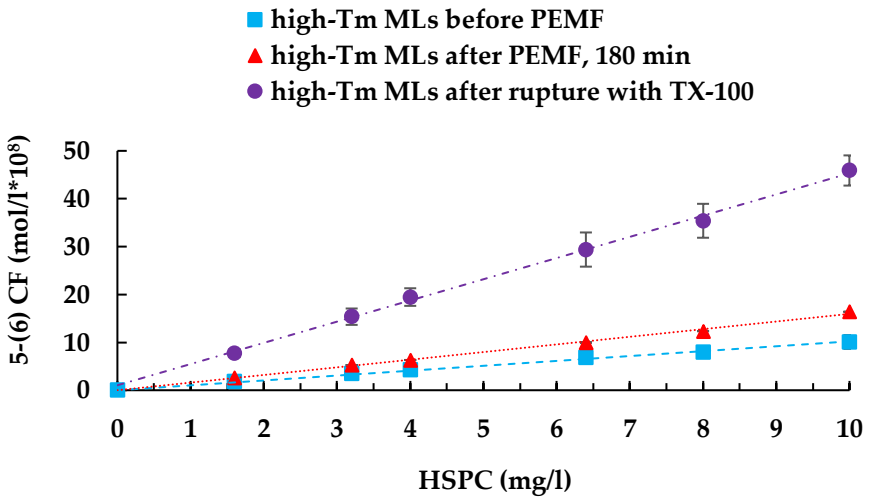


**Figure 4.5. Release data of 5-(6) CF from high-Tm MLs before and after PEMF exposure. The results are reported as molar concentration of marker for different lipid concentrations and compared with the total amount of fluorescent dye released, after complete destruction of high-Tm MLs with Triton X-100. The calibration curve, fluorescence (U.A.) = 1.47 x $10^9$ [5-(6) CF mol/l + 4.18], ($R^2$ = 1.00), was used to establish a relationship between 5-(6) CF fluorescent intensity and dye concentration (as reported in S.I.).**

The increase of the release as a function of exposure duration is an indicator of a dose-response effect as reported in Figure 4.6, where moving from 15 to 180 min of exposure the fluorescent release presents an overall three-fold increase. Nevertheless, it is important to say that the application of PEMF did not lead to the liposomes rupture.

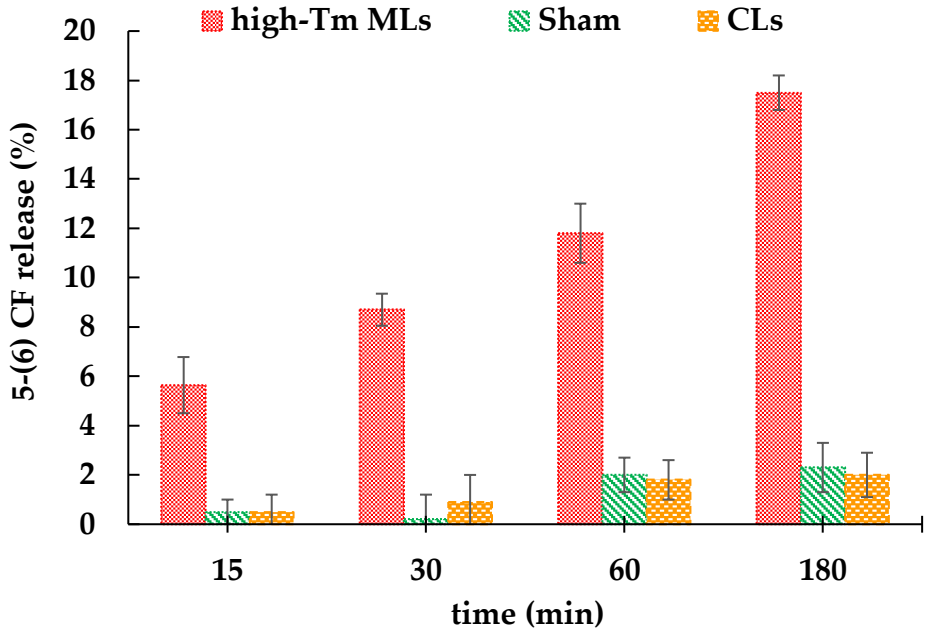


**Figure 4.6. Percentage of the 5-(6) CF release from high-Tm MLs, CLs and Sham at 15, 30, 60 and 180 min.**

In order to further show the effect of PEMF on the controlled drug release from high-Tm MLs, release of 5-(6) CF was carried out by commutatively switching on (3 h) and off (21 h) the PEMF as a function of time. An important feature of the graph, in Figure 4.7, is that 5-(6) CF can be released repetitively from high-Tm MLs (7% of extra release after the second stimulation is reported). Long off period (21 h) demonstrated also the stability of the high-Tm MLs against undesired leakage, when the B field is off.

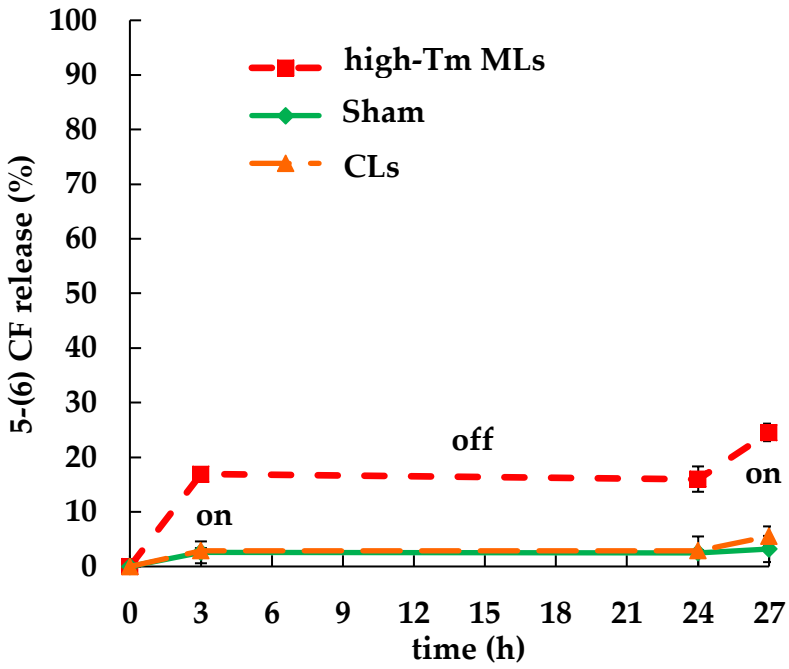


**Figure 4.7. Percentage of the 5-(6) CF release from high-Tm MLs, CLs and Sham under on-off modality.**

## 4.5 Discussion

Over the last years, magnetoliposomes were extensively investigated for controlled drug release. The localized heating, produced by movements of MNPs under a magnetic field of sufficient intensity and frequency, acts as the main trigger for drug release. In fact, when magnetic nanoparticles are combined with thermosensitive lipids, the release of the drug from the hybrid thermosensitive liposome/nanoparticle assemblies can be essentially attributed to the caloric effect resulting in the phase transition of the thermosensitive-liposome. In particular, the magnetically induced heat is transferred to the entire carrier, causing temperature increases from physiological temperature to tolerable hyperthermia (41–46 °C), with structural changes in the lipid bilayer that is designed to shift from a gel to liquid phase when this increase in temperature occurs. While the magnetically induced hyperthermia is the main applied approach in controlled drug delivery, it may indiscriminately affect every surrounding tissue, because it is generally very tricky to keep temperature inside the therapeutic window. Therefore, the magneto-mechanical approach

based on the vibration or rotation of iron oxide particles, not associated with heat generation, is of more wide application. In fact, magnetic field trigger, at frequencies and strength that are several orders of magnitude lower than those needed for the magnetic thermal approach, gives some supplementary advantages. In particular, low amplitude (<100 A/m, 20 kHz) AMFs are able to produce mechanical forces from magnetic nanoparticle, which generate transient deformations in the nanometer scale within the liposomal membrane [16]. Similarly, PEMFs proved to be an effective remote trigger. In fact, the obtained results demonstrate that high-Tm MLs respond to PEMF at temperature well below the main transition temperature of the bilayer (Tm=52 °C). Also, with this modality of magnetic field generation, the payload release from high-Tm MLs was due to the magnetic-impelled motions of the MNPs, which drive the destabilization of the bilayer without destruction of the liposome structure or modification of the arrangements of the phospholipids. Moreover, the content released from the high-Tm MLs, triggering repetitively by switching on and off the PEMF, demonstrated the possibility of using high-Tm MLs as depot system. Not least, the repetitive release from high-Tm MLs proved that liposomes structure was retained during PEMF exposure and that high-Tm MLs were stable and able to preserve their physical properties over time, for at least 30 days.

## 4.6 Conclusions

Overall, these achievements may be used to design novel PEMF-sensitive drug delivery systems, taking advantage from the mechanical stress induced on the liposomes membrane. In particular, the combination of magneto-carriers and PEMFs is an exciting dual approach, where synergistic properties of both modalities could be effectively utilized for inflammatory reduction and remotely-activated drug delivery. In particular, PEMFs demonstrated to exert an anti-inflammatory effect resulted in early pain control and enhanced functional recovery in the knee diseases, reducing knee osteoarthritic lesion progression with long term positive benefits for patients [25,26]. At the same time, it is well known that a single-dose intra-articular administration of liposomes within a synovial joint,

can be used to treat the inflammatory process [27, 28]. Therefore, a novel concept of enhanced localized treatments could be proposed combining the functionalities of the magneto-mechanical actuation and the healing properties of a non–thermal magnetic field. Both approaches could work in close synergy with drug-loaded nanocarriers, able to control drug release by the application of a remote magnetic field. In this way, the efficiency of anti-inflammatory therapies can be maximized in future medical applications.

## 4.7 Supplementary Information (S.I.).

In Figure 4.1 S.I. is reported the calibration curve used to establish the relationship between fluorescent intensity and concentration of 5-(6) CF.

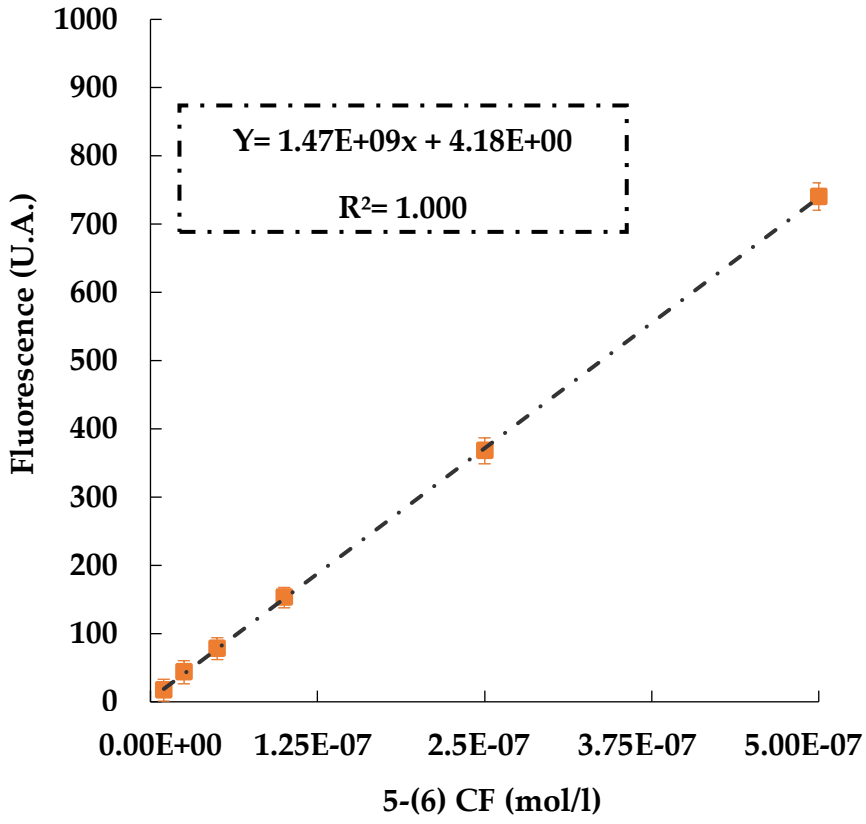


**Figure 4.1 S.I. Calibration curve of 5-(6) CF with the linear regression mentioned in Figure 4.5.**

***Acknowledgments.*** *This work was financially supported by the grant 000322_Scientific_Research from Sapienza University of Rome, "Control of drug release from liposome vesicles using electromagnetic fields." The authors are grateful to Ruggero Cadossi and Stefania Setti for the I-ONE pulse generator (Igea, Carpi, Italy).*
***Author Contributions.*** *F.A., M.L., S.P., P.P. conceived and designed the experiments; M.N. and E.d.V. contributed equally to this work by carrying out the experiments; M.R. contributed with the TEM characterization; F.A., M.L., S.P., P.P., E.d.V. and M.N. wrote the manuscript; further supervision was carried out by M.A.C.; all the authors analysed the data and revised the manuscript.*
***Conflicts of Interest.*** *The authors declare no conflict of interest.*

## 4.8 References

[1] Ganta, S.; Devalapally, H.; Shahiwala, A.; Amiji, M. *A review of stimuli-responsive nanocarriers for drug and gene delivery*. J. Control. Release. 2008, 126, 187–204.

[2] Mura, S.; Nicolas, J.; Couvreur, P. *Stimuli-responsive nanocarriers for drug delivery*. Nat. Mater. 2012, 12, 991–1003.

[3] Leung, S.J.; Romanowski, M. *Light-activated content release from liposomes*. Theranostics. 2012, 2, 1020–1036.

[4] Schroeder, A.; Kost, J.; Barenholz, Y. *Ultrasound, liposomes and drug delivery: Principles for using ultrasound to control the release of drugs from liposomes*. Chem. Phys. Lipids. 2009, 162, 1–16.

[5] Karanth, H.; Murthy, R.S. *pH-sensitive liposomes-principle and application in cancer therapy*. J. Pharm. Pharmacol. 2007, 59, 469–483.

[6] Pradhan, P.; Giri, J.; Rieken, F.; Koch, C.; Mykhaylyk, O.; Döblinger, M.; Banerjee, R.; Bahadur, D.; Plank, C. *Targeted temperature sensitive magnetic liposomes for thermo-chemotherapy*. J. Control. Release. 2010, 142, 108–121.

[7] Preiss, M.R.; Bothun, G.D. *Stimuli-responsive liposome-nanoparticle assemblies*. Expert Opin. Drug Deliv. 2011, 8, 1025–1040.

[8] Kurd, K.; Khandagi, A.A.; Davaran, S.; Akbarzadeh, A. *Cisplatin release from dual-responsive magnetic nanocomposites*. Artif. Cells Nanomed. Biotechnol. 2016, 44, 1031–1039.

[9] Babincová, M.; Cicmanec, P.; Altanerová, V.; Altaner, C.; Babinec, P. *AC-magnetic field controlled drug release from magnetoliposomes: Design of a method for site-specific chemotherapy*. Bioelectrochemistry. 2002, 55, 17–19.

[10] Viroonchatapan, E.; Sato, H.; Ueno, M.; Adachi, I.; Tazawa, K.; Horikoshi, I. *Release of 5-Fluorouracil from Thermosensitive Magnetoliposomes Induced by an Electromagnetic Field*. J. Control. Release. 1997, 46, 263–271.

[11] Gupta, A.K.; Naregalkar, R.R.; Vaidya, V.D.; Gupta, M. *Recent advances on surface engineering of magnetic iron oxide nanoparticles and their biomedical applications*. Nanomedicine. 2010, 2, 23–39.

[12] Nappini, S.; Fogli, S.; Castroflorio, B.; Bonini, M.; Bombelli, F.B.; Baglioni, P. *Magnetic field responsive drug release from magnetoliposomes in biological fluids*. J. Mater. Chem. B 2016, 4, 716–725.

[13] Golovin, Y.I.; Gribanovsky, S.L.; Golovin, D.Y.; Klyachko, N.L.; Majouga, A.G.; Master, A.M.; Kabanov, A.V. *Towards nanomedicines of the future: Remote magneto-mechanical actuation of nanomedicines by alternating magnetic fields*. J. Control. Release. 2015, 219, 43–60.

[14] Dobson, J. *Remote control of cellular behaviour with magnetic nanoparticles*. Nat. Nanotechnol. 2008, 3, 139–143.

[15] Klyachko, N.L.; Sokolsky-Papkov, M.; Pothayee, N.; Efremova, M.V.; Gulin, D.A.; Pothayee, N.; Kabanov, A.V. *Changing the Enzyme Reaction Rate in Magnetic Nanosuspensions by a Non-Heating Magnetic Field*. Angew. Chem. Int. Ed. 2012, 51, 12016–12019.

[16] Spera, R.; Apollonio, F.; Liberti, M.; Paffi, A.; Merla, C.; Pinto, R.; Petralito, S. *Controllable release from high-transition temperature magnetoliposomes by low-level magnetic stimulation*. Colloids Surf. B Biointerfaces. 2015, 131, 136–140.

[17] Spera, R.; Petralito, S.; Liberti, M.; Merla, C.; D'Inzeo, G.; Pinto, R.; Apollonio, F. *Controlled release from magnetoliposomes aqueous suspensions exposed to a low intensity magnetic field*. Bioelectromagnetics. 2014, 35, 309–312.

[18] Varani, K.; Gessi, S.; Merighi, S.; Iannotta, V.; Cattabriga, E.; Spisani, S.; Cadossi, R.; Borea, P.A. *Effect of low frequency electromagnetic fields on a2a adenosine receptors in human neutrophils*. Br. J. Pharmacol. 2002, 136, 57–66.

[19] Varani, K.; De Mattei, M.; Vincenzi, F.; Gessi, S.; Merighi, S.; Pellati, A.; Ongaro, A.; Caruso, A.; Cadossi, R.; Borea, P.A. *Characterization of adenosine receptors in bovine chondrocytes and fibroblast-like synoviocytes exposed to low frequency low energy pulsed electromagnetic fields*. Osteoarthr. Cartil. 2008, 16, 292–304.

[20] Varani, K.; Vincenzi, F.; Ravani, A.; Pasquini, S.; Merighi, S.; Gessi, S.; Setti, S.; Cadossi, M.; Borea, P.A.; Cadossi, R. *Adenosine receptors as a biological pathway for the anti-inflammatory and beneficial effects of low frequency low energy pulsed electromagnetic fields*. Mediators Inflamm. 2017, 2740963.

[21] Martina, M.S.; Fortin, J.P.; Menager, C.; Clement, O.; Barratt, G.; Grabielle-Madelmont, C.; Gazeau, F.; Cabuil, V.; Lesieur, S. *Generation of Superparamagnetic Liposomes Revealed as Highly Efficient MRI Contrast Agents for In Vivo Imaging*. J. Am. Chem. Soc. 2005, 127, 10676–10685.

[22] Y. Yoshida, E. Furuya, K. Tagawa. *A direct colorimetric method for the determination of phospholipids with dithiocyanatoiron reagent*. Journal of Biochemistry. 1980, 88, 463–468.

[23] Belikov, V.G.; Kuregyan, A.G.; Ismailova, G.K. *Standardization of magnetite*. Pharm. Chem. J. 2002, 36, 333–336.

[24] Kitayama, H.; Takechi, Y.; Tamai, N.; Matsuki, H.; Yomota, C.; Saito, H. *Thermotropic Phase Behavior of Hydrogenated Soybean Phosphatidylcholine–Cholesterol Binary Liposome Membrane*. Chem. Pharm. Bull. 2014, 62, 58–63.

[25] Veronesi, F.; Torricelli, P.; Giavaresi, G.; Sartori, M.; Cavani, F.; Setti, S.; Cadossi, M.; Ongaro, A.; Fini, M. *In vivo effect of two different pulsed electromagnetic field frequencies on osteoarthritis*. J. Orthop. Res. 2014, 32, 677–685.

[26] Gobbi, A.; Karnatzikos, G.; Chaurasia, S. *Pulsed Electromagnetic Fields for the Treatment of Symptomatic Patellofemoral Cartilage Lesions of the Knee*. In The Patellofemoral Joint; Gobbi, A.,

Mendes, J.E., Nakamura, N., Eds.; Springer: Heidelberg/Berlin, Germany, 2014; pp. 261–266. ISBN 978-3-642-54965-6.

[27] Van den Hoven, J.M.; Van Tomme, S.R.; Metselaar, J.M.; Nuijen, B.; Beijnen, J.H.; Storm, G. *Liposomal Drug Formulations in the Treatment of Rheumatoid Arthritis*. Mol. Pharm. 2011, 8, 1002–1015.

[28] Chuang, S.Y.; Lin, C.H.; Huang, T.H.; Fang, J.Y. *Lipid-Based Nanoparticles as a Potential Delivery Approach in the Treatment of Rheumatoid Arthritis*. Nanomaterials. 2018, 8, 42–58.

# Chapter 5

# Theoretical and experimental evaluation of the nanosecond electric pulses as triggers to permeabilize nano-lipid based drug delivery systems

Martina Nardoni[1], Laura Caramazza[2,3], Patrizia Paolicelli[1], Stefania Petralito[1], Maria Antonietta Casadei[1], Annalisa De Angelis[2], Micaela Liberti[2], Francesca Apollonio[2]

[1]*Department of Drug Chemistry and Technologies, "Sapienza" University of Rome, Piazzale Aldo Moro 5, 00185 Rome, Italy*

[2]*Department of Information Engineering, Electronics and Telecommunications (DIET), "Sapienza" University of Rome, Via Eudossiana 18, 00184 Rome, Italy*

[3]*Center for Life Nano Science@Sapienza, Italian Istitute of Technology,00161 Rome, Italy*

**Submitted**

***5.1 Abstract.*** *In this work it was reported the experimental proof-of-concept of the possibility to permeabilize unilamellar nanometer-sized liposomes, applying ultra-short (ns) and intense (MV/m) external pulsed electric fields (nsPEFs). In order to reach this purpose, a reproducible and reable experimental protocol was fine tuned for the 10 nsPEF application on unilamellar liposomes of egg phosphatydilcholine (Egg PC-Ls) of nanometer sizing. Therefore, the increasing membrane permeability of Egg PC-Ls was evaluated monitoring the release of a fluorescent dye, previously trapped in their core. Finally, to support the experimental data, a numerical model of the liposomal suspension exposed to 10 nsPEF was proposed, according with the experimental conditions.*

***Keywords:*** *electropermeabilization; electric field; nanosecond pulsed electric field; membrane permeability; liposomes of nanometer sizing; trigger; numerical model.*

## 5.2 Introduction

Recently, the ability of electric pulses in inducing biological effects proved to be an efficient strategy in the fields of biology, biotechnology, and medicine, e.g. for applications such as cell fusion [1-3], electrochemotherapy [4-9] and gene electrotransfer [10-14]. It is known that cell membrane behaves as a barrier that hinders the free diffusion of molecules, as ions and hydrophilic compounds, across the phospholipid bilayer. However, the cells membrane permeation can be transiently increased, applying an external electric field [15-17]. Thanks to this approach was developed a new antitumor treatment which consists in delivering electric pulses to the tumor mass, some minutes after an intravenous injection of bleomycin [18], gaining in this way the direct access of the drug to the cytosol of cells. Once again, the electrochemotherapy made possible the administration, in clinical trials, of highly cytotoxic molecules, such as the hydrophilic cisplatin [19]. Despite all investigations related to the membrane electropermeabilization process [20-22], there seems to be general agreement in the literature that little is known about what is really occurring during this elegant way to reach the cell interior. In fact, although the indirect proofs of the membrane permeabilization, mediated by an external electric field (e.g. gene transfer evaluation through the associated gene expression), it is not easy only with mathematical techniques to create a physical model that corresponds to the electropermeabilization process and, consequently, understand the molecular mechanisms at the single-cell level. Anyway, the theoretical achievements of the last few years suggest that, while it is difficult to identify all the steps that lead to the formation of pores in the membrane, the structural reorganization of the membrane seems to be connected with an increase of the transmembrane potential, thus exceeding the dielectric strength of the membrane itself, with respect to rest conditions [23, 24]. Due to this effect of the electric pulses applied, it should be the formation of transient aqueous pathways that, crossing the lipid barrier, result in a raised membrane permability and finally in the uptake of different foreign molecules into the cells cytosol [3, 25, 26]. Apart from the understanding of the process, one of the most important aspects to be evaluated, following the application of the electric field, is cell viability. The reversibility

of the electropermeabilization process, therefore cells outliving, could be compromised not only by the intensity, but also by the number and duration of the electric pulses. In fact, it was demonstrated that for high intensities of 300 kV/cm and duration of 300 ns, apoptotic phenomena were observed on up to 90% of cell population in less than 10 min following the application of the pulses [27]. Despite of this, reducing the pulse duration to 10 ns or less with intensity always in the order of kV/cm, cell membrane could be destabilized without causing cell death [28], so that the application of one or several electric pulses of 10 ns duration has become usual in nanoporation of cells [29–34]. In addition, to prevent the problem of apoptosis, this type of signals, with rise and fall times in the order of few nanosecond and amplitudes of about kV/cm, proved to be able to affect intracellular organelles. It was extensively supported, over time, the ability of the nanosecond electric pulses to be perceived in the cell interior: the permeabilization of intracellular granules [35], large endocytosed vacuoles [36], endocytotic vesicles [37], the nuclear envelope [38], the inner mitochondrial membrane [39], and moreover the trigger on the calcium release from endoplasmic reticulum [40-42] are all examples of this interesting evidence. The feasibility of intracellular organelles electroporation motivated some authors to investigate theoretically [43-45] the nanosecond pulsed electric field (nsPEF) applicability for drug delivery, specifically replacing intracellular components with liposomes of similar dimensions. This intuition stems from the similarity between biological and liposomal membrane, in terms of phospholipid composition. In this way it is possible to achieve two objectives: to facilitate drug release from liposomes to cells through a simultaneous electric permeation of both systems, placing carriers outside the cells; to have insight into the mechanism of electropermeabilization using a simpler membrane model, like the liposomal one [46-48]. According to the previously microdosimetric simulations [44], the main goal of this work was to determine the experimental proof-of-concept of the possibility to permeabilize nanometer-sized liposomes, applying as triggers ultra-short (ns) and intense (MV/m) external PEF, by means of a standard electroporation cuvette (consisting of two plate parallel electrodes with a gap of 1 mm). Apart from the intensity, the number and the

duration of signals, the external medium conductivity of vesicles is an important parameter which can influence the success of membrane permeabilization, also considering technological limits [44, 45, 49]. For this purpose, liposomes of egg phosphatydilcholine were prepared in two different conductivity buffered solutions and the efficiency in the bilayer permeabilization, after the application of the electric signals, was evaluated monitoring the release of a fluorescent dye, previously trapped in the aqueous core of liposomes. Moreover, is here proposed a methodology for the exposure of liposomes, with dimension in the nanometer scale, in terms of design of the experimental set-up for the electric stimulation of lipid vesicles, combined with an integral characterization of the exposure system and a numerical modelling evaluation of the electric field threshold, needed to enhance the liposomes membrane permeability, according with the experimental conditions.

## 5.3 Experimental section

### 5.3.1 Materials

Egg phosphatidylcholine (Egg PC) Lipoid 80 E, from Lipoid GmbH (Germany), was kindly offered by AVG Srl (Italy). 4-(2-hydroxyethyl) piperazine-1-ethanesulfonic acid (HEPES), 5-(6) carboxyfluorescein [5-(6) CF], Triton X-100 (TX-100), Sephadex G-50 medium grade, hydrochloric acid (HCl), thiocyanatoiron, iron (III) nitrate, ammonium thiocyanate and sodium hydroxide (NaOH) were purchased from Sigma Aldrich (Italy). Chloroform was obtained from Merck (Italy). Bidistilled water, sodium chloride (NaCl), ethanol and1,2-dichloroethane were supplied by CarloErba Reagents (Italy). Cyclopore polycarbonate membrane filters Whatman® were purchased from Cyclopore Track Etched Membrane.

### 5.3.2 Experimental set-up

The experimental configuration set-up used for the application of nsPEFs to a liposomal suspension is consituted by the following components:

- a high voltage 50 Ω pulse generator, which produces the pulsed signal needed for the stimulations
- an exposure system with an electroporation cuvette, containing the target suspension, and a coaxial cable connected to the cuvette holder
- a temperature probe, that detects information on the temperature in the exposed suspension
- a high power coaxial cable, able to transmit the signals from the generator to the exposure system.

In our case, the generator is a high voltage nanosecond pulse generator (FPG 10-1NM10, FID Technology, Burbach, Germany). It is designed to operate into a 50 Ω load impedance and to produce pulses ranging from 2 kV to 10 kV, with rise time of about 1.5 ns. According to the generator manual, the duration of the generated pulses is about 8-10 ns at 50% of the maximum amplitude. As fully described in [44], the exposure system is composed of a coaxial cable and an applicator device, with a standard electroporation cuvette (two stainless steel active electrodes, a surface of 10 × 8 $mm^2$ and a gap between them of 1 mm; 1002561E, BioGenerica, ITA) and a transition from the cuvette to the coaxial cable (Figure 5.1, a-b). Briefly, the cuvette holder provides the presence of two brass electrodes with area of 33 × 10 $mm^2$ and a thickness of 2 mm. The gap between the electrodes is 11 mm and allows the insertion of the electroporation cuvette. The central pin of the coaxial cable is connected with one of the two parallel electrodes, while the other one to the external sock. In order to mechanically stabilize the structure and, at the same time, avoid that the central pin is not protected, a Teflon box is placed at the bottom of the structure. All the components of the set-up must be matched to a 50 Ω impedance, reducing the signals waveform distortions.

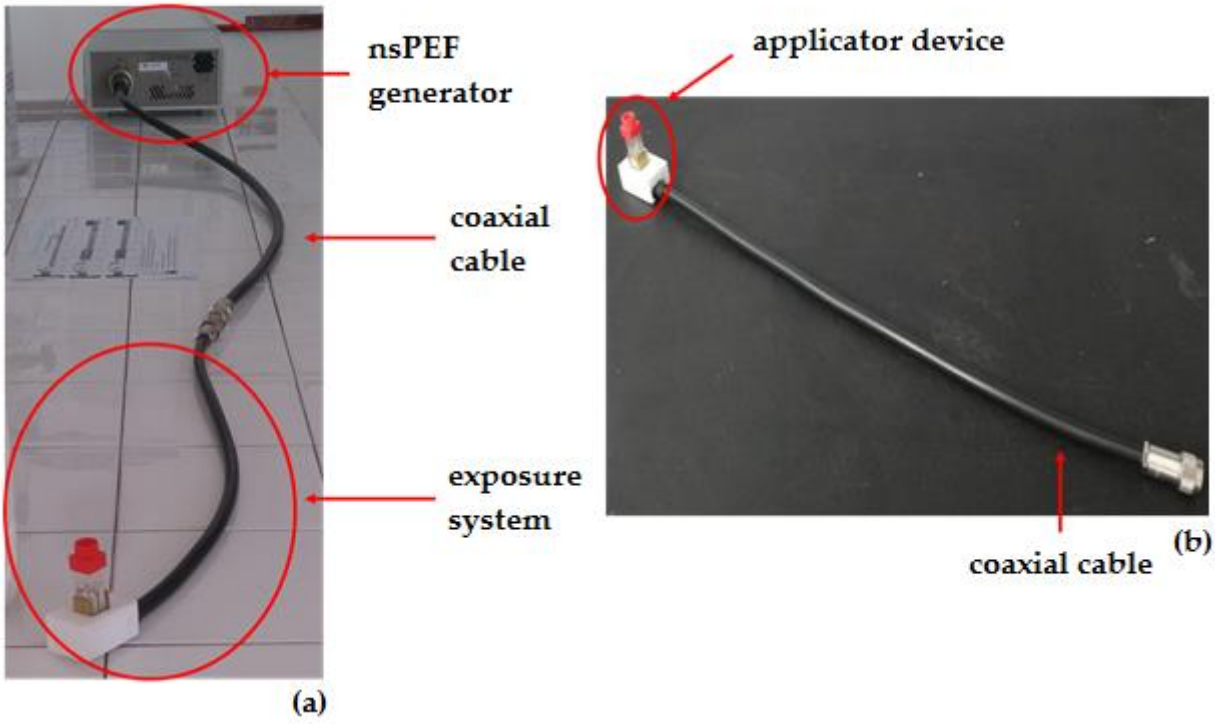


**Figure 5.1. In (a) is shown the final experimental chain composed by the nsPEF generator, the coaxial cable and the exposure system. In (b) is reported the detail of the coaxial cable connected to the applicator device.**

### 5.3.3 Characterization of the nsPEFs generator

Before arranging the experimental chain for the exposure of liposomes, it was necessary tuned a characterization set-up to measure the high voltage 50 Ω pulse generator signal waveform, using:

- an oscilloscope, able to measure nanosecond pulses coming from the generator
- a coaxial cable, that has the role to deliver the signals from the generator to the other electrical devices
- a series of four high voltage attenuators, to reduce the signal amplitude, protecting the oscilloscope.

As shown in Figure 5.2 the generator is connected by means of 4 attenuators (two-port high voltage attenuators; RFCS-30W-N-20Db, Temstron) to the input of the oscilloscope.

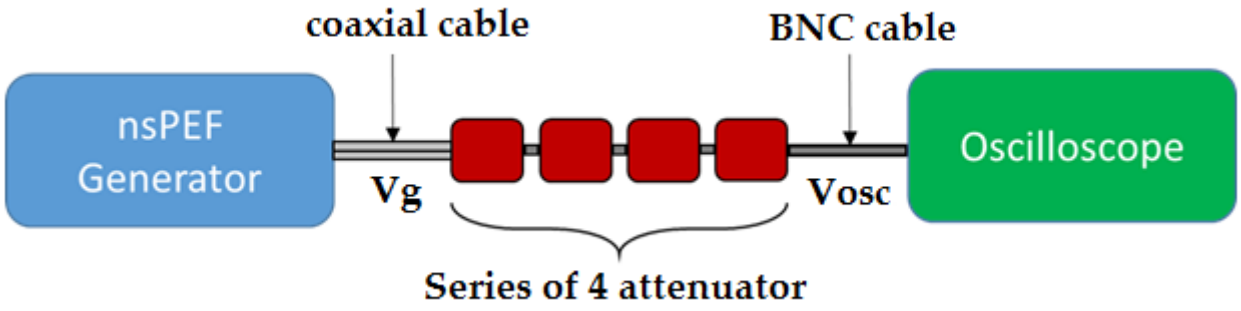


**Figure 5.2. Scheme of components used for the characterization of nsPEFs generator: the nsPEFs generator connected through the series of four attenuators to the oscilloscope.**

Data sheets referred to the attenuators as -40 dB devices, therefore, as a first step, their attenuation was measured and their behaviour characterized in the frequency domain, in the range 10-400 MHz, using the Agilent Technologies PNA Network Analyzer E8363C (10 MHz - 40 GHz) and acquiring the scattering parameters. Since the oscilloscope has to be able to measure trapezoidal/square electric pulses, with a duration of about 8 ns and rise and fall time of 1-2 ns, in this work was employed the Rohde & Schwarz RTO2044 Digital oscilloscope, characterized by 4 GHz of bandwidth and the possibility to detect a signal with a sampling rate of 20 Gsample/s. The generated pulse was analyzed in terms of shape, amplitude, width, rise and fall time, applying 7 kV between the electrods, at repetition rate of 2 Hz.

### 5.3.4 Experimental and numerical characterization of the applicator device

Always in accordance with [44], a new characterization of the exposure system has to be performed once different parameters are chosen, carrying out information about the real transmitted signal. Measurements in the frequency domain were performed with a ZVB8 Vector Network Analyzer – Rohde & Schwarz (300 kHz–8 GHz), in a range of frequency from 1.5 to 350 MHz, with the cuvette filled with solutions at different conductivity values, trying to understand the role of the medium conductivity in the efficiency of the structure. In this study, the HEPES buffer solutions (10mM, pH= 7.4), with three different conductivity

values of 0.04, 0.27 and 0.5 S/m, were investigated. The same HEPES buffer solutions were subsequently used to prepare liposomes suspensions for the electric stimulations. The conductivity values of the solutions were measured with a Precision LCR Meter E4980A from Agilent.

The numerical performance of the exposure system in frequency domain was simulated with finite element software ANSYS HFSS 2015. Starting from the project used to design the applicator device [44], the geometrical model was implemented. In fact, the coaxial cable length was increased to the value of 53 cm, with the aim of obtaining a more realistic model and applying a wave port to feed the coaxial cable.

Simulations were performed up to 1 GHz, with the three solutions at different conductivity, as reported in the Table 5.1.

**Table 5.1. Dielectric properties of the solutions. Relative permittivity values were found out in [44].**

| Solution | Conductivity (S/m) | Relative permittivity ($\varepsilon_r$) |
|---|---|---|
| a | 0.04 | 67 |
| b | 0.27 | 67 |
| c | 0.5 | 67 |

The time domain behaviour of the structure was also numerically investigated using the same project and parameter values, described for the frequency domain analysis, through the HFSS software. The coaxial cable was fed with a lumped port, using a pulse as excitation. The 10 nsPEF (1 V) was applied to the coaxial cable and the transmitted signal evaluated in the center of the cuvette gap.

### 5.3.5 Liposomes preparation

Liposomes were prepared by the thin film hydration method [50]. Egg PC was dissolved in the minimum volume of chloroform into a round bottom flask, then the organic solvent was evaporated under reduced pressure at 25 °C to form a thin film on the flask walls. Residual

traces of the solvent were further removed from the dry phospholipid film by means of an oil vacuum pump. The film was completely hydrated, at room temperature, above the main transition temperature of Egg PC (Tm in the range from -15 °C to -5 °C), with 5 ml of HEPES buffer solution (10 mM, pH= 7.4), containing 50 mM of the hydrophilic fluorescent marker 5-(6) CF. Two HEPES buffers, with different conductivity (σ) values, namely 0.04 S/m and 0.5 S/m, were used for the liposomes preparation. Specifically, 0.04 M of NaCl was added to HEPES buffer, in order to reach the higher conducitivity value. After the hydration process, the suspension of multilamellar liposomes (MLV) was submitted to five consecutive and rapid cycles of freezing and thawing, in order to improve loading efficiency of the dye. The obtained MLV were downsized by repeated extrusion (upon five times) through polycarbonate membrane filters of decreasing pore size (0.8 and 0.4 μm) to obtain a narrow size distribution of unilamellar liposomes. This step was carried out at 25 °C, using a Lipex extruder (Lipex Biomembranes, Canada). The extruded Egg PC liposomes (Egg PC-Ls) were subsequently purified by size exclusion chromatography technique (SEC), using a Sephadex G-50 column equilibrated with HEPES buffered solution (σ=0.04 S/m or σ=0.5 S/m), with the aim of removing the unencapsulated fluorescent marker. Samples with a final Egg PC concentration of 10 mM were obtained. All liposome formulations were stored at 4 °C, in the dark, and used within 1 week from their preparation.

### 5.3.6 Physicochemical characterization of liposomes

Hydrodynamic diameter, size distribution and ζ-potential of Egg PC-Ls were measured with a Zetasizer Nano ZS90 (Malvern Instruments Ltd., Malvern, UK). Hydrodynamic diameter and polydispersity index (PdI) were evaluated by dynamic light scattering (DLS) measurements, whereas the ζ-potential was determined by electrophoretic light scattering (ELS) measurements. Both the DLS and ELS techniques used a photon correlator spectrometer equipped with a 4 mW He/Ne laser source, operating at 633 nm. The particle size diameter was determined by Stokes-Einstein relationship. All experiments were

performed at a scattering angle of 90°, after opportune dilution of the samples with HEPES buffer solution (pH= 7.4, σ= 0.04 S/m or σ= 0.5 S/m) to obtain a count-rate of approximately 200 kcps, in order to avoid interference phenomena due to multiple scattering. The analysis were carried out at 25 °C and repeated in triplicate. Before samples dilution, the two different HEPES buffer solutions, were filtered through 0.2 μm polycarbonate filters to remove any interfering dust particles.

### 5.3.7 Phospholipid assay

Phospholipid concentration was determined using a phosphorus colorimetric assay [51]. Briefly, aliquots (0.4 ml) of phospholipids, in 50% v/v ethanol, were added to a mixture of 1 ml of thiocyanatoiron reagent (previously prepared by solubilizing 0.97 g of ferric nitrate and 15.2 g of ammonium thiocyanate in 100 ml of water) and 0.6 ml of 0.17 N HCl. The solution was incubated for 5 min at 37 °C and then the thiocyanatoiron–phospholipid complex formed was extracted with 3 ml of 1,2-dichloroethane, by vigorous shaking for 2 min in a vortex-type mixer. The mixture was centrifuged for 5 min, at 2000 rpm, to separate the aqueous phase from the organic one containing the complex. The absorbance of the organic phase was measured at 470 nm against a blank without the substrate, using a double beam Lambda 25 (Perkin Elmer, USA) UV–Vis spectrophotometer. The amount of lipid was obtained through an appropriate calibration curve, previously constructed. The measurements were repeated both before and after SEC purification of the extruded samples.

### 5.3.8 Loading and entrapment efficiency of 5-(6) CF

The 5-(6) CF stock solution was obtained dissolving 5-(6) CF with few drops of 1 M NaOH solution, followed by the addition of HEPES buffer solution up to obtain a 50 mM solution. The 50 mM solution of the fluorescent marker was loaded within the aqueous core of vesicles, during the thin film hydration phase. The amount of 5-(6) CF, entrapped in the inner compartment of liposomes, was determined measuring with the LS 50B Perkin Elmer

(USA) spectrofluorometer the fluorescence emitted at 512 nm, after excitation at 492 nm, by SEC-purified samples, pre-incubated at 25 °C with 30% w/v of the non-ionic surfactant TX-100, for the complete vesicles lysis. It is worth to say that the presence of TX-100 did not affect the direct dequenching of the dye signal. Captured 5-(6) CF, defined as μl of entrapped volume for mg of lipid, was established using a calibration curve of the dye (reported in S.I. of this paper). The fluorescence intensity of 5-(6) CF was found linear in the range of $10^{-7}$–$10^{-6}$ mol/l, with a correlation coefficient of 0.999. All experiments were performed in triplicate and the results reported as mean ± SD.

### 5.3.9 Determination of electropermeabilization after nsPEF application

Changes in the permeability of liposomes membrane, due to the effect of the nsPEF application, was evaluated measuring the diffusion of the 5-(6) CF through the bilayer and towards the external bulk. *In vitro* release of 5-(6) CF from Egg PC-Ls was determined by recording marker fluorescence de-quenching, as reported in section 5.3.8. Specifically, after the nsPEF application, the release profile of 5-(6) CF was monitored for 3 h, at the constant temperature of 25 °C. At the end of each series of measurements, all the liposomal vesicles were destroyed with the addition of 30% w/v of TX-100, in order to evaluate the residual amount of 5-(6) CF still contained in the samples. The percentage of 5-(6) CF released was calculated using the following Equation 5.1:

$$5-(6)\ CF\ released\ (\%) = \frac{(I_t - I_0)}{(I_{max} - I_0)} \cdot 100 \qquad (5.1)$$

where: $I_0$ is the initial fluorescence intensity of 5-(6) CF loaded into the liposomal core; $I_t$ is the fluorescence intensity measured at each sampling time; $I_{max}$ is the fluorescence intensity after the complete lysis of the liposomal vesicles with TX-100.

The effect of the electrical stimulation was compared with the results obtained testing appropriate controls, as reported in section 5.3.10.

## 5.3.10 Experimental protocol for the stimulation with nsPEF

In this paragraph is reported the experimental protocol used for the stimulation of liposomes with nsPEFs.

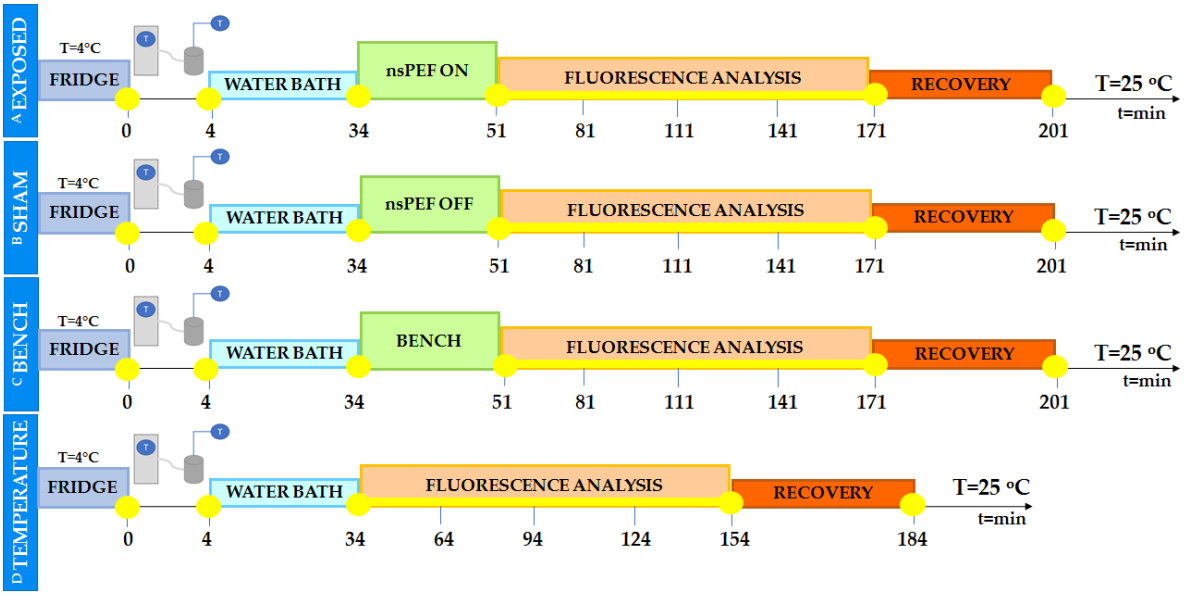


**Figure 5.3. Time line protocol tuned to the experimental phase. In the same experimental experience the [A]exposure, [B]sham, [C]bench and [D]temperature procedure was performed.**

As shown in Figure 5.3, Egg PC-Ls were first thermostated at 25 °C, then they were stimulated with 2000 electric pulses (f=2 Hz), each lasting 10 ns, applying 7 kV voltage between the brass electrodes (nsPEFs generator in ON modality). At the end of the exposure step, the fluorescence of the sample was continuosly monitored for 3 h, as reported in section 5.3.9. Finally, the probe recovery study was performed, adding 30% w/v of TX-100 to allow the vesicles lysis.

The same procedure was applied to the "sham" control. In this case, Egg PC-Ls were introduced in the cuvette with the generator in OFF modality (in absence of the electric field). Another sample of Egg PC-Ls (bench sample) was stored in the dark over the bench for 17 min (that is the time required for the electric stimulation). The last control was used to evaluate the spontaneous leakage of 5-(6) CF from the vesicles. For the exposure

experiments, three different liposomes formulations were prepared and each of them was tested twice. The results are reported as mean ± SD.

### 5.3.11 Microdosimetric modelling of the nsPEF application on liposomes

To support the experimental data regarding the electropermeabilization of liposomes membrane, a numerical study, modelling the effect of an electric stimulation, was elaborated. Specifically, a microdosimetric study of the 10 nsPEF signal, on a group of liposomes, was provided through the analysis of the evolution in time of two observables: the trasmembrane potential (*TMP*) and the consequent density of the pores across the membrane. The numerical simulations were conducted using the finite element method (FEM) software platform COMSOL Multiphysics v 5.3.

### 5.3.12 Construction of the model

In this regard, a geometrical and dielectric model, which was representative of the experimental conditions, was developed.

The 2D model consisted of a rectangular box with dimensions of 70 × 100 μm, representing the extracellular medium in the cuvette, where a random distribution of 144 liposomes was placed in a range position from -5.1 to 5.1 μm (Figure 5.4, b).

In this way, the electric field applied on the set of liposomes was uniform. The liposomes presented a diameter of 200 nm and a bilayer with a thickness of 5 nm.

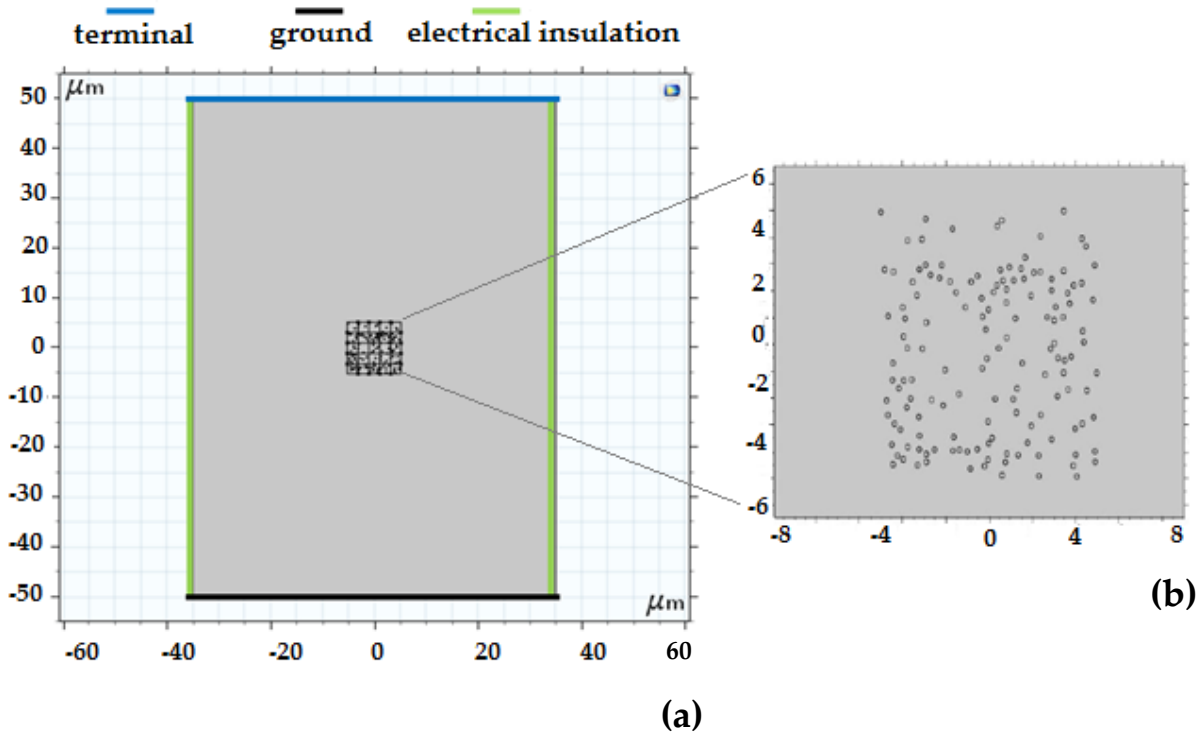


**Figure 5.4. The D (a) and 2D (b) model consisted of a rectangular box containing a non-uniformly distributed liposome population. The electric stimulus was applied to the upper electrode and the ground to the lower electrode. Both sides are electrically insulated.**

A non-uniform distribution of liposomes was obtained through a random position algorithm, implented in Matlab v. R2016b. All around the liposomes distribution it was placed a square box of 10.4 × 10.4 μm, divided in 25 smaller boxes to facilitate the computation on the entire set of 144 liposomes. The left and right sides of the rectangular box were modelled as electrically insulated, whereas the upper and the lower sides as electrodes. The lower electrode was set to the ground and the other was excited by a single 10 nsPEF (Figure 5.4, a), obtained by the function rect in COMSOL. The pulse parameters of the rect function were the same of the pulse used in the experimental part of this work: 2 ns rise and fall times, 10 ns pulse width at the half maximum amplitude. The pulse amplitude was set to value resulting in a desired electric field between the electrodes, calculated as the potential difference between the electrodes, divided by the electrode distance. The steady-state problem for the described geometry was solved in the Electric currents mode of the AC/DC module of COMSOL (Time Dependent Study), considering:

- the Electric Currents application mode of the AC/DC module (Time Dependent Study)
- the Boundary ODEs and DAEs application of the Mathematics module (Time Dependent Study).

The boundary conditions, imposed to the liposomes membrane, were set as Contact Impedance, in order to take into account the membrane conduction and displacement currents. In this way, the Equation 5.2 of the normal current, that flows across the bilayer, is reported below:

$$n \cdot J_{in} = h\left(\sigma_m + \varepsilon_m \frac{\partial}{\partial t}\right)(V_{in} - V_{ext}) \tag{5.2}$$

Here, $n$ is the unit vector normal to the surface, $V_{in}$ is the electric potential on the interior side of the boundary, $V_{ext}$ is the electric potential on the exterior side of the boundary, $h$ is the thickness of the membrane, $\sigma_m$ is the conductivity of the boundary (liposome membrane) and $\varepsilon_m$ the medium permittivity (liposome membrane).

The investigation of the pore formation dynamics was carried out including the asymptotic model proposed previously in [52]. In this model the pore formation in time is governed by the differential Equation 5.3:

$$\frac{dN}{dt} = \alpha e^{\left(\frac{TMP}{V_{ep}}\right)^2}\left(1 - \frac{N}{N_0} e^{-q\left(\frac{TMP}{V_{ep}}\right)^2}\right) \tag{5.3}$$

where $N$ is the pore density in the membrane, $N_0$ the equilibrium pore density in the membrane, when $TMP$= 0, and the parameters $\alpha$, $q$ and $V_{ep}$ are constants of the model.

The pore creation in the membrane due to electroporation phenomena, determines an increase in the membrane conductivity ($\sigma_{ep}$), that was calculated as in [53, 54], using the following Equation 5.4:

$$\sigma_{ep} = N \frac{2\pi {r_p}^2 \sigma_p h}{\pi r_p + 2h} \tag{5.4}$$

where $r_p$ and $h$ are the radius of the pores and the membrane thickness, respectively, and $\sigma_p$ is the effective conductivity of the solution inside the pores, which was approximated as in [53], using the Equation 5.5:

$$\sigma_p = \frac{\sigma_e - \sigma_i}{\ln(\frac{\sigma_e}{\sigma_i})} \tag{5.5}$$

Here $\sigma_e$ and $\sigma_i$ are the conductivity values of the extracellular and intracellular medium. The resulting membrane conductivity was represented by the following Equation 5.6, as in [55, 56]:

$$\sigma_m = \sigma_{m0} + \sigma_{ep} \tag{5.6}$$

with $\sigma_{m0}$ that is the membrane conductivity, when $TMP$= 0, and $\sigma_{ep}$ that is the conductivity increase, due to the poration phenomenon.

### 5.3.13 Parameters of the model

The simulation parameters chosen were those of the experimental conditions, such as $\sigma$=0.04 S/m of the medium, and the nsPEF amplitude calculated considering the efficiency in transmission of the structure. In addition, to avoid the computational stop, due to the natural logarithm in the equation for the $\sigma_p$ (5.4), the conductivity of the extracellular medium was chosen at $\sigma_e$=0.039 $S/m$, while the internal conductivity medium was set at $\sigma_i$=0.04 $S/m$. The parameters used in this microdosimetric study are reported in Table 5.2.

**Table 5.2. Model parameters used in the FEM simulations with the electroporation model reported in [52] to calculate the *TMP* and pore density during an electroporation pulse applied on randomly distributed liposomes.**

| Symbol | Value | Definition, justification or source |
|---|---|---|
| $\sigma m0$ | $1.1 \times 10^{-7}$ S/m | Membrane conductivity when TMP=0 if membrane thickness is 5 nm [44] |
| $\sigma_e$ | 0.039 S/m | Extracellular conductivity |
| $\sigma_i$ | 0.04 S/m | Intracellular conductivity |
| $h$ | 5 nm | Membrane thickness [57] |
| $\varepsilon e$ | 67 | Relative permittivity of the extracellular medium [44,58] |
| $\varepsilon i$ | 67 | Relative permittivity of the intracellular medium [44,58] |
| $\varepsilon_r m$ | 11.7 | Relative permittivity of the membrane [44,58] |
| $rp$ | 0.76 nm | Pore radius [52] |
| $q$ | 2.46 | Electroporation constant [52] |
| $\alpha$ | $10^9$ | Electroporation parameter [52] |
| $Vep$ | 0.258 V | Characteristic voltage of electroporation [52] |
| $N_0$ | $1.5 \times 10^9$ m$^{-2}$ | Equilibrium pore density when TMP=0 [52] |

The simulations were performed studying three more representative positions of liposomes in the suspension, in order to highlight possible differences in the electric field propagation. The positions investigated are the "isolated", the "central" (between two liposomes) and the "close" one (near to other liposomes). The *TMP* and the pore density were evaluated in that points of the liposome membrane where these observables show their maximum values. In each point the normal to the membrane surface is parallel to the direction of the electric field [45].

### 5.3.14 Parametric study of the $Vep$

The model proposed here, first introduced by DeBruin and Krassowska [52], was validated to study the nsPEF-induced electroporation on the membrane of cells with diameter in the order of micrometer. In this model an important parameter is the $Vep$, which corresponds to the threshold voltage for the electroporation onset, depending on the type of membrane and that is empirically set at 0.258 V on cells membrane [52]. Since in this work were used vesicles with a diameter in the order of 200 nanometer and considering that $Vep$ can differ

from the cellular, due to a variety in the liposomes bilayer components [44], a set of $Vep$ values (0.258 - 0.150 – 0.130 – 0.120 -0.100 V) were investigated for the liposomes membrane electroporation.

## 5.4 Results and Discussion

### 5.4.1 Experimental characterization of the nsPEFs generator

The generator was characterized at 7 kV (f=2Hz), according to the exposure conditions. The result of the generator characterization phase is shown in the Figure 5.5.

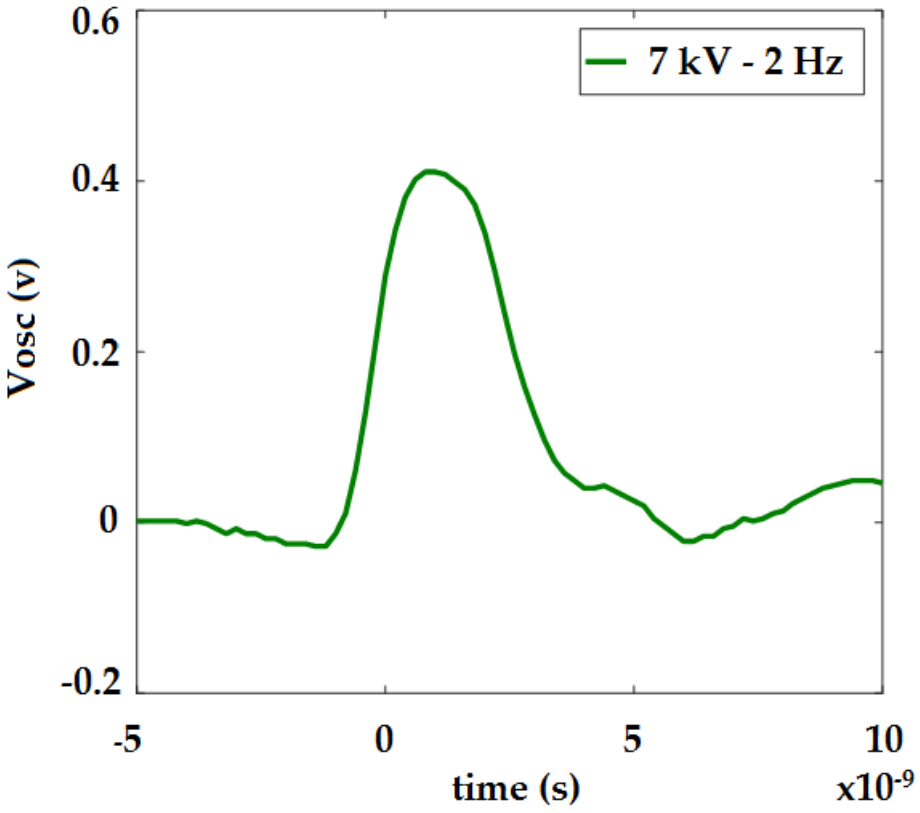


**Figure 5.5. Measured signal generated, applying 7 kV between the electrodes with a repetition rate of 2 Hz.**

From this result, it is possible to notice that measured signal generated presents: a rise time of 1.013 ± 0.056 ns; a fall time of 1.855 ± 1.032 ns; positive pulse duration at 50% of amplitude of 2.653 ± 0.292 ns; positive pulse duration at 90% of amplitude at 1.328 ± 0.551 ns. This

signal employment could be justified with its total nanosecond duration in the order of 10 ns and its rise and fall time in the order of 1-2 ns.

### 5.4.2 Experimental and numerical characterization of the applicator device

In order to characterize the structure and to explore the influence of the external medium conductivity in the membrane electropermeabilization [43, 49], measurements in the frequency domain were carried out, with the cuvette filled with solutions at different conductivity values (respectively of 0.04, 0.27 and 0.5 S/m), in the range of frequency from 1.5 to 350 MHz. In the same conditions, the performance in frequency domain was simulated. The numerical results were compared to the measurements, both performed changing the solution conductivity. In particular, the frequency domain behaviour of the reflection parameter S11 is reported in Figure 5.6. As evident from the S11 curves, the exposure system performance confirms the numerical data.

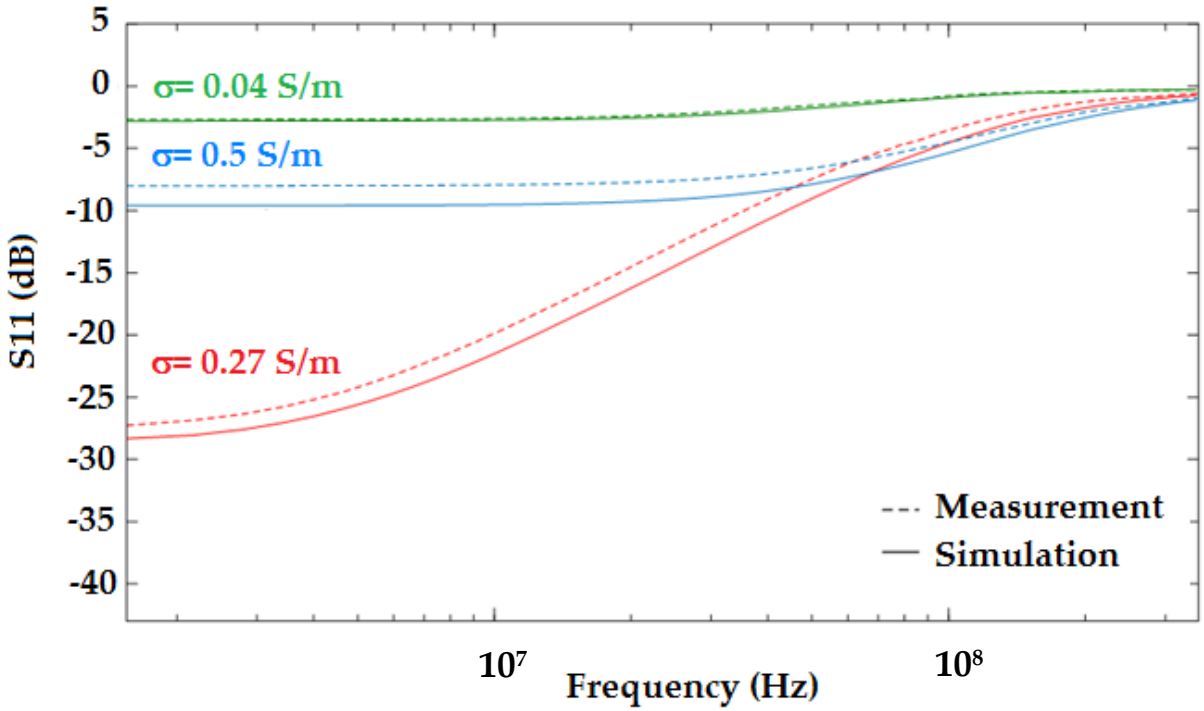


**Figure 5.6. S11 parameter comparison between measurements (dashed line) and simulation results (solid line), for the different conductivity solution: 0.04 - 0.27 - 0.5 S/m.**

In the range of conductivity from 0.04 to 0.5 S/m, as observed from the graph, the exposure system presents an acceptable frequency behaviour up to 100 MHz, corresponding to the frequency content of the 10 nsPEF.

Moreover, for the 0.27 S/m solution the S11 parameter values are lower than -10 dB up to 100 MHz, while with a conductivity of 0.5 S/m S11 is about -8 dB and -3 dB for 0.04 S/m condition. These evidences agree with the paper previously mentioned [44]. According to the S11 parameter results, the impedance performance, real and imaginary part, of the exposure system, was evaluated through numerical simulations. The results are reported in Figure 5.7 (a-c), in comparison with the measurements for each conductivity values, respectively for 0.04, 0.27 and 0.5 S/m conductivity of the medium.

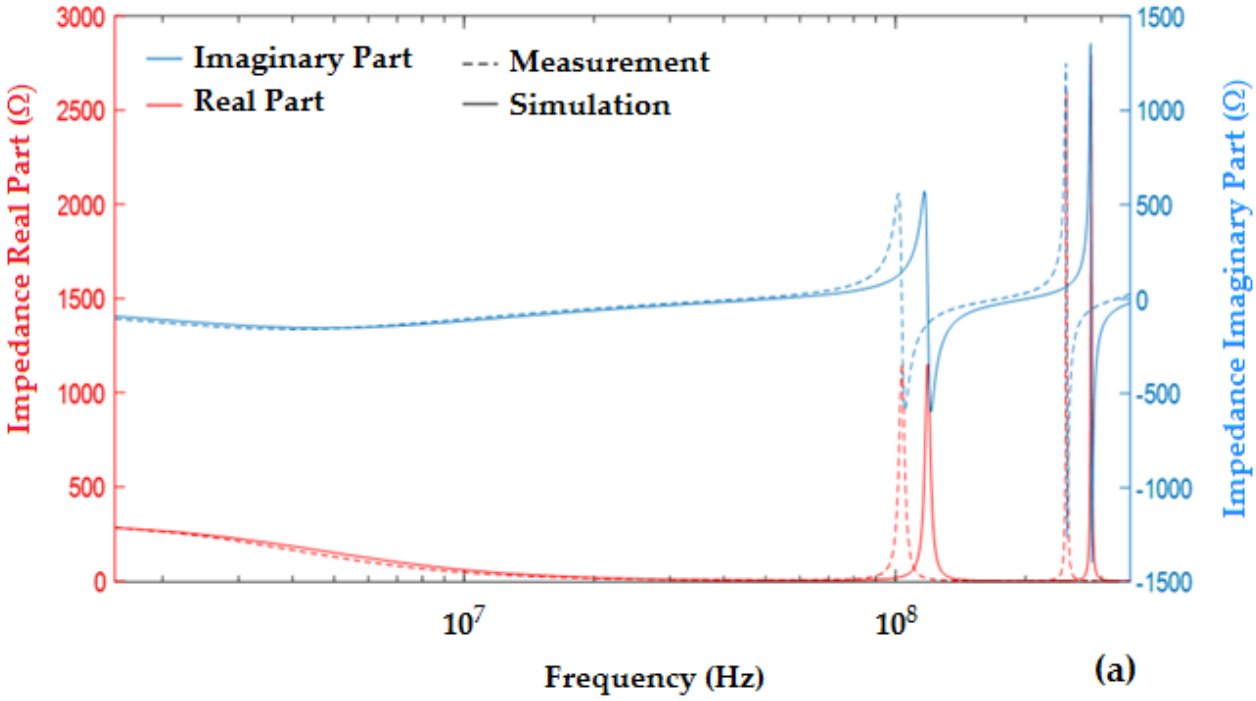

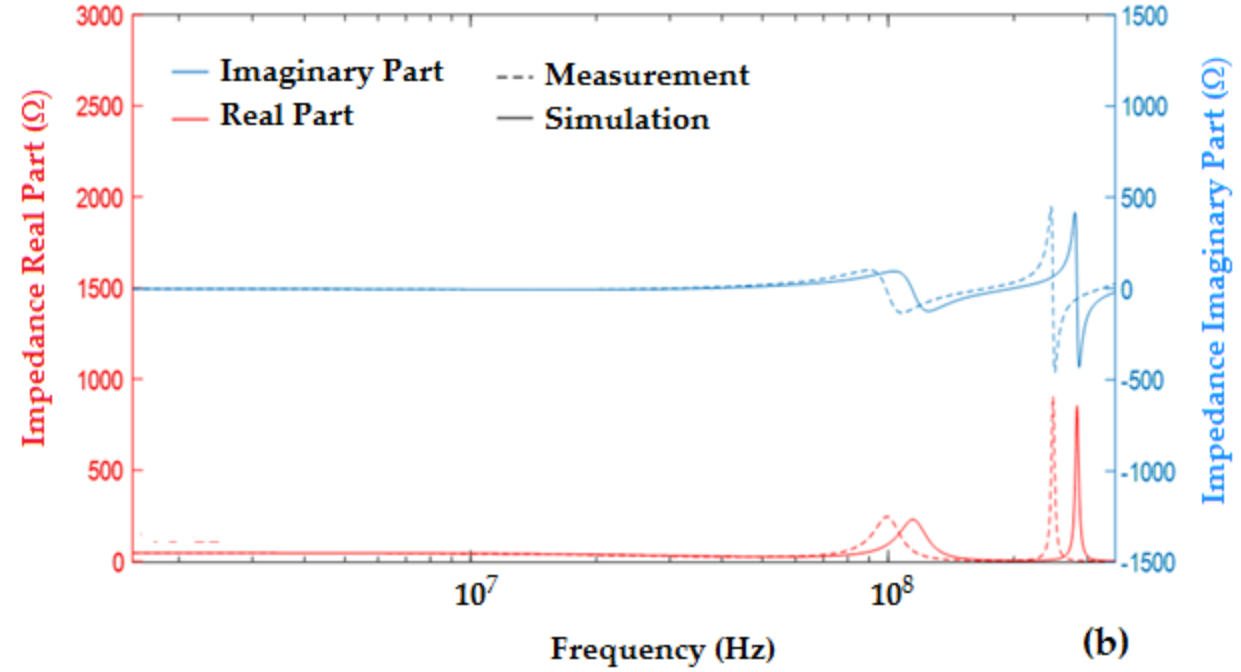


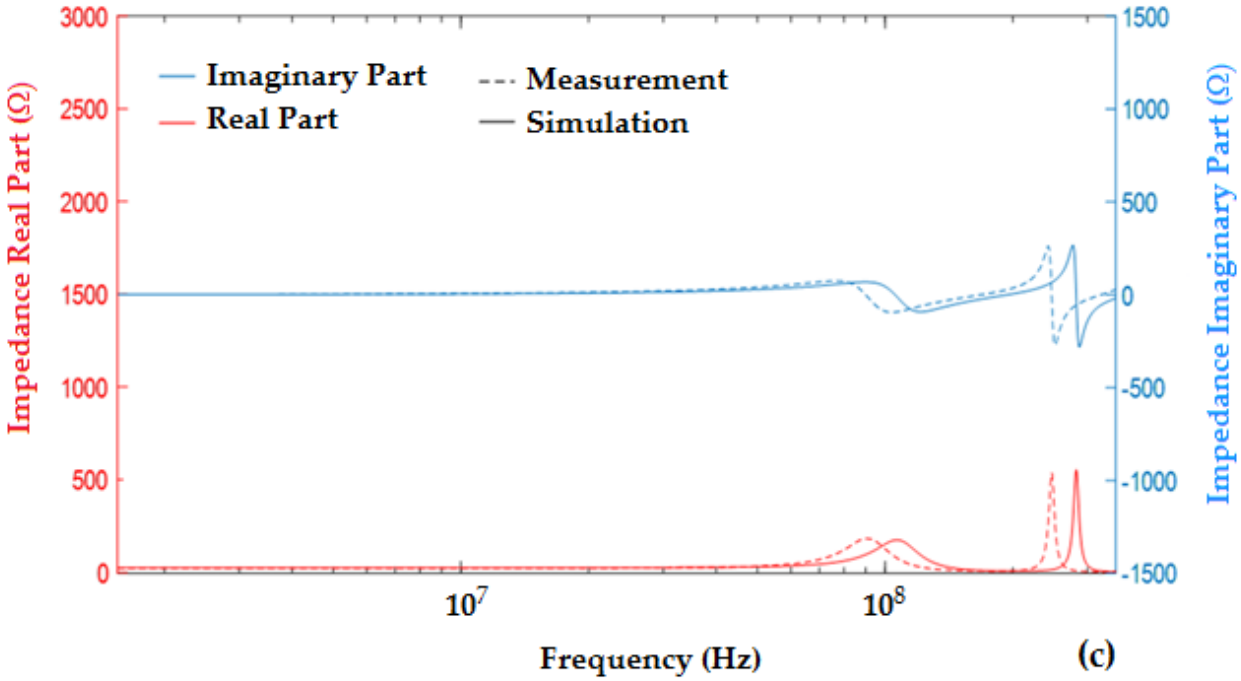


**Figure 5.7. Comparison between impedance, real and imaginary part, simulation and measurements results. For the solution conductivity σ=0.04 S/m (a), at low frequency the values of the impedance real part are about 300 Ω, as predicted with equation (5.2); for high frequency (from 10 MHz) the system presents impedance values real part about 50 Ω and low values of the imaginary part for this medium conductivity. For solution conductivity σ=0.27 S/m (b), from low**

**frequency up to 100 MHz the system presents impedance values real part about 50 Ω and low values of the imaginary part for this medium conductivity. For the solution conductivity σ=0.5 S/m (c), at low frequency the values of the impedance real part are about 21 Ω, as predicted with equation (5.2); the system presents impedance acceptable to work in a 50 Ω-impedance line in terms of real and imaginary part values, up to 100 MHz.**

From these results, it is possible to notice that measured and simulated results are comparable for all the analysed conductivities. Indeed, using a geometrical model with a coaxial cable of real length, the appearance of resonance effects occurs for frequency higher or equal to 100 MHz. This is in agreement with [44, 59], that reported a resonant behaviour for frequency of about 350 MHz, using a coaxial cable length lower than the experimental one used in this work.

Therefore, the behaviour of the exposure system in time domain was numerically characterized. The 10 ns pulse (1 V of amplitude) was applied to the extended coaxial cable and the simulated transmitted signals, in the center of the cuvette gap, for the three conductivity values, agree with data reported in the work of Denzi et al. [44], for the experiments carried out in 0.27 S/m and 0.5 S/m solution.

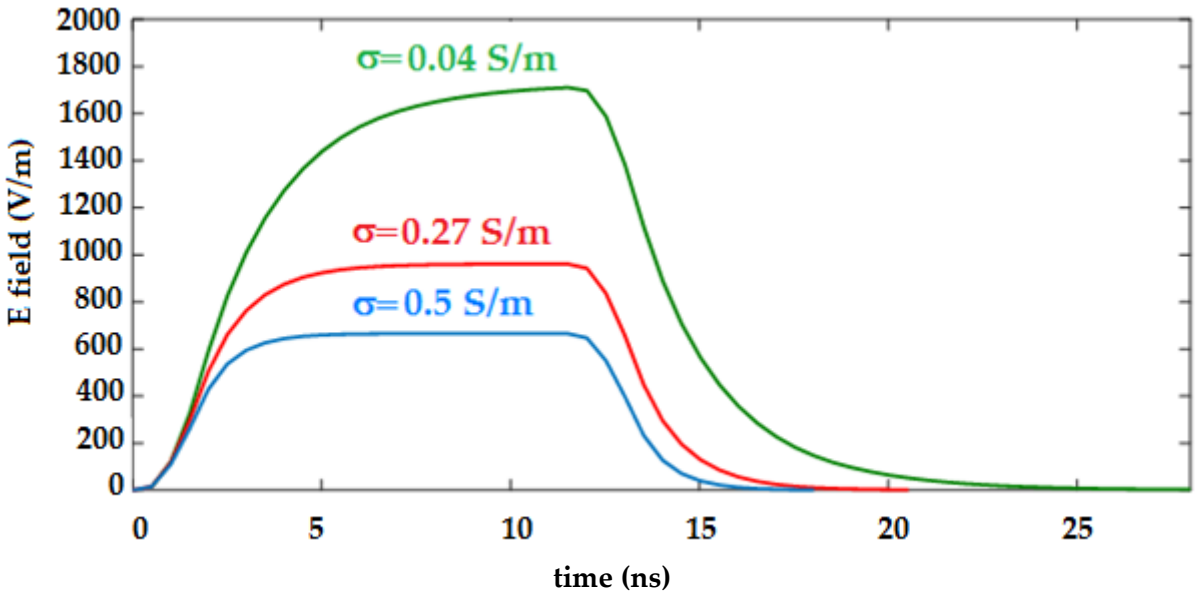


**Figure 5.8. Electric field (E) amplitude (V/m) recorded in the center of the cuvette (1 mm gap) for different conductivity values, applying 1 V.**

Since the maximum achievable value of the electric field (E), 1800 V/m (applying 1 V to the 1 mm gap), was observed with the conductivity of 0.04 S/m (Figure 5.8), it is clear that can be obtained a greater efficiency in transmission (η) decreasing the conductivity of the medium. To demonstrate this evidence, in the Table 5.3 are reported the efficiency in transmission values for each solution analyzed.

**Table 5.3. Efficiency in transmission (defined as the ratio between the electric field obtained in the gap, in kV/m, and the applied voltage at the generator, in V) obtained for the three conductivity values.**

| Conductivity solution value (S/m) | Efficiency in transmission (η) |
|---|---|
| 0.04 | 1.8 |
| 0.27 | 1 |
| 0.5 | 0.6 |

From this complete characterization, we can deduce that the use of the applicator, in the range of conductivity from 0.04 to 0.5 S/m, is permitted, despite the differences in the transmission efficiency of the system, when the conductivity changes. In this project, in particular, the possibility of electropermeabilizing the liposomal systems was evaluated setting the experimental conditions at the two extremities of this range, thus investigating the influence of conductivity parameter both at high and low values.

### 5.4.3 Preparation and characterization of Egg PC-Ls

Egg PC-Ls were prepared following a three-step procedure: 1) thin lipid film hydration; 2) extrusion; 3) SEC-purification to remove the not entrapped marker. Each step was optimized in order to achieve vesicles formation, homogeneous size distribution, regular shape and good stability over time. Since in literature the influence of the conductivity of the external medium, on the electroporation efficiency, represents a controversial issue [43, 45, 49], the vesicles were assembled in two buffer solutions at different conductivity. In particular, the hydration step was performed with HEPES buffer solutions at 0.04 S/m or 0.5 S/m. Moreover, to preserve their stability, liposomes were produced, in both cases,

mantaining the same conductivity selected in the internal and external compartment. Results, reported in Table 5.4, show that the operating conditions allow lipids to arrange in homogeneous nanometer-sized unilamellar vesicles. No differences are indeed observed in vesicles size between the two formulations, which are both characterized by a hydrodynamic diameter <300 nm and a monomodal distribution, with PdI values <0.200. The average size, size distribution and ζ–potential of the structures remained unaltered for at least 7 days, when stored at 4 °C, as evaluated by DLS measurements (data not shown).

**Table 5.4. Physical characterization of liposomes: the hydrodynamic diameter (Z-average), PdI values and ζ-potential values were determined immediately after SEC purification. Loading efficiency of 5-(6) CF is also reported.**

| Sample | Egg PC-Ls ($\sigma$=0.04S/m) | Egg PC-Ls ($\sigma$=0.5S/m) |
|---|---|---|
| **Hydrodynamic diameter (nm)** | 264.5±2.1 | 265.9±12.1 |
| **PdI** | 0.137±0.036 | 0.158±0.031 |
| **ζ-potential (mV)** | -7.2±0.5 | -6.2±0.1 |
| **5-(6) CF loading efficiency (µl/mg Egg PC)** | 1.02±0.08 | 1.07±0.11 |

Further proof of the successful liposomes formation, is the percentage of lipid molecules found in the self-closing bilayer of Egg PC-Ls, which never turned out lower than 75%, respect to the initial amount of lipid.

During the hydration phase, the fluorescent dye 5-(6) CF was loaded within the aqueous core of liposomes and used to evaluate the permeabilizing effect of the application of the nsPEF on nanometer-sized unilamellar vesicles. In both formulations a similar amount of the marker was captured into the vesicles core, as expressed by the value of entrapped volume to lipid ratio (µl/mg structured Egg PC) reported in Table 5.4.

### 5.4.4 Experimental results after the application of nsPEF

The electric stimulation was performed according to the protocol described in the section 5.3.10. The release profile of 5-(6) CF from Egg PC-Ls was studied under the effect of the electric field and the results were compared with appropriate controls, obtained in the

absence of the electric signal, in order to confirm the ability of nsPEF of changing membrane permeability of liposomes. Despite the different measured transmission efficiency of the exposure system, at the two different conductivity values, the experiments were designed to get an in-depth understanding of the impact of the external conductivity on the electropermeabilization efficacy. Therefore, the experimental demonstration of the nsPEF application on nanometer scale liposome was achieved both with Egg PC-Ls in 0.04 S/m and in 0.5 S/m medium.

The first formulation tested was Egg PC-Ls in the 0.04 S/m medium. Figure 5.9 displays the diffusion of the probe through the electrostimulated membrane, immediately after the exposure to 2000 nsPEF (with 7 kV between the brass electrodes and a repetition rate of 2Hz) and then at 0.5, 1, 2, 3 h from the electric stimulation.

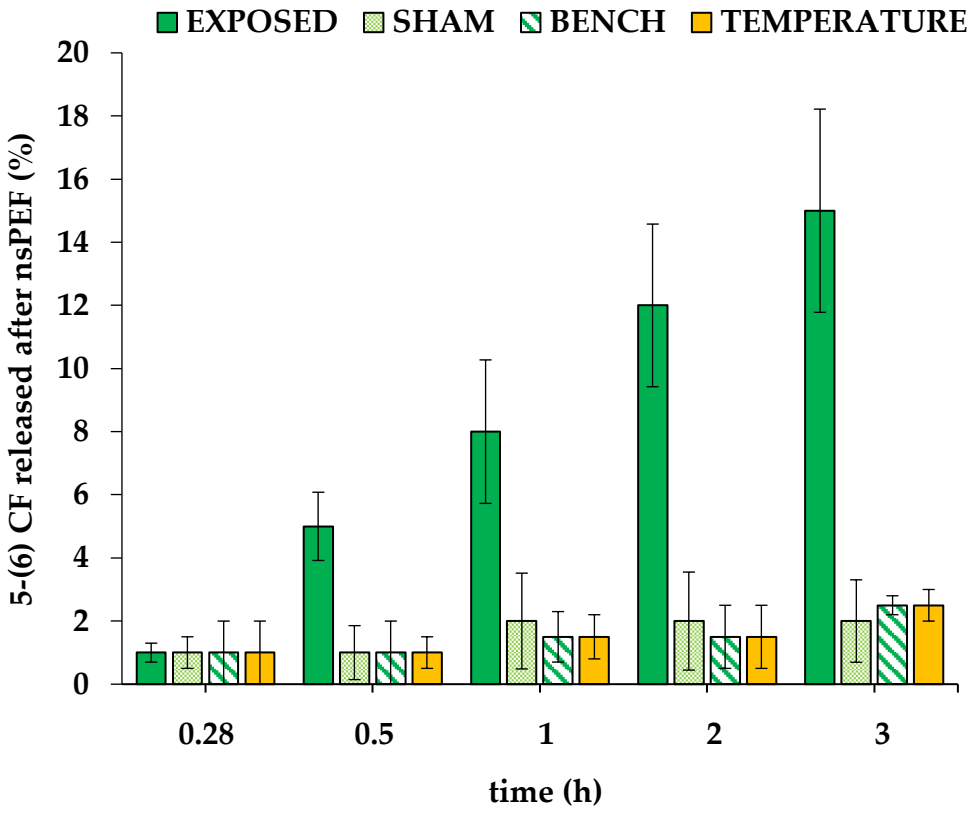


**Figure 5.9. Percentage of the 5-(6) CF released from Egg PC-Ls, after the application of nsPEF, in the 0.04 S/m medium.**

According to the results, the pulses train modify the membrane permeability, as indicated by the percentage of 5-(6) CF leakage, which increases in time up to 15%, respect to the amount of probe released from the "sham, bench and temperature" controls (<5%). Nevertheless, it is important to say that the application of nsPEF did not lead to the liposomes rupture as demonstrated by DLS carried out before and after stimulation (data not shown).

Differently, when the external medium of liposomes suspension was characterized by a conductivity of 0.5 S/m, the efficiency of permeabilization decreased, thus the liposomes bilayer behaviour reflected that of a non-electrostimulated membrane. From the release values, reported in the Figure 5.10, it is possible to deduce that the interaction of the nsPEF with the exposed sample is not efficient in this condition.

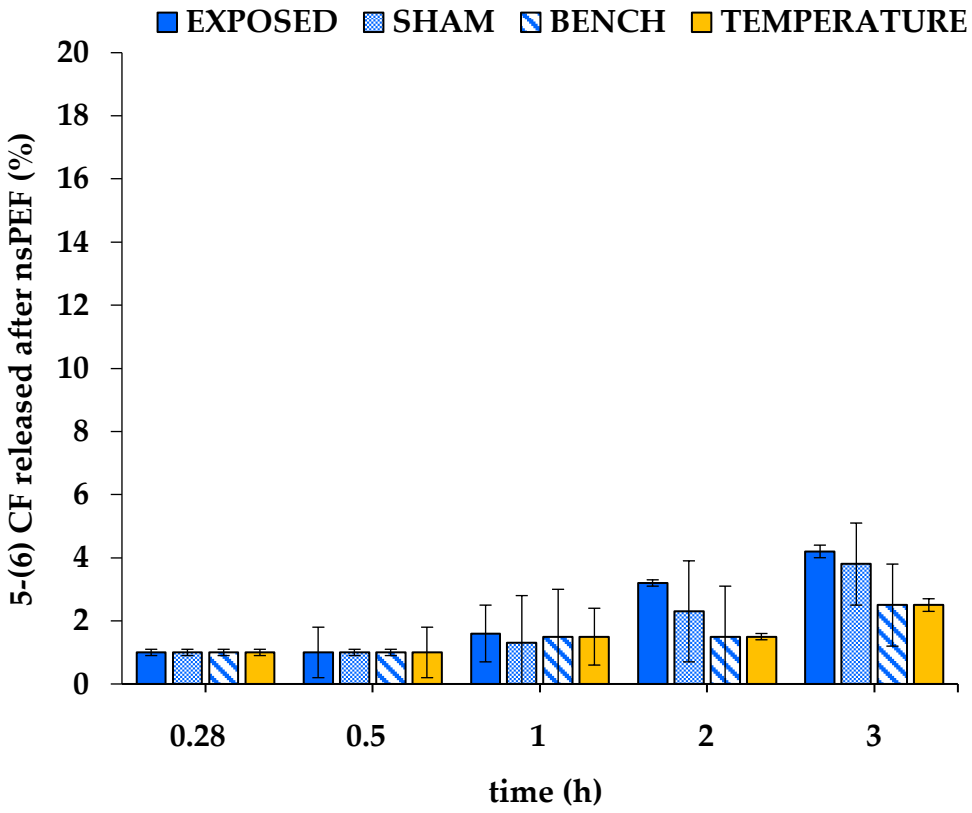


**Figure 5.10. Percentage of the 5-(6) CF released from Egg PC-Ls, after the application of nsPEF, in the 0.5 S/m medium.**

Probably the higher charge density on the external surface of the bilayer, could shield the liposomal system from the electrical signal transmitted through the external medium.

### 5.4.5 Microdosimetric modelling of the nsPEF application

The experimental data, obtained with Egg PC-Ls formulation in HEPES buffered solution of 0.04 S/m, were numerically supported by means a geometrical and dielectric model, which is representative of the operating conditions. As it is possible to notice, applying a nsPEF with an amplitude of 14 MV/m (corresponding to the electric amplitude value in the exposure cuvette, directly applied to the liposome solution) and a duration of 10 ns, the *TMP* trend (Figure 5.11) is similar for all the studied points and there is no evidence for the electropermeabilization of the liposome membrane. Indeed, the *TMP* increases during the application of the nsPEF. An efficient treatment with nsPEFs, whereas, should determines an initial growth of the *TMP* up to the critical value, followed by a reduction due to the formation of pores and the consequent increase of the membrane conductivity [56].

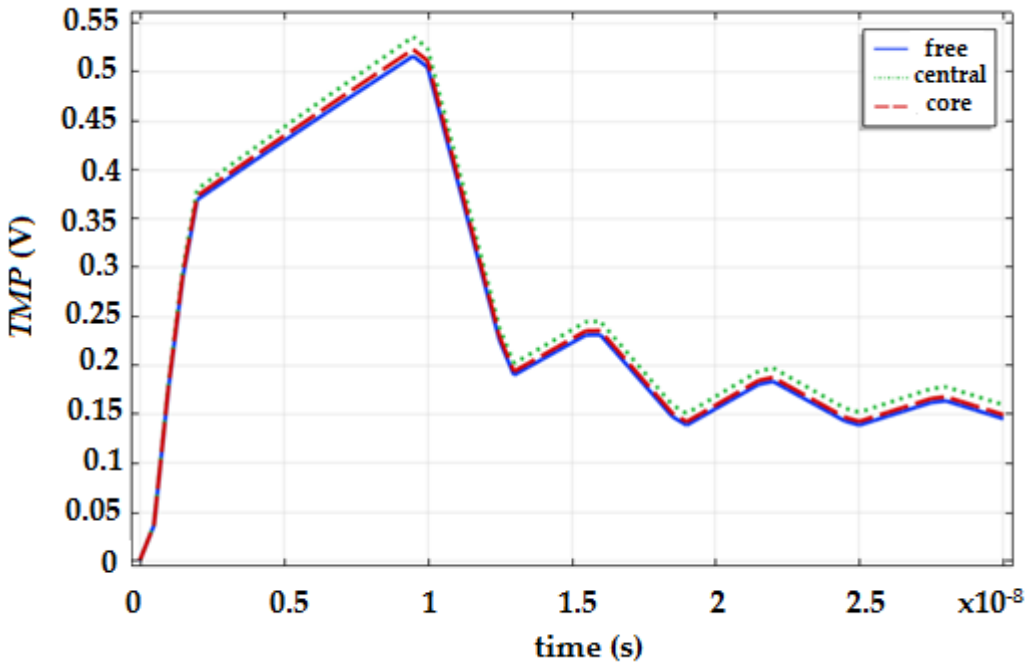


**Figure 5.11. *TMP* behaviour in time on the selected points (free-central-core), applying a nsPEF of 14 MV/m and 10 ns of duration.**

As the performed studies allowed us to appreciate the same result for all the tested positions of liposomes, here, for different values of the parameter $Vep$, only the variation in the *TMP* curve of the central point is reported (Figure 5.12).

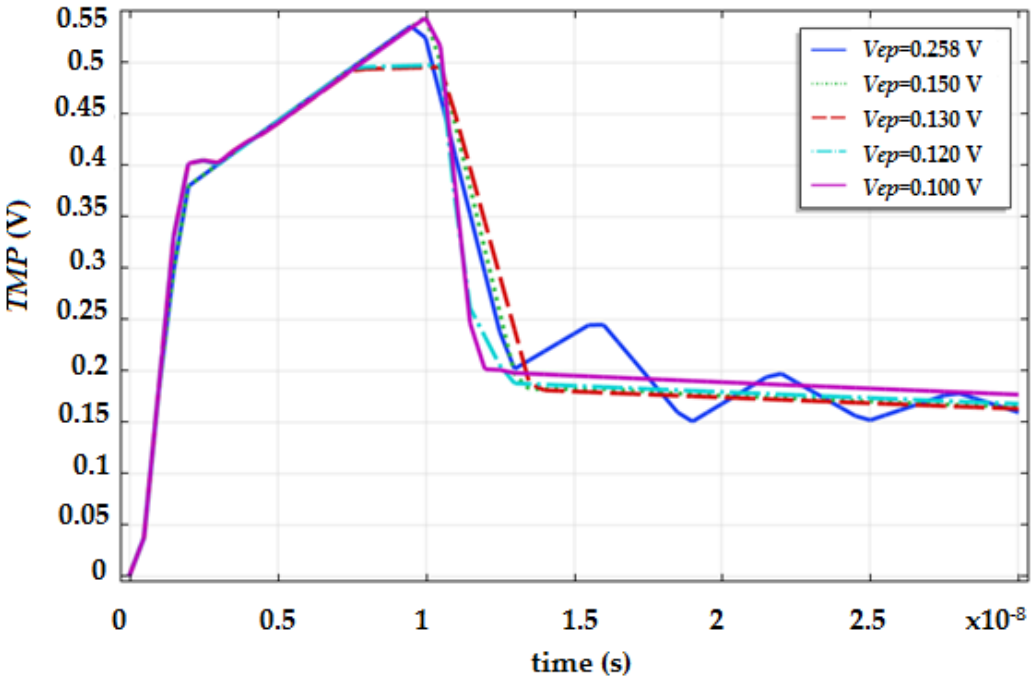


**Figure 5.12. *TMP* behaviour for different *Vep* parameter values.**

A significant information is obtained for a $Vep$= 0.100 $V$. Indeed, it is possible to notice that during the pulse period, *TMP* first increases, then slightly decreases after a few nanoseconds from the pulse onset and finally raises again until the pulse is at its maximum amplitude (Figure 5.13).

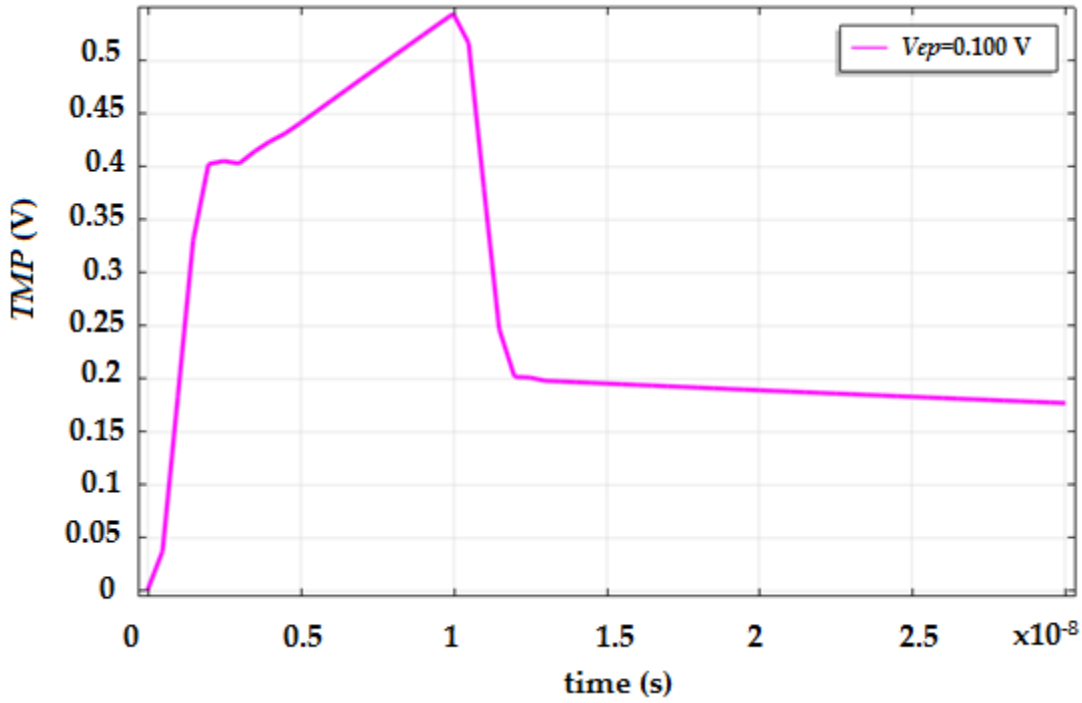


**Figure 5.13.** ***TMP*** **behaviour for the** ***Vep*****= 0.100 V. The decreasing of the slope curve stars from 1 ns, corresponding to a half amplitude of nsPEF applied respect to the 14 MV/m.**

Finally, the pore density, that can be considered a significant observable to compare the simulated and experimental results, because of its relationship with the release of a compound from the liposomal core, was estimated. As observed in Figure 5.14, the pore density increases, reaching a constant value of about $8 \times 10^{12}(\frac{1}{sm^2})$ at the end of the pulse duration (11 ns).

According to [45], this N(t) value can be considered representative of the electropermeabilization phenomenon, thus it is possible to assert that, setting a Vep= 0.100 V in the model, the changes in liposomes membrane occurs.

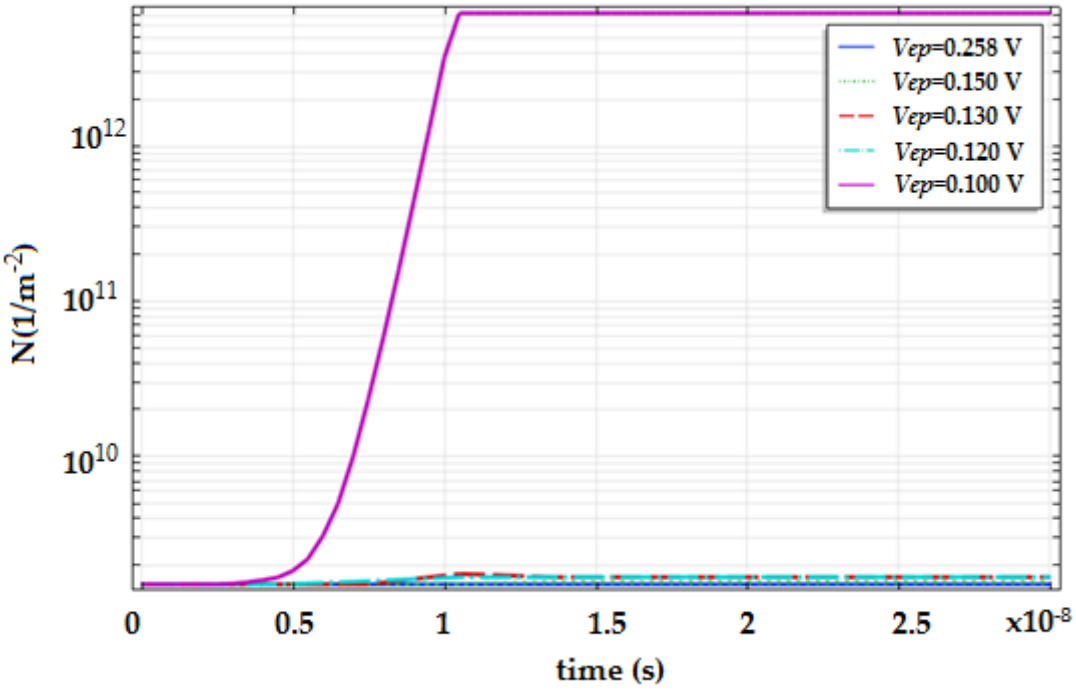


**Figure 5.14. Variation in time of N(t) using five values of *Vep* parameter. For *Vep*= 0.100 V it is possibile to obtain a value about $8 \times 10^{12}$ ($\frac{1}{sm^2}$) at time= 11 ns, corresponding to the half amplitude of the nsPEF applied respect to 14 MV/m.**

## 5.5 Conclusions

In this work was experimentally demonstrated the possibility of electropermeabilizing the membrane of nanometer-sized unilamellar liposomes with the application of high intensity nsPEF, with pulse duration of 10 ns. In particular, it was possible to modify the membrane permeability when the conductivity of the medium used to disperse the vesicles was of 0.04 S/m. In fact, under these conditions, liposomes were able to respond to the electric treatment, releasing a significative amount of a fluorescent dye, previously trapped in their core. On the contrary, no changes in membrane permability were observed when the conductivity value of the medium was increased up to 0.5 S/m. These experimental data were supported and confirmed by a numerical model which provided for a density of pore above the threshold of membrane poration for the 10 nsPEF exposure, when the conductivity of the suspension was at the lower limit of the tested range. These results, obtained in the different experiences, moreover suggest that the experimental protocol,

developed for this electrical stimulation, could be a promising tool for other future electropermeabilization studies. Overall, these preliminary investigations, conducted numerically and experimentally, demonstrate that nsPEFs can remotely trigger the permeation of nanometric lipid-based carriers as liposomes. Furthermore, since nsPEFs proved already to be able of enhancing the membrane permeability of cells, these external stimuli could represent a promising way to promote the transient simultaneous electropermeabilization of cellular and liposomal membrane, thus promoting the direct passage of drugs from the carrier to the target.

## 5.6 Supplementary Informations (S.I.)

In Figure 5.1 S.I. is reported the calibration curve used to establish the relationship between fluorescent intensity and concentration of 5-(6) CF, respectively in the 0.04 S/m (a) and 0.5 S/m solution.

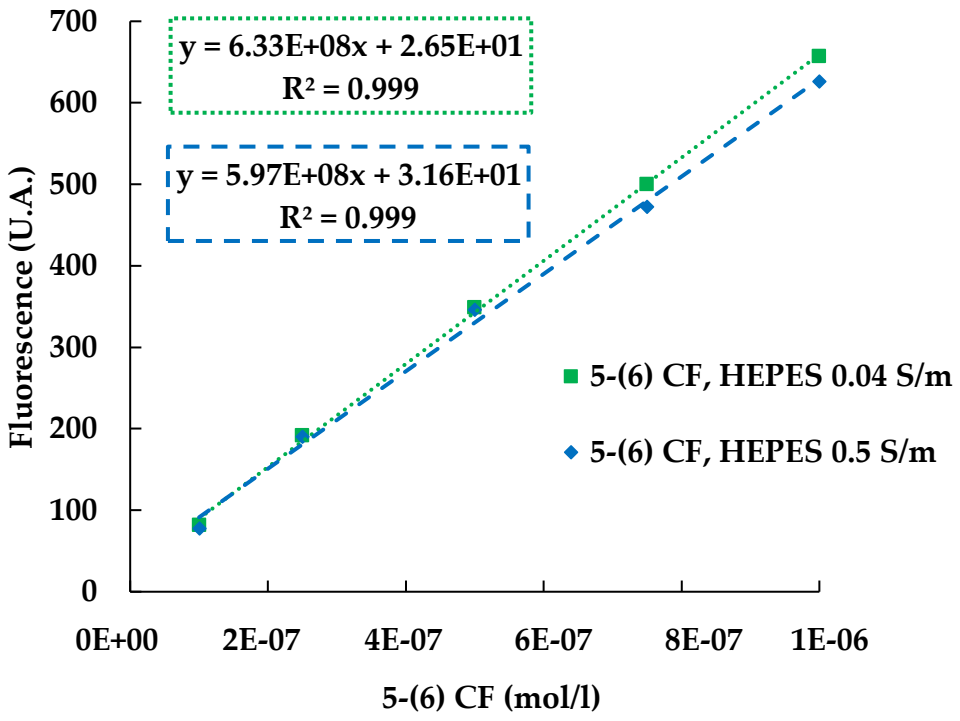


**Figure 5.1 S.I. Calibration curve of 5-(6) CF in HEPES buffer solution of 0.04 S/m and in HEPES buffer solution of 0.5 S/m, with the respective linear regression.**

Through the calibration line we were also able to quantify the μl of 5-(6) CF trapped in the aqueous core of liposomes for mg of lipid. Specifically, a template was designed to calculate the molarity of the marker for different lipid concentrations, respectively before and after the complete destruction of the vesicles with 30% w/v of TX-100. An example of the determination is reported hereafter in Figure 5.2 S.I.

| Column | | | | | Row |
|---|---|---|---|---|---|
| A | B | C | D | E | 1 |
| Calibration curve | | | | | 2 |
| Fluorescence (U.A.)= 6.33E+08*[5-(6) CF mol/l]+2.65E+01 | | | | | 3 |
| Egg PC (mg/ml) in liposomes | 0.8 | | | | 4 |
| 5-(6) CF (mol/l) for liposomes preparation | 0.05 | | | | 5 |
| | | | | | 6 |
| | 5-(6) CF fluorescence (U.A.) | | 5-(6) CF (mol/l) | | 7 |
| Egg PC (mg/l) tested | vesicles | destroyed vesicles | vesicles | destroyed vesicles | 8 |
| 0 | 0 | 0 | 0 | 0 | 9 |
| 4 | 113.8 | 238.1 | 1.9E-07 | 4.3E-07 | 10 |
| 6.5 | 176.6 | 361.3 | 3.1E-07 | 6.5E-07 | 11 |
| 8 | 215.1 | 436.1 | 3.8E-07 | 7.8E-07 | 12 |
| 9.5 | 269.8 | 529.4 | 4.8E-07 | 9.6E-07 | 13 |
| 12 | 318.9 | 624.9 | 5.7E-07 | 1.0E-06 | 14 |
| | | | | | 15 |
| mol 5-(6) CF / mg Egg PC destroyed vesicles | 1.0E-07 | REGR.LIN(E9:E14;A9:A14;FALSE) | | | 16 |
| mol 5-(6) CF / mg Egg PC vesicles | 4.9E-08 | REGR.LIN(D9:D14;A9:A14;FALSE) | | | 17 |
| | | | | | 18 |
| mol 5-(6) CF entrapped / mg Egg PC | | | 5.1E-08 | B16-B17 | 19 |
| l 5-(6) CF entrapped / mg Egg PC | | | 1.0E-06 | D20*B5 | 20 |
| μl 5-(6) CF entrapped / mg Egg PC | | | 1.0 | D21*1E+06 | 21 |

**Figure 5.2 S.I. Template used to calculate the capture 5-(6) CF volume in the aqueous core of liposomes prepared in HEPES of 0.04 S/m, by means the linear regression method.**

## 5.7 References

[1] Zimmermann, U.; Gessner, P.; Schnettler, R.; Perkins, S.; Foung, S.K. *Efficient hybridization of mouse-human cell lines by means of hypoosmolar electrofusion*. J. Immunol. Methods. 1990, 134(1), 43–50.

[2] Usaj, M.; Kanduser, M. *The systematic study of the electroporation and electrofusion of B16-F1 and CHO cells in isotonic and hypotonic buffer*. J. Membr. Biol. 2012, 245(9), 583–590.

[3] Rems, L.; Usaj, M.; Kanduser, M.; Rebersek, M.; Miklavcic, D.; Pucihar, G. *Cell electrofusion using nanosecond electric pulses*. Scientific Reports. 2013, 3, 3382.

[4] Heller, R.; Jaroszeski, M.J.; Reintgen, D.S.; Puleo, C.A.; DeConti, R.C.; Gilbert, R.A.; Glass, L.F. *Treatment of cutaneous and subcutaneous tumors with electrochemotherapy using intralesional bleomycin*. Cancer. 1998, 83(1), 148–157.

[5] Mir, L.M.; Gehl, J.; Sersa, G.; Collins, C.G.; Garbay, J.R.; Billard, V.; Geertsen, P.F.; Rudolf, Z.; O'Sullivan, G.C.; Marty, M. *Standard operating procedures of the electrochemotherapy: Instructions for the use of bleomycin or cisplatin administered either systemically or locally and electric pulses delivered by the CliniporatorTM by means of invasive or non-invasive electrodes*. Eur. J. Cancer Suppl. 2006, 4(11), 14–25.

[6] Sersa, G.; Cufer, T.; Paulin, S.M.; Cemazar, M.; Snoj, M. *Electrochemotherapy of chest wall breast cancer recurrence*. Cancer Treat. Rev. 2012, 38(5), 379–386.

[7] Teissie, J.; Escoffre, J.M.; Paganin, A.; Chabot, S.; Bellard, E.; Wasungu, L.; Rols, M.P.; Golzio, M. *Drug delivery by electropulsation: Recent developments in oncology*. Int. J. Pharm. 2012, 423(1), 3–6.

[8] Bettan, M.; Ivanov, M.A.; Mir, L.M.; Boissiere, F.; Delaere, P.; Scherman, D. *Efficient DNA electrotransfer into tumors.* Bioelectrochemistry. 2000, 52(1), 83–90.

[9] Miklavcic, D.; Sersa, G.; Brecelj, E. Gehl, J., Soden, D.; Bianchi, G.; Ruggieri, P.; Rossi, C.R.; Campana, L.G.; Jarm, T. *Electrochemotherapy: technological advancements for efficient electroporation-based treatment of internal tumors*. Medical and Biological Engineering and Computing. 2012, 50(12), 1213–1225.

[10] Kanduser, M.; Miklavcic, D.; Pavlin, M. *Mechanisms involved in gene-electrotransfer using high- and low-voltage pulses-an in vitro study*. Bioelectrochemistry. 2009, 74(2), 265–271.

[11] Escoffre, J.M.; Portet, T.; Favard, C.; Teissie, J.; Dean, D.S.; Rols, M.P. *Electromediated formation of DNA complexes with cell membranes and its consequences for gene delivery*. Biochim. Biophys. Acta. 2011, 1808(6), 1538–1543.

[12] Rowan, N.J.; MacGregor, S.J.; Anderson, J.G.; Fouracre, R.A.; Farish, O. *Pulsed electric field inactivation of diarrhoeagenic Bacillus cereus through irreversible electroporation*. Lett. Appl. Microbiol. 2000, 31(2), 110–114.

[13] Rols, M. *Gene delivery by electroporation in vitro: mechanisms*. Handbook of Electroporation. 2016, 1–16.

[14] Mir, L.M.; Bureau, M.F.; Gehl, J.; Rangara, R.; Rouy, D.; Caillaud, J.M.; Delaere, P.; Branellec, D.; Schwartz, B.; Scherman, D. *High-efficiency gene transfer into skeletal muscle mediated by electric pulses*. Proceedings of the National Academy of Sciences of the United States of America. 1999, 96(8), 4262–4267.

[15] Neumann, E.; Sowers, A.E.; Jordan, C.A. *Electroporation and Electrofusion in Cell Biology*. Plenum, New York, 1989.

[16] Weaver, J.C. *Electroporation theory. Concepts and mechanisms*. Methods Mol. Biol. 1955, 55, 3–28.

[17] Teissie, J.; Eynard, N.; Vernhes, M.C.; Bénichou, A .; Ganeva, V .; Galutzov, B .; Cabanes, P.A . *Recent biotechnological developments of electropulsation. A prospective review.* Bioelectrochemistry. 2002, 55(1–2), 107–112.

[18] Mir, L.M. Belehradek, M.; Domenge, C.; Orlowski, S.; Poddevin, B.; Belehradek, Jr.; Schwaab, G.; Luboinski, B.; Paoletti, C. *Electrochemotherapy, a new antitumor treatment: first clinical trial*. C R Acad Sci III. 1991, 313(13), 613-618.

[19] Sersa, G.; Stabuc, B.; Cemazar, M.; Jancar, B.; Miklavcic, D.; Rudolf, Z. *Electrochemotherapy with cisplatin: potentiation of local cisplatin antitumour effectiveness by application of electric pulses in cancer patients*. Eur. J. Cancer. 1998, 34(8), 1213–1218.

[20] Mir, L.M. Glass, L.F.; Sersa, G.; TeissiÃ©, J.; Domenge, C.; Miklavcic, D.; Jaroszeski, M.J.; Orlowski, S.; Reintgen, D.S.; Rudolf, Z., Belehradek, M., Gilbert, R.; Rols, M.P.; Belehradek, J.; Bachaud, J.M.; DeConti, R.; Stabuc, B.; Cemazar, M.; Coninx,

P.; Heller, R. *Effective treatment of cutaneous and subcutaneous malignant tumours by electrochemotherapy*. Br. J. Cancer. 1998, 77(12), 2336–2342.

[21] Mir, L.M. Devauchelle, P.; Quintin-Colonna, F.; Delisle, F.; Doliger, S.; Fradelizi, D.; Belehradek, J.; Orlowski, S. *First clinical trial of cat soft-tissue sarcomas treatment by electrochemotherapy*. Br. J. Cancer. 1997, 76(12), 1617–1622.

[22] Rols, M.P.; Tamzali, Y.; Teissie, J. *Electrochemotherapy of horses. A preliminary clinical report*. Bioelectrochemistry. 2002, 55(1–2), 101–105.

[23] Kotnik, T.; Pucihar, G.; Miklavcic, D. *Induced transmembrane voltage and its correlation with electroporation-mediated molecular transport*. Journal of Membrane Biology. 2010, 236(1), 3–13.

[24] Joshi, R.P.; Schoenbach, K.H. *Bioelectric effects of intense ultrashort pulses*. Critical Reviews in Biomedical Engineering. 2010, 38(3), 255–304.

[25] Casciola, M.; Tarek, M. *A molecular insight into the electrotransfer of small molecules through electropores driven by electric fields*. Biochimica et Biophysica Acta (BBA)—Biomembranes. 2016, 1858(10), 2278–2289.

[26] Cadossi, R.; Ronchetti, M.; Cadossi, M. *Locally enhanced chemotherapy by electroporation: clinical experiences and perspective of use of electrochemotherapy*. Future Oncology. 2014, 10(5), 877–890.

[27] Beebe, S.J.; Fox, P.M.; Rec, L.J.; Willis, E.L.K.; Schoenbach, K.H. *Nanosecond, high-intensity pulsed electric fields induce apoptosis in human cells*. The FASEB journal. 2003, 17(11), 1493-1495.

[28] Chopinet, L.; Rols, M.P. *Nanosecond electric pulses: A mini-review of the present state of the art*. Bioelectrochemistry. 2015, 103, 2-6.

[29] De Menorval, M.A.; Andre, F.M.; Silve, A.; Dalmay, C.; Français, O.; Le Pioufle, B.; Mir, L.M. *Electric pulses: a flexible tool to manipulate cytosolic calcium concentrations and*

*generate spontaneous-like calcium oscillations in mesenchymal stem cells*. Scientific Reports. 2016, 6, article 32331.

[30] Napotnik, T.B.; Rebersek, M.; Vernier, P.T.; Mali, B.; Miklavcic, D. *Effects of high voltage nanosecond electric pulses on eucaryotic cells (in vitro): a systematic review*. Bioelectrochemistry. 2016, 110, 1–12.

[31] Silve, A.; Leray, I.; Poignard, C.; Mir, L.M. *Impact of external medium conductivity on cell membrane electropermeabilization by microsecond and nanosecond electric pulses*. Scientific Reports. 2016, 6, article ID 19957.

[32] Silve, A.; Leray, I.; Mir, L.M. *Demonstration of cell membrane permeabilization to medium-sized molecules caused by a single 10ns electric pulse*. Bioelectrochemistry. 2012, 87, 260– 264.

[33] Ibey, B.L.; Roth, C.C.; Pakhomov, A.G.; Bernhard, J.A.; Wilmink, G.J.; Pakhomova, O.N. *Dose-dependent thresholds of 10-ns electric pulse induced plasma membrane disruption and cytotoxicity in multiple cell lines*. PLoS ONE. 2011, 6(1), article ID e15642.

[34] Pakhomov, A.G.; Phinney, A.; Ashmore, J.; Alker, K.; Kolb, J.F.; Kono, S.; Schoenbach, K.H. *Characterization of the cytotoxic effect of high-intensity, 10-ns duration electrical pulses*. IEEE Transactions on Plasma Science. 2004, 32(4), 1579–1586.

[35] Schoenbach, K.H.; Beebe, S.J.; Buescher, E.S. *Intracellular effect of ultrashort electrical pulses*. Bioelectromagnetics.l. 2001, 22(6), 440–448.

[36] Tekle, E.; Oubrahim, H.; Dzekunov, S.M.; Kolb, J.F.; Schoenbach, K.H.; Chock, P.B. *Selective field effects on intracellular vacuoles and vesicle membranes with nanosecond electric pulses*. Biophys. J. 2005, 89(1), 274–284.

[37] Napotnik, T.B.; Rebersek, M.; Kotnik, T.; Lebrasseur, E.; Cabodevila, G.; Miklavcic, D. *Electropermeabilization of endocytotic vesicles in B16 F1 mouse melanoma cells*. Med. Biol. Eng. Comput. 2010, 48(5), 407–413.

[38] Chen, N.; Schoenbach, K.H.; Kolb, J.F.; Swanson, R.J.; Garner, A.L.; Yang, J.; Joshi, R.P.; Beebe, S.J. *Leukemic cell intracellular responses to nanosecond electric fields*. Biochem. Biophys. Res. Commun. 2004, 317(2), 421–427.

[39] Napotnik, T.B.; Wu, Y.H.; Gundersen, M.A.; Miklavcic, D.; Vernier, P.T. *Nanosecond electric pulses cause mitochondrial membrane permeabilization in Jurkat cells*. Bioelectromagnetics. 2012, 33(3), 257–264.

[40] Vernier, P.T.; Sun, Y.; Marcu, L., Salemi, S.; Craft, C.M.; Gundersen, M.A. *Calcium bursts induced by nanosecond electric pulses*. Biochem. Biophys. Res. Commun. 2003, 310(2), 286–295.

[41] Scarlett, S.S.; White, J.A.; Blackmore, P.F.; Schoenbach, K.H.; Kolb, J.F. *Regulation of intracellular calcium concentration by nanosecond pulsed electric fields*. Biochim. Biophys. Acta. 2009, 1788(5), 1168–1175.

[42] Beebe, S.J.; White, J.; Blackmore, P.F.; Deng, Y.; Somers, K.; Schoenbach, K.H. *Diverse effects of nanosecond pulsed electric fields on cells and tissues*. DNA Cell Biol. 2003, 22(12), 785–796.

[43] Denzi, A.; della Valle, E.; Apollonio, F.; Breton, M.; Mir, L.M.; Liberti, M. *Exploring the applicability of nano-poration for remote control in smart drug delivery systems*. The Journal of Membrane Biology. 2017, 250(1), 31–40.

[44] Denzi, A.; della Valle, E.; Esposito, G.; Mir, L.M.; Apollonio, F.; Liberti, M. *Technological and Theoretical Aspects for Testing Electroporation on Liposomes*. BioMed Research International. 2017, 10 pages, article ID 5092704.

[45] Retelj, L.; Pucihar, G.; Miklavčič, D. *Electroporation of intracellular liposomes using nanosecond electric pulsesa theoretical study*. IEEE Transactions on Biomedical Engineering. 2013, 60(9), 2624-2635.

[46] Breton, M.; Mir, L.M. *Microsecond and nanosecond electric pulses in cancer treatments*. Bioelectromagnetics. 2012, 33(2), 106-123.

[47] Portet, T.; Mauroy, C.; Démery, V.; Houles, T.; Escoffre, J.M.; Dean, D.S.; Rols, M.P. *Destabilizing giant vesicles with electric fields: an overview of current applications*. The Journal of membrane biology. 2012, 245(9), 555-564.

[48] Breton, M.; Amirkavei, M., Mir, L.M. *Optimization of the electroformation of giant unilamellar vesicles (guvs) with unsaturated phospholipids*. The Journal of membrane biology. 2015, 248(5), 827-835.

[49] Silve, I.; Leray, C.; Poignard, C.; Mir, L.M. *Impact of external medium conductivity on cell membrane electropermeabilization by microsecond and nanosecond electric pulses*. Scientific reports. 2016, 6, 19957.

[50] Petralito, S.; Spera, R.; Memoli, A.; D'Inzeo, G.; Liberti, M.; Apollonio, F. *Preparation and characterization of lipid vesicles entrapping iron oxide nanoparticles*. Asia-Pacific J. Chem. Eng. 2012, 7, 335–341.

[51] Yoshida, Y.; Furuya, E.; Tagawa, K. *A direct colorimetric method for the determination of phospholipids with dithiocyanatoiron reagent*. J. Biochem. 1980, 88, 463–468.

[52] DeBruin, K.A.; Krassowska, W. *Modeling electroporation in a single cell. I. Effects of field strength and rest potential*. Biophys J. 1999, 77(3), 1213–1224.

[53] Li, J.; Lin, H. *The current–voltage relation for electropores with conductivity gradients*. Biomicrofluidics. 2010, 4(1), 1–17.

[54] Krassowska, W.; Filev, P.D. *Modeling electroporation in a single cell*. Biophys J. 2007, 92(2), 404–417.

[55] Ivorra, A.; Villemejane, J.; Mir, L.M. *Electrical modeling of the influence of medium conductivity on electroporation*. Phys Chem Chem Phys. 2010, 12(34), 10055–10064.

[56] Mercadal, B.; Vernier, P.T.; Ivorra, A. *Dependence of Electroporation Detection Threshold on Cell Radius: An Explanation to Observations Non Compatible with Schwan's Equation Model*. J Membrane Biol. 2016, 249(5), 663–676.

[57] Glaser, S.M.; Trueblood, C.E.; Dircks, L.K.; Cumsky, M.G. *Functional analysis of mitochondrial protein import in yeast*. J Cell Biochem. 1988, 36(3), 275-287.

[58] Merla, C.; Denzi, A.; Paffi, A.; Casciola, M.; d'Inzeo, G.; Apollonio, F.; Liberti, M. *Novel passive element circuits for microdosimetry of nanosecond pulsed electric fields*. IEEE Transactions on Biomedical Engineering. 2012, 59(8), 2302-2311.

[59] Kenaan, M.; El Amari, S.; Silve, A. *Characterization of a 50-Ω exposure setup for high-voltage nanosecond pulsed electric field bioexperiments*. IEEE Transactions on Biomedical Engineering. 2011, 58(1), 207–214.

# Chapter 6

# Wide field CARS microspectroscopy and real-time follow-ups of hydration changes induced by electropulsation of liposomes

Caterina Merla[1,2], Brigitte Attal-Tretout[4], Martina Nardoni[3], Stefania Petralito[3], Francesca Apollonio[5], Micaela Liberti[5], Michael Schermann[4], Lluis M. Mir[1]

[1]*Vectorology and Anticancer Therapies, UMR 8203, CNRS, "Paris-Sud" University, Gustave Roussy, "Paris-Saclay" University, 94805 Villejuif, France*

[2]*Division of Health Protection Technologies, "ENEA" National Italian Agency for New Technologies, Rome, Italy*

[3] *Department of Drug Chemistry and Technologies, "Sapienza" University of Rome, Piazzale Aldo Moro 5, 00185 Rome, Italy*

[4]*ONERA, BP 80100, 91123 Palaiseau Cedex, France5*

[5] *Department of Information Engineering, Electronics and Telecommunications (DIET), "Sapienza" University of Rome, Via Eudossiana 18, 00184 Rome, Italy*

**Submitted**

***6.1 Abstract.*** *Wide-field CARS microscopy and real-time acquisition of specific wavelengths, during exposure to nanosecond pulsed electric fields, were performed to analyze the behaviour of the lipid "C-H" and O"-H" stretch vibrational bands of water at the surface of liposomes. Nanosecond dye lasers, used in a non-phase-matching illumination, allow to perform a sensitive spectroscopy at interfaces between lipids and water molecules, with reduced non-resonant contribution from the bulk water itself. The major spectral components of the water/lipid interface were identified on the liposomes spectra, which differ from those of the pure water. The two main identified spectral zones were assigned to the water molecules located at the surface of liposomes (namely the bonds containing the hydrogen atoms of the interfacial water molecules) and to the interstitial water molecules (namely the water molecules inserted in between the lipids constituting the membrane). Their relative intensities were recorded with or without a previous exposure of the samples to intense nanosecond electric pulses. We proved, in this work, that the used pulse protocol leaded to the lipid bilayer rapid electroporation and to a long lasting permeabilization. The interstitial bands at 3400 $cm^{-1}$ became prominent in pulsed liposomes, whereas the interfacial bands at 3145 $cm^{-1}$ seem not affected. Our results suggest that electric pulses can modify membrane hydration. Therefore, the facilitated molecules transport across the membranes, during their electropermeabilized state, would be partly the consequence of the perturbation of the water structure within the lipid bilayer and at its surface. Then, CARS signals of single relevant wavelengths where further followed in real-time, during the electric exposure. In this case, CARS intensities were acquired with a time resolution of few ns comparable to the electric pulse time scale. The increase of the interstitial water signal was detected. These results clearly confirm our spectral analysis, highlighting, for the first time, the experimental evidence that the pore formation is initiated by intrusion of single water molecules (interstitial) into the membrane interior, leading to the bilayer reorganization into hydrophilic conductive defects.*

***Keywords:*** *wide-field CARS microspectroscopy; CARS real-time signatures; CARS spectra; electroporation; electropermeabilization; electric pulses; liposomes; interfacial water; interstitial water.*

## 6.2 Introduction

A widely used technique in biology, biotechnology and medical treatments deals with the application of short (from ms down to few ns) and high intense (from few kV/m up to tens of MV/m) electric pulses to facilitate the passage of small and large molecules from the outside to the inside of cells [1]. As an example, cell membrane permeabilization is widely exploited in a well-known treatment: the electrochemotherapy, which enables the potentiation from 100 to 10000 folds of the uptake of a chemotherapeutic agent [2]. However, pulses effects are not limited to membrane permeabilization, and other different outcomes ranging from nerves and heart stimulation, apoptosis induction, to modulation of intracellular calcium are investigated for translation in potential novel treatments for various pathologies [3, 4]. Even down millisecond and microsecond electric pulses are routinely used in hospitals and research laboratories and biological effects of very short nanosecond electric pulses, not yet at the clinical stage, are investigated from more than 15 years so far, the precise mechanisms inducing membrane rearrangements and the consequent increase of its permeabilization are still not completely comprised and highly debated [5]. Recently, the term electropulsation appears to indicate, in a single word, the double nature of the membrane reorganization phenomenon [6, 7]. The main idea is that membrane defects have a rapid phase, termed electroporation and a longer lasting phase termed electropermeabilization. The first electroporation phase accounts for hydrophilic pore formation, as predicted by molecular dynamics simulations, which rapidly reseal after the pulses end. While the electropermeabilization phase, observed experimentally through the late uptake of different molecules (e.g. DNA, fluorescent dyes, bleomycin), [8], is due to a sort of membrane instability. Recently, some papers propose lipid oxidation as one of the mechanisms responsible for long lasting permeabilization, demonstrating this possibility both experimentally and by MD simulations [6, 7]. Nevertheless, permeabilization can be more likely a combination of multiple and complex events, as the involvement of ion channels, structural modification of specific water channels (e.g. acquiporin), cytoskeleton rearrangements, cholesterol interactions, indicated by the term permeome [5].

Considering the role of lipid oxidation in long lasting membrane permeabilization, it was demonstrated that the amount of lipid oxidation pended on the electric pulses amplitude and on the delivered number but also on the pulse duration. Specifically, lipid oxidation decreases reducing the pulses duration. So, it appears that this chemical mechanism can contribute more to the membrane permeabilization when millisecond and microsecond pulses are involved and it is reduced when nanosecond pulses are applied to cells. In a recent paper of Tokman and colleagues [8], looking at MD simulations, authors reported instead that when short pulses in the nanosecond time scale are applied to membrane patches, the contribution from water molecules polarization predominates the fast electroporation process. These authors evidenced, by MD simulations, the role of water in electroporation, identified as the initiator of the process and then, also, as a responsible for the longer lasting defects [8]. This vision is not in contrast with the mechanism of permeabilization, driven by oxidation, as also lipid oxidation implies membrane water reorganization with long lasting processes. Due to this complex puzzle, in this paper we experimentally studied water and lipid reorganization, at different time scales during electropulsation. The study of water molecules reorganization is not easy task, since no staining techniques are available for tracking water. Similarly, the following of lipid chemical reactions is also a complex task [9]. In this context, non-linear optics techniques are among the best candidates for these purposes, allowing the label free and fast acquisition of vibration modes of specific chemical bound in samples. Coherent Anti-Stokes Raman Scattering (CARS) is one of these techniques and was already successfully applied to various biological samples, both on cells and tissues [9, 10]. Phospholipids, which are one of the main constituents of the membrane bilayer, are one of the molecular chains most commonly studied by CARS spectroscopy [9-11]. The vibration of the “C-H” bond of the hydrocarbon chain is characterized by a large cross-section, thus providing a large CARS signal. Moreover, vibrations of water, confined by lipid bilayers, can be selectively probed by CARS, proving the peculiar potentialities of this method [9, 10].

In a conventional excitation scheme, the CARS signal is generated using two tightly focused light beams and detailed images are generated, point-by-point, by scanning the sample in a confocal arrangement. However, this point-by-point technique is time-consuming and, more recently, different groups investigated wide field imaging geometries to capture several hundreds of $\mu m^2$ in a single shot of paired lasers. A different set-up was proposed by Toytman et al. [12, 13]. The illumination geometry relied on the use of two almost collinear beams, in order to avoid phase-matching in the whole area of the probed volume. Strong enough CARS signal was, thus, selectively generated on the object and the non-resonant background was efficiently reduced. Based on these developments, it was created by our group a geometry well suited for transparent objects in general, using a small angle (7°) of incidence for the Stokes laser beam [9]. Therefore, incident beams were arranged in a configuration inspired, but different, by Toytman's non collinear geometry, providing a simple design with a high scattering efficiency. Under this specific configuration, maximum CARS signal originates from the object itself and, more specifically, from the interphase between the object and its surroundings, where the refraction and the scattering of the beams result in local phase-matching conditions [14]. Performances of this geometry were fully tested on polystyrene beads and cells [15]. In this previous work, it was demonstrated that spectral profiles can be extracted from the wide field CARS hyperspectral image, using small- or medium-sized spatial regions, composed of a few pixels or a few tens of pixels respectively. The absence of damage on living cells, during CARS image acquisition, was also confirmed during these experiments [15-17].

In the present work, our attention was paid to the "C-H" (lipid heads and tails) and "O-H" vibration modes in the 3000-3500 $cm^{-1}$ frequency range observed on liposomes. The probed lipid/water vibrations correspond to those of molecules located at liposomes surfaces. These spherical vesicles constitute a simple model of a cell membrane, nonetheless maintaining a certain complexity, as they can be formed by several types of lipids. The extensive literature, dealing with liquid water spectroscopy, generally refers to strong and weak hydrogen bonding, corresponding respectively to short and large Raman shifts [9-11, 16].

Furthermore, pump-probe spectroscopy, as well as other techniques such as surface sum-frequency generation, revealed different lifetimes [18-21] and different spectra [12-14, 22] for the water molecules.

Far from the object surface, water molecules are mainly surrounded by other water molecules, not taking into account the few molecules of solutes that can be present, always in extremely low concentrations with respect to the water concentration. As a function of the level of ordering, water molecules structure is considered as "bulk-like" water.

When considering the water molecules located close to the objects, the concepts of bulk-like water are not appropriate. Indeed, in the presence of objects, there is an interface and the surface of the object impacts the hydrogen bonds of the water in two ways. The first one is linked to the roughness of the surface: if nano-interstices exist at the object surface, water molecules can be located in these interstices (it is the "interstitial" water). This water forms very weak hydrogen bonds with other water molecules, because water molecules in the nano-interstices fall apart from each other. When the object is a liposome, all the surface is composed of lipids. In this case, the "interstitial" water, which is close to the lipid molecules, not exposed at the surface of the lipids layer, was termed "lipid-associated" hydrogen bonding water. Actually, the spectral zone, corresponding to "lipid-associated" water, shows several bands that can be assigned to different types of hydrogen bonding, for example "carbonyl-associated O-H" bonding or "phosphate-associated O-H" bonding. In this article, we use the term "interstitial water" to refer to this whole spectral zone. The second one is linked to the surface ability to order and orient the water molecules, which are closed to the surface. This water is called the "interfacial" water. For the cell membrane, it is assumed to correspond to the few water layers occupying the first 1 to 2 Å over the membrane. In the case of the phospholipids-water interface, the interfacial water, located the closest to the phospholipids head, forms a clathrate cage around the choline group through hydrogen bonding that was termed "water-associated O-H" bonding [23]. At the lipid bilayer surface, the interfacial water constitutes some layers of water that can be ordered by the dipoles of the phospholipid heads. As phospholipids heads are regularly

placed at the lipid bilayer surface and are tightly packed, these particular water layers contribute to the impermeability and the absence of conductivity of the cell membrane.

In this paper, CARS spectroscopy was used for the first time in combination with pulsed electric fields to deep insight into the mechanism of electropulsation. Liposomes were used as test sample since they represent very stable spherical phospholipid bilayers, obtainable at high concentration. Evidently, liposomes are interesting structures for studying electroporation and long lasting membrane permeabilization, in order to understand mechanisms of lipid/water rearrangements. These structures were also proposed as smart drug delivery systems, controlled by electric pulses for innovative biomedical applications [7, 24]. Hence, the comprehension of electropulsation mechanisms has an interest for basic research, but also for its translation to new biomedical technologies in the area of smart drug delivery, mediated by the electric pulses. We report here novel observations of spectral features originating from the interfacial and the interstitial water in the CARS spectrum of liposomes, immediately after nanosecond pulses electric field exposure.

CARS signals of single relevant wavelengths, associated to lipids, the interfacial and the interstitial water, were further followed in real-time, during the electric stimulation. In this case, CARS intensities were acquired, for the first time, with a time resolution of few ns comparable to the time scale of the applied electric pulses.

## 6.3 Experimental section

### 6.3.1 Materials

Phosphatidylcholine from egg (Egg PC) Lipoid 80 E, from Lipoid GmbH (Germany), was kindly offered by AVG Srl (Italy). 4-(2-hydroxyethyl) piperazine-1-ethanesulfonic acid (HEPES), 5-(6) carboxyfluorescein [5-(6) CF], Triton X-100 (TX-100), Sephadex G-75 medium, sodium chloride (NaCl), iron thiocyanate, iron (III) nitrate, ammonium thiocyanate, sodium hydroxide (NaOH) and hydrochloric acid (HCl) were purchased from Sigma Aldrich (Italy). Bidistilled water, ethanol and chloroform were obtained from Merck

(Italy). Polycarbonate membrane filters Whatman® (800, 400 and 200 nm) were purchased from Cyclopore Track Etched Membrane.

### 6.3.2 Preparation of liposomes

The CARS investigations were performed on nanometer-sized lipid-based vesicles, exposed or sham exposed to very short electric pulses. Conventional thin film hydration method, followed by extrusion, was used to prepare unilamellar liposomes. Briefly, phosphatidylcholine from egg (Egg PC) was dissolved in the minimum volume of chloroform and the organic solution was poured into a round bottom flask. The organic solvent was evaporated under reduced pressure at 25 °C (above the gel-liquid crystalline transition temperature of the Egg PC, Tm) to form a film which was further dried under high vacuum, removing traces of the solvent. The resulting lipid film was hydrated with 5 ml of HEPES buffered saline solution (HEPES buffer 10 mM, pH= 7.4, 60 mM NaCl, $\sigma$=0.8 S/m). 20 mM of the hydrophilic fluorescent marker 5-(6) CF was also added to the buffered solution. The hydration process was carried out in a thermostated water bath at 25 °C (T>Tm). Five repetitive freeze-thaw cycles of liposomes aqueous suspension were performed, encouraging the greater entrapment of the probe in the core. The mixture was repeatedly extruded at 25 °C, through polycarbonate membranes of decreasing pore size using the Avanti Mini Extruder (Avanti Polar). The extrusion was carried on until a homogeneous size distribution was achieved (2 times through 800 nm membranes, 4 times through 400 nm membranes and 4 times through 200 nm membranes). Finally, liposomes were purified using a Sephadex G-75 gel filtration column. The purification step was considered with the aim of removing not entrapped material into vesicular structures. All liposome formulations were prepared at least in triplicate, were stored at 4 °C and were used within two weeks.

### 6.3.3 Physicochemical characterization of liposomes

- *Dynamic light scattering and ζ- potential measurements*

Particle size distribution of liposome was measured with a Zetasizer Nano ZS90 (Malvern Instruments Ltd., Malvern, UK). Hydrodynamic diameter and polydispersity index were evaluated by DLS experiments, whereas ζ-potential was measured by electrophoretic light scattering (ELS) experiments. All the experiments were performed at a scattering angle of 90° and were thermostatically controlled at 25 °C. Liposomes samples were diluted in HEPES (10 mM, pH = 7.4, σ=0.8 S/m) until a count-rate of about 200 kcps was obtained to avoid interfering multiple scattering phenomena. Size, polydispersity index ζ-potential values of the liposomes are the mean of three different preparation batches ± SD. Moreover, each analysis was performed in triplicate. The measurements were carried out immediately after vesicles preparation and repeated during the samples conservation at 4 °C, in order to evaluate their stability over time.

- *Phospholipid assay*

The amounts of phospholipids present in the liposomal formulation were determined using a colorimetric method. The assay is based on the formation of a hydrophobic thiocyanatoiron-phospholipid complex [25]. Briefly, aliquots (0.4 ml) of phospholipids in 50% (v/v) of ethanol were added to a mixture of 1 ml of thiocyanatoiron reagent, previously prepared by solubilizing 0.97 g iron (III) nitrate and 15.2 g of ammonium thiocyanate in 100 ml of water. Then the solution obtained was acidified with 0.6 ml of 0.17 N HCl. The thiocyanatoiron-phospholipid complex formed was extracted with 3 ml of 1,2-dichloroethane, by vigorous shaking for 2 min in a vortex-type mixer. The mixture was centrifuged for 5 min at 2000 rpm and the absorbance of the organic lower layer was measured at 470 nm against a blank without substrate, using a GloMax®-Multi Detection

System of Promega as spectrophotometer. Phospholipid concentration was gained through a suitable standard curve previously constructed.

- *Loading and entrapment efficiency of 5-(6) CF*

The 5-(6) CF sodium salt stock solution was obtained dissolving 5-(6) CF powder with few drops of 1M NaOH solution, followed by the addition of HEPES buffered solution up to the appropriate molarity (0.1 M). The 0.02 M 5-(6) CF fluorescent marker was loaded within the aqueous core of vesicles during the thin film hydration phase. The amount of entrapped probe in the inner compartment of liposomes was spectrofluorimetrically determined ($\lambda_{ex}$=492 nm; $\lambda_{em}$=512 nm) using a GloMax®-Multi Detection System of Promega spectrofluorimeter. The entrapment efficiency (E.E) of 5-(6) CF, defined as μl of entrapped volume for mg of lipid, was established using a linear regression plot, as reported in S.I. All experiments were performed in triplicate and the results reported as mean ± SD.

- *Thermal stability study of liposomes*

Before the application of the nanosecond pulsed electric field, the physical stability of any formulation was checked at 25 °C, to provide informations about the temperature profile of solute leakage from L$\alpha$-Egg PC vesicles. Liposomes, containing a defined quantity of probe, were inserted in amber glass vials, in a thermostated water bath (25 °C), under moderate magnetic stirring for 3 h. Samples were withdrawn at predetermined time intervals and the percentage leakage of 5-(6) CF was determined as follows:

$$5-(6)\ CF\ leakage\ (\%) = \frac{(I_t - I_0)}{(I_{max} - I_0)} \cdot 100 \qquad (6.1)$$

where: $I_t$ and $I_0$ are the intensities of fluorescence at each time and a $t_0$, respectively; $I_{max}$ is the total fluorescence after adding TX-100 (30% w/v).

Fluorescence emission spectra were recorded at excitation wavelength of 492 nm and the emission was monitored over wavelength the range of 400-600 nm ($\lambda_{em}$= 512 nm), using a GloMax®-Multi Detection System Promega as spectrofluorimeter. At the end of the study, the suspension was recovered and liposomes were characterized by DLS to verify their dimensional integrity. All procedure was repeated for three times and the experimental data were showed as mean ± SD.

### 6.3.4 Electrical set-up for applying nanosecond pulsed electric field to liposomes

To verify the electropermeabilization of the liposomes, in order to perform well controlled CARS experiments, vesicles were exposed to a train of electric pulses using a ground closed coplanar waveguide (GCCPW) as exposure system. The GCCPW structure and its transmission behaviour was already presented in [26]. In brief, the GCCPW is a planar bio-chip constituted by three parallel gold electroplated electrodes connected to a ground plane. Our GCCPW is perfectly matched up to 3.5 GHz, with a reflection coefficient less than -10 dB. Besides this good matching in reflection, our GCCPW presents a $S_{21}$ always above -3 dB, up to 3.5 GHz. Therefore, losses in transmission seem good and in line with other devices for single or multicellular electric exposure, as noted in [27, 28]. Hence, all the delivered electric pulses are undistorted transmitted to the liposomes samples. Liposomes were exposed between the central and lateral gold planar electrodes of the bio-chip, presenting an inter-electrode distance of 500 μm. This distance was fixed in order to allow lasers passages during the CARS micro-spectroscopy. A constant liposomes volume of 15 μl, at 25 °C, was exposed in a set of three independent experiments, repeated two times. Beside the exposed samples, our experimental configuration included sham exposed ones and the control sample not placed on the GPPW electrodes. This aliquot was leaved for the duration of the whole experiment in the water bath, thermostated at 25 °C. The fluorescent dye release was evaluated for all the samples (exposed, sham and control), taking into account the spontaneous leakage of the control samples at each collection of fluorescence data acquired,

immediately after exposure (0.28 h) and 1, 2, 3, 24 h after the pulse delivery trigger. Dynamic light scattering (DLS) experiments were carried out to assure integrity of the vesicles upon exposure. Temperature was measured before and immediately after the stimulation with a probe (Luma Sense), recording differences below 0.5 °C.

It is worth to remember that the GCCPW is also fully biocompatible, thanks to the material employed for its fabrication including gold, transparent calcium fluoride ($CaF_2$), limiting as much as possible eventual electrochemical effects during the electric pulses application.

Liposomes were pulsed using the following protocol: 2000 pulses, each lasting 10 ns, were delivered with and inter pulses frequency of 2 Hz. The pulses amplitude where fixed at 9 MV/m. Pulses were delivered using a Fid Technology generator (model Brand) and the delivery controlled by mean of an oscilloscope (Tecktronic 600 MHz or Lecroy 8 GHz), connected through a tape off (Barth type) following the measurement chain, as reported in [29, 30]. The same pulses protocol was also used for CARS experiments (as reported in the subsection Optical and electrical set-ups description) to retrieve spectra of liposomes in the lipid/water vibrational region.

### 6.3.5 Optical and electrical set-ups description

- *The CARS microscope*

The CARS images were acquired using a wide field CARS arrangement that was described previously in [31]. The excitation beams were provided by two pulsed narrowband tunable dye lasers, operating at 10 Hz, which are named pump and Stokes beams. Full laser line width at half maximum (FWHM) was 2 $cm^{-1}$ for the pump and 3 $cm^{-1}$ for the Stokes beams. The pulse durations were 4 ns (pump) and 2.8 ns (Stokes).

In our configuration, ω pump was fixed at 15 384 $cm^{-1}$ ($\lambda_{pump}$= 650.0 nm), while the ω Stokes (Stokes laser operated with the LDS 821 dye) could be tuned from 11876 to 12469 $cm^{-1}$ ($\lambda_{Stokes}$=

802 nm - 842 nm). This ω pump - ω Stokes scanning range allowed us to probe, with a maximal efficiency, the Raman bands of water molecules located between 2915 and 3508 $cm^{-1}$ [32, 33], which is the Raman range termed "water vibrations region". The "$CH_3$" choline bond, associated to lipid rearrangement, is further included in the observation region. Let us note that this range also includes polystyrene CARS bands, with a prominent band at 3054 $cm^{-1}$ ($\lambda_{Stokes}$= 811.0 nm) that is used in the alignment procedure.

Typical energies are per pulse range from 200 to 500 μJ for the pump, and from 130 to 300 μJ for the Stokes laser. After spatial filtering, the laser beams were focused into the sample using two long focal length lenses, 750 mm for the pump and 500 mm for the Stokes, resulting in a relatively large Gaussian spot at the sample plane, 120 μm in diameter for the pump and 110 μm for the Stokes. Thus, wide field imaging [13, 14] of liposomes could be achieved in a single laser shot 15. It is worth to notice that liposomes spatial resolution is not resolvable but retrieved CARS signals clearly indicate the presence of liposomes, due to variation of vibrational modes with respect to the simple water samples.

In our CARS arrangement, the main resonant susceptibility contribution χR (3) to the CARS signal 15 arose from the interface between the object itself and the closely surrounding medium, including the water resonances being studied here, as described in the Introduction. An inverted microscope (Zeiss Axiovert 200) was used and the sample was imaged by means of standard objectives (50 x, NA= 0.55). Image of the observation plane was formed on an intensified CCD camera (PIMAX 3 Camera, Roper Technologies, Sarasota, Florida). In the signal acquisition sequence, the camera was triggered by the laser pulse, using a delay generator (DG 545, Princeton instruments). The temporal gate width of the camera was set to 40 ns in most experiments. The very short gate width improved the filtering of the pulsed CARS signal from the stray light. To record a CARS spectrum, ω pump was kept constant, while ω stokes was scanned over the whole emission bandwidth of the LDS dyes. The scanning speed of the Stokes wavelength (30 pm/s) was adjusted according to the laser linewidth (3 $cm^{-1}$).

- *GCCPW coupled to the CARS microscope*

The GCCPW, used to verify the 5-(6) CF release from liposomes, e.g. a test demonstrating the effective liposomes permeabilization, was integrated into the previously presented CARS microscope to permit the acquisition of CARS spectra and the real-time follow-ups of CARS signal at specific wavelengths (Figure 6.1, B). Essentially the integration includes mechanical arrangement of the GCCPW into the CARS microscope stage and its optical coupling, using specific filters to reflect the Stokes and Pump beams and allowing the passage of the Anti-Stokes beam (Figure 6.1, A-B). The optical filters are positioned in specific locations and the first one has also the capability of maintaining the reflected signal with a low aperture angle in order to avoid reflection of the lasers near the metallic GCCPW electrodes. In front of the microscope objective, the GCCPW plane is constituted by the transparent $CaF_2$ substrate, one of the best materials for non-linear optics, which is in contact to a bandpass filter $F_1$ (CVI-CP-AG-540). The coated filter face was placed upward in order to reflect the pump and Stokes beams right, after interacting with the sample of interest. The filter ($F_1$) prevented the objective from being damaged by the high energies of the excitation beams (attenuation of 4 orders of magnitude) and allowed more than 90% transmission at anti-Stokes wavelength. Additionally, a set of bandpass filters (two FF01-750, 2 mm thick) was placed at the exit of the objective in front of the CCD camera, in order to block the residual light from the lasers beams and to spectrally filter the anti-Stokes scattering. These details and the full system are visible in the Figure 6.1.

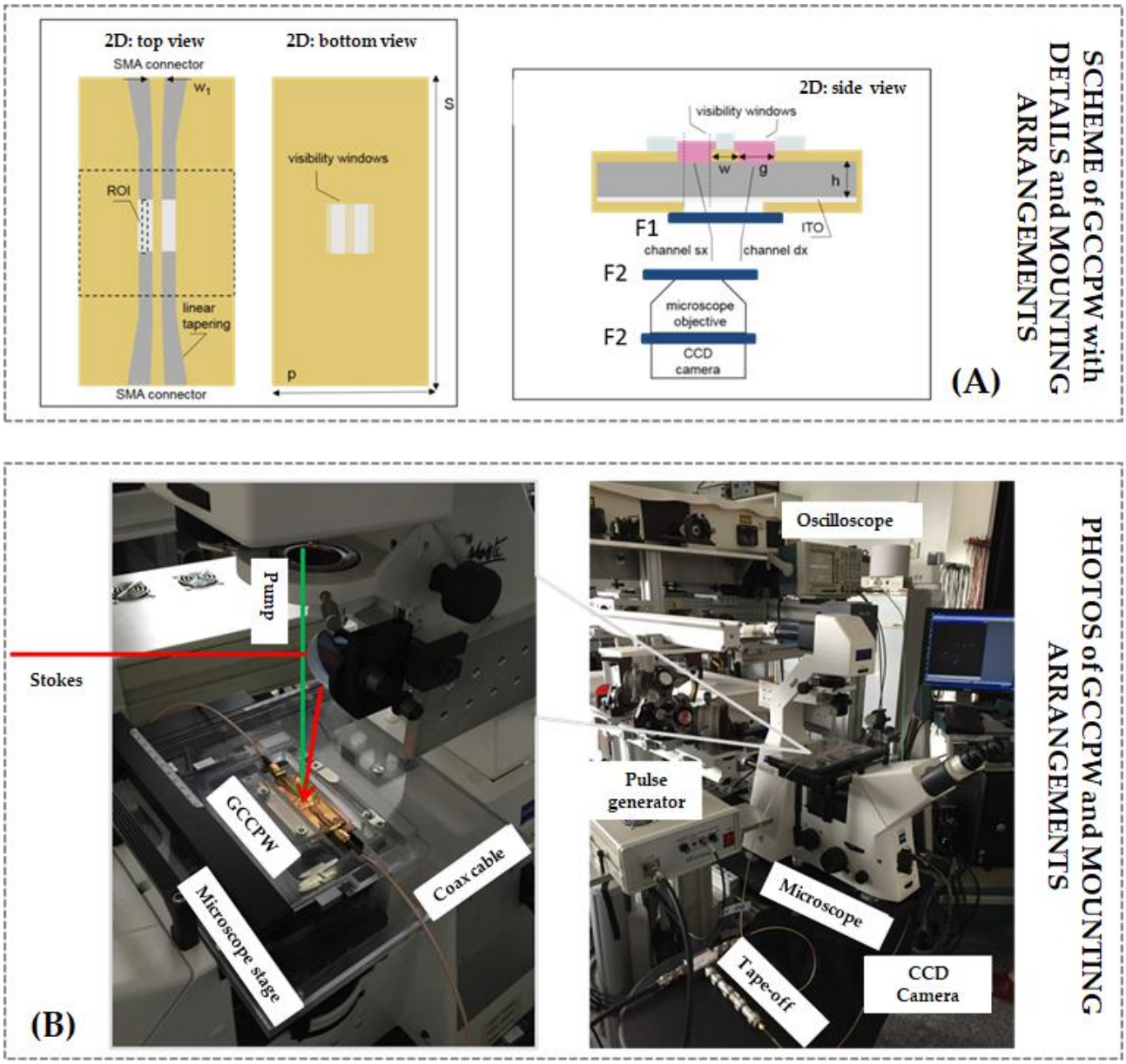


**Figure 6.1. Scheme of the GCCPW device, with details and mounting arrangements for its integration into the CARS microscope (A). Photos of the whole wide field CARS setup, with details of the GCCPW mounting and the connection to the pulse generator. The oscilloscope and tape-off necessary for electric pusles monitoring are also shown (B).**

## 6.3.6 Protocols for CARS experiments and data analysis

- *CARS spectra acquisition*

CARS spectra are acquired immediately after the nanosecond pulsed electric fields exposure. Protocol for spectra acquisition has the following scheme (Figure 6.2, A). First the samples were pulsed, second the laser beams were aligned and finally the spectra acquisition started. Spectra were collected in the range from 2850 to 3480 $cm^{-1}$ and 146 images were taken at equally spaced wavelengths, each image being the accumulation of 75 laser shots. To allow precise focusing of the laser beams on the $CaF_2$ substrate, where liposomes were placed, polystyrene bids were used as references. Particular attention was paid to collimate the lasers out of the bids, which only act as spatial reference due to their dimension (10 μm), visible under classical optical microscopy. However, these bids show a very well know CARS signature, which enable their discrimination in the acquired CARS spectra.

- *Real-time follow-ups of selected wavelengths*

The perfect synchronization of the laser beams and electric pulses is achieved by a DG (DG 545, Princeton instruments). In this set of experiments, the Stokes beam is fixed at specific wavelengths retrieved from the analyses of the spectra previously described and acquired. Investigated wavelengths are representative of the "C-H" bounds (head group and tails) of the interfacial water and of the interstitial ones. The synchronization of the optical pulses with the electric one is reported into the scheme of Figure 6.2 (B). The Pump and Stokes arrive exactly during the final part of the electric pulse, precisely at 6 ns from its beginning. In this way, the CARS image is formed exactly at the end of the electric pulse delivery corresponding also to the end of the optical pulses lasting 4 ns. Each image is accumulated 40 times and images are acquired for 14 consecutive minutes. The electric signal is off for the first 4 min, then the pulses start for a total duration of 6 min. The further 4 min are recorded to observe processes of eventual liposomes changes, after the end of the electric pulse delivery. The scheme of the temporal observation of the CARS signal is reported in Figure 6.2 (B). The fact that the images are acquired immediately after the electric pulse

exposure is completely novel. No experimental data exist with such time resolution (ns), making our analysis on the water/lipid role into permeabilization processes extremely interesting and unique.

- *CARS signals treatment procedures*

Post-acquisition treatment was conducted using MATLAB® (R2016a, The MathWorks). First, elimination of several electronic and optical noises contributions was performed by subtracting the images recorded with and without laser illumination. The collected data provided a hyperspectral image of the sample plane.

Each spectrum is built averaging a specific region of interest (ROI) of dimension of 10 x 10 pixel to assure that a sufficient number of liposomes are included in all the retrieved spectra. Then, for each spectrum, the averaging of at least three independent experiments was performed. Smoother spectrum was obtained by moving average filtering on a window of three sample at the expense of lowering the spectral resolution to 2.7 $cm^{-1}$. The spectrum intensity was then corrected for the Stokes laser energy curve. Similar analysis were employed for real-time CARS acquisition, using different number of images and accumulation of laser shots as already reported in previous sub-section. In order to compare spectra of exposed and sham exposed liposomes suspensions, belonging to different experiments, it was also necessary to standardize each spectrum. In particular, the standardization process modifies signals to obtain curves with null mean and unitary standard deviation, a technique usually employed in Raman spectroscopy.

With the aim to quantify the degree of similarity between the various spectra, constructed from each ROI of the image, the Pearson correlation coefficient, r, was calculated using MATLAB®. Indeed, the square value "$r^2$" quantifies the proportion of change of the recorded spectra. The coefficient "$r^2$" enables to evaluate the reliability of the measured spectra to describe the various experimental data retrieved from the hyperspectral image. Since the value of "r" is independent on the relative amplitude of the two correlated spectra, the spatial inhomogeneities of the signal, due to the illumination geometry, can be

overcome. The resulting correlation image, drawn from the calculation of these coefficients, provided us with an accurate spatial mapping of the multiple spectral features contained in one spectrum.

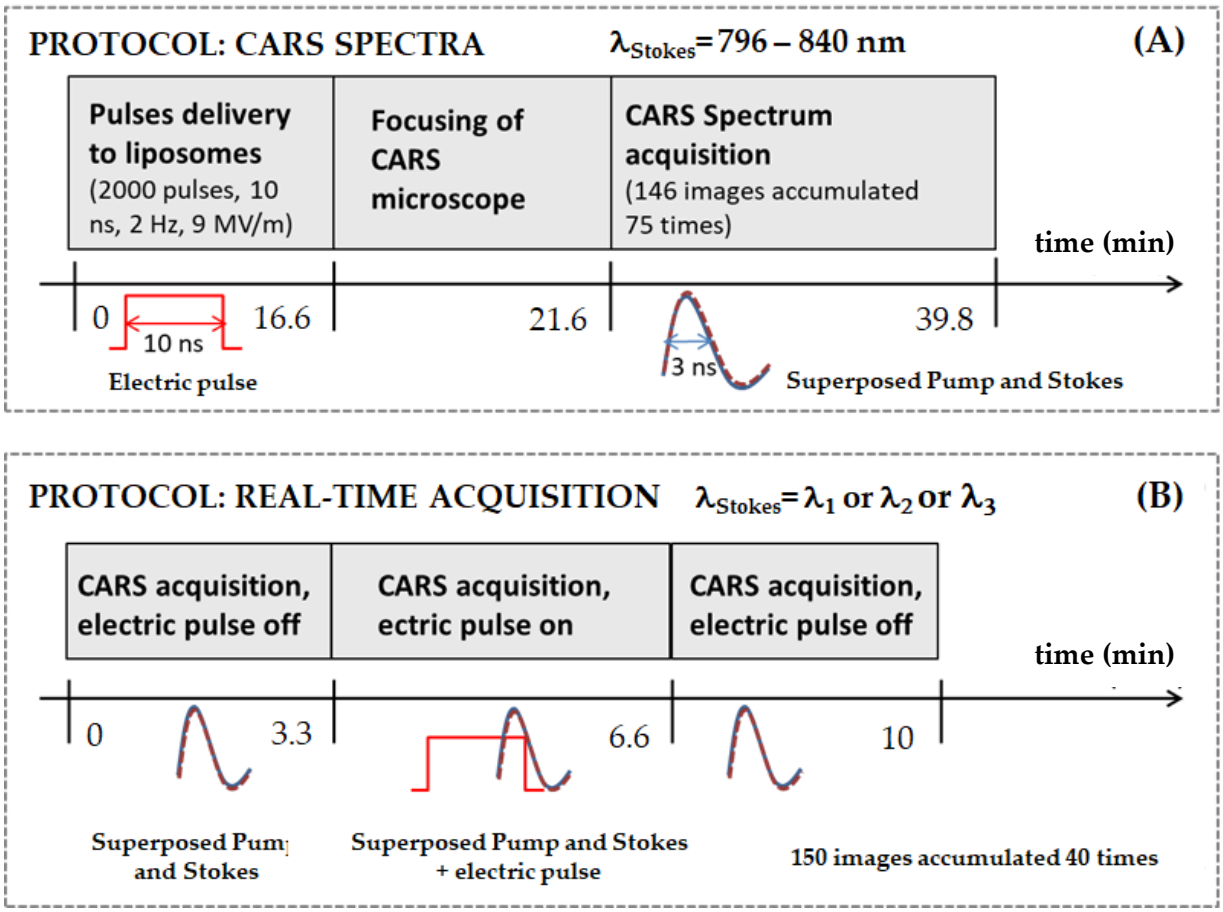


**Figure 6.2. Scheme of CARS spectra acquisition (A). Scheme of protocol employed for real-time acquisition of CARS signature (B).**

## 6.4 Results

### 6.4.1 CARS spectra of unexposed and exposed liposomes

In Figure 6.3 (A) CARS average spectra of the sham exposed and exposed samples are presented. These data are the average over five spectra (10 x 10 ROI), acquired in three

independent experiments. Standard deviations are also reported. The graph demonstrates a clear increase of the interstitial water band after the pulse delivery with peak at 3345 $cm^{-1}$. The interfacial water band seems only slightly modified and the observed increase resulted not statistically significant. Variations in the lower vibrational band, in the range between 2900 and 3100 $cm^{-1}$, are also negligible and no significant differences, between sham and pulsed samples, can be observed at 3033 $cm^{-1}$, corresponding to the vibrational model of the choline head groups and at 3005 $cm^{-1}$ assigned to the symmetric "C-H" stretch vibration of lipid.

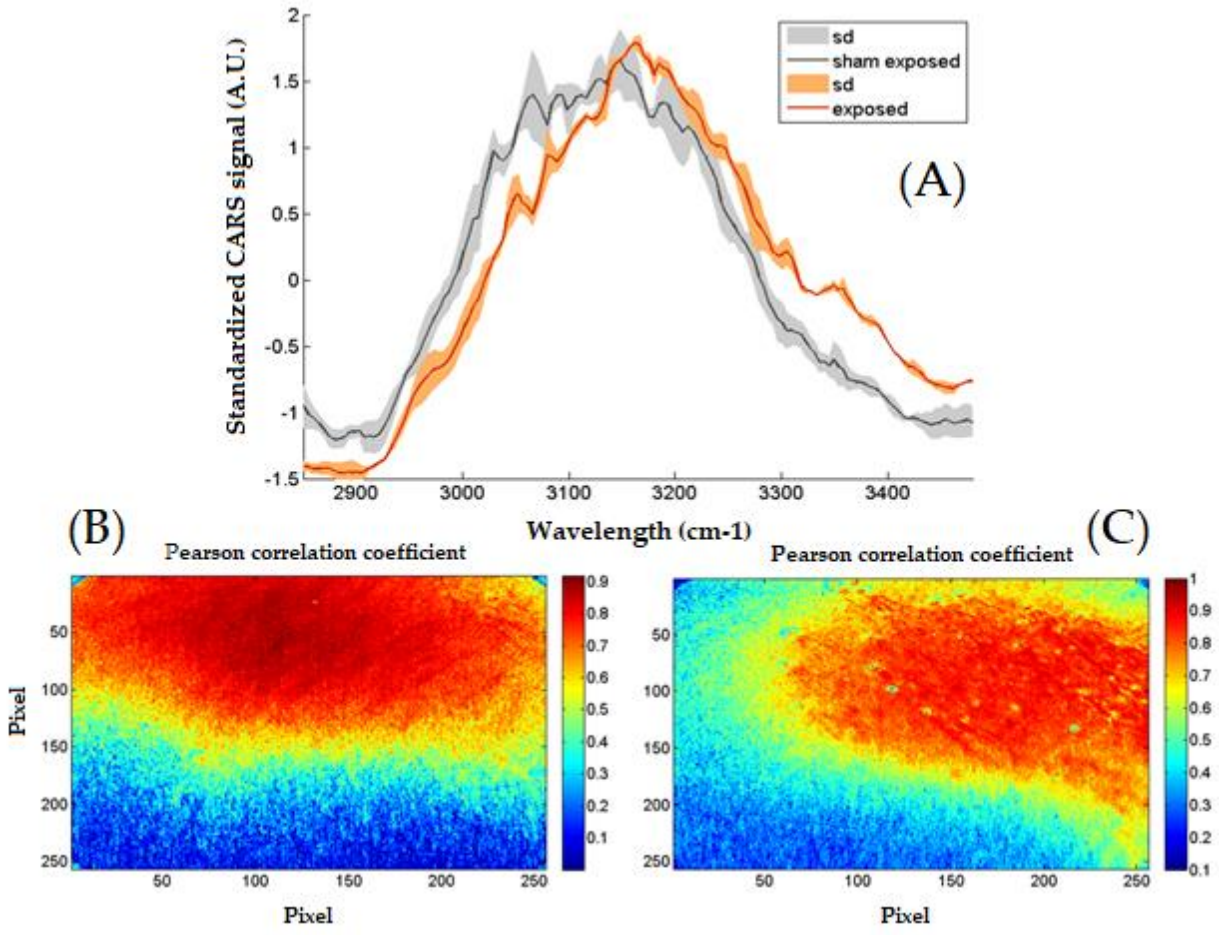


**Figure 6.3. Average spectrum with standard deviation (shadow) for exposed and sham exposed liposomes (A). In (B) and (C) Pearson correlation distributions for the grey spectrum and orange spectrum, respectively illustrated in (A).**

In these spectra, the contribution associated to the polystyrene bids is only slightly visible. They are used to determine the focal plane and their associated peak is visible at 3053 $cm^{-1}$. This is in complete agreement with the typical spectrum of single polystyrene bids. It is also worth to notice that, globally, the sham exposed and exposed spectra of liposomes suspensions differ from that of pure HEPES buffer, which presents a much more smoothed structure. At 3200 $cm^{-1}$ a single peak is present, associable to the bulk-like water that preponderantly constitutes the solution. In Figure 6.3 (B) and (C), the Pearson correlation coefficients for the sham and exposed samples are presented. These distributions show the similarity of the average spectra with respect to full-analysed area. Looking at the Figure 6.3 (B and C), it is clearly visible the zone where the CARS signal is higher, which corresponds to the area where the correlation coefficient is higher. This demonstrates that in the area of intense CARS signal the average spectra highly represents the vibrational behaviour of the whole sample, further supporting the robustness and repeatability of our data. Finally, in Figure 6.3 (C), the small green dots, within the red region, are associable to the bids presence, with a vibrational spectrum completely different (correlation coefficient lower than 0.3) from the liposomes suspension one.

We would like also to remember that the modifications in sham and exposed spectra (Figure 6.3) are observed within 20 min after the delivery of electric pulses; therefore, they can give information on the lipid/water structure in the long lasting phase of the electropulsation phenomenon.

### 6.4.2 Follow-up of single wavelengths of unexposed and exposed liposomes

From the analysis of previously presented CARS spectra, we selected three interesting wavelengths followed in real-time, as described in the paragraph 6.3.6. The selected wavelengths correspond to the vibrational mode of the choline head group at $\lambda_1$=3033 $cm^{-1}$. This wavelength was chosen for its interest in relation to our liposomal sample, but also because is characterized by a good intensity of the CARS signal. Indeed, decreasing the wavelengths, we assisted to a decrease of CARS signal intensity, due to the limited energy

associated to the Stokes beam, tunable only over a limited band. A second selected wavelength, $\lambda_2$=3145 $cm^{-1}$, is associated to the interfacial water peak (Figure 6.4, B). Finally, the third followed wavelength, $\lambda_3$=3345 $cm^{-1}$, is relative to the peak of the interstitial water vibrational band (Figure 6.4, C).

Figure 6.4 shows the trend of the average CARS signal over time (five acquisitions in three independent experiments) for these three wavelengths, before the exposure (3.3 min), during the exposure (lasting 3.3 min) and after the exposure (3.3 min). Standard deviations connected to the average CARS trends are also reported.

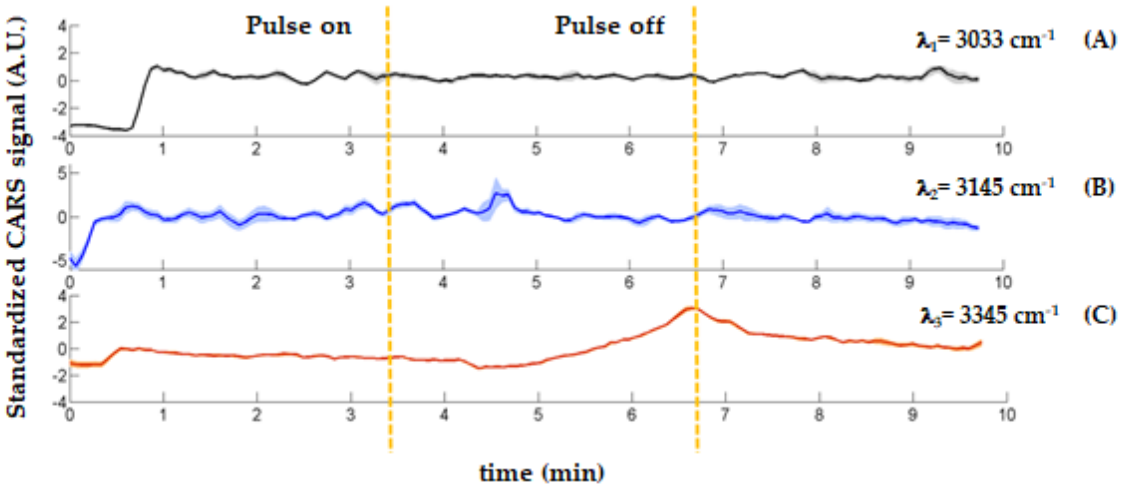


**Figure 6.4. Real-time CARS signal acquired at $\lambda_1$=3033 $cm^{-1}$ for the vibrational mode of the choline head group (A), at $\lambda_2$=3145 $cm^{-1}$ for the vibrational mode of the interfacial water (B) and at $\lambda_3$=3345 $cm^{-1}$ for the vibrational mode of the interstitial water (C). Shadow indicates standard deviation of the data.**

Interestingly, the CARS signal of the interstitial water starts to increase after the delivery of 400 electric pulses, meaning that hydrogen bonds are changing because of the external stimulation. Hydrogen bond modification leads to the creation of more isolated water molecules at the liposome interface, more strictly associated to the lipid head groups. The increase of the interstitial water continues up to the end of the pulse delivery, demonstrating that this vibrational mode modification is a result of the changes induced by the electric

stimulation. In concomitance to the beginning of the interstitial water increase, the average CARS trend, associated to the interfacial water, presents a peak. It can be due to some rearrangement of "O-H" bonds of water molecules, which seems to break their symmetry. This makes possible the formation of the isolated interstitial water molecules, which present more asymmetric "O-H" vibrational modes that are translated towards higher wavelengths.

No modifications are associated to the average CARS trend of the choline vibrational mode. This could be eventually linked to a lower detection ability of the system, at this lower wavelength, but nonetheless this result can indicate that the lipid head structure is unaltered during and after the electric pulse delivery. In Figure 6.5, the Pearson correlation coefficients for the three CARS trends at $\lambda_1$, $\lambda_2$ and $\lambda_3$ are reported.

These data demonstrate that, in the area of intense CARS signal for $\lambda_3$, the average CARS trend, over time, appropriately represents the vibrational behaviour of the whole sample, making our data on the increase of the interstitial water entirely robust. Pearson correlation coefficients are lower, but always above 0.5, for CARS trend associated to $\lambda_1$ and $\lambda_2$, probably due to a higher variability of the acquired signals.

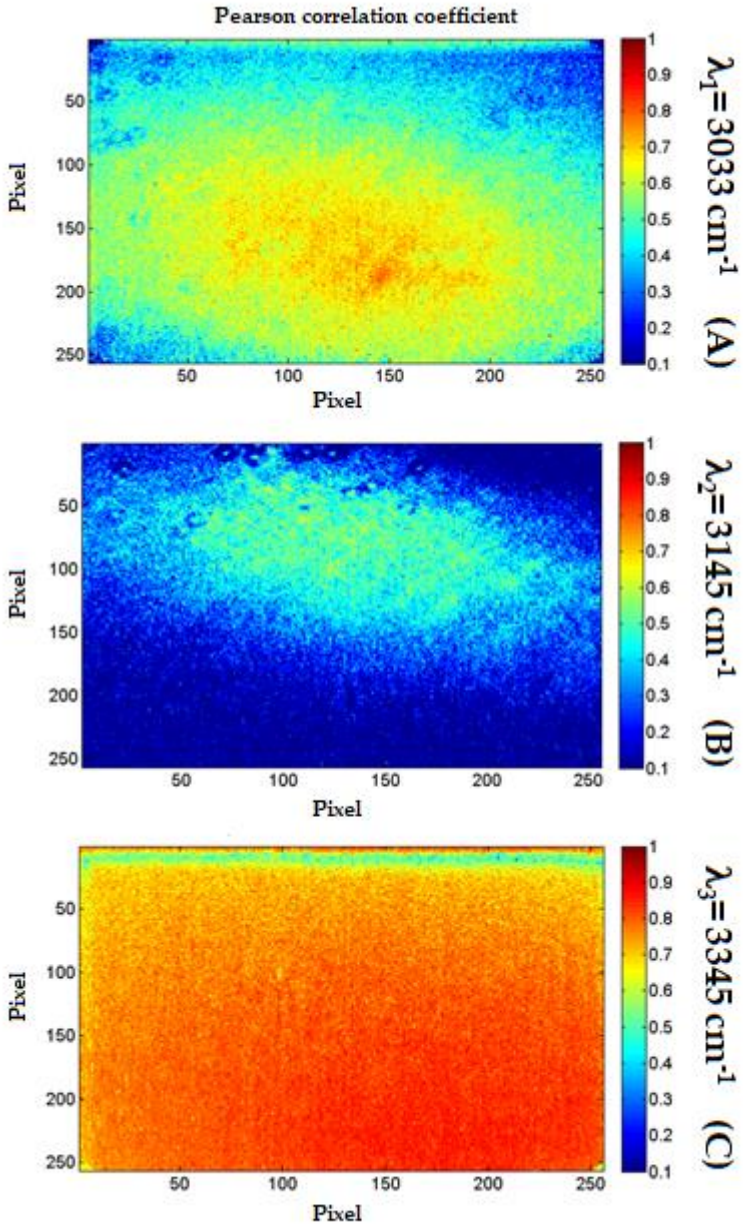


**Figure 6.5. Pearson correlation distribution for CARS signals acquired respectively at $\lambda_1$=3033 $cm^{-1}$ (A), at $\lambda_2$=3145 $cm^{-1}$ (B) and at $\lambda_3$=3345 $cm^{-1}$ (C).**

### 6.4.3 Assessment of liposomes permeabilization

Liposomes were prepared as a suitable test sample for CARS investigation on the role of water molecules in the electropulsation phenomenon. For this purpose, liposomes characterized by homogeneous size distribution and good stability over time were realized. The operating conditions adopted (see paragraph 6.3.2) allow lipids to arrange themselves

in homogeneous nanometer-sized vesicles. Egg PC liposomes obtained, after the extrusion of multilamellar vesicles through membranes of progressively lower mesh-size and purification by size exclusion chromatography (SEC), showed monomodal size distribution curves, with polydispersity index lower than 0.150, thus indicating that the distribution size of vesicles was homogeneous.

Furthermore, the amount of structured lipid was about 80%, and ζ–potential values were within the range from -7 to -6 mV, according to the zwitterionic nature of the phospholipid employed. No changes were observed in vesicles after storage at 4 °C, in the dark for 15 days. The amount of probe entrapped in the inner compartment of liposomes, expressed as volume of dye for mg of lipid, was μl 1.41±0.15/mg of structured Egg PC.

Before the application of the electric field, the thermal stability of any formulation was checked at 25.0±0.5 °C, in order to provide information about the temperature profile of solute leakage from L$\alpha$-Egg PC liposome membrane. This characterization is of paramount importance since the Egg PC vesicles can exist only in the disordered state at 25.0±0.5 °C, so they are more prone to a spontaneous leakage. Nevertheless, it was observed that, in conditions of null electric field at 25.0±0.5 °C, the extent of dye release is always <5%, despite the disordered-state membranes of lipid vesicles. Therefore, liposomes represent a suitable carrier model to put in evidence the electropermeabilization effect of the electric field on drug delivery. Immediately after the application of 2000 10 ns electric pulses, the release of 5-(6) CF was detected and evaluated, as a function of the stimulation. Figure 6.6 (A) displays the release behaviour of Egg PC liposomes, reporting the percentage of 5-(6) CF released after 20 min of continuous electric field application and of sham condition, respectively. According to the results, nanosecond electric pulses modify the membrane permeability, as indicated by the marker leakage, which reaches about 20%, respect to the sham exposed [5-(6) CF release <5%]. The increased permeability of the bilayer suggested to be related to the geometry of lipids, which, upon electric pulses, promotes the induction of local defects in the liposome bilayer, leading to dye release. Specifically, the persistent interposition of water molecules within the acyl chains of phospholipids is probably important in

modulating and controlling the membrane structure and its permeability. These data release strongly support the results of the interstitial water increase, observed in CARS spectra of exposed sample (Figure 6.3, A). Nevertheless, it is important to underline that the application of the electric pulses did not lead to the liposomes rupture, as demonstrated by the superposition of DLS curves before and after the electric treatment (see Figure 6.6, B).

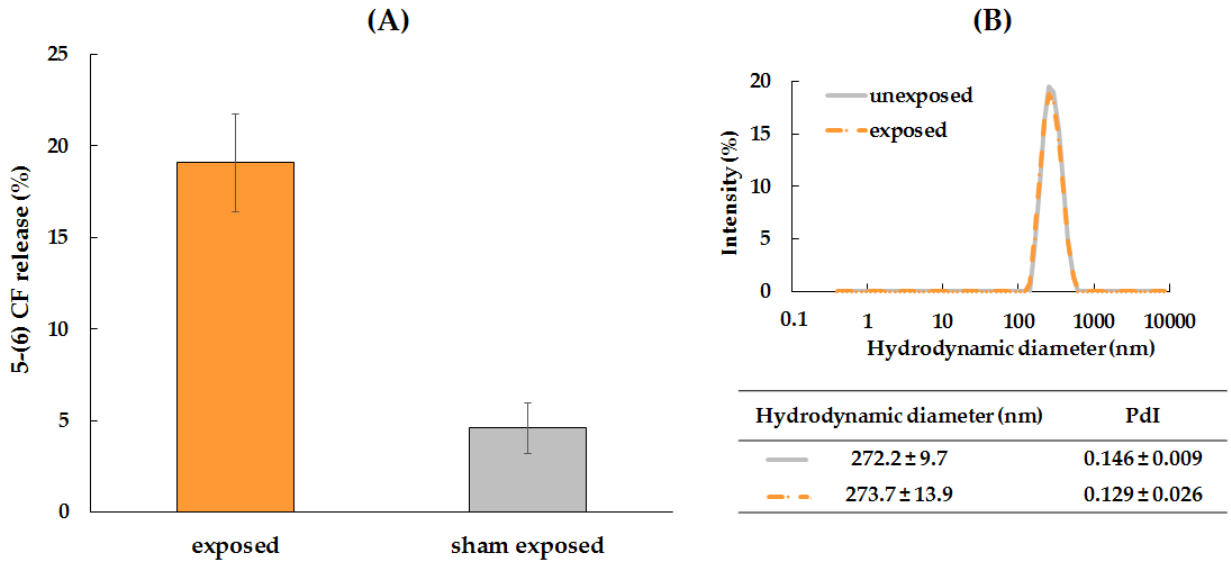


**Figure 6.6. Percentage of the 5-(6) CF release from Egg PC liposomes, under exposed and sham exposed conditions (A). In (B) are reported: the DLS graph with the size curves of Egg PC liposomes before and after the electric stimulation; the table with the relative hydrodynamic diameter (Z-average) and distribution (PdI) of unexposed and exposed samples.**

## 6.5 Discussion

In this work, we experimentally followed, using CARS signatures, chemical modifications in the water vibrational band, occurring during the electropulsation of liposomeS suspensions. The alteration in the CARS interstitial water signature, e.g. the presence of single water molecules more associated to lipid heads, is observed for the first time at the instant of each pulse delivery. These results can be compared directly with MD simulations predicting, on a comparable time scale, water disorganization and appearance of a less packed lipid bilayers [7]. From the graph of Figure 6.4 (C), it is further possible to define the

minimal number of pulses (here equal to 600) necessary to determine the increase of the interstitial water, responsible for the initiation of water defects, which lead to pore formation. The decrease, but not the return to the initial basal level, after pulses, of these interstitial water signatures (Figure 6.4, C) can be interpreted as a long term modification of the hydration state of the bilayer (with a time constant of obtained applying an exponential decay to fit the experimental data of Figure 6.4, C). The maintenance of the interstitial water presence long, after the exposure, is similarly evidenced in the acquired CARS spectra of the exposed liposomal suspensions (Figure 6.3, A). Further, we monitored the 5-(6) CF release up to 3 h after the pulses, in order to understand if the insertion of water molecules in the lipid bilayer, hypothesized from the analysis of CARS spectra and real-time acquisitions, is also permanent after the pulses delivery. Figure 6.7 shows at least a nearly constant release of the probe (up to 27% at 3 h), in comparison with the sham exposed sample.

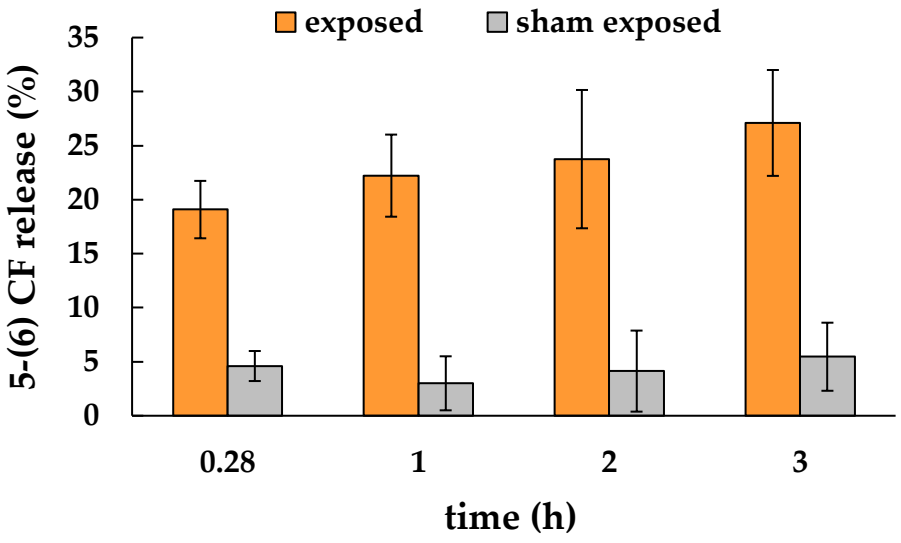


**Figure 6.7. Monitoring of the 5-(6) CF release (%), from exposed and sham exposed Egg PC liposomes, up to 3 h after the electric treatment. At 0.28 h is reported, as in Figure 6.6, the percentage of 5-(6) CF release immediately after the application of 2000 10 ns electric pulses.**

This different behaviour of the treated samples is maintained and even increased up to 24 h, with a 5-(6) CF release of 56% for the exposed sample versus a 10% for the unexposed one. In this last case, the amount of dye recorded is a consequence of the natural leakage of the Egg PC vesicles, thermostatically stored at 25 °C.

The proposed data, as a whole, lead to hypothesize a fundamental role of the interstitial water in the electroporation process as schematically sketched in Figure 6.8.

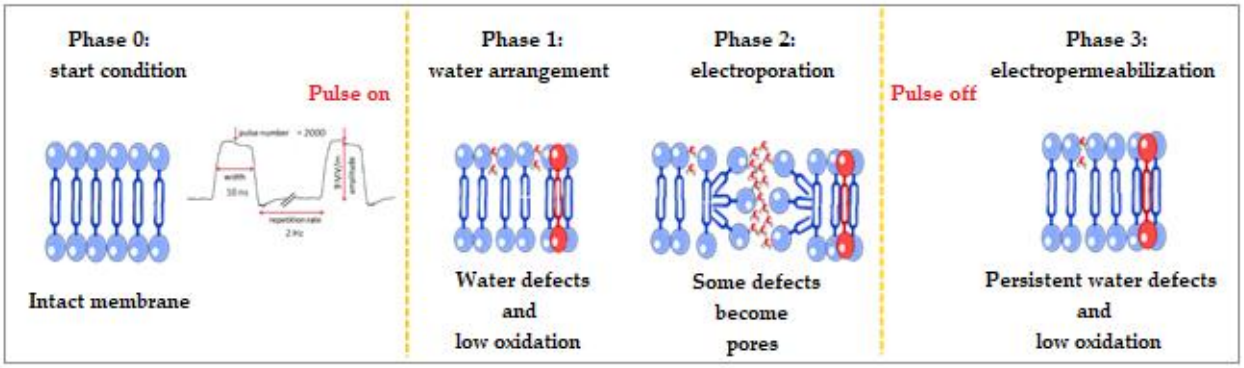


**Figure 6.8. Schematic vision of liposomal membrane organization before and after the exposure to the electric field. Blue symbols stand for phospholipids of bilayer, whereas red ones symbolize the oxidized lipids that can be occured during the pulses delivery. In addition is illustrated the possible insertion of water molecules within acyl chains, which leads to pore formation as predicted by MD simulations. Persistent water defectes justify the long term permeabilization.**

An intact phospholipid bilayer, during the application of pulses, is subject to a first phase of rearrangements, where water network reorganizes itself. A shift of the "O-H" stretch modes of water, towards the asymmetric region (at higher wavelengths over 3300 $cm^{-1}$), is observed (Figure 6.4), weakening the strength of the hydrogen in the network. The plausible creation of single water molecules leads to the appearance of the so called water defects, as predicted by MD simulations [7]. In this first phase (Figure 6.8), it appears also possible, as suggested in [7], the oxidation of phospholipids proportionally to the delivered electric pulses. In our experiments, very short pulses were used, each lasting 10 ns. At a certain

point, after the application of the pulses, the created water defects become hydrophilic pores and an eventual increase of lipid oxidation can concomitantly occurs [34, 35].

To verify the level of lipid oxidation in the bilayer, which can not be directly observed from the acquired CARS signals, mass spectrometry analysis on exposed and sham exposed liposomal suspensions was carried out. Lipid oxidation, detected from mass spectroscopy of our samples and expressed as the ratio between exposed and sham exposed sample oxidation, is around 1.5. These data evidence a low oxidation of lipid bilayer, which clearly maintains its structure, as also demonstrated by CARS data, where no alterations in the choline vibration mode were detected (Figure 6.3 and 6.4). Therefore, for this short nanosecond pulses, the preponderant phenomenon driving the electropermeabilization phase, as shown in Figure 6.8, after the end of pulses delivery, is the existence of permanent water defects, experimentally observed from CARS investigation and further supported by the long persistence 5-(6) CF release. After the end of electric pulses application, the phospholipid bilayer becomes a less packed structure with a higher hydration degree. This phenomenon of permanent water defects, created by the electric field application, is well observable in our synthetic vesicles, as they do not present any type of recovery process that whereas occurring in eukaryotic cells, after a certain time. Molecular dynamics simulations of lipid bilayers demonstrate the formation of nanometer-sized aqueous pores, only during pulses application. The kinetics of opening and closure of these pores appear to be in the order of nanoseconds [7]; here we established an experimental proof of water initiating pore formation and its role at long term. Some recent studies, indeed, hypothesize that water dipole reorientation, leading to the intrusion of the water molecules into the bilayer, determines a general disorganization of the bilayer, with various water molecules stacked up in the membrane interior. This ultimately generates a less packed phospholipid distribution [8, 36, 37]. High level of membrane disorder was also experimentally observed in mammalian cells after microsecond pulses application [38]. The mentioned membrane disorganization was, however, not correlated with loss of cell viability.

## 6.6 Conclusions and perspectives

In summary, CARS, employing nanosecond lasers pulses and the properties of our wide field arrangement microscope and its intrinsic ability to sense complex interferences, provided us with an appropriate diagnostic tool. Thanks to this set-up, we were able to observe the spectrum arising from the interfacial and the interstitial water.

The spectroscopic study of liposomes was undertaken in the spectral domain of water bands. The wide field geometry, presented in this paper, enabled us to obtain CARS images and spectra of water in the absence of the non-resonant contribution, that originates far from the object surface. Indeed, the colinearity of the illumination scheme to the collection direction, along with the scattering at low angles were able to generate strong enough CARS signal of the thin membranes. This geometry was applied to optically thin objects, like liposomes, with the aim of studying the chemical phenomena induced by nanosecond electric pulses. We observed that the interfacial water is present around liposomes. It dominates the CARS profile at about 3100-3200 $cm^{-1}$. Another set of "O-H" vibrations was observed at a higher Raman shift (at 3345-3385 $cm^{-1}$). Images, drawn from correlation procedures, were used as a complementary tool for this assignment. After the delivery of the electric pulses, the interstitial water (which corresponds to the water molecules located in the membrane at the level of the deepest parts of the phospholipid heads) is much more affected than the interfacial water (the water located at the surface of the membrane). All these results bring new information about the electropermeabilized state of the membrane after the pulses delivery, characterized by a facilitated transport of hydrophilic molecules across the membrane itself. Indeed, our observations reveal not only that the membrane is more permeable to the hydrophilic molecules, because of the presence of oxidized lipids, but moreover that the barrier constituted by the water, organized at the membrane surface, is broken. In conclusion, our new CARS data, collected by means of an original geometry of the lasers illumination in a wide field CARS microscope, add new experimental insight into the understanding of the electropermeabilization phenomenon. The follow-ups of the interfacial and the interstitial water changes of liposomes, during the electric pulses

delivery, allow to explain both the increase in the short term and in the long-term membrane permeability, as driven by water molecules, which alternate the membrane hydration state. This phenomenon is clearly visible in liposomes as irreversible, due to the absence of membrane repairing mechanisms. The liposomes permeabilization was also confirmed by 5-(6) CF release up to 24 h after the exposure, evidencing the interest of our results not only for the basic understanding of the electroporation mechanism, but also for liposomes possible exploitation in drug delivery, as smart carriers triggerable by electric pulses.

## 6.7 Supplementary Information (S.I.)

In Figure 6.1 S.I. is reported the calibration curve used to establish the relationship between fluorescent intensity and concentration of 5-(6) CF. The fluorescence intensity of 5-(6) CF was found linear in the range of $10^{-8}$–$10^{-6}$ mol/l, with a correlation coefficient of 0.999.

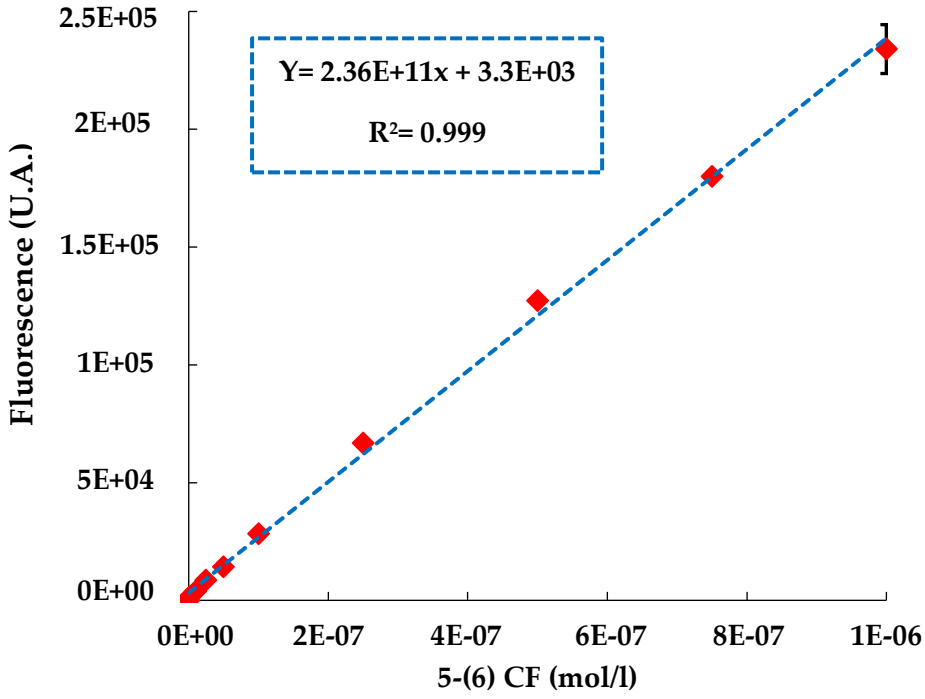


**Figure 6.1 S.I. Calibration curve of 5-(6) CF in HEPES buffer solution, with the respective linear regression.**

Through the calibration line we were also able to quantify the μl of 5-(6) CF trapped in the aqueous core of liposomes for mg of lipid. Specifically, a template was designed to calculate the molarity of the marker for different lipid concentrations, respectively before and after the complete destruction of the vesicles with 30% w/v of Triton X-100. An example of the determination is reported hereafter in Figure 6.2 S.I.

| Column | | | | | Row |
|---|---|---|---|---|---|
| A | B | C | D | E | 1 |
| Calibration curve | | | | | 2 |
| Fluorescence (U.A.)= 2.36E+11*[(5-(6) CF mol/l]+3.30E+03 | | | | | 3 |
| Egg PC (mg/ml) in liposomes | 0.9 | | | | 4 |
| 5-(6) CF (mol/l) for liposomes preparation | 0.02 | | | | 5 |
| | | | | | 6 |
| | 5-(6) CF fluorescence (U.A.) | | 5-(6) CF (mol/l) | | 7 |
| Egg PC (mg/l) tested | vesicles | destroyed vesicles | vesicles | destroyed vesicles | 8 |
| 0 | 0 | 0 | 0 | 0 | 9 |
| 4.5 | 2.29E+04 | 5.44E+04 | 9.71E-08 | 2.17E-07 | 10 |
| 8.9 | 4.37E+04 | 1.06E+05 | 1.71E-07 | 4.37E-07 | 11 |
| 11.1 | 5.42E+04 | 1.36E+05 | 2.16E-07 | 5.64E-07 | 12 |
| 13.4 | 6.81E+04 | 1.59E+05 | 2.74E-07 | 6.59E-06 | 13 |
| | | | | | 14 |
| mol 5-(6) CF / mg Egg PC destroyed vesicles | 4.97E-07 | REGR.LIN(E9:E13;A9:A13;FALSE) | | | 15 |
| mol 5-(6) CF/mg Egg PC vesicles | 2.00E-08 | REGR.LIN(D9:D13;A9:A13;FALSE) | | | 16 |
| | | | | | 17 |
| mol 5-(6) CF entrapped /mg Egg PC | | | 2.97E-08 | B15-B16 | 18 |
| l 5-(6) CF entrapped /mg Egg PC | | | 1.48E-06 | D19*B5 | 19 |
| μl 5-(6) CF entrapped /mg Egg PC | | | 1.48 | D20*1E+06 | 20 |

**Figure 6.2 S.I. Template used to calculate the capture 5-(6) CF volume in the aqueous core of liposomes prepared in HEPES, by means the linear regression method.**

## 6.8 References

[1] Breton, M.; Mir, L.M. *Microsecond and nanosecond electric pulses in cancer treatments*. Bioelectromagnetics. 2012, 33(2), 106-123.

[2] Gothelf, A.; Mir, L.M.; Gehl, J. *Electrochemotherapy: results of cancer treatment using enhanced delivery of bleomycin by electroporation*. Cancer Treat Rev. 2003, 29(5), 371-387.

[3] Casciola, M.; Xiao, S.; Pakhomov, A.G. *Damage-free peripheral nerve stimulation by 12-ns pulsed electric field*. Scientific Reports. 2017, 7, article number: 10453.

[4] Nuccitelli, R.; Tran, K.; Lui, K.; Huynh, J.; Athos, B.; Kreis, M.; Nuccitelli, P.; De Fabo, E.C. *Non-thermal nanoelectroablation of UV-induced murine melanomas stimulates an immune response*. Pigment Cell Melanoma Res. 2012, 25(5), 618-629.

[5] Sözer, E.B.; Levine, Z.A.; Vernier, P.T. *Quantitative Limits on Small Molecule Transport via the Electropermeome — Measuring and Modeling Single Nanosecond Perturbations*. Scientific Reports. 2017, 7, article number: 57.

[6] Breton, M.; Mir, L.M. *Investigation of the chemical mechanisms involved in the electropulsation of membranes at the molecular level*. Bioelectrochemistry. 2018, 119, 76-83.

[7] Rems, L.; Viano, M., Kasimova, M.A.; Miklavčič, D.; Tarek, M. *The contribution of lipid peroxidation to membrane permeability in electropermeabilization: A molecular dynamics study*. Bioelectrochemistry. 2018, 125, 46-57.

[8] Tokman, M.; Lee, J.H.J.; Levine, Z.A.; Ho, M.C.; Colvin, M.E.; Vernier, P.T. *Electric Field-Driven Water Dipoles: Nanoscale Architecture of Electroporation*. PLoS One. 2013, 8(4), e61111.

[9] Volkmer, A. *Vibrational imaging and microspectroscopies based on coherent anti-Stokes Raman scattering microscopy*. Journal of Physics D: Applied Physics. 2005, 38, 59-81.

[10] Evans, C.L.; Potma, E.O.; Puoris'haag, M.; Côté, D.; Lin, C.P.; Xie, X.S. *Chemical imaging of tissue in vivo with video-rate coherent anti-Stokes Raman scattering microscopy*. Proceedings of the National Academy of Sciences of the United States of America. 2005, 102(46), 16807-16812.

[11] Evans, C.L.; Xu, X.; Kesari, S.; Xie, X.S.; Wong, S.T.C.; Young, G.S. *Chemically-selective imaging of brain structures with CARS microscopy*. Optics Express. 2007, 15(19), 12076-12087.

[12] Toytman, I.; Simanovskii, D.; Palanker, D. *On illumination schemes for wide-field CARS microscopy*. Optics Express. 2009, 17(9), 7339-7347.

[13] Toytman, I.; Cohn, K.; Smith, T.; Simanovskii, D.; Palanker, D. *Wide-field coherent anti-Stokes Raman scattering microscopy with non-phase-matching illumination*. Optics Letters. 2007, 32(13), 1941-1943.

[14] Silve, A.; Dorval, N.; Schmid, T.; Mir, L.M.; Attal-Trétout, B. *A wide-field arrangement for singleshot CARS imaging of living cells.* J. Raman Spectrosc. 2012, 43, 644-650.

[15] Scatena, L.F; Brown, M.G.; Richmond, G.L. *Water at hydrophobic surfaces: weak hydrogen bonding and strong orientation effects*. Science. 2001, 292(5518), 908-912.

[16] Potma, E.O.; and Xie, X.S. *Direct visualization of lipid phase segregation in single lipid bilayers with coherent anti-Stokes Raman scattering microscopy*. ChemPhysChem. 2005, 6(1), 77-79.

[17] Nagata, Y.; Mukamel, S. *Vibrational Sum-Frequency Generation Spectroscopy at the Water/Lipid Interface: Molecular Dynamics Simulation Study*. J. Am. Chem. Soc. 2010, 132 (18), 6434–6442.

[18] Li, L.; Wang, H.; Cheng, J.X. *Quantitative Coherent Anti-Stokes Raman Scattering Imaging of Lipid Distribution in Coexisting Domains*. Biophysical Journal. 2005, 89(5), 3480-3490.

[19] Zumbusch, A.; Langbein, W.; Borri, P. *Nonlinear vibrational microscopy applied to lipid biology*. Progress in Physics research. 2013, 52(4), 615-632.

[20] Cheng, J.X.; Pautot, S.; Weitz, D.A.; Xie, X.S. *Ordering of water molecules between phospholipid bilayers visualized by coherent anti-Stokes Raman scattering microscopy*. PNAS. 2003, 100(17), 9826-9830.

[21] Wurpel, G.W.H.; Müller, M. *Water confined by lipid bilayers: A multiplex CARS study*. Chem. Phys. Letters. 2006, 425, 336-341.

[22] Durickovic, I.; Claverie, R.; Bourson, P.; Marchetti, M.; Chassot, J.M.; Fontana, M.D. *Water–ice phase transition probed by Raman spectroscopy.* J. Raman Spectrosc. 2011, 42(6), 1408-1412.

[23] Gruenbaum, S.M.; Skinner, J.L. *Vibrational spectroscopy of water in hydrated lipid multi-bilayers. I. Infrared spectra and ultrafast pump-probe observable.* The Journal of Chem. Phys. 2011, 135(7), 075101.

[24] Denzi, A.; Della Valle, E.; Apollonio, F.; Breton, M.; Mir, L.M.; Liberti, M. *Exploring the Applicability of Nano-Poration for Remote Control in Smart Drug Delivery Systems*. J Membr Biol. 2017, 250(1), 31-40.

[25] Yoshida, Y.; Furuya, E.; Tagawa, K. *Direct Colorimetric Method for the Determination of Phospholipids with Dithiocyanatoiron Reagent*. Journal of Biochemistry. 1980, 88, 463-468.

[26] Merla, C.; Liberti, M.; Marracino, P., Muscat, A.; Azan, A.; Apollonio, F.; Mir, L.M. *A wide-band bio-chip for real-time optical detection of bioelectromagnetic interactions with cells*. Scientific Reports. 2018, 8, article number: 5044.

[27] Paffi, A.; Apollonio, F.; Lovisolo, G.A.; Marino, C. Pinto, R.; Repacholi, M.; Liberti, M. *Considerations for developing an RF exposure system: a review for in vitro biological experiments*. IEEE Transactions on Microwave Theory and Techniques. 2010, 58, 2702-2714

[28] Casciola, M.; Liberti ,M.; Denzi, A.; Paffi, A.; Apollonio, F.; Casciola, M.; Denzi, A.; Merla, C. *A computational design of a versatile microchamber for in vitro nanosecond pulsed electric fields experiments*. Integration, the VLSI Journal in press. 2017, 58, 446-453.

[29] Merla, C.; Amari, S.E.; Kenaan, M.; Liberti, M.; Apollonio, F.; Arnaud, D.; Couderc, V.; Leveque, P. *A 10-Ω High-Voltage Nanosecond Pulse Generator*. IEEE Transactions on Microwave Theory and Techniques. 2010, 58(12), 4079-4085.

[30] Kenaan, M.; El Amari, S.; Silve, A.; Merla, C.; Mir, L.M.; Couderc, V.; Arnaud-Cormos, D.; Leveque, P. *Characterization of a 50- Ω exposure setup for high-voltage nanosecond pulsed electric field bioexperiments.* IEEE Trans Biomed Eng. 2011, 58(1), 207-214.

[31] Silve, A.; Vezinet, R. ; Mir, L.M. *Nanosecond-duration electric pulse delivery in vitro and in vivo: experimental considerations*. IEEE Transactions on Instrumentation and Measurement. 2012, 61(7), 1945-1954.

[32] Eftekhari-Bafrooei, A.; Borguet, E. *Effect of Surface Charge on the Vibrational Dynamics of Interfacial Water*. Journal of the American Chemical Society. 2009, 131(34), 12034-12035.

[33] Eftekhari-Bafrooei, A.; Borguet, E. *Effect of Hydrogen-Bond Strength on the Vibrational Relaxation of Interfacial Water.* Journal of the American Chemical Society. 2010, 132(11), 3756-3761.

[34] Azan, A.; Untereiner, V.; Gobinet, C.; Sockalingum, G.D., Breton, M.; Piot, O.; Mir, L.M. *Demonstration of the Protein Involvement in Cell Electropermeabilization using Confocal Raman Microspectroscopy*. Scientific Reports. 2017, 7, article number: 40448.

[35] Azan, A.; Untereiner, V.; Descamps, L.; Merla, C.; Gobinet, C.; Breton, M.; Piot, O.; Mir, L.M. *Comprehensive Characterization of the Interaction between Pulsed Electric Fields and Live Cells by Confocal Raman Microspectroscopy*. Anal Chem. 2017, 89(20), 10790-10797.

[36] Vernier, P.T.; Levine, Z.A.; Ho, M.C.; Xiao, S.; Semenov, I.; Pakhomov, A.G. *Picosecond and Terahertz Perturbation of Interfacial Water and Electropermeabilization of Biological Membranes*. The Journal of Membrane Biology. 2015, 248(5), 837–847.

[37] Levine, Z.A.; Vernier, P.T. *Life cycle of an electropore: field-dependent and field-independent steps in pore creation and annihilation*. J Membr Biol. 2010, 236(1), 27-36.

[38] Escoffre, J.M.; Bellard, E.; Faurie, C.; Sébaï, S.C.; Golzio, M.; Teissié, J.; Rols, M.P. *Membrane disorder and phospholipid scrambling in electropermeabilized and viable cells*. Biochimica et Biophysica Acta (BBA) - Biomembranes. 2014, 1838(7), 1701-1709.

# Chapter 7

# Gelation of liposomal internal core: a new method of vesicular stabilization and modified drug delivery

Stefania Petralito[1], Patrizia Paolicelli[1], Martina Nardoni[1], Michela Relucenti[2], Settimio Pacelli[3], Laura Di Muzio[1], Maria Antonietta Casadei[1]

[1] *Department of Drug Chemistry and Technologies, "Sapienza" University of Rome, Piazzale Aldo Moro 5, 00185 Rome, Italy*

[2] *BioIntel Research Laboratory, Department of Chemical and Petroleum Engineering, "School of Engineering" University of Kansas, Lawrence, USA*

[3] *Department of Anatomical, Histological, Forensic Medicine and Orthopedic Science, "Sapienza" University of Rome, Piazzale Aldo Moro 5, 00185 Rome, Italy*

**Submitted**

***7.1 Abstract.*** *Since the advent of nanotechnology revolutionized drug delivery in terms of improving drug efficacy and safety, both polymer-based and lipid-based drug-loaded nanocarriers demonstrated clinical benefit to date. However, to address the multifaceted drug delivery challenges ahead and further expand the spectrum of therapeutic applications, hybrid lipid-polymer nanocomposites were designed to merge the beneficial features of both polymeric drug delivery systems and liposomal technology in a single nanocarrier. Within this scenario, the present project aims to develop novel hybrid vesicles following the recent strategy of stabilizing liposomes by working on their internal structure. Specifically, polyethylene glycol-dimethacrylate (PEG-DMA), with different molecular weight (MW 750 and MW 4000) and degree of hydrophilicity, trapped within unilamellar liposomes of hydrogenated soybean phosphatidylcholine/cholesterol (HSPC/Chol), was photopolymerized by UV irradiation, in order to transform the aqueous inner core of liposomes into a soft and elastic hydrogel. After appropriate optimization of the preparation and gelation procedures of these new Gel-in-Liposomes (GiL) systems, the primary objective of this work was to analyze the effect of the molecular weight of PEG-DMA on the principal properties of the hybrid nanosystems. Indeed, varying the molecular weight of PEG-DMA also its hydrophilic/lipophilic balance is modified; for this reason, a various localization of the polymer within the structure of liposomes and a different interaction with their membrane may be expected. Therefore, the effect of the presence of the polymer and the length of its oxyethylene chain were carefully studied in order to have insight on the stability, loading efficiency and permeability of GiL respect to conventional vesicles. Finally, preliminary cytotoxicity studies were performed to evaluate the biological safety of these novel gelled core liposomes and their suitability as innovative material for potential applications in the field of drug delivery.*

***Keywords:*** *hydrogel; hybrid lipid-polymer nanocarrier; gelled core liposomes; stability; different molecular weight; membrane properties; drug delivery systems.*

## 7.2 Introduction

In the field of nanomedicine, phospholipid-based systems and mainly liposomes are certainly the most investigated platform for drug delivery, due to their wide range of recognized advantages including good biocompatibility, good biodegradability, low antigenicity and the unique ability to entrap both hydrophilic and hydrophobic compound. For these features, in the 1970s liposomes were proposed as interesting and appealing drug delivery vehicles [1, 2]. Despite all these advantages, pre-clinical and clinical studies, carried out over the years, highlighted that liposomal delivery systems also have some drawbacks. Physical and chemical stability issues are one of the main limits in the pharmaceutical use of these self-assembled lipid vesicles; in particular, liposomes may suffer from poor mechanical properties depending on susceptibility of the phospholipid composition to chemical and physical injury, frequently resulting in unwanted burst release of the carried therapeutic molecule. Even if these issues were not forbidden the clinical use of liposomal formulations of drugs, it is evident that their overcoming should further empowered application of liposomes in the pharmaceutical field.

For this reason, various strategies were developed in order to obtain a more efficient lipid-based carrier with improved drug delivery performance. One of the most applied approaches to overcome the still unsolved drawbacks consists in the combination of different biomaterials within the same system. Hybrid phospholipid vesicles, resulting from the combined self-assembly of both polymers and lipids, attracted particular interest over the last five years and their appealing features were largely documented in papers and patents literature [3-19]. Such assemblies may be viewed as advanced vesicular drug carriers, which join together peculiarity of both polymeric drug delivery systems and liposomes in a single nanocarrier.

So far, following this concept, versatility in liposomal surface functionalization to attach different molecules allowed to change the surface properties of the bilayer.

In particular, the bilayer coating, with water-soluble polymers, permits to increase the vesicle stabilization against chemical and mechanical stresses. The rationale behind polymer

coating of liposomes is to increase their physical resistance. One of the first successful demonstrations of the use of polymers for liposome stabilization was reported by Papahadjopoulos and co-workers [20], who incorporated glycosylated phospholipids to increase blood circulation time of liposomes. Building on this success, Klibanov and coworkers [21] grafted polyethylene glycol (PEG) polymers on the surfaces of liposomes to obtain the so called "Stealth Liposomes", resulting in less macrophage cellular uptake and therefore prolonged blood circulation times.

More recently, it was shown that the stability of liposomes can be enhanced working on the internal structure of liposomes, with the aim to convert the aqueous inner core into a soft and elastic hydrogel [22]. In this perspective, a lot of research was focused on the gelation of the precursor component entrapped in the vesicle core.

In the pioneering works on hydrogel-liposome assemblies, phospholipid vesicles were employed only as a nanoreactors to control the diameter of the hydrogel nanoparticles formed in the core [23]. After polymerization of the liposome-encapulated monomer, the surrounding lipid bilayer was removed, for the nanohydrogel recovering, and the hydrogel-liposome assembly is destroyed.

Since this initial work, several studies had been emerging, investigating the properties of the hydrogel-liposome assemblies in toto. These hybrid structures showed attractive features and structural properties, which could be used to design appealing new drug delivery systems. Particularly, the inner nanogel core can offer mechanical support to the surrounding membrane mimicking the elastic protein network of the cytoskeleton in the cells. Therefore, to form a polymeric gel within the core of liposomes can be a key step in the design of innovative and more stable phospholipid-based delivery systems [24].

The inner hydrogel can serve as diffusion-controlling barrier, which may allow bioactive molecules to be released first from the hydrogel matrix, then from the liposomal bilayer coating, in a controlled manner over an extended period. Moreover, the interactions between polymers and phospholipid constituents can alter the thermotropic phase

behaviour of liposome membrane and in this way, it may prevent any unwanted drug leakage, due to membrane destabilization consequent to local defects.

Spherical structures, made of a hydrogel-core, coated with a lipid bilayer, can be obtained by anchoring the lipid bilayer on the surface of preformed hydrogels after mixing, as in lipobeads [6, 8, 10], or by cross-linking encapsulated hydrophilic monomers inside the inner core of liposomal vesicles [16, 25, 26]. Based on the assembling procedure used, final spherical hydrogel/lipid bilayer structures, of similar narrow dimensional distribution but dissimilar in size, are obtained. In particular, only the second approach allows obtaining nanosized gel in liposome assemblies. Therefore, in this way, novel gel-stabilized liposomes for the development of realistic drug delivery carriers, with improved stability features, can be prepared. The first lipid vesicles filled with a hydrogel was reported by Torchillin in 1987 [27]; in this pioneristic work a successful polymerization of the encapsulated hydrophilic monomers within liposomes, by UV irradiation, was proposed. Aim of that work, was to overcome the poor stability of the liposome vesicles; pre-gel components and hydrogel, presumably, could play a crucial role in the stabilization of the phospholipid bilayer. Particularly, hydrogel could be considered as the cytoskeleton supporting the bilayer, enhancing the structural strength of the liposome vesicles. In addition, both the hydrogel and the bilayer can be considered a diffusional barrier to the flow of the drug and, synergistically, they can regulate the drug release.

Within 30 years of experimentation, the research on gel-core liposome resulted in numerous studies on the interactions between hydrogels and liposomes.

Petralito and coworkers successfully prepared hydrogel-in-liposome nanoconstructs, demostrating that the hydrophilic monomers-phospholipid interactions existing in the new Gel-in-Liposome (GiL) system [24].

For the design of GiL, in particular, a polyethylen glycol-dimethacrylate (PEG-DMA) hydrogel core was formed inside liposomes, through UV-initiated free radical polymerization of PEG-DMA monomers. The authors demonstrated that the obtained inner hydrogel network, within the hybrid construct, affects the permeability properties of the

lipid bilayer around the modified aqueous core. Thus, the polymeric nanogel-lipid interaction resulted in a modified release behaviour of the newly GiL systems, respect to conventional liposomes, limiting any unwanted leakage of the encapsulated molecules.
With the aim to better understanding the behaviour of the GiL system and in order to optimize the drug release profile from such hydrogel/liposome complex systems, here a novel hybrid lipid-polymer nanocomposite is proposed. Specifically, PEG-DMA, at two different molecular weights, was first encapsulated within unilamellar vesicles made of hydrogenated soybean phosphatidylcholine and cholesterol. Then it was converted into a hydrogel by UV-initiated free radical polymerization. An accurate and optimized experimental set-up was used to evaluate the properties of the newly produced GiL carrier, compared to conventional ones.

## 7.3 Experimental section

### 7.3.1 Materials

Hydrogenated soybean phosphatidylcholine (HSPC) Phospholipon® 90H from Lipoid GmbH was kindly gifted by AVG; 5-(6) carboxyfluorescein [5-(6) CF] was obtained from Kodak; $\alpha$-cyano-4-hydroxycinnamic acid ($\alpha$-CHCA) and sodium chloride (NaCl) were purchased from Fluka. Cholesterol (Chol), deuterium oxide ($D_2O$), 1,2-dichloroethane, chloroform, 4-(2-hydroxyethyl)piperazine-1-ethanesulfonic acid (HEPES), polyethylene glycol-dimethacrylate (PEG-DMA) MW 750, polyethylene glycol (PEG) MW 4000, 2-hydroxy-4′-(2-hydroxyethoxy)-2-methylpropiophenone (IRGACURE 2959), Triton X-100 (TX-100), Sephadex G-50 medium grade, alumina, dialysis bag made of benzoylated cellulose (cut-off 2,000 Da), methacrylic anhydride (MA), diethyl ether, 1-methyl-2-pyrrolidone, sodium hydroxide (NaOH), iron (III) nitrate, ammonium thiocyanate, uranyl acetate, fetal bovine serum (FBS), L-glutamine, penicillin/streptomycin solution, trypsin, 3-[4,5-dimethylthiazol-2-yl]-2,5-diphenyl-tetrazolium bromide (MTT), human insulin,

dimethyl sulfoxide (DMSO) and phosphate buffer saline (PBS) were purchased from Sigma Aldrich. Eagle's Minimum Essential Medium (EMEM), sodium pyruvate and sodium bicarbonate were obtained from Unimed Scientifica. Bidistilled water, hydrochloric acid 37% (HCl) and ethanol were supplied by Carlo Erba Reagents. Polycarbonate membrane filters Whatman® (800, 400 and 200 nm) were purchased from Cyclopore Track Etched Membrane.

### 7.3.2 PEG-DMA$_{4000}$ synthesis and characterization

Polyethylene glycol-dimethacrylate (PEG-DMA) was synthesized by esterification of polyethylene glycol (PEG, MW 4000) with methacrylic anhydride (MA), following a previously optimized procedure [28], with microwave irradiation. Briefly, 10 g of PEG$_{4000}$ and 4 ml of MA were inserted into a microwave reaction vial. The reaction conditions provided for a reaction time of 20 min and an irradiation of 100 W, at 100 °C. At the end of the reaction, the polymer was precipitated by the addition of diethyl ether and the resulting solid was filtered and then left to dry for 12 h, at room temperature. Subsequently, PEG-DMA$_{4000}$ was solubilized in 9 ml of chloroform and purified on alumina column to remove the methacrylic acid produced during the reaction. The eluate was evaporated under reduced pressure. The purified dry polymer was solubilized in bidistilled water, freezed at -30 °C in a HETO CT 110 cryostat and lyophilized. The obtained PEG-DMA$_{4000}$ was stored in the dark, before its use.

The methacrylation of PEG-DMA$_{4000}$ was evaluated by FT-IR and $^1$H-NMR analyses. FT-IR spectra were recorded by performing 64 scans in the range 4000-400 cm$^{-1}$, with a resolution of 1 cm$^{-1}$, on KBr pellets. $^1$H-NMR spectra were recorded in $D_2O$.

Finally, a MALDI-TOF analysis was performed to quantify the functionalization of the hydroxyl groups of the starting PEG and to determine the presence of by-products, such as PEG monomethacrylate and non-functionalized PEG. The instrument is equipped with a $N_2$ laser ($\lambda$= 337 nm) with a pulse width of 2 ns. The ions are accelerated to a potential of 22 kV,

with a delay time of 400 ns. The spectra obtained are the sum of 256 scans. $PEG_{4000}$ and $PEG\text{-}DMA_{4000}$ were solubilized separately in 10 ml of bidistilled water and added with NaCl (100 μl of a 25 mg/ml solution) as an ionizing agent. Subsequently, 20 μl of $\alpha$-CHCA solution was added to 20 μl of the polymeric solution (1 mg/ml). Human insulin (MW=5808.6 g/mol) was used to calibrate the instrument.

### 7.3.3 Preparation and optimization of Gel-in-Liposome (GiL) system

Conventional thin film hydration method, followed by extrusion, was used to prepare Conventional Liposome (CL) and Gel-in-Liposome (GIL) systems, as described in [24]. Briefly, HSPC and Chol (1:0.1 weight ratio) were dissolved in the minimum volume of chloroform (3 ml) and the organic solution was poured into a round bottom flask. The organic solvent was evaporated under reduced pressure at 60 °C (above the gel-liquid crystalline transition temperature of the lipids, Tm) to form a lipid film, which was further dried under high vacuum to remove traces of the organic solvent. The resulting lipid film was hydrated with 5 ml of HEPES buffer solution (10 mM, pH=7.4) containing a mixture of $PEG\text{-}DMA_{750}$ or $PEG\text{-}DMA_{4000}$ (0.8% w/v) and IRGACURE 2959 (0.45 mM). 20 mM of the hydrophilic fluorescent marker 5-(6) carboxyfluorescein [5-(6) CF] was also added to the buffered solution. The hydration process was carried out above the Tm of the lipids in a water bath at T= 60 °C. A final HSPC concentration of 10 mM was obtained. The mixture was repeatedly extruded at T= 60 °C, through polycarbonate membranes of decreasing pore size using a thermobarrel Extruder, Lipex Biomembrane (Canada). The extrusion was repeated until a homogeneous size distribution was achieved (2 times through 800 nm membranes, 2 times through 400 nm membranes and finally 6 times through 200 nm membranes). Finally, liposomes were purified using a Sephadex G-50 gel filtration column. The purification step was carried out with the aim of removing all the not entrapped material from vesicular structures. Following the same procedure without the addition of PEG-DMA, conventional HSPC/Chol liposomes were prepared and used as a control. All liposome formulations were stored at 4 °C and used within two weeks from preparation.

### 7.3.4 Gelation of the liposome core

Liposomes formulations, containing PEG-DMA$_{750}$ or PEG-DMA$_{4000}$, were exposed to UV irradiation for 30 min, in a Helios Italquartz Photochemical Multirays Reactor (Italy), equipped with ten, 14 W medium pressure, mercury lamps G15T8-E LAWTRONICS ($\lambda_{max}$=310 nm). Following this procedure, the crosslinking of the polymers inside the lipid vesicles leads to the formation of GiL$_{UV\ 750}$ and GiL$_{UV\ 4000}$ samples.

The UV stability of 5-(6) CF, over the 30 min of radiation time, was verified. To this end, solutions with different concentration of the marker were treated in the same conditions adopted for the photopolymerization of PEG-DMA in the two GiL systems. At the end of the exposure, the emission fluorescence emitted by the marker at 512 nm was recorded, after excitation at 492 nm. The fluorescence spectrum was compared to that of the not irradiated control solutions. The stability study was carried out both in the presence and in the absence of the IRGACURE 2959 radical photoinitiator.

### 7.3.5 Physicochemical characterization of liposomes

- *Dynamic light scattering and ζ–potential measurements of liposomes and nanogels.*

Particle size distribution and ζ-potential were measured with a Zetasizer Nano ZS90 (Malvern Instruments Ltd., UK). Hydrodynamic diameter and polydispersity index were evaluated by DLS experiments, whereas ζ-potential was measured by electrophoretic light scattering (ELS) experiments. The DLS and ELS techniques used a photon correlator spectrometer equipped with a 4 mW He/Ne laser source operating at 633 nm. All experiments were performed at a scattering angle of 90°, at 25 °C. Liposomes samples were diluted in 10 mM HEPES buffer (pH= 7.4) until a count-rate of about 200 kcps was obtained to avoid interfering multiple scattering phenomena. The analysis were performed

immediately after preparation and after photopolymerization, furthermore after conservation of the samples at 4 °C, in order to evaluate the stability of each formulation over time. Size, polydispersity index and ζ-potential values of the liposome formulations are the mean of three different preparation batches ± SD and all the analyses were performed at least in triplicate.

Crosslinking of PEG-DMA and consequent formation of nanogels were confirmed by DLS measurements, carried out after removal of the lipid bilayer by addition of TX-100 (30% w/v). After this treatment, PEG-DMA nanogels were recovered by a Sephadex G-50 gel filtration column. Similar experiments were also carried out on plain liposomes (not containing PEG-DMA) and not crosslinked GiL samples.

- *Transmission electron microscopy*

Transmission electron microscopy (TEM) of GiL, GiL$_{UV}$ and CL samples was performed on Zeiss EM 10 microscope operating at 60 kV equipped with a Soft Imaging System CCD camera. TEM observations were carried out after negative staining of the samples. To this end, diluted liposomes suspensions were dropped onto 200-mesh Formvar copper grids, then stained with 1% w/v of uranyl acetate solution for 1-2 min. The excess of the uranyl acetate solution was removed and the samples were dried at room temperature, for almost 30 min before the observation.

- *Phospholipid assay*

The amount of phospholipids structured to form liposome vesicle in the CL formulation was determined using a colorimetric method reported in [29]. The assay is based on the

formation of a hydrophobic thiocyanatoiron-phospholipid complex. Briefly, aliquots (0.4 ml) of phospholipids in 50% v/v of ethanol were mixed with 1 ml of thiocyanatoiron reagent, previously prepared by solubilizing 0.97 g iron (III) nitrate and 15.2 g of ammonium thiocyanate in 100 ml of water. The obtained solution was acidified with 0.6 ml of 0.17 N HCl. The thiocyanatoiron-phospholipid complex was extracted with 3 ml of 1,2-dichloroethane by vigorous shaking for 2 min in a vortex-type mixer. The mixture was centrifuged for 5 min at 2000 rpm and the absorbance of the organic lower layer was measured at 470 nm, using a double beam Lambda 25 (Perkin Elmer, USA) UV-Vis spectrophotometer. Phospholipid concentration was obtained through a suitable standard curve previously constructed.

The amount of phospholipids, present in the $GiL_{750}$ and $GiL_{4000}$ suspensions, was indirectly evaluated, by means of an empirical correlation between the phospholipid amount found in the samples and the optical properties of the suspensions.This method was developed knowing that polymer does not interfere with the optical density measurements and verifying that the average diameter of the lipid-polymer hybrid constructs was similar to the CL sample diameter.

The optical density (OD) of samples, at different concentration, in the range 20-200 nmol, was measured at $\lambda$=436 and 600 nm, and the OD values were correlated with the phospholipid amount evaluated, as reported above.

- *Loading and entrapment efficiency of 5-(6) CF*

5-(6) CF stock solution was made by dissolving 5-(6) CF powder in few drops of 1N NaOH solution followed by the addition of HEPES buffer (10 mM, pH=7.4) up to the appropriate volume. The 20 mM 5-(6) CF fluorescent marker was loaded within the aqueous core of liposomal vesicles during the thin film hydration phase. The amount of 5-(6) CF entrapped in the internal aqueous compartment of the lipid vesicles was determined measuring the

fluorescence emitted by the marker at 512 nm, after excitation at 492 nm. To this end, purified GiL and CL samples were incubated with TX-100 (30% w/v) for vesicles lysis and the fluorescence was measured, considering that the fluorescence intensity of 5-(6) CF was linear in the range of $10^{-7}$ – $10^{-6}$ mol/l. Captured volume was defined as μl of entrapped volume for mg of lipid (see Figure 7.1 and 7.2 of S.I.). All experiments were performed in triplicate and the results reported as mean ± SD.

- *Differential scanning calorimetry*

Calorimetric measurements were performed using a DSC131 (Setaram, France) scanning calorimeter. Typically, measurements were performed under nitrogen flow (20 ml/min) by setting an initial isotherm at 30 °C for 300 seconds, a heating ramp from 30 to 70 °C or 30 to 170 °C and a second isotherm at 70 °C or 170 °C for 300 seconds, respectively for the measurements performed in hydrated or anhydrous conditions. Samples were obtained by solubilizing HSPC, PEG-DMA$_{750}$ (or PEG-DMA$_{4000}$) and cholesterol in the minimum volume of chloroform (3 ml) into a round bottom flask. The organic solvent was evaporated under reduced pressure at 60 °C to form a lipid film, which was further dried under high vacuum to remove traces of the solvent. Aliquots of 5 mg of each dried film were gently scraped from the flask and weighed in sealable aluminum pans. At least three heating cycles were performed on each sample and the thermograms were recorded at scan rate of 5 °C/min. An empty aluminum pan was used as reference.

- *Release in vitro of 5-(6) CF*

*In vitro* release profiles of the fluorescent 5-(6) CF marker from hybrid systems, irradiated and not, were determined at T= 37.0 ± 0.5 °C and at T= 60.0 ± 0.5 °C (T>Tm of HSPC), under magnetic stirring, and compared with the release profile of CL sample. Aliquots of each sample (1 ml) was diluted 1:100 with HEPES buffer (10 mM, pH=7.4) and the suspension monitored over time, in order to determine the amount of marker released by the structures.

At predetermined time intervals, aliquots (3 ml) were sampled and replaced with the same volume of fresh buffer, maintained respectively at T= 37.0 ± 0.5 °C and at 60.0±0.5 °C, respectively. Marker concentrations were spectrofluorimetrically determined and the percentage of 5-(6) CF, released from the different liposome suspensions, was calculated using the Equation 7.1.

$$5-(6)\ CF\ released\ (\%) = \frac{(I_t - I_0)}{(I_{max} - I_0)} \cdot 100 \qquad (7.1)$$

where: $I_0$ is the initial fluorescence intensity of 5-(6) CF loaded; $I_t$ is the fluorescence intensity measured at time *t*; $I_{max}$ is the fluorescence intensity after the complete lysis of the liposomal vesicles with TX-100.

At the end of the release study, all samples were characterized by DLS measurements to verify vesicles integrity, and finally the residual amount of the dye still present within the liposomal core was recovered. All experiments were performed in triplicate

- *Interaction process of TX-100 with liposomes*

The ability of the surfactant TX-100 to interact with GiL structures was studied and compared with CL, in order to test the stability of the hybrid nanocarriers. Aliquots of 3 ml of $GiL_{750}$ and $GiL_{4000}$, after UV irradiation, were mixed with opportune volumes of TX-100 (0.1% w/v), at sublytic concentration. The systems were equilibrated for 10 min at 37.0±0.5 °C. Then, the interactions between vesicles and TX-100 were monitored by continuous measurement of the fluorescence emitted by the hydrophilic marker, over 30 min. At the end of the analysis, a lytic concentration of TX-100 (30% w/v) was added to the suspensions, thus allowing to determine the maximum content of 5-(6) CF in each sample. The percentage of 5-(6) CF, released from the different samples, following the mechanical destabilization mediated by TX-100, was calculated using the Equation 7.1. All the experiments were performed at least in triplicate.

- *In vitro evaluation of biocompatibility*
- *Cell culture*

The human fibroblast cell line (WI-38) was purchased from American Type Culture Collection (ATCC® CCL-75™ – Milan, Italy). The cells were grown in EMEM, supplemented with FBS (10% v/v), L-glutamine, sodium pyruvate, sodium bicarbonate, HEPES, penicillin (100 U/ml) and streptomycin (100 μg/ml). Fibroblasts were sub-cultured 1:3 in 25 $cm^2$ flasks, maintained at 37 °C and 5% of $CO_2$ in a humidified environment, and the medium was renewed two times a week, as recommended by the supplier. For the experiments, cells were seeded in 24-well plates at a density of 3 x $10^4$ cells/well. After 72 h, cells (about 80% confluent) were exposed to different concentrations of $GiL_{UV\ 750}$ and $GiL_{UV\ 4000}$ for 24, 48 and 96 h.

- *Cytotoxicity test*

The MTT assay (index of mitochondrial function) was used for cytotoxicity evaluation. The test is based on the conversion of the tetrazolium salt MTT to an insoluble purple formazan by mitochondrial dehydrogenase enzymes of living cells. MTT was performed as previously described [30]. Briefly, 5 mg/ml of MTT was added to each well and, after 80 min of incubation period, the medium was removed and 250 μl of DMSO was added. The 24-well plate was shaken for 5 min, and the absorbance of the converted dye was measured by a molecular device kinetic microplate reader (Bio-Rad, Hercules, USA), at a wavelength of 595 nm. All data were expressed as mean ± SD of two independent experiments, carried out using six replicates. Statistical comparison was performed using the *Student's t-test* and $p < 0.05$ was considered statistically significant.

## 7.4 Results and Discussion

### 7.4.1 Preparation and characterization of GiL$_{750}$ and GiL$_{4000}$

The objective of this study was to prepare a liposomal carrier with a gelled core, aiming for a modification of the release rate of any encapsulated drug and for an improvement of the vesicles stability. In order to get these aims, polyethylene glycol-dimethacrylate (PEG-DMA), at two different molecular weights (MW 750 and 4000), was used as gel-forming material to prepare Gel-in-Liposome (GiL) carriers, via UV initiated free radical polymerization of the polymer entrapped into the vesicles. The entrapment of the polymer was achieved during the vesicles formation, obtained via the thin lipid film hydration, followed by extrusion and size esclusion chromatography (SEC) purification. Table 7.1 shows the amounts of HSPC, Chol and PEG-DMA MW 4000 or MW 750 used to prepare the polymer–lipids hybrid vesicles. The polymer/lipid weight ratio was varied from 0 to 2. Both PEG-DMA, at a 1:1 polymer/lipid weight ratio, lead to the formation of vesicles, whereas the employment of higher amounts of PEG-DMA$_{4000}$ resulted in aggregates.

**Table 7.1. HSPC/PEG-DMA weight ratio for the preparation of GiL$_{4000}$ and GiL$_{750}$.**

| HSPC (mg) | Chol (mg) | PEG-DMA (mg) | PEG-DMA (MW) | HSPC/PEG-DMA (w/w) | Note |
|---|---|---|---|---|---|
| 40 | 4 | 20 | 4000 | 1:0.5 | Vesicles |
| 40 | 4 | 40 | 4000 | 1:1 | Vesicles |
| 40 | 4 | 50 | 4000 | 1:1.25 | Aggregates |
| 40 | 4 | 80 | 4000 | 1:2 | Aggregates |
| 40 | 4 | 20 | 750 | 1:0.5 | Vesicles |
| 40 | 4 | 40 | 750 | 1:1 | Vesicles |
| 40 | 4 | 50 | 750 | 1:1.25 | Vesicles |
| 40 | 4 | 80 | 750 | 1:2 | Vesicles |

Regardless of the molecular weight differences, after extrusion and SEC purification of the multilamellar vesicles containing gel-forming material, the obtained unilamellar samples, with both PEG-DMA at a 1:1 polymer/lipid weight ratio, presented almost similar

hydrodynamic diameter and monomodal size distribution curves, with a polydispersity index lower than 0.150 (Table 7.2).

**Table 7.2. The amount of HSPC, Chol, PEG-DMA$_{4000}$ and PEG-DMA$_{750}$ used to prepare CL, GiL$_{4000}$ and GiL$_{750}$ systems are reported. Physical characterization was performed in terms of hydrodynamic diameter (Z-average), PdI values and ζ-potential values of liposomes embedding not polymerized PEG-DMA$_{4000}$ and PEG-DMA$_{750}$ as compared to the control CL.**

| HSPC (mg) | Chol (mg) | PEG-DMA (MW) | PEG-DMA (mg) | Size (nm) | PdI | ζ-potential (mV) |
|---|---|---|---|---|---|---|
| 40 | 4 | - | 0 | 192.1 ± 8.3 | 0.11 ± 0.01 | -9.5 ± 1.4 |
| 40 | 4 | 4000 | 40 | 206.3 ± 3.5 | 0.09 ± 0.09 | -13.1 ± 0.9 |
| 40 | 4 | 750 | 40 | 201.7 ± 17.2 | 0.05 ± 0.02 | -16.1 ± 3.3 |

Furthermore, the amount of structured lipid, in both cases, was about 80%, which is only slightly lower than the value obtained for conventional HSPC/Chol liposomes (90%).

Irrespective of the polymer properties, ζ–potential values of SEC-purified hybrid liposomes were more electronegative with respect of the value obtained for control HSPC/Chol liposomes. According to the ζ-potential results, we hypothesized that the ability of the gel-forming material to interact with the chain-melted solid state lipid bilayer, during vesicles formation, was not neglectable. It is likely that PEG-DMA$_{4000}$ can diffuse or aggregate within the plane of the membrane, remainig localized predominantly in the inner aqueous core of the GiL. More so, some amount of PEG-DMA$_{750}$, considering its lipophilia, might have insert in the bilayer, during the hydration step, and protrude onto the surface of liposomes. To confirm this hypothesis, DSC measurements were performed in order to evaluate the effect of the polymer on the thermal properties (transition temperature and the magnitude of heat capacity of the peak) of the bilayer.

In Figure 7.1 are reported the thermograms of plain HSPC/Chol, HSPC/Chol/PEG DMA$_{4000}$ and HSPC/Chol/PEG DMA$_{750}$ mixtures. The liquid-ordered phase *L0*, associated to HSPC/Chol 1:0.1 weight ratio mixture, contains fast diffusing lipids, with their acyl chains all in the trans configuration, similar to the gel phase.

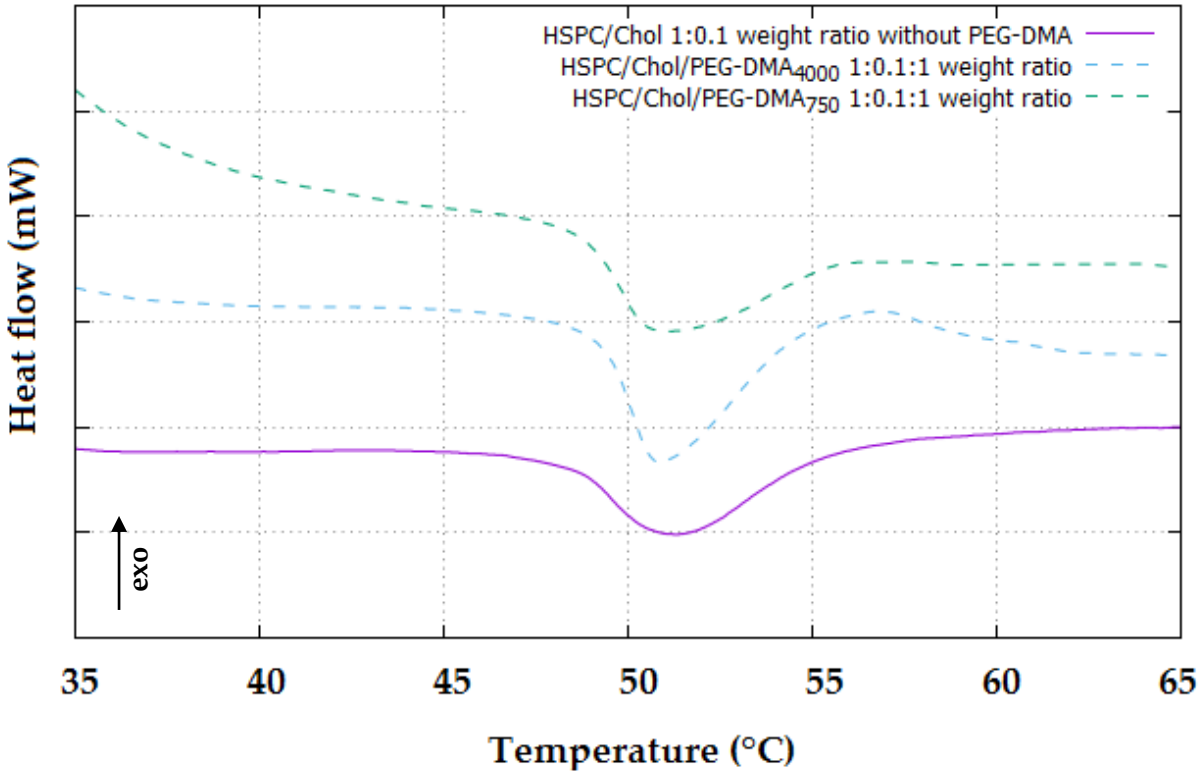


**Figure 7.1. Thermotropic phase behaviour of the hydrogenated soybean phosphatidylcholine-cholesterol and PEG-DMA$_{4000}$ or PEG-DMA$_{750}$ mixture, at scan rate 5 °C/min, in the temperature range 30-70 °C.**

PEG-DMA$_{4000}$ and PEG-DMA$_{750}$, both at 1:1 HSPC/polymer weight ratio, induced peak broadening and decrease in the transition enthalpy, associated to HSPC/Chol transition temperature. From these thermotropic results, it seems evident that a partial interaction of the gel-forming precursors with the bilayer occurs during the vesicles formation. In fact, compared to plain HSPC/Chol mixture, the presence of the polymer seems to increase the phosphate-to-phosphate distance across the bilayer. As a consequence, a reduction of the relatively fast lipid lateral diffusion of the acyl chains of HSPC/Chol mixture was obtained, the interaction of the hydrophobic chains of the phospholipids becomes less cooperative and the intensity of HSPC/Chol calorimetric peak decreases and broadens. These findings suggest that, although the PEG-DMA$_{750}$, in a 1:1 weight ratio with the lipid, decreases less the conformational motions of the acyl chains, respect to PEG-DMA$_{750}$ in a 20:1 weight ratio [24], the polymer can modify the bilayer structure. In particular, at this 1:1 weight ratio, despite its greater lipophilia, with the respect of PEG-DMA$_{4000}$ one, PEG-DMA$_{750}$ could be in

part confined in the vesicular aqueous core, in the same way of the precursor at higher molecular weight. Therefore, a 1:1 HSPC to PEG-DMA$_{750}$ weight ratio was considered in the following experiments, since it is seemed the most suitable quantity for comparative studies with PEG-DMA$_{4000}$-liposomes hybrids.

The nanosystems studied were loaded with a fluorescent marker, 5-(6) CF, able to mimic the behaviour of a hydrophilic drug, in order to evaluate the release properties of the hybrid liposomal vesicles, compared to conventional ones. The encapsulation efficiency (EE) of the marker in the control and in the polymer modified liposomes was evaluated by fluorescence spectroscopy. Control liposomes showed a trapped volume of 2.11 ±0.28 μl of 5-(6) CF/mg HSPC. In the presence of PEG-DMA, irrespective from its molecular weight, the EE slightly decreases, most likely for the polymer presence in the inner core of the structures.

The use of phospholipid/polymer 1:1 weight ratio allowed the passive loading of the fluorescent probe, during the hydration step of the thin lipid film hydration method. On the contrary, previous results, from this research group, showed that the use of a 1:20 HSPC/ PEG-DMA$_{750}$ weight ratio required a marker active loading into preformed liposomes, driven by a transmembrane pH gradient [24]. These results are particularly interesting because, while the active loading of drugs into liposomes is a well-established loading technique, it can not be generally applied, since it can be successfully applied only to ionizable molecules. Non-ionizable drugs into preformed liposomes result in poor loading efficiencies, thus a passive loading, in this case, could be the only one chance to succeed.

Dynamic Light Scattering (DLS) measurements, conducted on vesicular systems loaded with the 5-(6) CF, were similar, in terms of size and surface charge, to those of empty liposomes (data not shown).

After the purification of the vesicles, PEG-DMA was photo-polymerized by exposure to UV irradiation for 30 min. The results showed that the photo-polymerization step preserved the vesicular integrity, without leading to significant changes in the mean diameter and size distribution of GiL$_{UV}$ liposomes, as reported in the Table 7.2, respectively for embedding not-polymerized PEG-DMA$_{4000}$ and PEG-DMA$_{750}$.

TEM analysis, carried out on conventional and PEG-DMA modified liposomes, before and after photo-polymerization, did not evidence any morphological changes due to the polymer introduction and its subsequent polymerization (Figure 7.2), in comparison with conventional vesicles. Moreover, TEM images highlight morphological difference between irradiated and non-irradiated hybrid structures, suggesting that UV irradiation can effectively lead to the polymerization of the PEG-DMA$_{750}$ and PEG-DMA$_{4000}$ methacrylic groups, with consequent polymer cross-linking and formation of a gelled core.

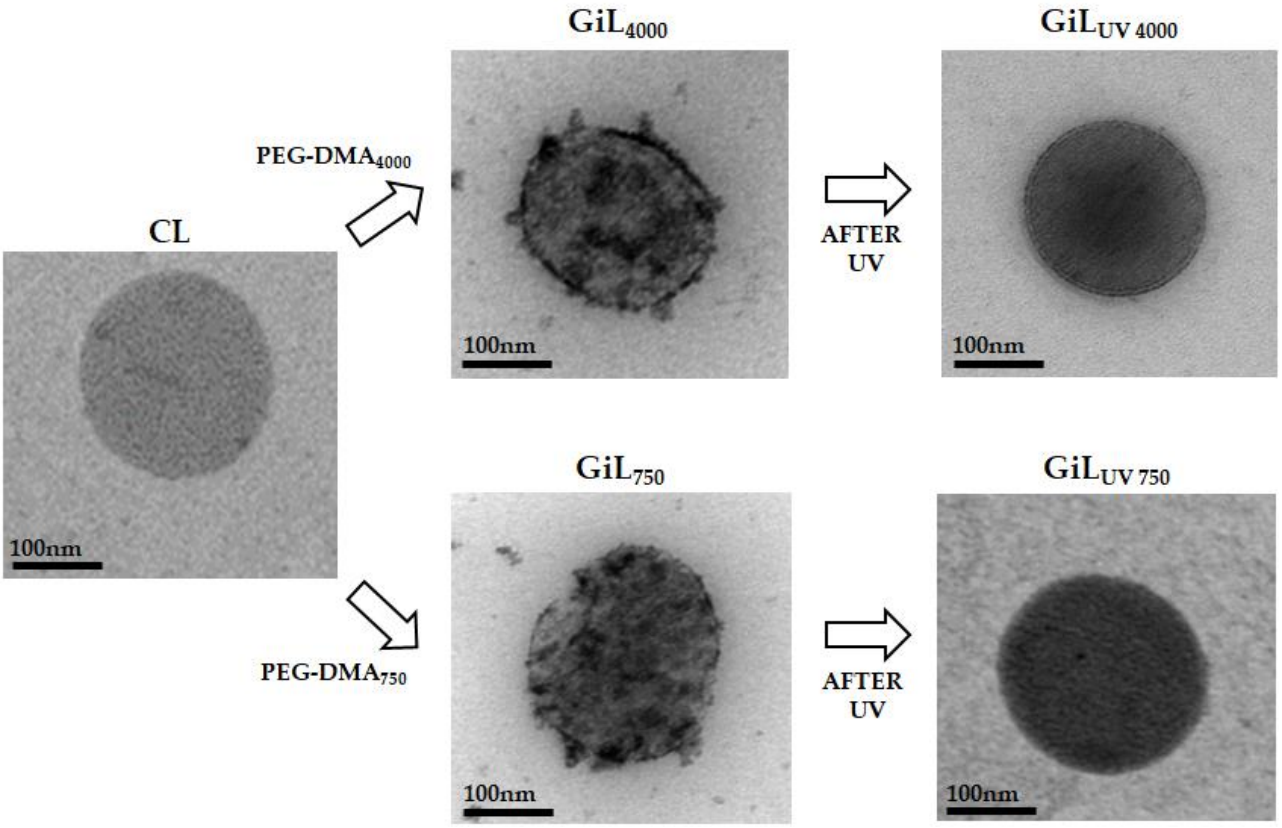


**Figure 7.2. Morphological characterization by TEM. Effect of the presence of PEG-DMA$_{4000}$ and PEG-DMA$_{750}$ on vesicles morphology, before and after UV photopolymerization, compared to samples. Samples were stained with uranyl acetate.**

Since the photo-polymerization process was performed on vesicles entrapping the dye, a photostability study of the 5-(6) CF, after UV irradiation, was necessary. The graph, reported

in Figure 7.2 of the S.I. of this paper, suggests that the photo-polymerization step does not significantly alter the fluorescent properties of the dye, both in the presence and absence of the IRGACURE 2959 radical photoinitiator. The study of the probe photochemical stability became an integral part of the characterization, because provides information on the possibility of carrying out a direct loading of an active molecule, exceeding the limits of a loading onto preformed vesicles [24].

The average size, size distribution and ζ–potential of the GiLUV remained unaltered for at least 14 days, when stored at 4 °C, as evaluated by DLS measurements (data not shown).

Furthermore, polymer within liposome structures allows to delay the flocculation process that generally occurs in conventional liposomal suspensions, during storage at 4 °C.

As evident from the Figure 7.3, after 14 days from vesicles preparation, samples, stored at 4 °C, show a different behaviour. In GiLUV structures the presence of the polymer prevents the phase separation, while the conventional liposomes exhibit an evident flocculation. Since nanocarriers colloidal stability can be enhanced through the addition of small amounts of polymer to the external medium, we can speculate that a small amount of PEG-DMA could be stick out from the vesicles into the bulk, avoiding the typical liposomes coagulation. This is also confirmed by the ζ-potential values of gel-core-liposomes, already reported in Table 7.2.


**Figure 7.3. Different colloidal stability of CL (A), GiL$_{UV\ 750}$ (B) and GiL$_{UV\ 4000}$ (C), after 14 days from the liposomes preparation. All samples were stored at 4 °C.**

In order to confirm the polymerization of PEG-DMA and the formation of nanogels, the lipid bilayer of the vesicles was removed with the non-ionic detergent TX-100. After the addition of lytic concentrations (2.45 mol/l) of TX-100, the treatment results in a stable dispersion of mixed micelles, before UV exposition. Before UV crosslinking, indeed, a polymeric solution is contained within the vesicles core and, after removal of the phospholipid bilayer, PEG-DMA was diluted in the external bulk, as indicated by the disappearance of the peak at 200 nm (Figure 7.4), in the same way of plain control liposomes.

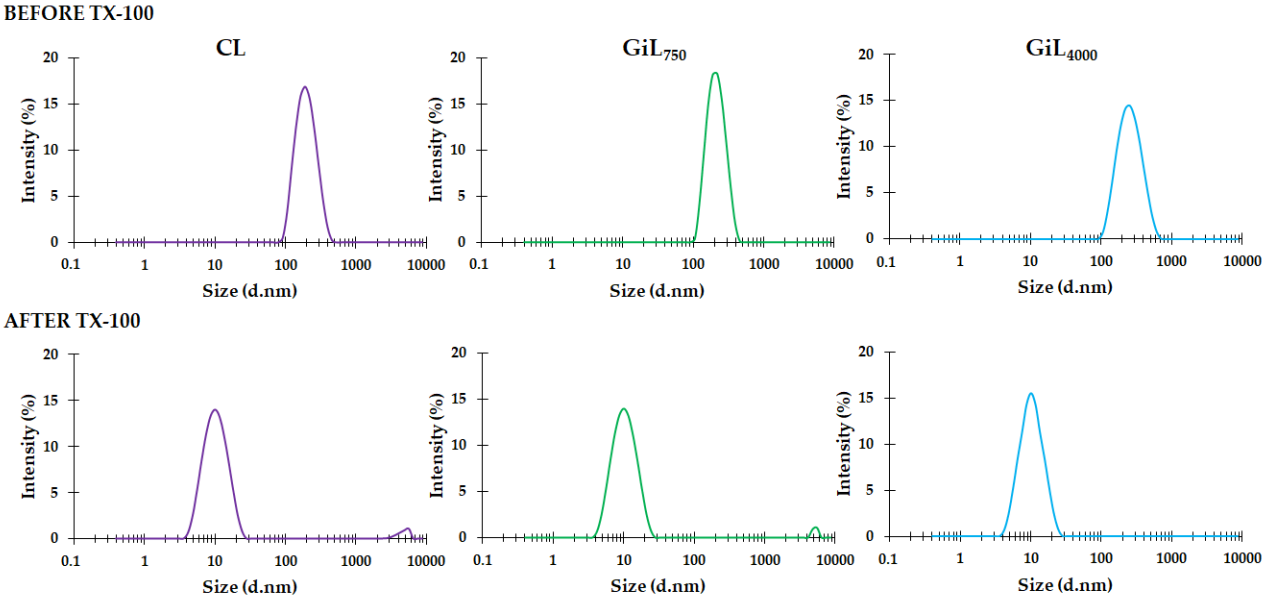


**Figure 7.4. Size distribution by intensity: comparison between CL, GIL$_{750}$ and GIL$_{4000}$ systems before and after treatment with TX-100. At 10 nm is shown the typical peak of mixed micelles, resulting from the complete removal of double lipid layer.**

Instead, after photo-polymerization, the lytic treatment results in a stable dispersion of mixed micelles and PEG-DMA nanogels; the addition of TX-100 to the crosslinked PEG-DMA modified liposomes, removes, in fact, the external lipid layer, while preserves the spherical structure of the nanogels formed within the liposomes (Figure 7.5).

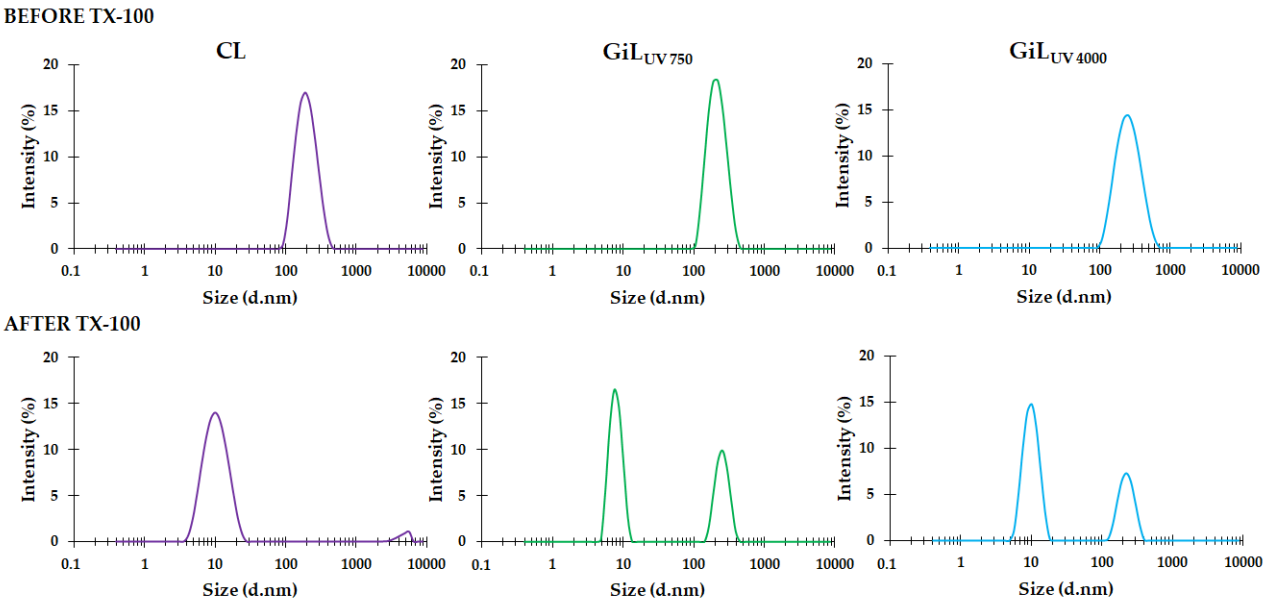

**Figure 7.5. Size distribution by intensity: comparison between CL, GIL$_{UV\ 750}$ and GIL$_{UV\ 4000}$ systems before and after treatment with TX-100. After the addition of TX-100, the polymerized formulations show the typical peak of mixed micelles (10 nm), as a consequence of the complete removal of the double lipid layer, and an extra peak at 200 nm, resulting from the formation of nanohydrogel.**

Note that the peak scattered intensity from the nanogels is about 5% fold weaker than that from the GiL, which means that the number density of nanogels is low compared to the liposomes. Further, to confirm gel formation, after TX-100 treatment, the nanogels were recovered from the dispersion by SEC purification and analyzed through DLS and TEM, for mean diameter and morphology respectively. Results reported in Figure 7.6 show that nanogels have a mean diameter of about 210 nm, thus slightly larger than the template liposomes. This evidence can be due in part to their tendency to swell in solution, when they are not confined by the phospholipid bilayer. Overall, however, the sizes of the two structures (MW 4000 or 750) are quite comparable. In addition, the nanogels were directly characterized by microscopic observation using TEM. TEM images of PEG-DMA nanogels presented in Figure 7.6 early prove the hollow sphere morphology of the pure polymer particles. Nanohydrogels preserve their spherical shape also when they are not confined by the phospholipid bilayer. Apparently, the crosslinking density of the polymer network structures reflects the difference of the molecular weight of the monomers used to form the hydrogel. Particularly, morphology is correlated to PEG-DMA interaction with templating vesicles. Portion of the monomers MW 750, solubilized in the bilayer, is polymerized, while intra-core aliquots plays only a minor role on the nanohydrogel formation (Figure 7.6, B). In the case of the monomers MW 4000 (Figure 7.6, C), both the portion aliquots, interacting with the bilayer and the intra-core, seem to be involved in the structuring of the polymeric network. This difference, probably, is due to the higher hydrophilicity of the PEG-DMA$_{4000}$, which results in a greater distribution in the aqueous core with respect to the PEG-DMA$_{750}$.

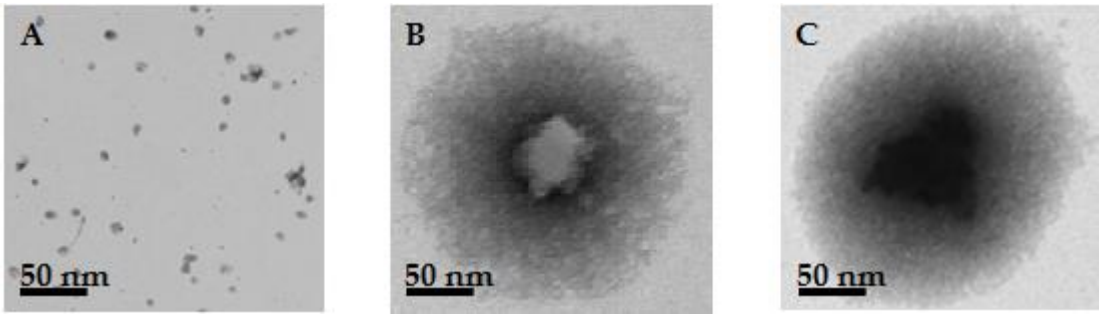


**Figure 7.6. Morphological characterization by TEM of mixed micelles (A), PEG-DMA$_{750}$ nanohydrogel (B) and PEG-DMA$_{4000}$ nanhydrogel (C), obtained after treatment with lytic concentration of TX-100, respectively from CL, GIL$_{UV\ 750}$ and GIL$_{UV\ 4000}$. The structural aspect of gel in the core of liposomes depends on physical-chemical characteristics of the polymer.**

## 7.4.2 Stability studies of GiL$_{UV}$ with TX-100

To obtain a deeper understanding of how the hydrogel, in the hybrid structures, can modify the properties of the conventional vesicles, our strategy was to use sub-lytic concentrations of the non-ionic surfactant TX-100, in order to have informations about the physical properties of the GiL membrane.

When the detergent is present at sub-lytic concentrations, liposomal vesicles retain their structural integrity, but the integration of the detergent within the membrane changes their structure and properties. In particular, the intercalation of the surfactant molecules into the bilayer alters phospholipid packing, with consequent modification of the membrane permeability and induced release of the entrapped dye. In fact, the diffusion of 5-(6) CF, across phospholipid bilayers, first depends on the lipid composition, but it can also be influenced by the presence of non-lipid components within the vesicle membrane, such as PEG-DMA in GiL systems. Specifically, depending on the molecular weight, PEG-DMA can assume different arrangements within the lipid vesicles, and, in this way, it could give a different resistance to the membrane against the penetration of TX-100 into the outer monolayer and its trans-bilayer diffusion towards the inner leaflet.

Therefore, the fluorescence of 5-(6) CF was continuously monitored over time in presence of sub-lytic concentrations of TX-100 (results are reported in Figure 7.7).

No significant marker release was detected before the detergent addition for both CL and GiL systems (data not shown), but when amounts of 1.6E-03 M of TX-100 were added, in a stepwise manner, to 3 ml of liposomes suspension, maintained at 37.0±0.5 °C under stirring, a release of 5-(6) CF occurs.

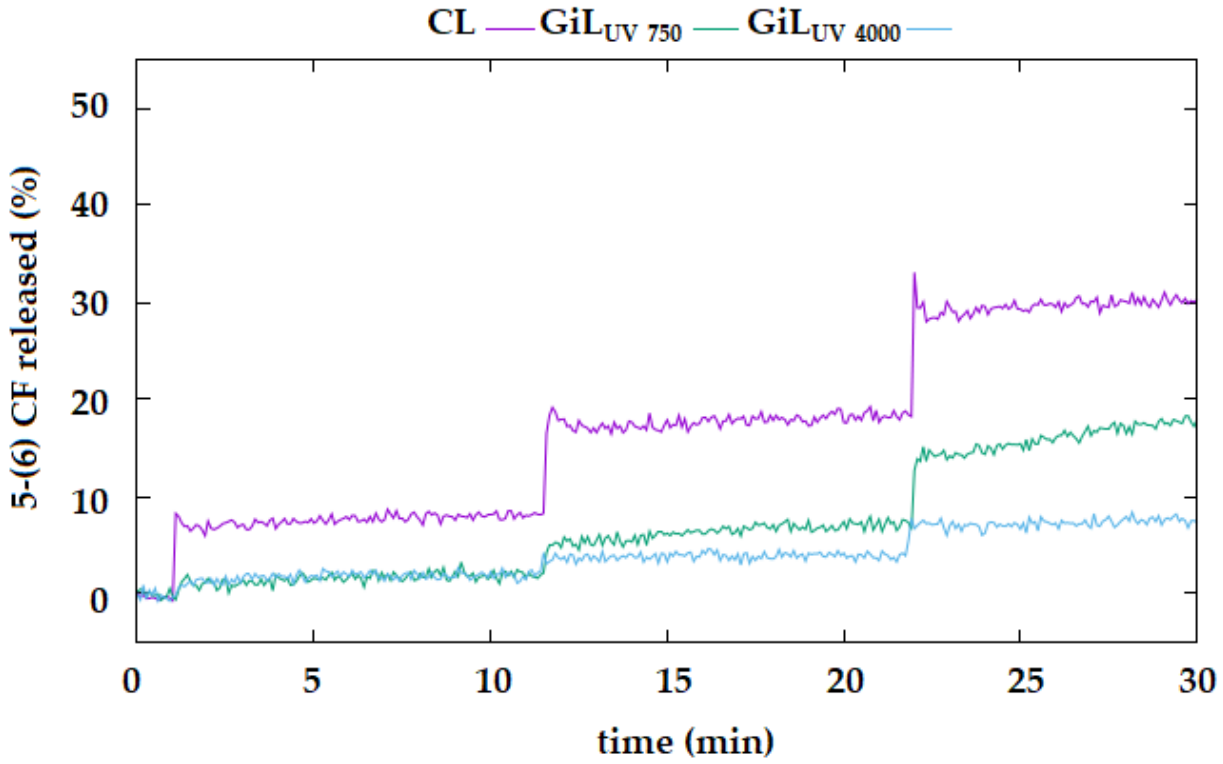


**Figure 7.7. Mechanical destabilization studies of CL, GIL$_{UV\ 750}$ and GIL$_{UV\ 4000}$ induced by the non-ionic surfactant TX-100, at sub-lytic concentration, until three additions.**

In particular, it can be observed that for CL sample, around 10% of the marker is released from the vesicles after the first addition of TX-100. The effect of the surfactant is almost instantaneous, in fact, the fluorescence intensity and so the marker concentration rapidly reaches a constant value. At the same surfactant concentration, the amount of marker released from the GiL structrures is always lower than CL, probably due to the presence of the polymer, which hampers the surfactant penetration into the vesicle membrane, the consequent deleterious effect of the detergent and the marker release. Similar results were obtained with further additions of TX-100 (Figure 7.8).

However, it can be observed that at a certain lipid/TX-100 molar ratio (1:5) the instantaneous release of the fluorescent marker is followed by a continuous slow leakage, particularly evident for GiL$_{UV\ 750}$ systems.

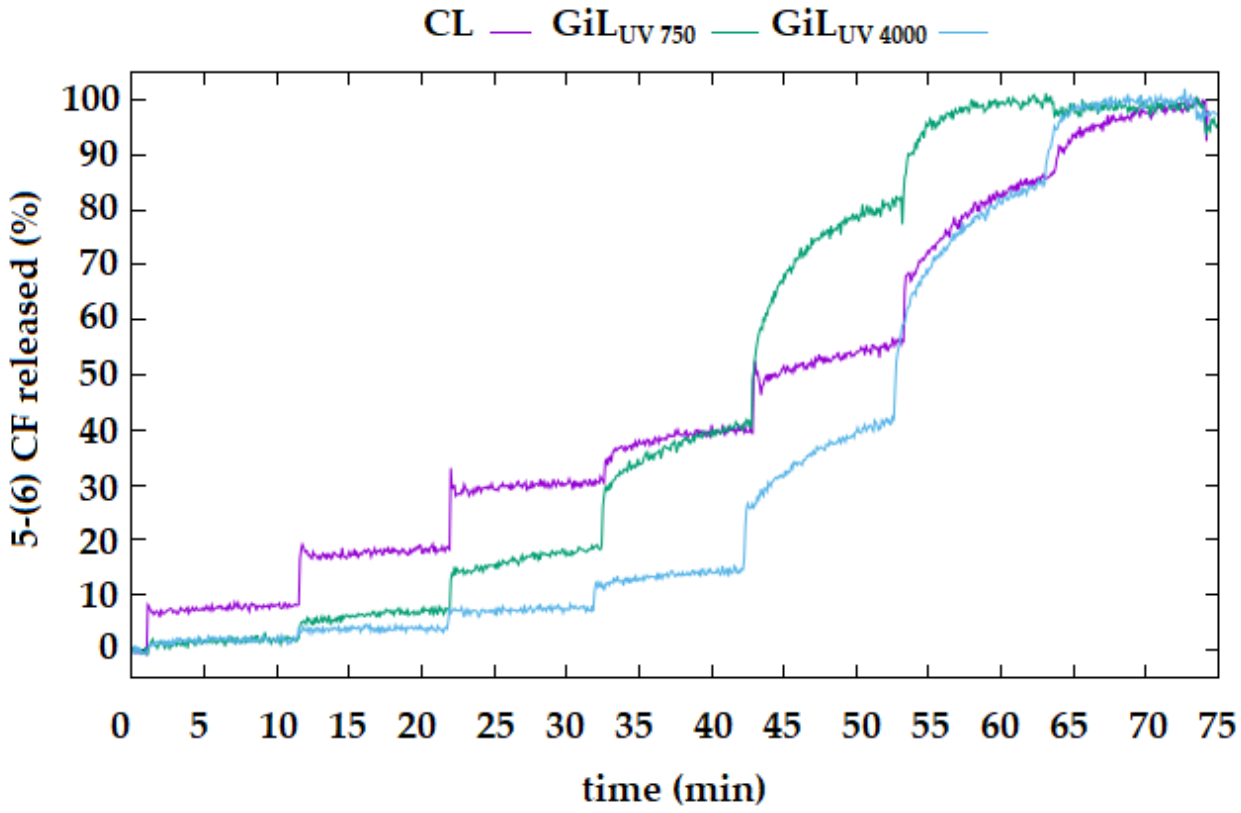


**Figure 7.8. Mechanical destabilization studies of CL, GIL$_{UV\ 750}$ and GIL$_{UV\ 4000}$ induced by the non-ionic surfactant TX-100, at sub-lytic concentration, until the total release of dye entrapped in the core of liposomes.**

We assume that the bilayer perturbation, induced by the non–ionic surfactant, can be influenced by interaction of PEG-DMA with lipids (phospholipids and cholesterol) composing the membrane. The presence of the polymer may affect packing of the lipids and the consequent permeability of the membrane, with a potential final effect, for PEG-DMA$_{750}$ and PEG-DMA$_{4000}$, dependent on the different balance between the hydrophilic and hydrophobic portions of the two polymers. In fact, the presence of PEG-DMA within the membrane may sterically hinder the penetration of surfactant molecules within the bilayer,

contributing to the enhanced mechanical stability of the resulting hybrid systems. This effect is especially evident after the first two additions of TX-100.

On the contrary, after the third surfactant addition a different effect is observed particularly for $GiL_{UV\,750}$ systems. It is probable that, in the presence of the polymer, a non-homogeneous distribution of the molecules of TX-100 is obtained within the phospholipid bilayer. In these domains of the bilayer the detergent/lipid ratio reaches a high value, with a consequent prominent increase of the local permeability of the membrane, responsible for the continuous slow release of the liposomal payload. This effect is less evident with PEG-$DMA_{4000}$, probably due to the predominance of the hydrophilic portion, which may form a more uniform superficial corona, which better prevents the penetration of the surfactant and is responsible for a fewer release of the entrapped dye. Instead, PEG-$DMA_{750}$ may form more localized clusters and expose some regions of the bilayer to the TX-100 attack, where high detergent/lipid ratios are reached.

Overall, these results suggest that the addition of non-lipid components to liposomes may represent an interesting strategy for the modification of the structural and mechanical properties of the bilayer.

### 7.4.3 Release study *in vitro* of 5-(6) CF

The effect of the hydrogel presence, within vesicles, on the release of the encapsulated marker, was investigated, by studying the fluorescence dequenching of the 5-(6) CF from GiL, before and after UV polymerization and was compared with that of the control liposomes.

Results obtained (Figure 7.9), thermostating the systems at 37 °C, showed that hybrid systems release the 5-(6) CF for a prolonged period of time, respect to the conventional vesicles.

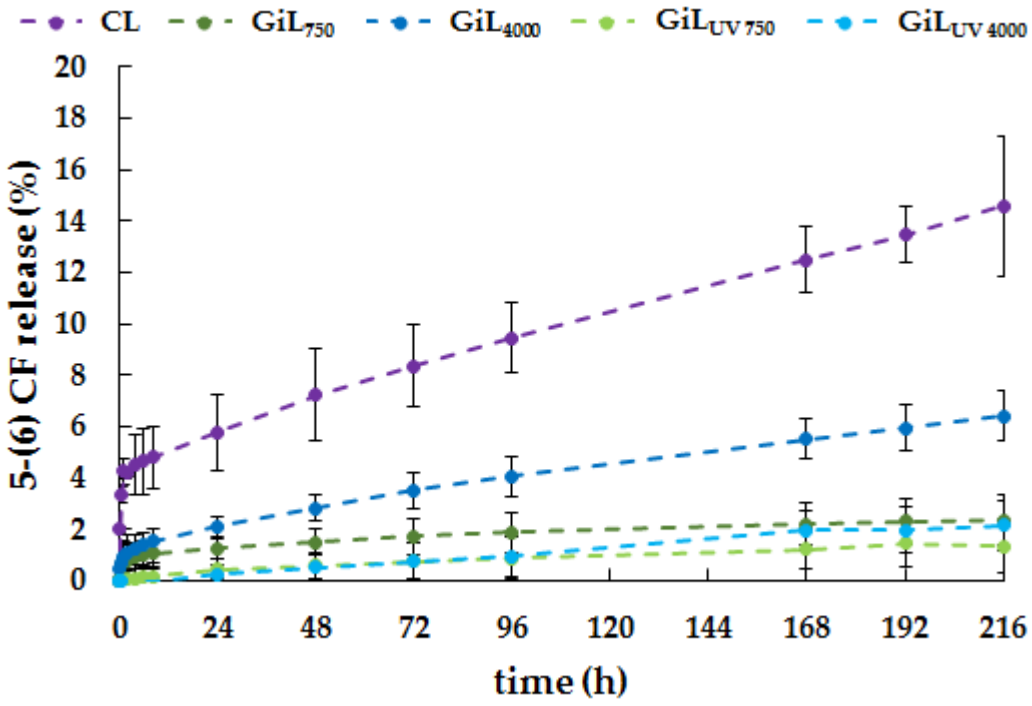


**Figure 7.9. 5-(6) CF release studies from CL, GiL$_{750}$ and GiL$_{4000}$, before and after UV irraditation, at 37 °C. Results were plotted reporting the percentage of fluorescent marker released as a function of time. Values are the mean of three independent experiments ± SD.**

The rate release of the marker seems to be controlled by two diffusion processes: the diffusion through the meshes of the soft polymer hydrogel; the diffusion through the phospholipid bilayer. Perm-selectivity of the membrane can be controlled by the modifications caused from gel precursors on the lipid organization of hybrid structures. In turn, the ability of the gel- forming material to interact with the chain-melted solid state of the lipid bilayer, during vesicles formation, depends on the polymer grade of lipophilia. By changing molecular weight and, thus, the lipophilia of the polymer, it can be possible to alter the 5-(6) CF diffusion across the membrane. In fact, also before the cross-linking process, the major distribution of the PEG-DMA$_{750}$ into the bilayer leads to a significant slowdown in the probe diffusion from the core of GiL$_{750}$ to the bulk of suspension, respect to GiL$_{4000}$, despite the fact that, in both cases, the hydrogel was not already formed. Although these results, highlighted the different release profiles of the hydrophilic marker for CL, GiL$_{750}$ and GiL$_{4000}$, before and after the polymerization, they proved to be not the best

experimental conditions. In fact, below the Tm, the investigations required more than a week to appreciate the different dye percentage released by the liposomal structures. This in accordance with the well know thermotropic behaviour of the investigated bilayer (Tm=52 °C), that, at 37 °C, is all in a sealed ordered state and so less prone to a spontaneous leakage.

To solve this problem, release studies were conducted at T=60 °C, above the main phase transition temperature of the lipid.

The release profile of GiL systems, illustrated in Figure 7.10 (A), supports what already observed in Figure 7.8: polymeric additional components, assembled within the hybrid lipid vesicles, modify the membrane permeability properties, probably interfering with the thermotropic characteristics of the lipid mixture. At 60 °C, HSPC/Chol mixture is in a liquid-crystalline phase that exhibits an increased permeability to the diffusion of the drug. CL sample, in fact, release almost the 90% of 5-(6) CF, already after 2 h. On the contrary, GiL systems after 8 h still retain about the 40% of their vescicular content.

After the UV irradiation, $GiL_{UV\ 750}$ and $GiL_{UV\ 4000}$ structures exhibit once again a prolonged release of 5-(6) CF, respect to the conventional liposomes (Figure 7.10, B), but, in this case, an initial slight inversion in the GiL release trends can be noticed.

We hypothesized that the explanation of this inversion of behaviour, between the $GiL_{UV}$ structures, could be linked to the morphology of the two hydrogels. In Figure 7.6 (B) is shown how in the $GiL_{UV\ 750}$ the nanohydrogel is less densely packed in the central portion, respect to the nanohydrogel in the $GiL_{UV\ 4000}$. The lower presence of cross-linked polymeric chains in the core of the liposomes, could determine a lower ability to retain the probe in the vesicles. Hence, both the two diffusion processes, previously mentioned (the diffusion through the meshes of the hydrogel and the diffusion through the phospholipid bilayer) are facilitated. This evidence becomes more clear especially when the bilayer is in a crystalline liquid phase; in fact, in addition to the minor contribution of the $PEG\text{-}DMA_{750}$ hydrogel on the release, the diffusion of the probe is less hindered also because the perm-selectivity of the membrane increases when the temperature is above the Tm of the lipid. In the case of

PEG-DMA$_{4000}$, instead, both the polymer portion in the bilayer and in the core seem take part in the structuring of the hydrogel (Figure 7.6, C). Therefore, the precence of a thick network of polymeric chains makes GiL$_{UV\ 4000}$, although the increased fluidity of the bilayer linked to the temperature, more able to hold the probe.

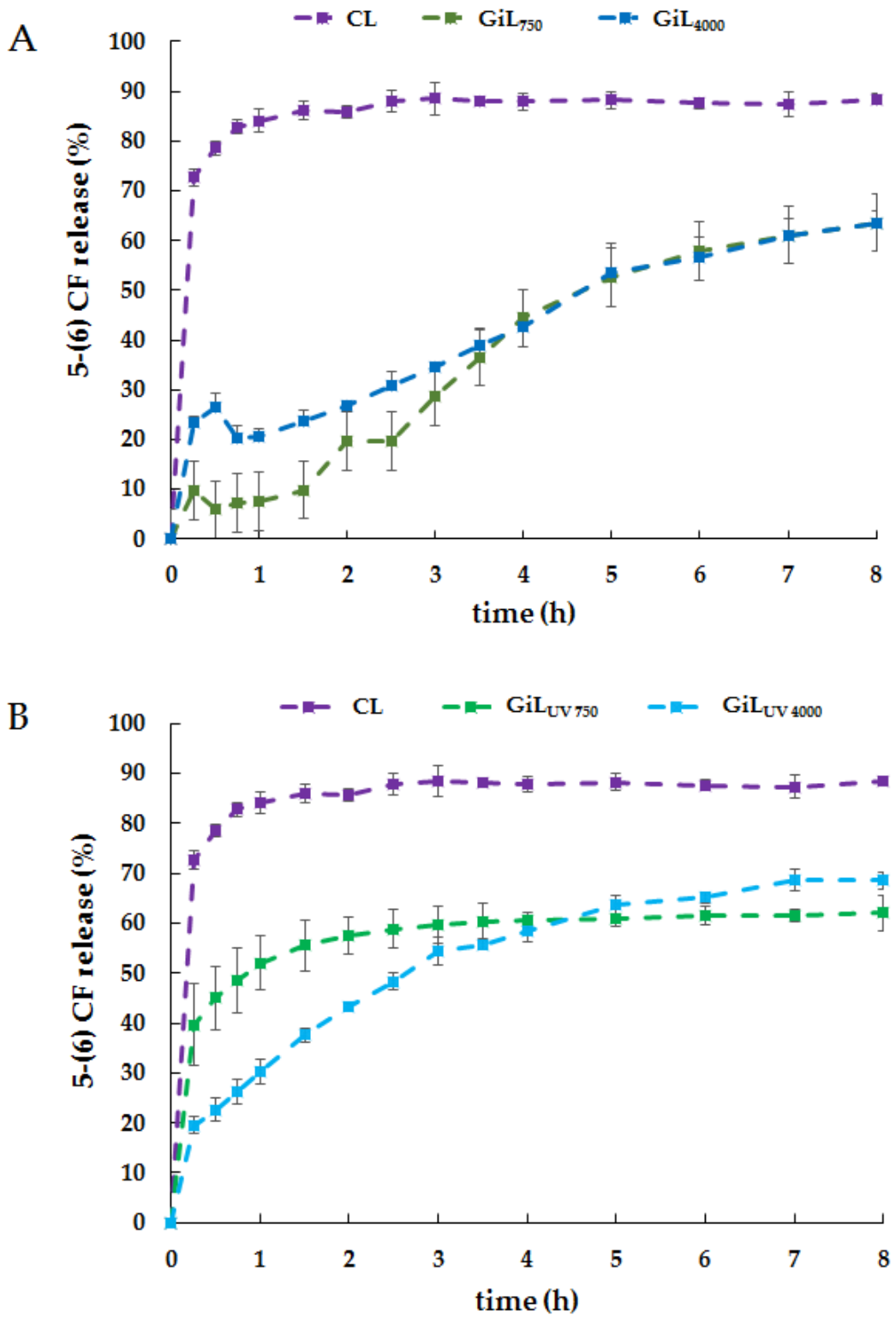


**Figure 7.10. 5-(6) CF release studies from CL, GiL$_{750}$ and GiL$_{4000}$, before (A) and after (B) UV irraditation, at 60 °C. Results were plotted reporting the percentage of fluorescent marker released as a function of time. Values are the mean of three independent experiments ± SD.**

To support the data release and have insight onto the interactions between the polymer and the phospholipid membrane, we performed DSC measurements in anhydrous conditions, since the presence of water molecules could mask the real packing state of the HSPC/Chol/PEG-DMA bilayer. As shown in Figure 7.11 the same quantity of polymer, at the two molecular weight, affects the membrane organization capacity in a different way. On one side, the PEG-DMA$_{750}$, thanks to its affinity for the hydrophobic component, can originate homogeneous bilayer structures consisting of lipids and polymer chains. Thus, the polymer plays an important role in modifying the thermotropic properties, but also the permeability of the membrane. On the other side, PEG-DMA$_{4000}$ confirms its lowered integration in the bilayer, not causing the disappearance of the peak at about 78 °C, which is commonly associated to "cholesterol-rich domain" (the peak at 91 °C is associated to the "cholesterol-poor domain"). Therefore, in HSPC/Chol/PEG-DMA$_{4000}$ systems, the thermotropic behaviour is mainly determined by the presence of cholesterol.

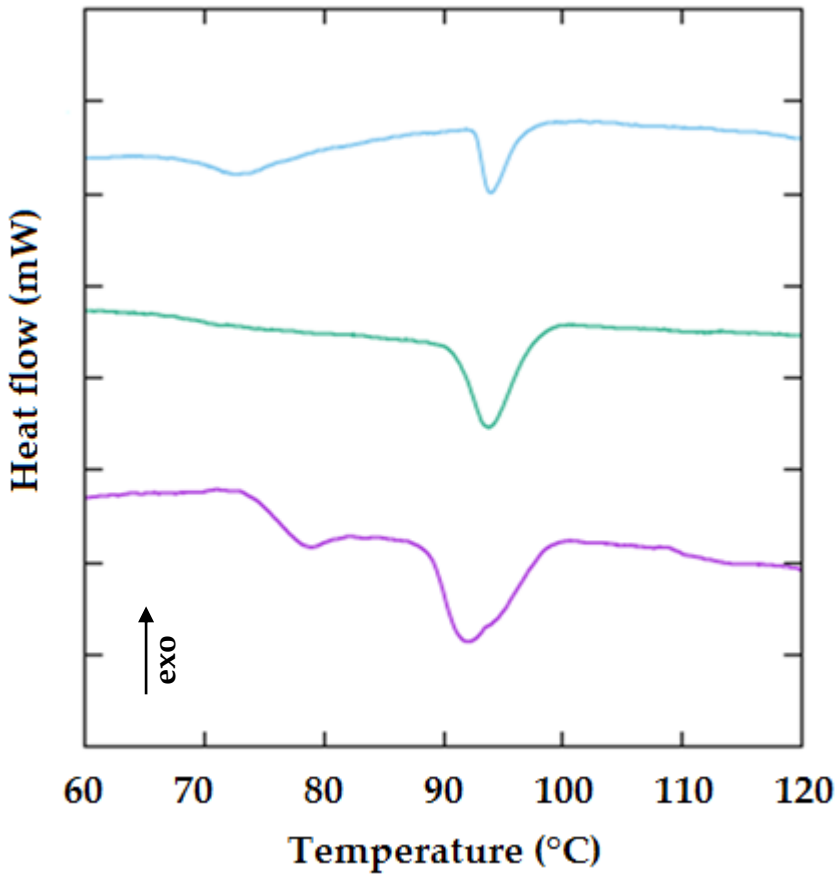

**Figure 7.11. Thermotropic phase behaviour of the hydrogenated soybean phosphatidylcholine-cholesterol (purple line) and PEG-DMA$_{750}$ (green line) or PEG-DMA$_{4000}$ (light blue line) mixture, at scan rate 5 °C/min, in the temperature range 30-170 °C.**

Anyway, the slight shift of the main transition temperature of the hybrid bilayers, towards higher values, suggests that the lipid-polymer interactions stabilize the phospholipid membrane in the ordered phase.

The high mechanical stability and reduced permeability of GiL carriers can be viewed as both positive factor, in particular when a controlled diffusion of drugs through the carrier is required.

## 7.4.4 Cytotoxicity studies

The effect of GiL$_{UV\ 750}$ and GiL$_{UV\ 4000}$ on the mitochondrial function of human fibroblasts, WI-38, was assessed by the MTT reduction test. According to the results reported in Figure 7.12 the hybrid vesicles did not provoke any inhibition of WI-38 proliferation, over the concentration range tested, with the exception of the effect of the highest concentration of PEG-DMA$_{750}$ and only after 96 h of exposure. However, even if statistically significant ($p= 0.04$), that decrease could be considered not biologically relevant as the reduction in cell viability was less than 22%.

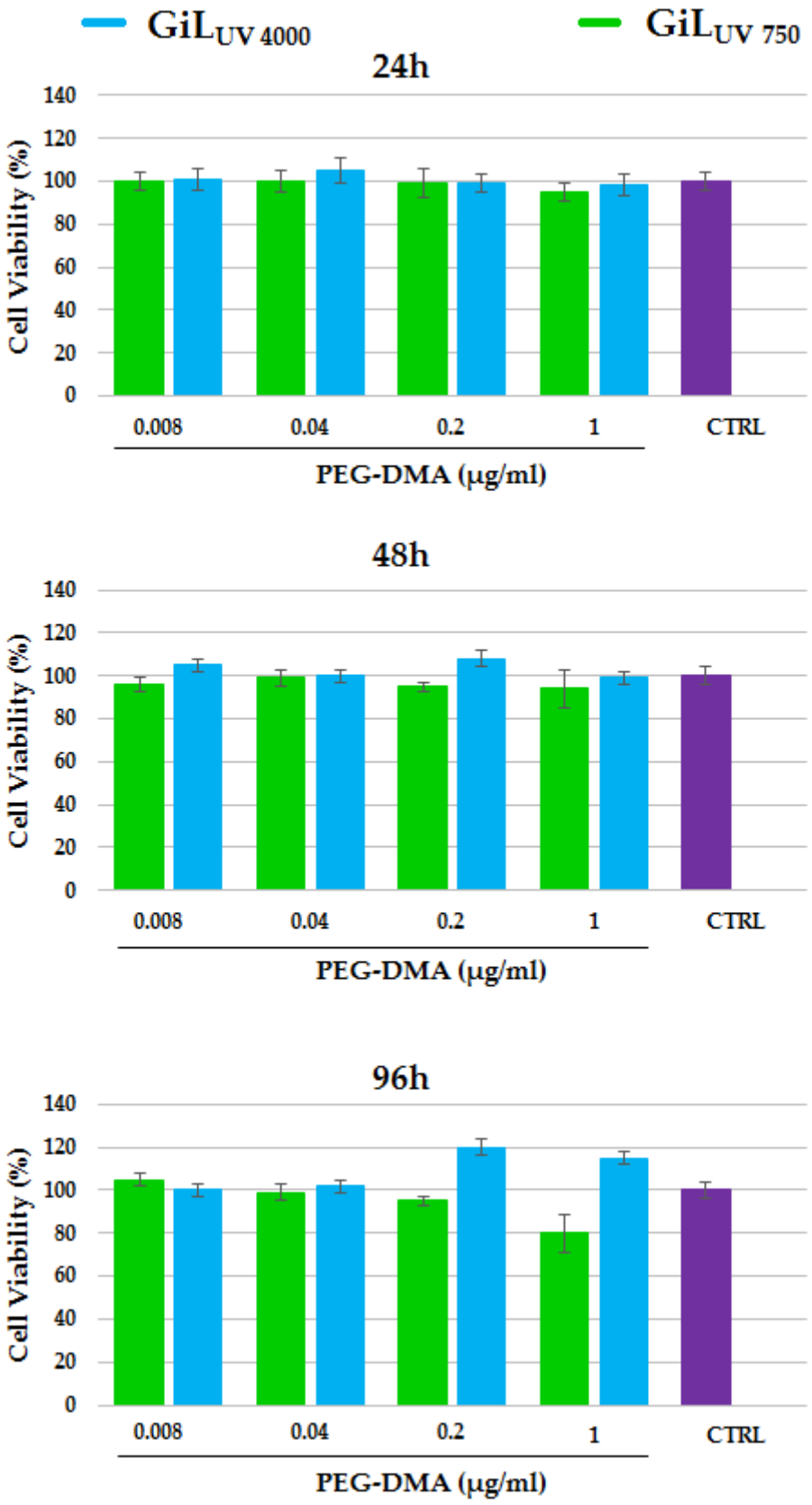


**Figure 7.12. MTT assay performed on WI-38 human fibroblasts at 3 different time points: 24 - 48 - 96 h. Cells were kept in contact with different concentrations of GIL$_{UV\ 750}$ and GIL$_{UV\ 4000}$, ranging from 0.008 to 1 µg/ml. CL samples were used as control.**

## 7.5 Conclusions

PEG-DMA, with different molecular weights and degree of hydrophilicity, HSPC and Chol were combined in appropriate weight ratio in order to obtain GiL hybrid vesicles. The presence of the polymer allowed, upon UV irradiation, the conversion of the aqueous inner core of vesicles into a hydrogel, which did not affect the size and morphology of the novel constructs, respect to the traditional liposomes. The HSPC/PEG-DMA weight ratio, investigated in this work, permitted the direct probe loading during the vesicles formation. The entrapment efficiency of the fluorescent marker was slightly reduced by the presence of the nanohydrogel, whose effective formation in the vesicles core was confirmed by measurements of DLS and TEM, performed after the complete removal of the bilayer. The interactions of the polymer with the liposomal bilayer, compatibly with its lipophilicity, alter the organization of the GiL membrane, with respect to the conventional structures. Specifically, the nanohydrogel seems to modify the bilayer in a more stable and tightly packed membrane. Consequently, the GiL nanocarriers were more resistant than conventional liposomes against a mechanical stress, avoiding any unwanted leakage of the encapsulated compounds, due to defects provided by the possible insertion into the bilayer of surfactants and proteins *in vivo* conditions. Furthermore, the probe diffusion is modified by the presence of the polymeric network. It highlights the possibility of having, with GiL systems, a greater control on the release properties, feature often required in the field of drug delivery. In conclusion, these novel hybrid GiL structures, characterized by enhanced stability, modified release properties and good biocompatibility, can be considered an evolution of the liposomal structure, as well as an effective future drug delivery system.

## 7.6 Supplementary Information (S.I.)

In Figure 7.1 S.I. is reported the calibration curve used to establish the relationship between fluorescent intensity and concentration of 5-(6) CF.

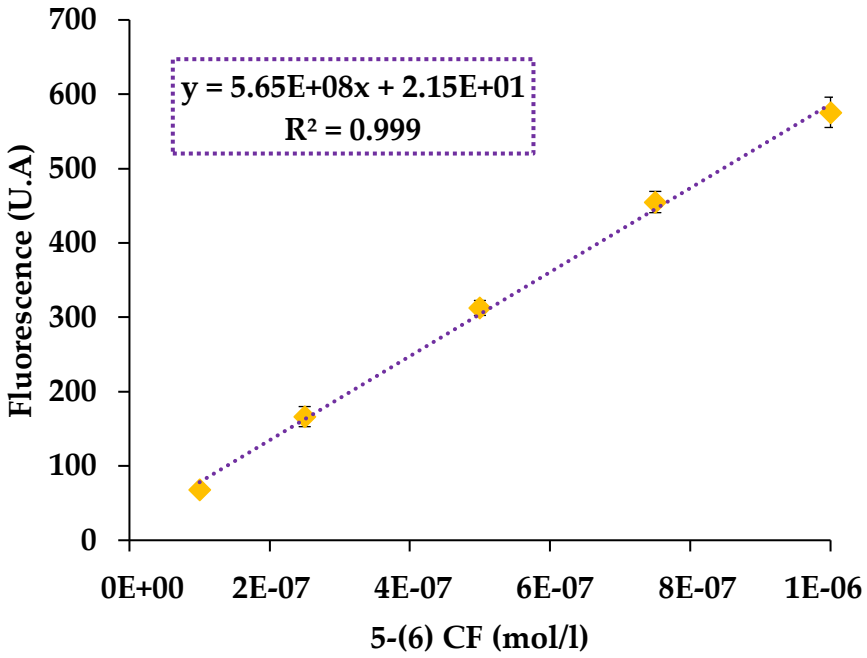


**Figure 7.1 S.I. Calibration curve of 5-(6) CF in HEPES buffer solution, with the respective linear regression.**

Through the calibration line we were also able to quantify the μl of 5-(6) CF trapped in the aqueous core of liposomes for mg of lipid. Specifically, a template was designed to calculate the molarity of the marker for different lipid concentrations, respectively before and after the complete destruction of the vesicles with 30% w/v of TX-100. An example of the determination is reported hereafter in Figure 7.2 S.I.

| Column | | | | | Row |
|---|---|---|---|---|---|
| A | B | C | D | E | 1 |
| Calibration curve | | | | | 2 |
| Fluorescence (U.A.)= 5.65E+08*[(5-(6) CF mol/l]+2.15E+01 | | | | | 3 |
| HSPC (mg/ml) in liposomes | 0.8 | | | | 4 |
| 5-(6) CF (mol/l) for liposomes preparation | 0.02 | | | | 5 |
| | | | | | 6 |
| | 5-(6) CF fluorescence (U.A.) | | 5-(6) CF (mol/l) | | 7 |
| HSPC (mg/l) tested | vesicles | destroyed vesicles | vesicles | destroyed vesicles | 8 |
| 0 | 0 | 0 | 0 | 0 | 9 |
| 4 | 66.61 | 133.21 | 1.17E-07 | 2.35E-07 | 10 |
| 8 | 106.80 | 251.82 | 1.88E-07 | 4.45E-07 | 11 |
| 10 | 132.72 | 301.55 | 2.35E-07 | 5.33E-07 | 12 |
| 12 | 158.33 | 363.41 | 2.80E-07 | 6.42E-07 | 13 |
| | | | | | 14 |
| mol 5-(6) CF / mg HSPC destroyed vesicles | 5.43E-08 | REGR.LIN(E9:E13;A9:A13;FALSE) | | | 15 |
| mol 5-(6) CF/mg HSPC vesicles | 2.38E-08 | REGR.LIN(D9:D13;A9:A13;FALSE) | | | 16 |
| | | | | | 17 |
| mol 5-(6) CF entrapped /mg HSPC | | | 3.05E-08 | B15-B16 | 18 |
| l 5-(6) CF entrapped /mg HSPC | | | 1.53E-06 | D19*B5 | 19 |
| µl 5-(6) CF entrapped /mg HSPC | | | 1.53 | D20*1E+06 | 20 |

**Figure 7.2 S.I. Template used to calculate the capture 5-(6) CF volume in the aqueous core of liposomes prepared in HEPES, by means the linear regression method.**

The results of the photostability study, through which it was possible to confirm the non-influence of UV irradiation on the fluorescence probe and the possibility of the probe direct loading in liposomes, are reported below (Figure 7.3 S.I.).

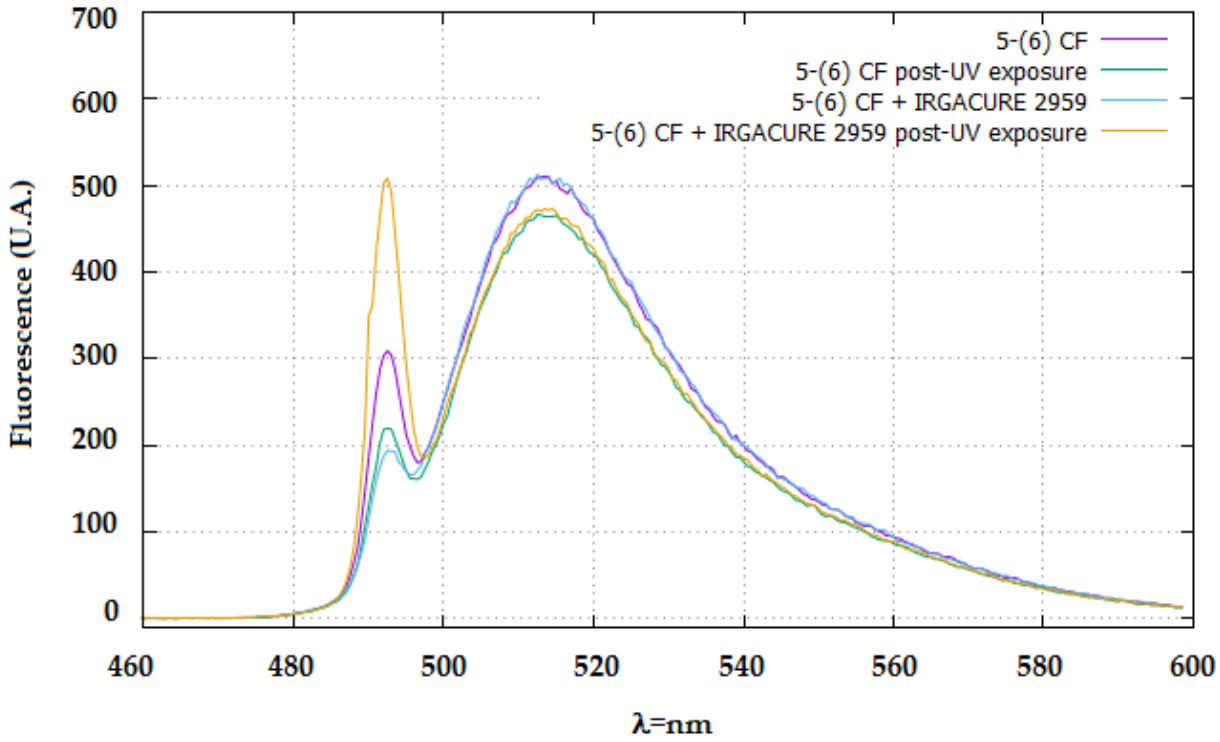


**Figure 7.3 S.I. Study of the influence of the UV irradiation on the fluorescent marker 5-(6) CF. The emission spectra of the probe, at λ=512 nm, pre and post- UV exposure, were recorded in the presence and in the absence of the IRGACURE 2959 radical photoinitiator ($\lambda_{ex}$= 492 nm).**

***Acknowledgements.*** *This work was financially supported by a grant from the "Sapienza" University of Rome.*

## 7.7 References

[1] Elbayoumi, T.A.; Torchilin, V.P. *Current trends in liposome research*. Methods in Molecular Biology. 2010, 605,1-27.

[2] Allen, T.M.; Cullis, P.R. *Liposomal drug delivery systems: from concept to clinical applications*. Adv. Drug Deliver. Rev. 2013, 65(1), 36-48.

[3] von Hoegen, P. *Synthesis biomimetic supra molecular Biovector™ (SMBV™) particles for nasal vaccine delivery*. Advanced Drug Delivery Reviews. 2001, 51, 113-125.

[4] Kiser, P.F.; Wilson, G.; Needham, D. *A synthetic mimic of the secretory granule for drug delivery*. Nature. 1998, 394, 459-462.

[5] Kiser, P.F.; Wilson, G.; Needham, D. *Lipid-coated microgels for the triggered release of doxorubicin*. Journal of Controlled Release. 2000, 68(1), 9-22.

[6] Jin, T.; Pennefather, P.; Lee, P.I. *Lipobeads: a hydrogel anchored lipid vesicle system*. FEBS Letters. 1996, 397(1), 70-74.

[7] Ng, C.C.; Cheng, Y.L.; Pennefather, P.S. *One-Step Synthesis of a Fluorescent Phospholipid-Hydrogel Conjugate for Driving Self-Assembly of Supported Lipid Membranes*. Macromolecules. 2001, 34(17), 5759-5765.

[8] Ng, C.C.; Cheng, Y.L.; Pennefather, P.S. *Properties of a Self-Assembled Phospholipid Membrane Supported on Lipobeads*. Biophysical Journal. 2004, 87(1), 323-331.

[9] Buck, S.; Pennefather, P.S.; Xue, H.Y.; Grant, J.; Cheng, Y.L.; Allen, C.J. *Engineering lipobeads: Properties of the Hydrogel Core and the Lipid Bilayer Shell*. Biomacromolecules. 2004, 5(6), 2230-2237.

[10] Kazakov, S.; Levon, K. *Liposome-nanogel structures for future pharmaceutical applications*. Current Pharmaceutical Design. 2006, 12(36), 4713-4728.

[11] Kazakov, S.; Levon, K. *Lipobeads as Drug Delivery Systems*. NSTI-Nanotech 1. 2006, 467-470.

[12] Kazakov, S.; Kaholek, M.; Levon, K. *Lipobeads and their production*. US Patent 7618565 B2. 2009.

[13] Campillo, C.C.; Schroder, A.P.; Marques, C.M.; Pépin-Donat, B. *Composite gel-filled giant vesicles: Membrane homogeneity and mechanical properties*. Materials Science and Engineering C. 2009, 29(2), 393-397.

[14] Saleem, Q.; Liu, B.; Gradinaru, C.C.; Macdonald, P.M. *Lipogels: Single-Lipid-Bilayer-Enclosed Hydrogel Spheres*. Biomacromolecules. 2011, 12(6), 2364-2374.

[15] Liu, J.; Lu, N.; Li, J.; Weng, Y.; Yuan, B.; Yang, K.; Ma, Y. *Influence of Surface Chemistry on Particle Internalization into Giant Unilamellar Vesicles*. Langmuir. 2013, 29(25), 8039-8045.

[16] Tiwari, S.; Goyal, A.K.; Khatri, K.; Mishra, N.; Vyas, S.P. *Gel core liposomes: An advanced carrier for improved vaccine deliver*. Journal of Microencapsulation. 2009, 26(1), 75-82.

[17] An, E.; Jeong, C.B.; Cha, C.; Kim, D.H.; Lee, H.; Kong, H.; Kim, J.; Kim, J.W. *Fabrication of Microgel-in-Liposome Particles with Improved Water Retention*. Langmuir. 2012, 28(9), 4095-4101.

[18] Helwa, Y.; Dave, N.; Liu, J. *Electrostatically directed liposome adsorption, internalization and fusion on hydrogel microparticles*. Soft Matter. 2013, 9(26), 6151-6158.

[19] Park, J.; Wrzesinski, S.H.; Stern, E.; Look, M.; Criscione, J.; Ragheb, R.; Jay, S.M.; Demento, S.L.; Agawu, A.; Limon, P.L.; Ferrandino, A.F.; Gonzalez, D.; Habermann, A.; Flavell, R.A.; Fahmy, T.M. *Combination delivery of TGF-inhibitor and IL-2 by nanoscale liposomal polymeric gels enhances tumour immunotherapy*. Nature Materials. 2012, 11(10), 895-905.

[20] Papahadjopoulos, D.; Allen, T.M.; Gabizon, A.; Mayhew, E.; Matthay, K.; Huang, S.K.; Lee, K.D.; Woodle, M.C.; Lasic, D.D.; Redemann, C.; Martin, F.J. *Sterically stabilized liposomes: improvements in pharmacokinetics and antitumor therapeutic efficacy.* Proceedings of the Nationals Academy of Sciences of the USA. 1991, 88(24), 11460-11464.

[21] Klibanov, A.L.; Maruyama, K.; Torchilin, V.P.; Huang, L. *Amphipathic polyethyleneglycols effectively prolong the circulation time of liposomes.* FEBS Lett. 1990, 268, 235-237.

[22] Raemdonck, K.; Braeckmans, K.; Demeester, J.; De Smedt, S.C. *Merging the best of both worlds: hybrid lipid-enveloped matrix nanocomposites in drug delivery*. Chem. Soc. Rev. 2014, 43, 444-472.

[23]An, S.Y.; NgocBui, M.P.;Nam, Y.J.; Han, K.N.;Li, C.A.;Choo, J.;Lee, E.K.; Katoh, S.; Kumada, Y.; Seong, G.H. *Preparation of monodisperse and size-controlled poly(ethylene glycol) hydrogel nanoparticles using liposome templates*. J. Colloid Interface Sci. 2009, 331, 98-103.

[24] Petralito, S.; Spera, R.; Pacelli, S.; Relucenti, M.; Familiari, G.; Vitalone, A.; Paolicelli, P.; Casadei, M.A. *Design and development of PEG-DMA gel-in-liposomes as a new tool for drug delivery*. Reactive and functional polymers. 2014, 77, 30-38.

[25] Kazakov, S.; Kaholek, M., Teraoka, I.; Levon, K. *UV-Induced Gelation on Nanometer Scale Using Liposome Reactor*. Macromolecules. 2002, 35(5), 1911– 1920.

[26] Van Thienen, T.G.; Lucas, B.; Flesch, F.M.; van Nostrum, C.F.; Demeester, J.; De Smedt, S.C. *On the Synthesis and Characterization of Biodegradable Dextran Nanogels with Tunable Degradation Properties*. Macromolecules. 2005, 38, 8503–8511.

[27] Torchilin, V.P.; Klibanov, A.L.; Ivanov, N.N.; Ringsdorf, H.; Schlarb, B. *Polymerization of liposome-encapsulated hydrophilic monomers*. Macromolecular Rapid Communications. 1987, 8 (9), 457-460.

[28] Pacelli, S.; Paolicelli, P.; Pepi, F.; Garzoli, S.; Polini, A.; Tita, B.; Vitalone, A.; Casadei, M.A. *Gellan gum and polyethylene glycol dimethacrylate double network hydrogels with improved mechanical properties*. Journal of Polymer Research. 2014, 21, 409.

[29] Yoshida, Y.; Furuya, E.; Tagawa, K. *Direct Colorimetric Method for the Determination of Phospholipids with Dithiocyanatoiron Reagent*. Journal of Biochemistry. 1980, 88, 463-468.

[30] Vitalone, A.; Di Giacomo, S.; Di Sotto, A.; Franchitto, A.; Mammola, C.L.; Mariani, P.; Mastrangelo, S.; Mazzanti, G. *Cassia angustifolia Extract Is Not Hepatotoxic in an in vitro and in vivo Study*. Pharmacology. 2011, 88, 252-259.

## Summary and Conclusions

As whole, this Ph.D. thesis, focused in the nanomedicine panorama, wants to be a multidisciplinary and multiscale approach for the investigation on the feasibility of liposomes as drug delivery systems, improving their characteristics and functionalities. Neverthless liposomes represent interesting carriers, because of their unique properties, some limits still need to be overcome. Thus, several strategies were considered in this research work, in order to design drug delivery carriers which can explain extensively their use in pharmacy and medicine. More in detail, tightening a network of cooperation with other research groups, the attention was focused on twofold aims: from one side the possibility of activating remotely the cargo release from liposomes, under the application of external stimuli; from the other side the chance of increasing the stability of liposomes, modifying their inner compartment.

Among the external stimuli that can be used to trigger the release from these lipid vesicles, the magnetic field was explored. Specifically, in close collaboration with the Department of Information Engineering, Electronics and Telecommunications, the Department of Chemical, Material and Environmental Engineering of Sapienza, University of Rome, and the Unit of Radiation Biology and Human Health of Enea, Research Center of Rome, it was possibile the investigations on the role of $Fe_3O_4$ magnetic nanoparticles (MNPs) in inducing drug delivery from MNPs-containing liposomes, when exposed to a low intensity non-thermal alternating magnetic field (AMF). As reported in **Chapter 3**, apart from the advantage of increasing their stability and reactivity, until to be considered a promising alternative for application in water decontamination, MNPs within phospholipid vesicles, under the AMF, can oscillate next to the liposomes membrane and stimulate only mechanically the release of the encapsulated drug. This magneto-mechanical approach can be used to destabilize both liposomes having membrane in liquid disordered or in liquid ordered, without witnessing the typical involvement of the increase in temperature, linked to the movements of the MNPs in the magneto-hyperthermia strategy. Starting from the

encouraging experimental results obtained using an AMF, produced by a couple of copper square magnetic coils, it was decided to shift the attention on the use of an electromagnetic device already on the market for the treatment of post-traumatic joint diseases, due to its ability to down-regulate specific cytokines in an inflamed environment, thus passing from a laboratory signal to a magnetic one already employed in clinical practice. In **Chapter 4** are reported the results obtained applying a non-thermal pulsed electromagnetic field (PEMF) on high-transition temperature magnetoliposomes (high-Tm MLs). Anyway, as in the AMF case, the MNPs motions, promoted by PEMF, can effectively increase the bilayer permeability of magnetoliposomes. In addition, the content released can be triggered repetitively by switching "on" and "off" the magnetic stimulus, because of the reversible and controllable permeability change of the bilayer, rather than the liposomes rupture. Even if both modalities of magnetic field generation resulted equally efficient in triggering release from magnetic liposomes, the experimental data of **Chapter 4**, obtained applying PEMF, provides not only for an exciting proof-of-concept of the ability of the non-thermal magnetic field stimulus to trigger drug release, but also for a new scenario of enhanced localized treatments, combining the functionalities of the magneto-mechanical actuation and the healing properties of the PEMFs.

Always thanks to the collaboration with the Department of Information Engineering, Electronics and Telecommunications of Sapienza, University of Rome, it was possible to explore the electric field application as external trigger for drug delivery purpose. Specifically, considering that recently ultra short (ns) and high intensity (MV/m) pulsed electric fields (nsPEFs) were proved to be able to permeabilize not only cells membrane, but also the lipid barrier of intracellular organelles, of a much smaller size, without irreversibly damaging their structure, it was thought to use electric signals of nanosecond duration as triggers to remotely control release from nanometer-sized liposomes. As reported in **Chapter 5**, the efficiency of this technique was evaluated experimentally, after a careful characterization of the exposure system, in accordance with the operating conditions

adopted for the electrical stimulations. In particular, the experiments were designed to get an in-depth understanding of the impact of the conductivity on electropermeabilization efficacy. According to the results, the pulses train modify the membrane permeability when the conductivity of the external medium decreases, as indicated by the percentage of probe release, which grows in time after the electric stimulation. On the contrary, no changes in bilayer permeability are observed for the higher conductivity value. From these data it is possible to deduce that the conductivity strongly influences the transmission efficiency of the exposure system, which in this case is represents by a standard electroporation cuvette, as fully described in **Chapter 5**. The experimental evidences were further supported and confirmed by a numerical model that provided a density of pore above the threshold of membrane poration for the operating conditions adopted. These preliminary studies conducted numerically and experimentally, demonstrated for the first time that nsPEFs can actually trigger the permeation of nanometric lipid-based carriers, representing a promising way to remotely induce the transient simultaneous electropermeabilization of cellular and liposomal membrane, thus promoting the direct passage of drugs from the carrier to the target.

Within the research project "Toward the comprehension of primary bioelectromagnetic interactions: non-linear real time OPTICal imaging of BIO-samples under ElectroMagnetic exposure (OPTIC BIOEM)", and thanks to the collaboration with the Joint Research Unit of the CNRS of the University of Southern Paris and the Unit of Radiation Biology and Human Health of Enea, Research Center of Rome, it was possible to investigate the bio-physical mechanisms underlying the membrane electropermeabilization process of lipid nanocarriers. In this context, I had the opportunity to spend part of the second year of my Ph.D. at the Gustave Roussy, Oncological Institute in Paris. Here it was tried to solve experimentally the complex puzzle of mechanisms at the bases of electropermeabilization. Since non-linear optics techniques are among the best candidates for these purposes, allowing the label free and fast acquisition of vibration modes of specific chemical bound in

samples analyzed, Coherent Anti-Stokes Raman Scattering (CARS) technique was successfully employed. In detail, in this project CARS spectroscopy was used for the first time with a time resolution of few ns, comparable to the time scale of the applied electric pulses, in order to deep insight into all the steps of vesicles permeabilization. Liposomes were used as test sample since they represent very stable spherical phospholipid bilayers for the comprehension of electropermeabilization and because of their feasible future implication in new biomedical technologies, in the area of smart drug delivery mediated by the electric pulses (as also described in **Chapter 5**). Novel observations of spectral features originating from the interfacial and the interstitial water in the CARS spectra of liposomes, acquired in real-time modality and immediately after nanosecond pulses electric field exposure, were reported in **Chapter 6**. The presence of single water molecules of the interstitial phase more associated to lipid heads, observed for the first time at the instant of each pulse delivery, suggested that the increased permeability of liposomes could be related to the local defects in bilayer, promoted by the insertion of water molecules within the phospholipids. Furthermore, the persistent interposition of water molecules seems important in modulating and controlling over time the membrane organization and its permeability, on which depends the release profile of these nanocarries. All these results bring new information about the electropermeabilized state of the membranes after the pulses delivery, characterized by a facilitated transport of hydrophilic molecules across the membrane.

Finally, in the contrail of the recent interesting results, obtained in terms of physical stabilization of liposomal bilayer following modification of the aqueous core, in **Chapter 7** is described an innovative approach to design hybrid liposomes as drug delivery systems, with improved vesicles stability and modified release properties. More specifically, PEG-DMA$_{750}$ and PEG-DMA$_{4000}$ were encapsulated within the aqueous core of liposomes without affecting the possibility to load weak acid drugs, which represents a very important aspect for drug delivery applications. When PEG-DMA cross-linking was induced, the liposomal

fluid core was turned into a soft and elastic hydrogel, as verified through TEM and DLS analysis, after the complete removal of the bilayer with lytic concentration of a non-ionic detergent. The different degree of hydrophilicity of the two PEG-DMA results in a different distribution of the polymer in the novel Gel-in-Liposome (GiL) hybrid structures, and furthermore, in a different structural aspect of the nanohydrogels observed through TEM investigation. Mechanical and thermal destabilization tests showed how these hybrid systems result in more stable carriers, as compared to conventional liposomes, satisfying, at the same time, the biocompatibility criteria expected for a drug delivery system. Therefore, these Gel-in-Liposome constructs meet the requirement for an effective drug delivery system and offer a convenient new way of envisioning lipid vesicles and further broadening their clinical impact.

# Appendix

In this Ph.D. thesis the efficacy of conventional liposomal systems in improving the pharmacological potential of natural substances, defined "poorly water-soluble drugs", was also evaluated. Specifically, in this section is reported the ability of the soy phosphatidylcholine-based liposomes in increasing the bioavailability and the absorption of the natural sesquiterpene β-caryophyllene in cancer cells.

Part of this Ph.D. thesis was also focused on the synthesis and characterization of polymeric systems. Specifically, below are reported several strategies in order to engineer different polysaccharides and, finally, employing them to design hydrogels and oral thin films as new tools for specific applications in drug delivery.

# SPC liposomes as possible delivery systems for improving bioavailability of the natural sesquiterpene β-caryophyllene: lamellarity and drug-loading as key features for a rational drug delivery design

Antonella Di Sotto[1], Patrizia Paolicelli[2], Martina Nardoni[2], Lorena Abete[1], Stefania Garzoli[2], Silvia Di Giacomo[1], Gabriela Mazzanti[1], Maria Antonietta Casadei[2], Stefania Petralito[2]

[1]*Department of Physiology and Pharmacology "V. Erspamer", "Sapienza" University of Rome, Piazzale Aldo Moro 5, 00185 Rome, Italy*

[2]*Department of Drug Chemistry and Technologies, "Sapienza" University of Rome, Piazzale Aldo Moro 5, 00185 Rome, Italy*

**Accepted [Pharmaceutics, ISSN 1999-4923]**

***Abstract.*** *The natural sesquiterpene β-caryophyllene (CRY) has been highlighted to possess interesting pharmacological potentials, particularly due to its chemopreventive and analgesic properties. However, the poor solubility of this sesquiterpene in aqueous fluids can hinder its uptake into cells, resulting in inconstant responses of biological systems, thus limiting its application. Therefore, identifying a suitable pharmaceutical form for increasing CRY bioavailability represents an important need for exploiting its pharmacological potential. In the present study, the ability of soybean phosphatidylcholine (SPC) liposomes to improve bioavailability and absorption of CRY in cancer cells has been evaluated. Liposomal formulations of CRY, differing for lamellarity (i.e. unilamellar and multilamellar vesicles or ULV and MLV) and for the drug loading (i.e. 1:0.1, 1:0.3 and 1:0.5 mol/mol between SPC and CRY) were designed with the aim of maximizing CRY amount in the liposome bilayer, while avoiding its leakage during storage. The low-loaded formulations significantly potentiated the antiproliferative activity of CRY in both HepG2 and MDA-MB-468 cells, reaching a maximum IC50 lowering (from two to five folds) with 1:0.3 and 1:0.1 SPC/CRY MLV. Conversely, increasing liposome drug-loading reduced the ability for CRY release, likely due to a possible interaction between SPC and CRY that affects the membrane properties, as confirmed by physical measures.*

***Keywords:*** *lipophilic compound; sesquiterpene β-caryophyllene; antiproliferative activity; liposomes; lamellarity; drug loading.*

***Graphical abstract.***

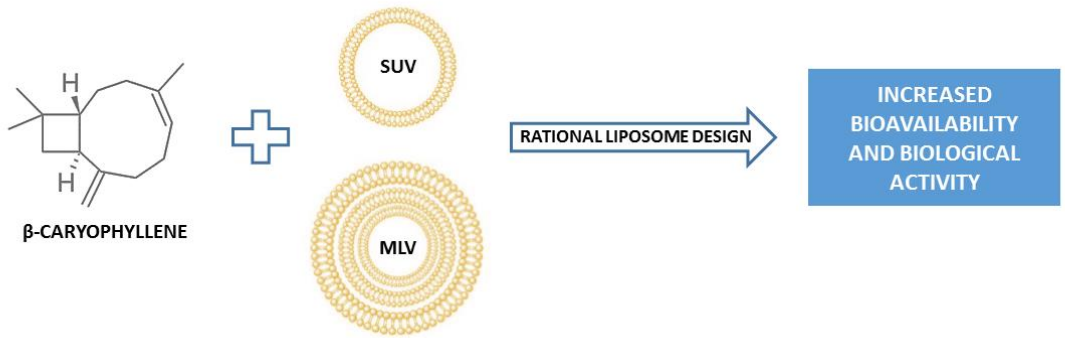

## 1. Introduction

β-caryophyllene or (-)-trans-caryophyllene (CRY), a bicyclic sesquiterpene with a rare cyclobutane ring (Figure 1), is a volatile compound, found in large amounts in the essential oil of many different spice and food plants, particularly from *Eugenia caryophyllata* L., *Copaifera multijuga* (copaiba) and *Cannabis sativa* L [1].

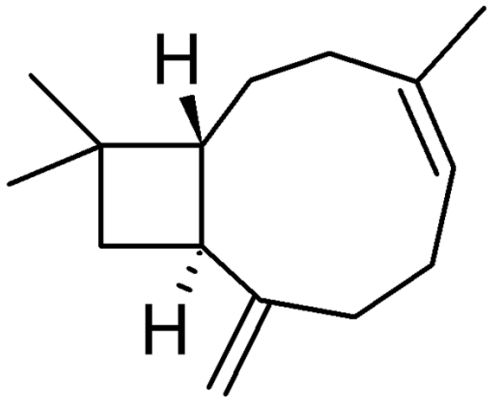


**Figure 1. Chemical structure of β-caryophyllene.**

In nature, β-caryophyllene is usually found together with small amount of its isomers α-caryophyllene and γ-caryophyllene or in a mixture with its oxidation product, β-caryophyllene oxide. Several biological activities have been reported for β-caryophyllene, including antimicrobial, antileishmanial, antimalarial, local anesthetic, spasmolytic and anticonvulsivant activities [2]. It has been reported to partly act as an agonist of CB2 receptor, which represents a therapeutic target for the treatment of inflammation, pain, atherosclerosis, and inflammatory-based diseases, including colitis, cerebral ischemia and brain inflammation [3-7]. Also, it has been recently shown to possess chemopreventive properties [1, 8-11] and displayed a chemosensitizing power when administered in combination with anticancer drugs, thus resensitizing chemoresistant cancer cells [12]. It was found able to interfere with targeted signalling pathways involved in inflammation and cancer, including HMGB1/TLR4 signalling and STAT3 [10, 13-14]. Despite these promising biological activities, β-caryophyllene is characterized by high lipophilicity and poor stability

in hydrophilic media (such as biological fluids), which limit its bioavailability and absorption into cell. Bioavailability depends on nature and chemical-physical properties of a molecule and is mainly due to water solubility (or dissolution rate) and membrane permeability [15]. Low bioavailability is a common feature for different natural substances, defined as "poorly water-soluble drugs", and can hinder their administration, clinical application and market entry. In this context, improving bioavailability represents an important requirement for exploiting the pharmacological potential of such natural substances and sustain the need of suitable pharmaceutical formulations. To this end, various strategies, including formulation in complex forms as micelles, liposomes, polymeric nanoparticles and lipid nanoparticles, have been approached. Among them, liposomes have been extensively applied in the years as biomembrane models and as drug carriers in the pharmaceutical and medical fields, owing to their excellent biocompatibility and biodegradability, low toxicity and lack of immunogenicity [16-17]. They have been also adopted as efficient systems for incorporating natural compounds, such as essential oil components, and improving their solubility and chemical stability [18]. Liposome structure allows the incorporation of different types of drugs: hydrophilic substances are encapsulated in the inner aqueous compartments, while lipophilic drugs are mainly entrapped within the lipid bilayer [19]. According to lamellarity and size, they are usually classified as multilamellar vesicles (MLV; greater than 0.5 μm), small unilamellar vesicles (SUV; between 20 and 100 nm) and large unilamellar vesicles (LUV; greater than 100 nm) [20]. Taking into account the strong lipophilicity of CRY and its low dissolution rate in biological fluids, in the present study, we propose a rational design of soy phosphatidylcholine (SPC) liposomal formulations for improving cellular uptake of CRY and then its antiproliferative activity in cancer cells, focusing on lamellarity and drug-loading as major key features to develop optimized delivery systems. SPC is commonly used in different types of drug delivery formulations, due to its structural similarity with biomembrane phospholipids, and seems to represent an interesting molecule to be used for designing liposomal chemotherapy formulations, since it could enhance the

antiproliferative activity of anticancer drugs, by affecting the cholesterol-induced stiffening of cancer cell biomembrane, thus favoring drug permeability. It is well accepted that cancer cells, respect to normal cells, are characterized by changes in biomembrane phospholipid composition and a constitutive activation of the fatty acid biosynthesis seems to support the increased cell proliferation [21]. Particularly, higher accumulation of cholesterol leads to a more rigid and low-permeable membrane, with increased resistance to cancer chemotherapy. In order to characterize the best features of SPC liposomes in improving dissolution of CRY in biological fluids and its cellular uptake, both unilamellar (ULV) and multilamellar (MLV) formulations were studied. In fact, due to the physico-chemical properties of CRY, it is expected that the drug is incorporated within the phospholipid bilayer of liposomes. Therefore, liposomal formulations of CRY have been rationally designed taking into account that loading of CRY in the bilayer of liposomes, while avoiding its leakage during storage, requires special consideration in product development and represents a key feature for optimizing the formulation. The lipid composition, lamellarity, the manufacturing process and drug incorporation can all influence the physicochemical properties of a liposomal formulation, including the drug release performance. Therefore, when liposomes are investigated as drug delivery vehicles of hydrophobic drugs, the influence of drug-lipid ratio on the arrangement of the nonpolar region of the vesicles membrane should be considered to design a delivery vehicle that is at the same time able to catch and release the encapsulated payload in order to achieve the therapeutic purpose [22]. In line with this evidence, in the present study, different formulations at three loading degree, characterized by SPC phospholipid and CRY molar ratio of 1:0.1, 1:0.3 and 1:0.5, as well as different lamellarity were prepared. A physicochemical characterization by dynamic light scattering, fluorescence anisotropy and entrapment efficiency of CRY were performed. The increased bioavailability was evaluated on the basis of the cytotoxicity potency of the formulations encapsulating CRY with respect to the substance alone. In specific, the antiproliferative activity of CRY-loaded SPC ULV and MLV respect to that of CRY alone as

studied in liver cancer HepG2cells. Also, triple negative MDA-MB-468 breast cancer cells were used being high-responsive to CRY cytotoxicity respect to HepG2 cells.

## 2. Materials and Methods

### *2.1. Materials*

β-Caryophyllene (CRY >98.5% purity), soybean phosphatidylcholine (Phospholipon90, SPC), HEPES [4-(2-hydroxyethyl) piperazine-1-ethane-sulfonic acid], thiocyanatoiron (III), 1,6-Diphenyl-1,3,5-hexatriene (DPH), cholesterol (Chol) and (4,5-dimethyl-2-thiazolyl)-2,5-diphenyl-2H-tetrazolium bromide (MTT, ≥97.5% purity), were purchased from Sigma-Aldrich Co (St. Louis, MO, USA). Dulbecco's Modified Eagle's medium (DMEM) was from Aurogene (Rome, Italy). Chloroform, dimethyl sulfoxide, ethanol, 1,2-dicloroethane and hydrochloric acid were supplied by Carlo Erba Reagents (Arese, Italy) and were of analytical grade. All solutions were prepared in the better solvent, sterilized by filtration and stored for a just conservation time, at recommended temperature, e.g room temperature or refrigerated conditions (from 4 °C to -20 °C). For the cytotoxicity assay, the sesquiterpene was dissolved in absolute ethanol (100% v/v) at the tested concentrations. The percentage of ethanol was less than 1% v/v in the final mixture, in order to exclude a potential toxicity due to the solvent. Conversely, both the CRY-loaded and plain SPC liposomes were directly dispersed in the culture medium, at different concentrations.

### *2.2. Liposome preparation*

Liposomes were prepared by the thin-film hydration method followed by extrusion [23]. In specific, 250 mg of SPC and different amount of CRY (7, 20 or 33 mg) were dissolved in a 50 mL round-bottom flask in the minimum volume of chloroform to give lipid-to-drug molar ratio of 1:0.1, 1:0.3 and 1:0.5. The solvent was removed by rotary evaporation under reduced pressure to form a thin layer on the flask wall. The resultant thin film was further dried with a high vacuum oil pump for at least 2 h. Dried film was hydrated in 5 mL of a 10 mM HEPES

buffer solution (pH 7.4) at 25 °C and the dispersion was shaken vigorously with a vortex mixer to form multi-lamellar vesicles (MLV). The generated multilamellar vesicles were repeatedly extruded at 25 °C through polycarbonate membranes of decreasing pore size using a thermobarrel Extruder, (Lipex Biomembrane, Canada) until a defined size distribution was achieved (2 times through 400 nm membranes and finally 6 times through 200 nm membranes). All liposome formulations were flushed with nitrogen gas, stored at 4 °C and used within two weeks.

*2.3. Gas chromatographic-mass spectrometric (GC-MS)*

Purity of CRY and its concentration obtained in the liposomal dispersion was determined by gas chromatographic/mass spectrometric (GC-MS) technique. The GC-MS analyses were performed on a Clarus 500 series from Perkin Elmer instruments (Waltham, MA, USA) operating in the electron impact mode (70 eV) and equipped with NIST libraries. A Stabilwax fused-silica capillary column (Restek, Bellefonte, PA, USA) (60 m x 0.25 mm, 0.25 mm film thickness) was used with helium as carrier gas (1.0 mL/min). 1 μL of sample was injected into the GC injector at the temperature of 280 °C and in splitless mode. The oven of GC was programmed to rise from 90 °C to 200 °C at 3 °C/min and then held at 200 °C for 2 min. All analyses were performed at constant flow. A calibration curve was generated by running various solutions containing graded amounts of the CRY and injecting a constant volume of each standard solution exactly measured. The calibration curve was obtained by plotting the peaks area (automatically calculated by the computer) on the ordinate and the amounts on the abscissa.

*2.4. Physicochemical characterization of liposomes*

*2.4.1. Dynamic light scattering and ζ-potential measurements*

Particle size distribution and ζ-potential were measured with a Zetasizer Nano ZS90 (Malvern Instruments Ltd., UK). Hydrodynamic diameter and polydispersity index were

evaluated by dynamic light scattering (DLS) experiments, whereas ζ-potential was measured by electrophoretic light scattering (ELS) experiments. The DLS and ELS techniques used a photon correlator spectrometer, equipped with a 4 mW He/Ne laser source operating at 633 nm. All measurements were performed at a scattering angle of 90° and were thermostatically controlled at 25 °C. Size, polydispersity index and ζ-potential values of the liposome formulations are the mean of three different preparation batches ± standard deviation.

*2.4.2. Phospholipid assay*

Phospholipid content in liposomes was quantified as reported in literature [24]. Briefly, 0.4 ml of sample (20–200 nmol) was mixed with 0.2 ml of ethanol, 1 ml of thiocyanatoiron (III) and 0.6 ml of 0.17 N hydrochloric acid. 3 ml of 1,2-dichloroethane were added to extract the thiocyanatoiron–phospholipid complex formed after shaking for 2 min. The sample was then centrifuged for 5 min at 12,000 rpm. The absorbance of the organic phase was read at a wavelength of 470 nm in a Lambda 25 spectrophotometer (Perkin Elmer, USA). The calibration curve was obtained with several solutions of known SPC concentration.

*2.4.3. Evaluation of CRY loading in liposomes*

Phospholipids and drug molecules dissolved in the organic phase may be get lost during solvent removal under vacuum and high-pressure extrusion steps. Considering that CRY is a liquid with a starting boiling point of 129 °C, to evaluate the amount of the sequiterpene actually present in the different liposomal formulations, it was first extracted from vesicles and then its concentration was determined by the GC-MS technique reported in section 2.3. Particularly, 5 mL of CRY-loaded SPC ULV were diluted with 10 mL of 10 mM HEPES (pH 7.4) and extracted with $CHCl_3$ (5 mL). To promote the separation of the two phases, $CaCl_2$ (460 mg) was added to the biphasic system and the organic phase then collected. The extraction procedure was repeated three times, all the organic phases were mixed and made up to known volume before GC-MS analysis.

*2.4.4. Steady-state and time resolved fluorescence measurements*

Steady state anisotropy of DPH in liposomes was measured to assess the effect of CRY and its concentration on the fluidity of SPC liposome membranes. To this end, DPH-loaded SPC liposomes were prepared by the thin-film hydration method reported in section 2.2, dissolving SPC (250 mg) and DPH (0.15 mg; $6.46 \cdot 10^{-4}$ mmol) in a 50 mL round-bottom flask in the minimum volume of chloroform to give lipid-to-DPH molar ratio of 1:0.002. The solvent was removed as previously described and the resultant thin film was hydrated in 5 mL of a 10 mM HEPES buffer solution (pH 7.4) at 25 °C. The generated multilamellar vesicles were repeatedly extruded at 25 °C through polycarbonate membranes of decreasing pore size. DPH normally is located within the hydrophobic region of the bilayer membrane. DPH responds to changes in physical properties of the acyl chain region of the membrane that affect its ability to rotate. Probe movement is quantified by measuring the degree to which DPH fluorescence emission is depolarized following excitation by polarized light. These fluorescence anisotropy measurements respond to changes in the order degree of the DPH surrounding environment: changes in the liquid-crystalline state organization of the liposome membrane alter the rate of probe movement; in particular, more disordered the membrane environment, the greater is the motional freedom of the fluorophore and hence the lower the observed anisotropy. An increase in steady state anisotropy of DPH in membranes may imply a reduction in mobility of lipids. Steady-state fluorescence anisotropy measurements, for DPH-loaded liposomes, were carried out at room temperature with a Perkin-Elmer LS50B spectrofluorometer. The excitation and emission wavelengths were 350 and 450 nm, respectively, and all slits were set to a width of 2.5/2.5 nm. Samples, opportunely diluted with 10 mM HEPES buffer pH 7.4, were illuminated by vertically (V) or horizontally (H) polarized monochromatic light at $\lambda$=350 nm and the emitted fluorescence intensities (I) parallel or perpendicular to the direction of the excitation beam were recorded at $\lambda$=450 nm. Total fluorescence intensity $\left[I_f = \left(I_{/\!/}\right)V + 2G(I_{\perp})H\right]$ is obtained by addition of the respectively horizontally $[I_{\perp}]$ and vertically $\left[I_{/\!/}\right]$ intensities

polarised light emission. The stationary fluorescence anisotropy (r) was determined using the typical Equation:

$$r = \frac{(I_{/\!/})V - G(I_{\perp})H}{I_f} \quad (1)$$

Total fluorescence intensity and anisotropy measurements required correction for the gain of photomultipler detector $[G = (I_{/\!/})H/(I_{\perp})H]$. The effect of CRY incorporation on the phospholipid bilayer of SPC liposomes was evaluated by comparison with the well-known effect produced by cholesterol (Chol) on the membrane behaviour. Anisotropy data are represented as the mean ± SD.

*2.5 Cytotoxicity studies*

*2.5.1 Human cancer cell lines*

Liver cancer HepG2 cells were a kind gift of Prof. Eufemi (Sapienza University of Rome, Italy), while triple negative MDA-MB-468 breast cancer cells were purchased from IRCCS AOUSan Martino - IST (Genoa, Italy). The cells were grown under standard conditions (37 °C and 5% $CO_2$) in DMEM-F12 medium containing L-glutamine (1% v/v) and HEPES (15 mM) and supplemented with 10% heat-inactivated FBS, 100 U/mL penicillin and 100 μg/mL streptomycin in 75 $cm^2$ flasks. Subcultures were prepared every 4 days, renewing growth medium every 2-3 days. All experiments were performed when cells reached the logarithmic growth phase.

*2.5.2 Cytotoxicity assay*

The cultured cells were seeded into 96-well microplates (20,000 cells/well), allowed to grow for 24 h, then treated with CRY (1 - 75 μg/mL in EtOH 1 % v/v) or CRY loaded SPC liposomes. The concentrations of pure CRY were prepared by progressive dilution in EtOH 100% v/v, then added to cells at 1% v/v in the final mixture, at which ethanol was nontoxic. A vehicle control (EtOH 1% v/v in the final mixture for CRY and 10 mM HEPES for SPC

ULV and MLV), corresponding to 100% cell viability and a standard cytotoxic agent (i.e. doxorubicin, 10 μg/mL in the final mixture) were also included in the experiments. After 24 h incubation, the cytotoxicity of the treatment was measured by the 3-[4,5-dimethylthiazol-2-yl]-2,5-diphenyl tetrazolium bromide (MTT) assay according to previous published methods [25]. The assay was carried out at least in three biological replicates and in each experiment, each concentration was tested in six technical triplicates. The treatment was considered cytotoxic when the cell viability was lower than 70% with respect to vehicle treated cells [26]. The results were expressed as percentage of cell viability (about three experiments including 8-10 replicates for each treatment) with respect to the vehicle.

Results of cytotoxicity studies are expressed as mean ± SE. The concentration–response curves were constructed using the Hill Equation (2):

$$E = \frac{E_{max}}{[1 + (10^{logIC50 - A)\,Hill\,Slope}]} \quad (2)$$

where E is the effect at a given concentration of the substance, $E_{max}$ is the maximum activity, IC50 is the concentration that produces a 50% of the inhibitory response, A is the substance molar concentration, HillSlope is the curve slope.

### *2.6 Statistical analysis*

Statistical analysis was performed by GraphPad Prism™ (Version 4.00) software (GraphPad Software, Inc., San Diego, California, USA). The one-way analysis of variance (one-way ANOVA), followed by Dunnett's Multiple Comparison Post Test, was used to analyze the difference among different treatments, while the Student's t-test was applied to determine the statistical significance between two different experimental conditions. The values of $P < 0.05$ were considered significant.

## 3. Results

### *3.1 Physicochemical characterization of SPC ULV and MLV*

Results obtained by DLS measurements highlighted that high pure CRY did not alter the vesicles formation, since no significant changes in physicochemical features (i.e. mean diameter, zeta-potential and size distribution) of CRY-loaded SPC ULV and MLV, compared to conventional liposomes, were found even at the highest molar ratio tested (1:0.5 mol/mol) (Tables 1 and 2). Moreover, no loss of CRY was observed during the preparation process. In fact, GC-MS analysis performed after extraction of CRY from liposomes evidenced a perfect overlap of the actual recovered amount with the theoretical one, thus indicating that no losses of sesquiterpene occurred. When the physicochemical features of liposomes were evaluated in the presence of cell medium, no interferences with the dimensional analysis were highlighted, thus suggesting a suitable stability of the formulation in cell culture environment (data not shown). The amount of structured phospholipids in the liposomal suspensions, with and without CRY, resulted to be not affected by the presence of the sesquiterpene, thus suggesting their compatibility.

**Table 1. Physicochemical features of SPC ULV liposomes.**

| Sample | Hydrodynamic diameter (nm) | PdI | ζ- potential (mV) | % SPC |
|---|---|---|---|---|
| **Unloaded SPC ULV** | 180.6 ± 4.7 | 0.079 ± 0.015 | -15.3 ± 0.4 | 92.2 ± 1.7 |
| **SPC/CRY ULV (mol/mol)** | | | | |
| **1:0.1** | 185.5 ± 4.2 | 0.076 ± 0.006 | -14.1 ± 0.2 | 89.5 ± 1.2 |
| **1:0.3** | 176.7 ± 7.5 | 0.075 ± 0.005 | -14.3 ± 0.5 | 88.5 ± 0.5 |
| **1:0.5** | 181.4 ± 2.1 | 0.085 ± 0.012 | -13.5 ± 0.6 | 85.2 ± 2.2 |

**Table 2. Physicochemical features of SPC MLV liposomes.**

| Sample | Hydrodynamic diameter (nm) | PdI |
|---|---|---|
| **Unloaded SPC MLV** | 699.73 ± 6.57 | 0.359 ± 0.069 |
| **SPC/CRY MLV (mol/mol)** | | |
| **1:0.1** | 643.93 ± 13.59 | 0.339 ± 0.045 |
| **1:0.3** | 631.53 ± 21.12 | 0.371 ± 0.005 |
| **1:0.5** | 497.13 ± 7.91 | 0.387 ± 0.025 |

*3.2 Cytotoxicity of CRY and plain SPC-based liposomes*

Under our experimental conditions, CRY did not affect the cell viability of HepG2 cells up to 10 μg/ml, although a slight cell viability reduction (about 10 %) was found starting from 5 μg/mL. A significant decrease of cell viability (about 45 % reduction respect to control) was found at 25 μg/mL, reaching a greatest inhibition of about 90% at 75 μg/mL (Figure 2). In MDA-MB-468 cells, CRY produced early toxicity signs (inhibition of 10%) at 2.5 μg/mL, with a biologically significant effect at 15, 25 and 50 μg/mL (inhibition of 38%, 84% and 98% respectively) (Figure 2). The IC50 values were 44.7 (C.L. 19.5-96.8) and 19.2 (C. L. 15.4-23.8) μg/mL in HepG2 and MDA-MB-468 cells, respectively.

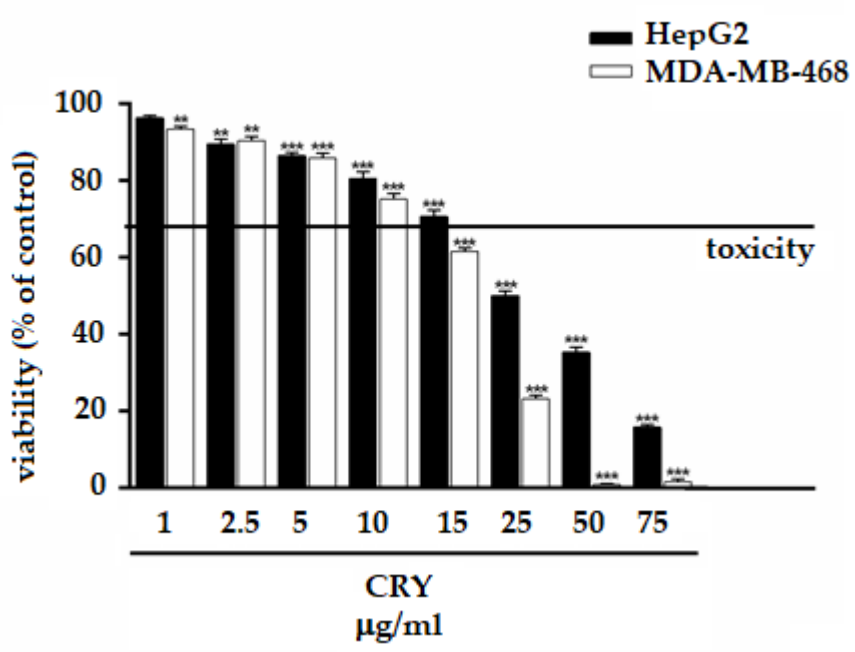


**Figure 2. Effect of CRY on the viability of HepG2 and MDA-MB-468 cells. ** p <0.01 and *** p <0.001 (ANOVA + Multiple Dunnett's Comparison Post-test); denotes a statistically significant reduction of cell viability compared to control (i.e. vehicle-treated cells). A cell viability lower than 70% respect to control was considered as cytotoxic [26].**

The cytotoxicity of plain SPC ULV and MLV (1-1000 μg/mL) in HepG2 and MDA-MB-468 cells was preliminarily evaluated, in order to define the maximum concentration at which liposomal formulations did not affect cell viability. Plain SPC ULV were nontoxic up to the concentration of 100 μg/mL in both HepG2 and MDA-MB-468 cells, with biologically significant cytotoxic effects (from 40% to 56 % inhibition of cell viability) starting from 200

μg/mL (Figure 3). Conversely, plain SPC MLV produced biologically significant cytotoxic effects (from 40% to 50% inhibition of cell viability) at 1000 μg/mL in both HepG2 and MDA-MB-468 cells, with early toxicity signs (about 25% inhibition of cell viability) at 500 μg/mL (Figure 3).

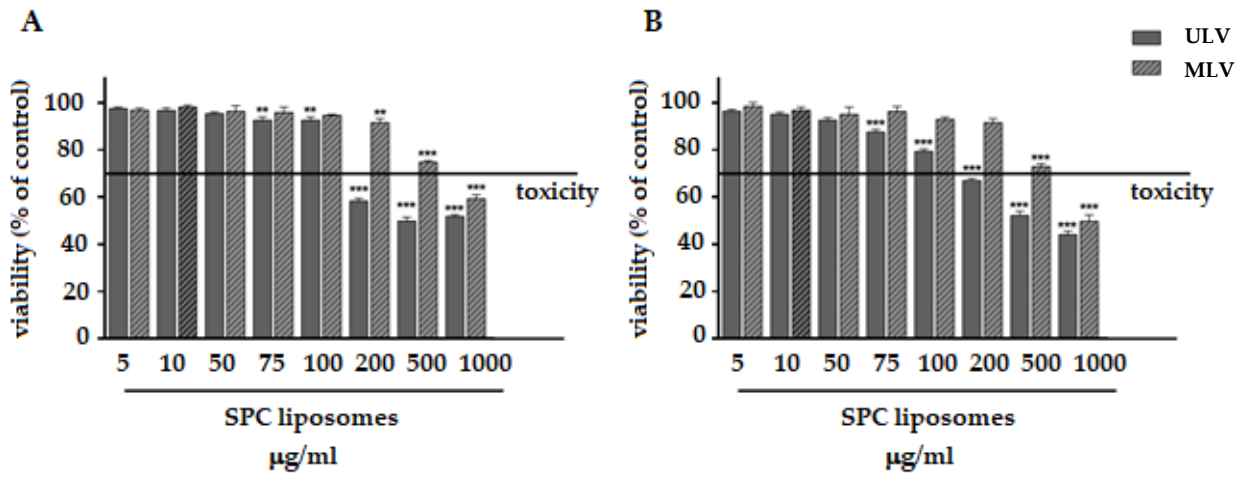


**Figure 3. Effect of SPC ULV and MLV on the viability of HepG2 (A) and MDA-MB-468 (B) cells. ** p <0.01 and *** p <0.001 vs. control (i.e. vehicle-treated cells), denotes a statistically significant reduction of cell viability compared to control (ANOVA + Multiple Dunnett's Comparison Post-test). A cell viability lower than 70% respect to control was considered as cytotoxic [26].**

*3.3 Cytotoxicity of CRY-loaded SPC ULV liposomes at different molar ratio*

When assessed in HepG2 cells, a different behaviour was found for CRY-loaded SPC ULV respect to pure CRY, as a function of their molar ratio (Figure 4). Particularly, the 1:0.1 molar ratio between SPC and CRY produced about a 40% cytotoxicity increase of CRY at low concentrations of 0.1, 1, 5 and 10 μg/mL, which were noneffective when CRY was administered as pure compound. Conversely, a progressive loss of the cytotoxic effect of CRY was found at highest concentrations of 25, 50 and 75 μg/mL of 1:0.1 SPC/CRY ULV, reaching a maximum 40% inhibition (Figure 4). Despite a biologically significant cytotoxicity of low-dose 1:0.1 SPC/CRY ULV, the 1:0.3 and 1:0.5 unilamellar formulations produced nonbiologically relevant cytotoxic effects and progressively reduced the

antiproliferative activity of pure CRY at all the tested concentrations, reaching a maximum of 63% inhibition (Figure 4).

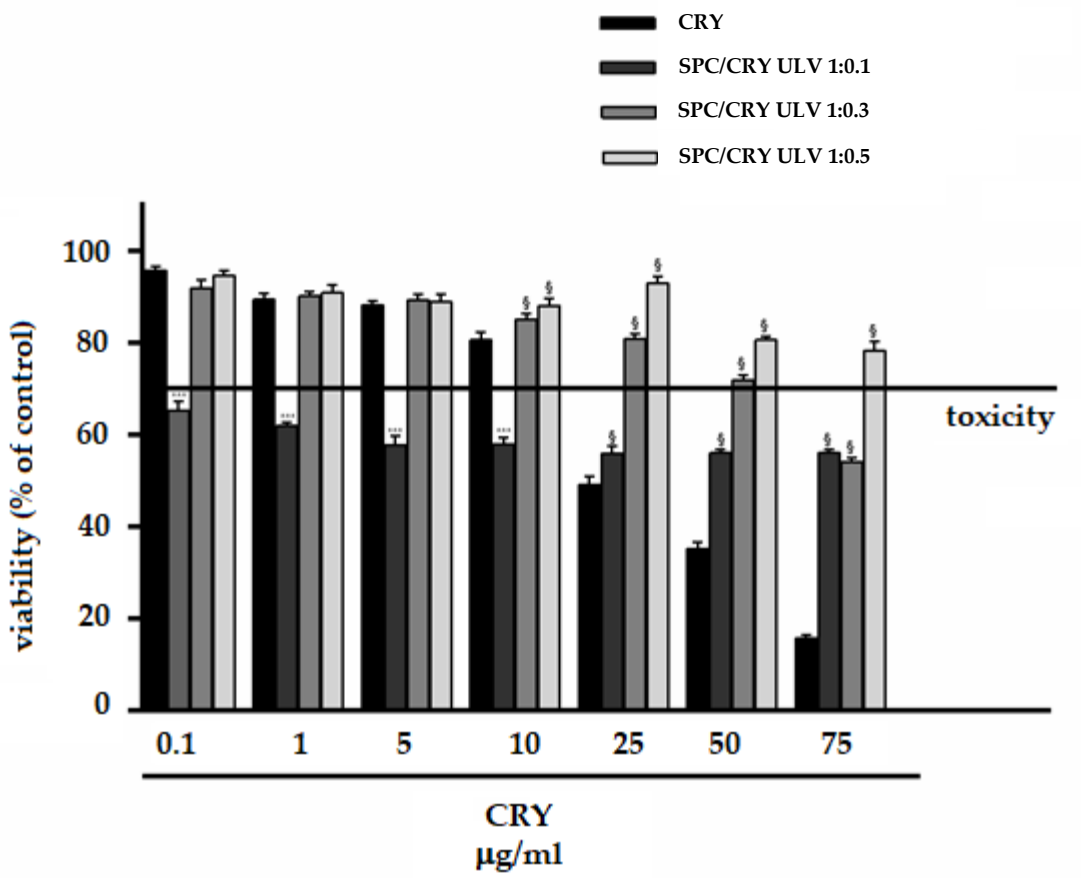


**Figure 4. Cytotoxicity of SPC ULV differently loaded with CRY (1:0.1, 1:0.3 and 1:0.5 mol/mol) in HepG2 cells after 24 h incubation. *** p <0.001 vs CRY; denotes a statistically significant increase of cytotoxicity respect to pure CRY (ANOVA + Multiple Dunnett's Comparison Post-test). § p <0.001 vs. CRY, denotes a statistically significant reduction respect to CRY cytotoxicity (ANOVA + Multiple Dunnett's Comparison Post-test). A cell viability lower than 70% respect to control (i.e. vehicle-treated cells) was considered as cytotoxic [26].**

Furthermore, the highest doses of loaded liposomes (starting from 25 µg/mL of 1:0.1 and 1:0.3 SPC/CRY ULV) significantly reduced the cytotoxicity of plain SPC ULV, at the corresponding concentrations (Figure 4). This evidence suggested that increasing molar ratio between SPC and CRY in ULV formulations can hinder CRY release and retain the molecule into liposomes; also, some interactions between SPC and CRY could be expected, so explaining the reduced toxicity of plain SPC ULV. A similar behaviour was observed in MDA-MB-468 cells for 1:0.5 SPC/CRY ULV, which did not potentiate CRY cytotoxicity in all

the experimental conditions, while inhibiting the antiproliferative activity of pure CRY of about 20%, at concentrations of 25 and 50 μg/mL (Figure 5). Conversely, the 1:0.1 loaded formulation induced a significant potentiation of CRY cytotoxicity (from about 20 to 30%) at concentrations of 2.5 and 5 μg/mL, which disappeared at the highest tested concentrations.

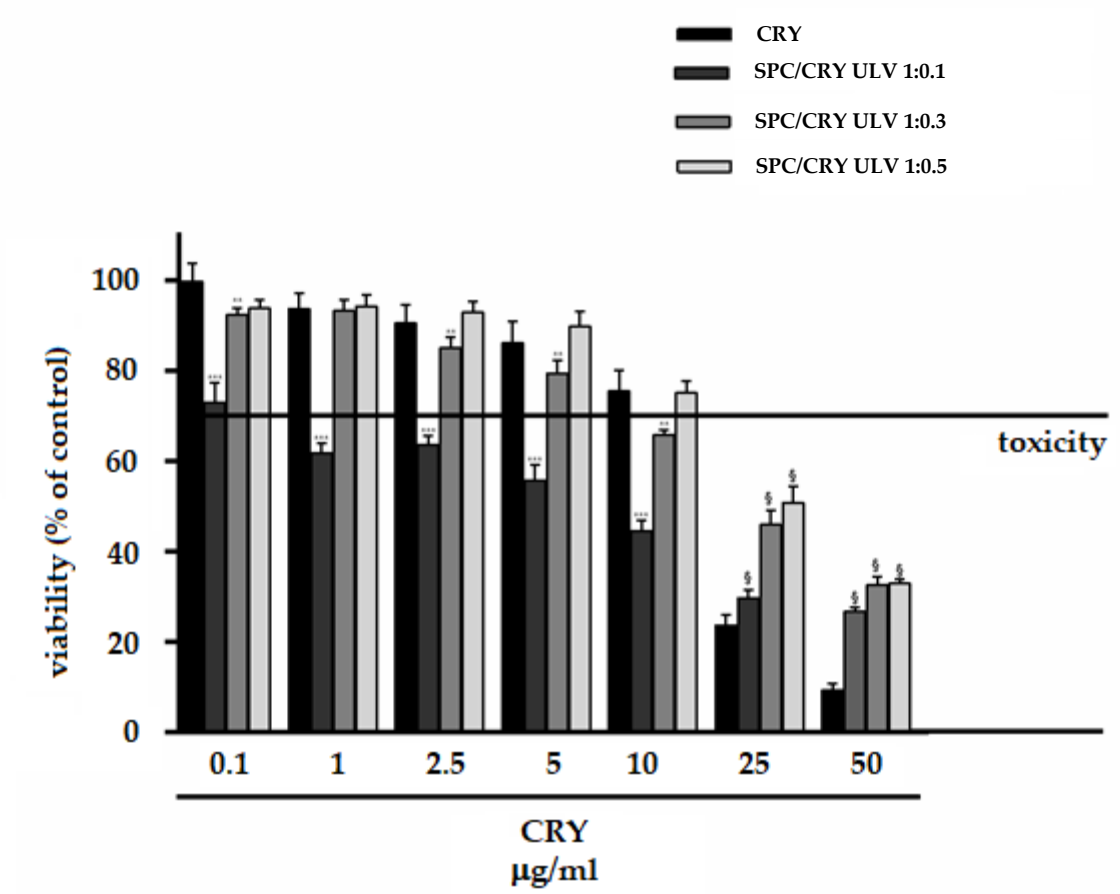


**Figure 5. Cytotoxicity of SPC ULV differently loaded with CRY (1:0.1, 1:0.3 and 1:0.5 mol/mol) in MDA-MB-468 cells after 24 h incubation. *** p <0.001 vs. CRY, denotes a statistically significant increase of cytotoxicity respect to pure CRY (ANOVA + Multiple Dunnett's Comparison Post-test). § p <0.001 vs. CRY, denotes a statistically significant reduction respect to CRY cytotoxicity (ANOVA + Multiple Dunnett's Comparison Post-test). A cell viability lower than 70% respect to control (i.e. vehicle-treated cells) was considered as cytotoxic [26].**

Similarly, the 1:0.3 SPC/CRY ULV produced a slight (about 10%) but significant increase of CRY toxicity at concentrations of 2.5 and 5 μg/mL. It is noteworthy that potentiation occurred at noneffective concentrations of CRY administered as pure compound. For all loaded formulations, the highest concentrations of 25 and 50 μg/mL induced a significant

inhibition (from about 10 to 28%) of CRY antiproliferative activity, thus suggesting a possible loss of activity of the drug or the loss of the carrier's ability to deliver the incorporated substance (Figure 5).When CRY was administered as 1:0.1 SPC ULV, the IC50 values were not evaluable in HepG2 cells, while a slight reduction (about 1.5 folds) was obtained in MDA-MB-468 cells (Table 3).

**Table 3. IC50 values of CRY administered as pure compound or as ULV and MLV formulations in HepG2 and MDA-MB-468 cells.**

| | HepG2 | MDA-MB-468 |
|---|---|---|
| | IC50 (CL*) μg/ml *RR*** | |
| **CRY** | 44.7 (19.5-96.8) | 19.2 (15.4-23.8) |
| **SPC/CRY ULV (mol/mol)** | | |
| **1:0.1** | ne*** | 12.4 (6.4 – 109.9) 1.5 |
| **1:0.3** | ne | ne |
| **1:0.5** | ne | ne |
| **SPC/CRY MLV (mol/mol)** | | |
| **1:0.1** | ne | 4.9 (2.4 – 9.9) 3.9 |
| **1:0.3** | 9.1 (2.6 – 32.0) 4.9 | 8.3 (6.1 – 11.2) 2.3 |
| **1:0.5** | ne | ne |

CL* confidential limits; RR** reversal ratio (ratio between the IC50 values of CRY alone and CRY-loaded SPC liposomes); ne*** not evaluable as a lower than 80% inhibition of cell viability was reached.

*3.4 Cytotoxicity of CRY-loaded SPC MLV liposomes at different molar ratio*

Under our experimental conditions, multilamellar liposomes produced different cytotoxic effects as a function of drug loading. In HepG2 cells, 1:0.1 SPC/CRY MLV did not affect the cell viability up to 1 μg/mL, while produced a marked potentiation of CRY cytotoxicity, at concentrations from 5 to 25 μg/mL, reaching the greatest effect of about 45% at 5 μg/mL (Figure 6). A significant and progressive increase of CRY antiproliferative activity was also produced by 1:0.3 loaded multilamellar formulation at concentrations from 1 to 50 μg/mL

(Figure 6), reaching a maximum potentiation of about 40% at 10 μg/mL: within these concentrations, the IC50 value of CRY was reduced of about five-folds (Table 3). Conversely, the 1:0.5 molar ratio between SPC and CRY increased the biological activity of CRY at concentrations of 5 and 10 μg/mL, with a maximum potentiation of 30% at 5 μg/mL (Figure 6). At the highest concentration of 75 μg/mL, all the CRY-loaded multilamellar formulations markedly reduced the antiproliferative activity of pure CRY, reaching a maximum 26% inhibition (Figure 6). Analogously, in MDA-MB-468 cells, the 1:0.1 SPC/CRY MLV induced a significant potentiation of CRY cytotoxicity from 0.1 to 10 μg/mL, with a maximum increase of about 30 % at 5 and 10 μg/mL (Figure 7). The 1:0.3 and 1:0.5 loaded formulations produced lower potentiation of CRY activity (about 10-25%) from 0.1 to 10 μg/mL. Conversely, the highest concentrations of 25 and 50 μg/mL reduced the antiproliferative activity of pure CRY, reaching a maximum 30% inhibition (Figure 7).

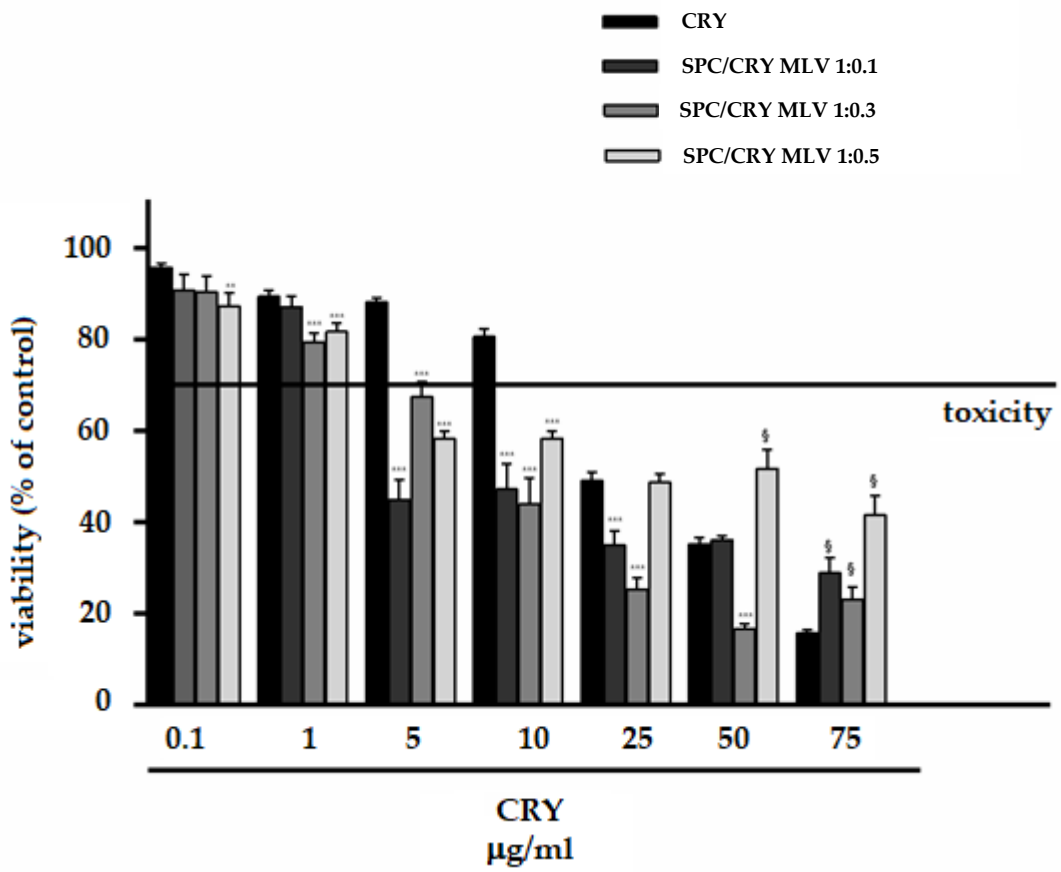


**Figure 6. Cytotoxicity of SPC MLV differently loaded with CRY (1:0.1, 1:0.3 and 1:0.5 mol/mol) in HepG2 cells after 24 h incubation. * p <0.05, ** p <0.01 and *** p <0.001 vs CRY;**

**denotes a statistically significant increase of cytotoxicity respect to pure CRY (ANOVA + Multiple Dunnett's Comparison Post-test). § p <0.001 vs. CRY, denotes a statistically significant reduction respect to CRY cytotoxicity (ANOVA + Multiple Dunnett's Comparison Post-test). A cell viability lower than 70% respect to control (i.e. vehicle-treated cells) was considered as cytotoxic [26].**

Within the concentrations from 0.1 to 25 μg/mL, the IC50 value of CRY was reduced of about four-folds when CRY was administered as 1:0.1 MLV, while of about two-folds when CRY was administered as 1:0.3 MLV (Table 3).

Furthermore, the highest dose (75 μg/mL) of 1:0.5 SPC/CRY MLV significantly reduced the cytotoxicity of plain SPC MLV at the corresponding concentration, thus displaying a behaviour similar to that found for CRY-loaded ULV (Figure 7). Accordingly, a possible segregation of CRY into liposome, due to its interaction with SPC could be expected.

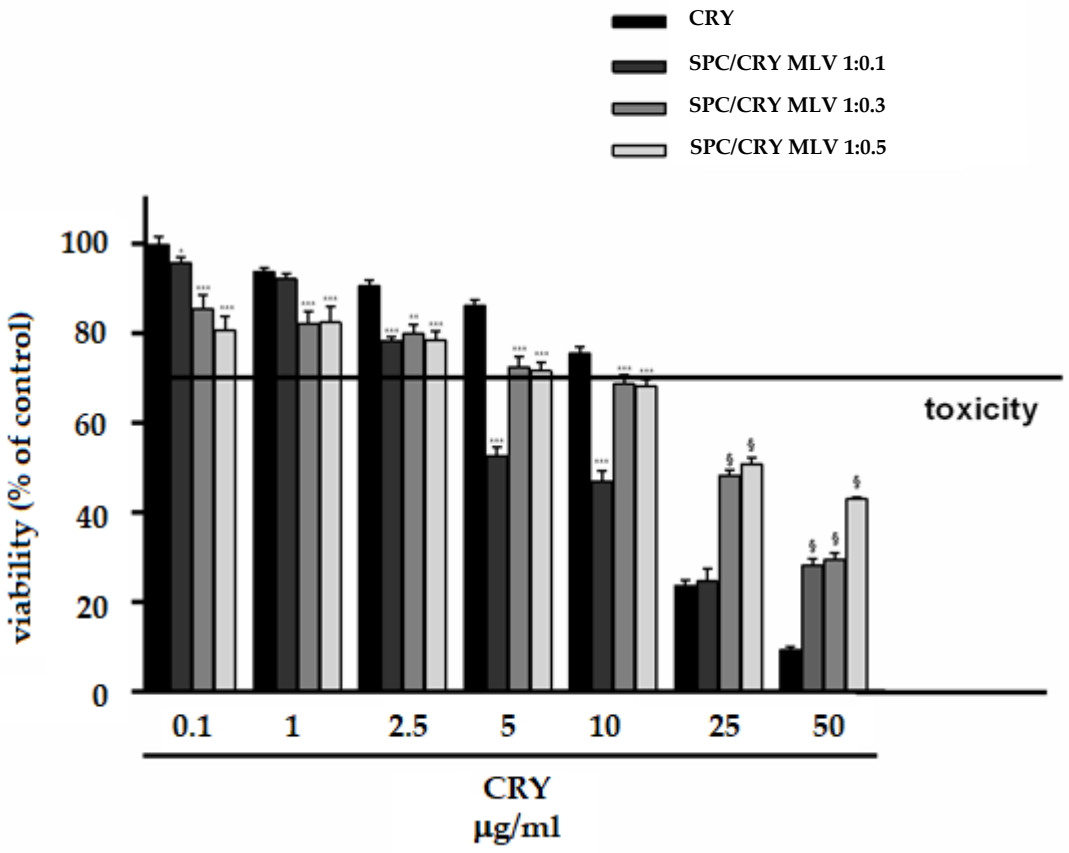


**Figure 7. Cytotoxicity of SPC MLV differently loaded with CRY (1:0.1, 1:0.3 and 1:0.5 mol/mol) in MDA-MB-468 cells after 24 h incubation. * p <0.05, ** p <0.01 and *** p <0.001 vs. CRY, denotes a statistically significant increase of cytotoxicity respect to pure CRY (ANOVA + Multiple Dunnett's Comparison Post-test). § p <0.001 vs. CRY, denotes a statistically significant reduction respect to CRY cytotoxicity (ANOVA + Multiple Dunnett's Comparison**

**Post-test). A cell viability lower than 70% respect to control (i.e. vehicle-treated cells) was considered as cytotoxic [26].**

*3.5 Evaluation of the potential interaction between CRY and SPC-based ULV*

In order to better characterize the possible interaction between CRY and SPC ULV, additional experiments in which the two separate components were co-administered to cells, at the same concentrations found in liposome formulations, were performed in HepG2 cells. When administered in the presence of SPC ULV, CRY exhibited a lower cytotoxic behaviour respect to the pure compound. Despite a biologically relevant toxicity of the pure compound alone, the presence of SPC ULV induced a significant loss of CRY bioactivity. About a 30% reduction of its antiproliferative effect is observed (Figure 8) and probably due to the high hydrophobic nature of CRY, which is therefore carried off by liposomes.

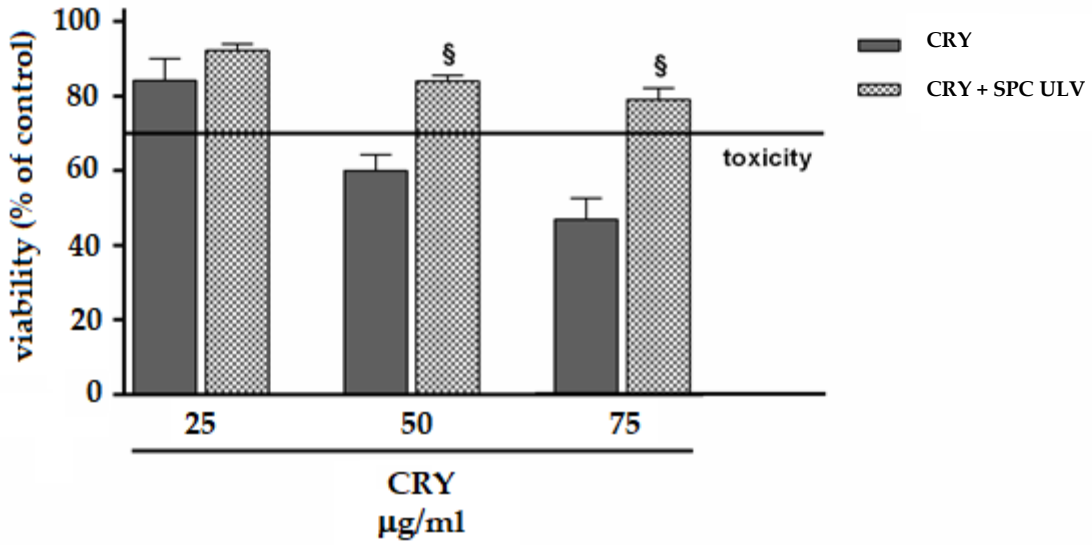


**Figure 8. Cytotoxicity of CRY and the combination of SPC/CRY ULV (1:0.5 mol/mol) in HepG2 cells after 24 h incubation. § p <0.001 vs. CRY, denotes a statistically significant reduction respect to CRY cytotoxicity (ANOVA + Multiple Dunnett's Comparison Post-test). A cell viability lower than 70% respect to control (i.e. vehicle-treated cells) was considered as cytotoxic [26].**

Similar results were reported by Botré et al. [27], who observed that the addition of empty liposomes to urine samples containing free steroids interfere with the recovery of the drugs, with consequent important implication on doping analysis. These results support our

hypothesis that the reduced bioactivity of CRY, when administered as SPC ULV with low molar ratio or at high concentration of the drug, could be due to a close interaction of the substance with phospholipid components as a consequence of its high-grade lipophilicity.

To test this hypothesis, fluorescence anisotropy studies were carried out in order to evaluate the effect of CRY and its concentration on the fluidity of the SPC bilayer membrane of liposomes. The obtained results were compared with that produced by cholesterol (Chol) on the membrane behavior (Figure 9). Fluorescence anisotropy studies have found that lipophilic molecules, such as cholesterol and caryophyllene sesquiterpene, can affect the typical fluidity of SPC-based vesicles and reduce the mobility of the hydrocarbon chains of membrane fatty acids. In order to determine how CRY affects membrane structure, we analyze the extent to which this molecule mimics the behavior of cholesterol in Ld liposomes. Liposomes made of SPC, SPC/Chol and SPC/CRY respectively were tested.

As shown in Figure 9, conventional SPC ULV liposomes produced an average anisotropy value of 0.062. SPC bilayer was expected to be in a homogenous liquid disordered (Ld) state; the low anisotropy value obtained reflects the freedom of movement of the DPH fluorophore in the fluid disordered state of plain SPC liposome.

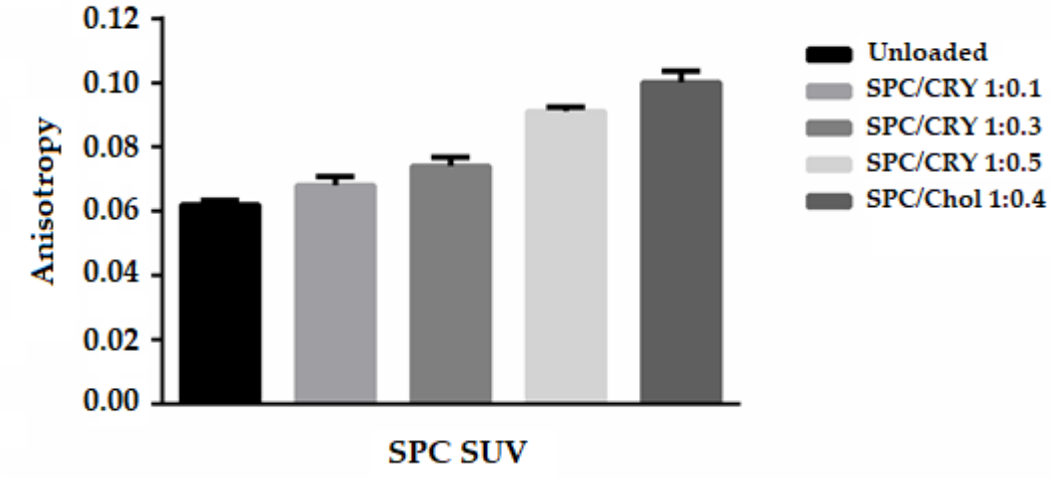


**Figure 9. Anisotropy measures obtained by DPH-probe fluorescence for 1:0.1, 1:0.3 and 1:0.5 SPC/CRY ULV and 1:0.4 SPC/cholesterol (Chol) ULV.**

The thickening effect obtained as a result of cholesterol addition to a fluid bilayer is well documented [27] and the results reported in Figure 9 are in good agreement with previous

published data. When cholesterol 40% mol/mol was incorporated in Ld SPC/Chol bilayer, in fact, the DPH fluorescence anisotropy increases, thus indicating that at this cholesterol amount, a greater order level exists for the phospholipid acyl chain packing. According to Marsh [28], cholesterol in the liposomal fluid bilayer promotes the formation of a phase that coexists with the Ld phase. In SPC/Chol liposomes the close contact between the sterol and adjacent phospholipids results in the formation of the so-called liquid-ordered (Lo) phase. This new intermediate fluid phase exhibits translational degrees of freedom of the lipid molecules that are similar to those in a conventional fluid bilayer state, while the conformational degrees of freedom of the lipid hydrocarbon chains resemble those of the gel state. In contrast, a progressive increase of the anisotropy value appeared for CRY-loaded liposomes, that is proportional to the amount of drug incorporated into the vesicles bilayer. Increasing the mixing ratios between SPC and CRY, the fluorescence anisotropies of DPH were increased almost linearly, suggesting that rotational motion of DPH in SPC liposomes was restricted by CRY entrapment. Comparing the behaviour of SPC/CRY ULV with a 1:0.5 molar ratio and that of SPC/Chol ULV, very similar anisotropy values were found (Figure 9). In line with these results, our hypothesis is that liposome formulations with a higher than 1:0.1 molar ratio between SPC and CRY, can modify the phospholipid bilayer organization, thus hindering drug release.

## 4. Discussion

Low solubility of the natural sesquiterpene β-caryophyllene (CRY) in aqueous fluids and the subsequent poor bioavailability represent key aspects limiting its use in therapy. CRY also exhibited sensitivity to light, oxygen, humidity, and high temperatures [29]: these conditions decrease its stability and limit its biological effectiveness. A possible strategy to overcome these problems is the use of drug delivery systems, which may provide much higher bioavailability of this compound and ensure obtaining desired biological effects. Previous studies proposed cyclodextrin complexation to improve bioavailability of CRY [30-32]. Recently, oil/water microemulsions have been also reported to possess suitable

properties for effective topical delivery of β-caryophyllene [33]. Many synthetic and herbal drugs possess the problem of poor oral bioavailability, due to their very low water solubility or poor permeation through the biological membranes, thus leading to a limited dissolution profile in biological fluids and inefficacy in therapy. Increased reports highlighted the promising role of phospholipid-based formulations as effective drug delivery systems for natural bioactive constituents [34]. Being the main components of cellular membrane, phospholipids are characterized by an excellent biocompatibility; also, they possess amphiphilic structures and surface-active wetting characteristics, which allow enhancing the hydrophilicity of hydrophobic compounds. In water, phospholipids self-assemble into supramolecular aggregates, among which liposomes displayed high cell affinity and tissue compatibility, improving drug stability and ability to deliver both hydrophilic and lipophilic substances [34]. In line with this evidence, in the present study the internalization of CRY into the cells was increased using soybean phosphatidylcholine (SPC) liposomes Our hypothesis was that CRY, when administered as liposomal formulations, rationally designed in term of drug to lipid ratio, can be easily uptaken from cells, thus leading to an improved antiproliferative activity. SPC has been used as phospholipid molecule forming the lipid bilayer not only for its structural similarity with cell biomembrane constituents, but also for its ability to affect the cholesterol-induced stiffening of cancer cell biomembrane, which has been found responsible for reduced drug permeability and chemoresistance development in cancer cells [21]. In our cancer cell models, high concentrations of SPC exhibited early cytotoxicity signs, likely due to its ability to increase the permeability of cancer cell biomembrane, through the interference with cholesterol accumulation. In line with this evidence and considering that previous studies highlighted the ability of phosphatidylcholine to induce cholesterol depletion and to be inversely related to cholesterol amount [35-36], we hypothesize that the cytotoxicity found at higher concentrations of plain SPC liposomes can be, at least in part, due to a cholesterol transfer between liposomes and cells. Liposomes could reduce the cholesterol/phospholipid ratio and increase lipid disorder in cell membrane. Depletion of cholesterol in cell thus, could

make cell more vulnerable, also to physical stress [37]; similarly, methyl-beta-cyclodextrin has been used for cholesterol removal, although the effect was incomplete [38].

Under our experimental conditions, the encapsulation of CRY within SPC liposomes highlighted that the cellular uptake of CRY can be improved or reduced as a function of the molar ratio between SPC and CRY. Characterizing the optimal concentration of CRY in liposomal formulations represents a key point for the increase of its antiproliferative effectiveness. Both ULV and MLV liposomes loaded with the highest molar ratio between SPC and CRY (i.e. 1:0.5) induced a progressive loss of the antiproliferative potential of the sesquiterpene. The obtained results highlighted that, despite a possible improvement of low-dose CRY cytotoxicity, increased molar ratio between SPC and CRY markedly interfere with the biological activity of pure compound. This phenomenon suggests that the substance can be greatly retained and got stuck into liposomes, likely due to a stable interaction between CRY and phosphatidylcholine and a stiffening of the membrane structure, which hinder the sesquiterpene release by vesicles and its uptake into cells. Accordingly, Sarpietro et al. [39] showed that CRY possessed a great capacity to interact with membrane phospholipids and to spread through the lipophilic matrix, determining an alteration of the cooperativity. This hypothesis is also in agreement with the more accepted ordering effect induced by cholesterol in biomembrane bilayer and SPC ULV [28]. Therefore, we hypothesize that incorporating high concentrations of CRY in ULV bilayer can alter membrane packing of SPC liposomes by inducing conformational phospholipid ordering, thus leading to a decreased fluidity and permeability of the bilayer of the phospholipid carrier. The enhanced rigidity of the membrane, that could be generated by the inclusion of hydrophobic CRY, might seal the system and reduce the drug release. Moreover, the release of high CRY concentrations embedded within the lipid bilayers could be compromised due to strong hydrophobic interactions that might develop between the drug and the phospholipid acyl chains. The trend displayed by SPC multilamellar vesicles support the hypothesis of the reduced bioactivity of CRY due to a condensing effect of this molecule on the bilayer. In fact, the results observed with the MLV system were partly

similar to SPC ULV only at the highest CRY concentrations. We reasonable speculate that CRY reduces the fluidity of the SPC MLV bilayer to a lesser extent respect to SPC ULV. In fact, for a fixed SPC/CRY ratio, the number of CRY molecules included in each of the lamella of the multilamellar carrier was smaller respect to ULV, thus leading to a reduced extent of the stiffness effect.

## 5. Conclusions

In the present study, SPC liposomes have been developed as potential effective delivery systems to increase the in vitro bioavailability and stability of the natural sesquiterpene CRY. According to widely accepted evidence that release is governed by molecule lipophilicity and liposome features, our results allow to hypothesize that CRY release by SPC liposomes is strictly dependent on lamellarity and drug-to lipid ratio. Lipid-to-drug ratio is a critical parameter as it may influence the therapeutic efficacy of the drug, in particular with lipophilic drugs. The increase of drug encapsulation could be not a valid strategy in liposomal formulation, as the drug release properties of the liposomal product could be negatively affected by the molar concentration of drug in liposomes. In fact, as SPC liposome loading increases, a condensing effect of the loaded molecule on the fluid bilayer occurs. As a consequence, the substance can be greatly retained, and its release restrained. In the case of CRY, this feature can negatively affect and hinder its anticancer effectiveness. Therefore, SPC to CRY ratio seems to represent a key tool for the development of optimized liposomal formulation to control membrane fluidity and permeability of SPC liposomes, and thus predicts the release abilities. In fact, low-loaded MLV appear to induce the maximum increase of CRY antiproliferative activity in both HepG2 and MDA-MB-468 cells, thus suggesting the ability of these formulations to better carry the lipophilic cargo inside cells. However, further in vitro studies are necessary to effectively measure the CRY release by SPC vesicles and the achieved intracellular levels. In conclusion, our results highlight the importance of rationally designing formulations to develop the optimal liposomal composition, taking into account not only the chemical nature of the payload but also that

the high drug loading in liposomes could be critical for the maximum usefulness of its therapeutic potential.

***Acknowledgements.*** *This work was partly financed by "Sapienza" University grant (A. Di Sotto; prot. C26A14MWNR). Fellowships of A. Di Sotto and S. Di Giacomo were supported by Enrico and Enrica Sovena Foundation (Italy).*

***Conflicts of Interest.*** *The authors have nothing to declare.*

## 6. References

[1] Di Sotto, A.; Evandri, M.G.; Mazzanti, G. *Antimutagenic and mutagenic activities of some terpenes in the bacterial reverse mutation assay*. Mutat Res. 2008, 653(1-2), 130-133.

[2] Fidyt, K.; Fiedorowicz, A.; Strządała, L.; Szumny, A. *β-caryophyllene and β-caryophyllene oxide-natural compounds of anticancer and analgesic properties*. Cancer Med. 2016, 5(10), 3007-3017.

[3] Gertsch, J. *Antiinflammatory cannabinoids in diet towards a better understanding of CB2 receptor action?* Communicative & Integrative Biology. 2008, 1(1), 26-28.

[4] Bento, A.F.; Marcon, R.; Dutra, R.C.; Claudino, R.F.; Cola, M.; Leite, D.F.; Calixto, J.B. *β-Caryophyllene inhibits dextran sulfate sodium-induced colitis in mice through CB2 receptor activation and PPARγ pathway*. Am J Pathol. 2011, 178(3), 1153-1166.

[5] Chang, H.J.; Kim, J.M.; Lee, J.C.; Kim, W.K.; Chun, H.S. *Protective effect of betacaryophyllene, a natural bicyclic sesquiterpene, against cerebral ischemic injury*. Journal of medicinal food. 2013, 16, 471-480.

[6] Liu, H.; Song, Z.; Liao, D.; Zhang, T.; Liu, F.; Zhuang, K.; Luo, K.; Yang, L. *Neuroprotective effects of trans-caryophyllene against kainic acid induced seizure activity and oxidative stress in mice*. Neurochem Res. 2015, 40(1), 118-123.

[7] Viveros-Paredes, J.M.; González-Castañeda, R.E.; Gertsch, J.; Chaparro-Huerta, V.; López-Roa, R.I.; Vázquez-Valls, E.; Beas-Zarate, C.; Camins-Espuny, A.; Flores-Soto, M.E.

*Neuroprotective Effects of β-Caryophyllene against Dopaminergic Neuron Injury in a Murine Model of Parkinson's Disease Induced by MPTP*. Pharmaceuticals (Basel). 2017, 10(3).

[8] Di Sotto, A.; Mazzanti, G.; Carbone, F.; Hrelia, P.; Maffei, F.; Mazzanti, G. *Inhibition by beta-caryophyllene of ethyl methanesulfonate-induced clastogenicity in cultured human lymphocytes*. Mutation Research. 2010, 699(1-2), 23-28.

[9] Di Giacomo, S.; Mazzanti, G.; Di Sotto, A. *Mutagenicity of cigarette butt waste in the bacterial reverse mutation assay: The protective effects of β-caryophyllene and β-caryophyllene oxide*. Environ Toxicol. 2016, 31(11), 1319-1328.

[10] Di Giacomo, S.; Abete, L.; Cocchiola, R.; Mazzanti, G.; Eufemi, M.; Di Sotto, A. *Caryophyllane sesquiterpenes inhibit DNA-damage by tobacco smoke in bacterial and mammalian cells*. Food and Chemical Toxicology. 2018, 111, 393–404.

[11] Hanušová, V.; Caltová, K.; Svobodová, H.; Ambrož, M.; Skarka, A.; Murínová, N.; Králová, V.; Tomšík, P.; Skálová, L. *The effects of β-caryophyllene oxide and trans-nerolidol on the efficacy of doxorubicin in breast cancer cells and breast tumor-bearing mice*. Biomed. Pharmacother. 2017, 95, 828-836.

[12] Di Giacomo, S.; Di Sotto, A.; El-Readi, M.Z.; Mazzanti, G.; Wink, M. *Chemosensitizing Properties of β-Caryophyllene and β-Caryophyllene Oxide in Combination with Doxorubicin in Human Cancer Cells*. Anticancer Research. 2017, 37(3), 1191-1196.

[13] Fontes, L.B.A.; Dias, D.D.S.; Aarestrup, B.J.V.; Aarestrup, F.M.; Da Silva Filho, A.A.; Corrêa, J. *β-Caryophyllene ameliorates the development of experimental autoimmune encephalomyelitis in C57BL/6 mice*. Biomed Pharmacother. 2017, 91, 257-264.

[14] Zhou, L.; Zhan, M.L.; Tang, Y.; Xiao, M.; Li, M.; Li, Q.S.; Yang, L.; Li, X.; Chen, W.W.; Wang, Y.L. *Effects of β-caryophyllene on arginine ADP-ribosyltransferase 1-mediated regulation of glycolysis in colorectal cancer under high-glucose conditions*. Int J Oncol. 2018, 53(4), 1613-1624.

[15] Kawabata, Y.; Wada, K.; Nakatani, M.; Yamada, S.; Onoue, S. *Formulation design for poorly water-soluble drugs based on biopharmaceutics classification system: basic approaches and practical applications*. Int. J. Pharm. 2011, 420, 1–10.

[16] Sarfraz, M.; Afzal, A.; Raza, S.M.; Bashir, S.; Madni, A.; Khan, M.W.; Ma, X.; Xiang, G. *Liposomal co-delivered oleanolic acid attenuates doxorubicin-induced multi-organ toxicity in hepatocellular carcinoma*. Oncotarget. 2017, 8(29), 47136–47153.

[17] Yang, G.; Yang, T.; Zhang, W.; Lu, M.; Ma, X.; Xiang, G. *In vitro and in vivo antitumor effects of folatetargeted ursolic acid stealth liposome*. J Agric Food Chem. 2014, 62, 2207–2215.

[18] Coimbra, M.; Isacchi, B.; van Bloois, L.; Torano, J.S; Ket, A.; Wu, X.; Broere, F.; Metselaar, J.M.; Rijcken, C.J.; Storm, G.; Bilia, R.; Schiffelers, R.M. *Improving solubility and chemical stability of natural compounds for medicinal use by incorporation into liposomes*. Int. J. Pharm. 2011, 416, 433-442.

[19] Rodríguez, J.; Martín, M.J.; Ruiz, M.A.; Clares, B. *Current encapsulation strategies for bioactive oils: From alimentary to pharmaceutical perspectives*. Food Research International. 2016, 83, 41-59.

[20] Mishra, G.P.; Bagui, M.; Tamboli, V.; Mitra, A.K. *Recent applications of liposomes in ophthalmic drug delivery*. Journal Drug Delivery. 2011, article ID 863734, 14 pages.

[21] Lladó, V.; López, D.J.; Ibarguren, M.; Alonso, M.; Soriano, J.B.; Escribá, P.V.; Busquets, X. *Regulation of the cancer cell membrane lipid composition by NaCHOleate: Effects on cell signaling and therapeutical relevance in glioma*. Biochim Biophys Acta. 2014, 1838(6), 1619-1627.

[22] Kannan, V.; Balabathula, P.; Divi, M.K.; Thoma, L.A.; Wood, G.C. *Optimization of drug loading to improve physical stability of paclitaxel-loaded long-circulating liposomes*. J. Liposome Res. 2015, 25, 308-315.

[23] Bangham, A.D. *Properties and uses of lipid vesicles: an overview*. Ann N Y Acad Sci. 1978, 308, 2-7.

[24] Yoshida, Y.; Furuya, E.; Tagawa, K. *A direct colorimetric method for the determination of phospholipids with dithiocyanatoiron reagent*. J Biochem. 1980, 88(2), 463-468.

[25] Di Sotto, A.; Mazzanti, G.; Savickiene, N.; Staršelskyt, R.; Baksenskaite, V.; $Di Giacomo, S.; Vitalone, A. *Antimutagenic and antioxidant activity of a protein fraction from aerial parts of Urtica dioica*. Pharmaceutical Biology. 2014, 53(6), 935-938.

[26] International Organization for Standardization. Biological evaluation of medical devices - Part 5: Tests for in vitro cytotoxicity (ISO 10993-5). Geneva: International Organization for Standardization, 2009.

[27] Botrè, F.; Esposito, S.; de la Torre, X. *How we risk: liposomes and steroids*. In: Schanzer, W.; Geyer, H.; Gotzmann, A.; Mareck, U. Recent Advances in Doping Analysis (19), Koln. 2011, 24-33.

[28] Marsh, D. *Liquid-ordered phases induced by cholesterol: a compendium of binary phase diagrams*. Biochim Biophys Acta. 2010, 1798(3), 688-699.

[29] Sköld, M.; Karlberg, A.T.; Matura, M.; Börje, A. *The fragrance chemical β-caryophyllene air oxidation and skin sensitization*. Food and chemical toxicology. 2006, 44, 538-545.

[30] Liu, H.; Yang, G.; Tang, Y.; Cao, D.; Qi, T.; Qi, Y.; Fan, G. *Physicochemical characterization and pharmacokinetics evaluation of β-caryophyllene/β-cyclodextrin inclusion complex*. Int J Pharm. 2013, 450(1-2), 304-310.

[31] Lou, J.; Teng, Z.; Zhang, L.; Yang, J.; Ma, L.; Wang, F.; Tian, X.; An, R.; Yang, M.; Zhang, Q.; Xu L, Dong Z. *β-Caryophyllene/Hydroxypropyl-β-Cyclodextrin Inclusion Complex Improves Cognitive Deficits in Rats with Vascular Dementia through the Cannabinoid Receptor Type 2 - Mediated Pathway*. Front Pharmacol. 2017, 8(2).

[32] Quintans-Júnior, L.J.; Araújo, A.A.; Brito, R.G.; Santos, P.L.; Quintans, J.S.; Menezes, P.P.; Serafini, M.R.; Silva, G.F.; Carvalho, F.M.; Brogden, N.K.; Sluka, K.A. *β-caryophyllene, a dietary cannabinoid, complexed with β-cyclodextrin produced anti-hyperalgesic effect involving the inhibition of Fos expression in superficial dorsal horn*. Life Sci. 2016, 149, 34-41.

[33] de Oliveira Neves, J.K.; Apolinário, A.C.; Alcantara Saraiva, K.L.; da Silva, D.T.C.; de Freitas Araújo Reis, M.Y.; de Lima Damasceno, B.P.G.; Pessoa, A.; Moraes G.; Marcos Aurélio, S.; Luiz Alberto L.; da Silva, V.J.; da Converti, J.A.; Attilio, J.O. *Microemulsions containing Copaifera multijuga Hayne oil-resin: Challenges to achieve an efficient system for β-caryophyllene delivery*. Industrial Crops & Products. 2018, 111, 185–192.

[34] Li, C.; Zhang, J.; Zu, Y.J.; Nie, S.F.; Cao, J.; Wang, Q.; Nie, S.P.; Deng, Z.Y.; Xie, M.Y.; Wang, S. *Biocompatible and biodegradable nanoparticles for enhancement of anti-cancer activities of phytochemicals*. Chin J Nat Med. 2015, 13(9), 641-652.

[35] Akopian, D.; Kawashima, R.L.; Medh, J.D. *Phosphatidylcholine-Mediated Aqueous Diffusion of Cellular Cholesterol Down-Regulatesthe ABCA1 Transporter in Human Skin Fibroblasts*. Int. J. Biochem. Res. Rev. 2015, 5, 214-224.

[36] Nuñez-Garcia, M.; Gomez-Santos, B.; Buqué, X.; García-Rodriguez, J.L.; Romero, M.R.; Marin, J.J.G.; Arteta, B.; García-Monzón, C.; Castaño, L.; Syn, W.K.; Fresnedo, O.; Aspichueta, P. *Osteopontin regulates the cross-talk between phosphatidylcholine and cholesterol metabolism in mouse liver*. J. Lipid Res. 2017; 58; 1903-1915.

[37] Simons, K.; Ehehalt, R. *Cholesterol, lipid rafts and disease*. J. Clin. Invest. 2002, 110, 597-603.

[38] Litz, J.P.; Thakkar, N.; Portet, T.; Keller, S.L. *Depletion with Cyclodextrin Reveals Two Populations of Cholesterol in Model Lipid Membranes*. Biophys J. 2016, 110(3), 635-645.

[39] Sarpietro, M.G.; Di Sotto, A.; Accolla, M.L.; Castelli, F. *Differential Scanning Calorimetry Study on the Interaction of β-Caryophyllene and β-Caryophyllene Oxide with Phospholipid Bilayers*. Thermochimica Acta. 2015, 600, 28-34.

Carbohydrate Polymers 174 (2017) 960–969

Contents lists available at ScienceDirect

Carbohydrate Polymers

journal homepage: www.elsevier.com/locate/carbpol

# DESIGN AND CHARACTERIZATION OF A BIOCOMPATIBLE PHYSICAL HYDROGEL BASED ON SCLEROGLUCAN FOR TOPICAL DRUG DELIVERY

Patrizia Paolicelli[a,*], Gabriele Varani[b], Settimio Pacelli[c], Elisa Ogliani[a], Martina Nardoni[a], Stefania Petralito[a], Alessandra Adrover[b], Maria Antonietta Casadei[a]

[a] Department of Drug Chemistry and Technologies, Sapienza University of Rome, P.le Aldo Moro 5, 00185 Rome, Italy
[b] Department of Chemical, Material and Environmental Engineering, Sapienza University of Rome, Via Eudossiana 18, 00184 Rome, Italy
[c] BioIntel Research Laboratory, Department of Chemical and Petroleum Engineering, School of Engineering, University of Kansas, Lawrence, KS, 66045,USA

ARTICLE INFO

*Article history:*
Received 12 October 2016
Received in revised form 14 June 2017
Accepted 4 July 2017
Available online 6 July 2017

*Keywords:*
Carboxymethyl scleroglucan
physical hydrogels
topical formulation
diffusion coefficient
Fickian and non-Fickian transport models

ABSTRACT

Physical hydrogels of a high-carboxymethylated derivative of scleroglucan (Scl-$CM_{300}$) were investigated as potential systems for topical drug delivery using three different therapeutic molecules (fluconazole, diclofenac and betamethasone).

Rheological tests were carried out on drug-loaded hydrogels along with *in-vitro* release studies in a vertical Franz cell, in order to investigate if and how different drugs may influence the rheological and release properties of Scl-$CM_{300}$ hydrogels.

Experimental results and theoretical modeling highlighted that, in the absence of drug/polymer interactions (as for fluconazole and betamethasone) Scl-$CM_{300}$ matrices offer negligible resistance to drug diffusion and a Fickian transport model can be adopted to estimate the effective diffusion coefficient in the swollen hydrogel. The presence of weak drug/hydrogel chemical bonds (as for diclofenac), confirmed by frequency sweep tests, slow down the drug release kinetics and a non-Fickian two-phase transport model has to be adopted.

*In-vivo* experiments on rabbits evidenced optimal skin tolerability of Scl-$CM_{300}$ hydrogels after topical application.



## 1. Introduction

Topical formulations are a valid strategy to treat common disorders, including acute and chronic inflammations, skin infections and acute pain (Arnstein, 2012). The use of the skin as a portal of entry for drugs is particularly attractive since it can overcome the challenges associated with other administration routes (Touitou, 2002). However, beside its great accessibility, the skin possesses highly efficient barrier properties, which frequently hamper drug delivery through it. In this context, hydrogels represent a primary solution to design innovative topical formulations (Caló & Khutoryanskiy, 2015). In fact, their soft consistency combined with their ability to swell, make them the perfect candidate for topical applications. Moreover, they possess a pleasant texture, which does not create any greasy residue on the skin compared to creams and ointments (Trookman & Rizer, 2011).

Hydrogels properties can be modulated by varying the type of polymer and the crosslinking step during their fabrication. Chemical or physical bonds can hold the polymeric matrix together, and its swelling behavior can be tuned by introducing pH-sensitive functional groups (Hoare & Kohane, 2008).

For all these reasons, hydrogels offer a versatile platform as carriers of a variety of drugs for topical delivery. This concept particularly holds true for physical hydrogels made of biocompatible polysaccharides where the presence of hydrogen bonds, ion-dipole, and electrostatic interactions are the driving forces responsible for the hydrogel formation. The same interactions can influence the hydrogel strength and elasticity as well as the release behavior of the loaded drugs from the hydrophilic matrix.

Scleroglucan (Scl) is an example of a natural polysaccharide produced by the fungi of the genus *Sclerotium* (Ioannis, Harvey & McNeil, 2005), which possesses several structural properties particularly useful for the design of physical hydrogels for topical applications. Specifically, the polymer consists of a main backbone of (1-3)-linked-β-D-glucopyranosyl residues with a single (1-6)-linked-β-D-glucopyranosyl unit linked in side chain every third sugar molecule of the main chain. In aqueous solutions, Scl

* Corresponding author.
*E-mail address:* patrizia.paolicelli@uniroma1.it (P. Paolicelli).

http://dx.doi.org/10.1016/j.carbpol.2017.07.008
0144-8617/

reassembles in a triple helix conformation that can only be broken into random coil chains at pH 12 or in dimethylsulfoxide (DMSO) (Palleschi, Bocchinfuso, Coviello & Alhaique, 2005; Guo, Stokke & Elgsaeter, 1996). Scl finds application in the industrial and pharmaceutical field as a thickening agent and for the preparation of modified-release dosage forms for oral and topical delivery (Coviello et al., 2005a; Corrente et al., 2009; Viñarta, François, Daraio, Figueroa, & Fariña, 2007).

In addition, Scl can be easily modified with pH-responsive groups, which have a profound effect on the main characteristics of the polymer (Corrente, Abu Amara, Pacelli, Paolicelli & Casadei, 2013; Cerreto et al., 2013). For example, a carboxymethyl derivative of scleroglucan (Scl-CM) is obtained by reaction with chloroacetic acid in a basic medium, and the number of carboxylic groups introduced has a significant influence on the corresponding gel properties. Specifically, a Scl-CM derivative with a high degree of functionalization is capable of forming physical hydrogels without the addition of any salt. These physical gels have been already proposed as carriers for the oral administration of anti-inflammatory drugs proving to adequately protect the gastrointestinal mucosa from any drug-induced damage while modulating the release rate of the loaded molecules (Corrente et al., 2012).

To further extend the potentiality of high carboxymethylated Scl-based hydrogels in the pharmaceutical field, their use as a topical formulation for a variety of drugs including antifungal, steroidal and non-steroidal anti-inflammatory molecules, was here attempted.

Specifically, three different therapeutic drugs, namely diclofenac, betamethasone, and fluconazole, were tested in this work. Flow curves and frequency sweep tests were carried out on the loaded Scl-$CM_{300}$ hydrogels along with release studies in a vertical Franz cell.

Particular attention was paid to possible interactions between the hydrogel matrix and the loaded drugs, and how their presence could influence both the rheological and release properties of the corresponding physical hydrogels. Mathematical models, describing transport and possible interactions between the selected drugs and Scl-$CM_{300}$, were adopted to estimate the effective diffusion coefficient of these molecules in the polymeric network. Numerical solutions were obtained by COMSOL 3.5 multiphysics.

Finally, preliminary *in-vivo* experiments were carried out on rabbits to verify the skin tolerability of the Scl-$CM_{300}$-based formulations.

## 2. Materials and methods

### 2.1. Chemicals

All used reagents were of analytical grade. Scleroglucan with $M_w = 1.4 \cdot 10^6$, as evaluated by viscosimetric measurements in 0.01 M NaOH, was provided by Carbomer (USA). Dimethylsulfoxide (DMSO) and chloroacetic acid were purchased from Fluka (Switzerland). Diclofenac sodium salt, DOWEX 50WX4-50 ion exchange resin, acetonitrile, and methanol were purchased from Sigma-Aldrich (England). Betamethasone phosphate sodium salt and fluconazole were received as gifts from Sigma-Tau (Italy) and Recordati S.p.A. (Italy), respectively. Dialysis membranes with cut-off 12,000-14,000 Da were purchased from Medicell International (UK).

### 2.2. Synthesis of carboxymethyl scleroglucan (Scl-$CM_{300}$)

Scleroglucan was modified into its carboxymethyl derivative (Scl-$CM_{300}$) following a reported procedure (Corrente et al., 2012) (see supplementary material, Fig. S1). Scleroglucan (1.0 g) was dissolved in water (40 ml) at 60°C for 24 h. NaOH (28.0 g) was then added to the polymeric solution in an ice bath to disrupt the triple helix. Finally, chloroacetic acid (40.0 g) was added dropwise to start the reaction. The polymeric mixture was kept under stirring at 60°C for 24 h followed by neutralization with glacial acetic acid. The obtained Scl-$CM_{300}$ was purified by exhaustive dialysis (cellophane membrane, Visking tubing, cut-off 12,000-14,000 Da) to remove the excess of salts and unreacted products. The dialyzed solution was eluted through a DOWEX 50WX4-50 ion-exchange resin column previously treated with 2.0 M HCl, to obtain all the carboxylic groups in the undissociated form.

The number of carboxylic groups added to the backbone of the polymer was quantified by potentiometer titration. Fully protonated Scl-$CM_{300}$ (100 mg) was dissolved in water and submitted to potentiometer titration using $1 \cdot 10^{-2}$ M NaOH. The amount of acid in mmol (equal to the mmol of NaOH used) was inserted in the following equation:

$$Scl - CM\ amount\ (mg) = X \cdot MW_{repetitive\ unit} + (mmol\ of\ acid) MW_{acid\ group}$$

allowing the calculation of X which represents the mmoles of repetitive units of the polymer. The ratio between the mmol of acid and the mmol of the repetitive units of the polymer multiplied by 100 is necessary to obtain the degree of derivatization (DD). This value represents the number of carboxylic groups per 100 repetitive units. A derivative having a DD equal to $300 \pm 10$ was obtained (labeled as Scl-$CM_{300}$) and used for all the studies. The freeze-dried polymer was mixed with KBr and characterized by FT-IR spectroscopy in the range of 4000–650 $cm^{-1}$ (resolution of 1 $cm^{-1}$), using a FT-IR Perkin Elmer Paragon 1000 spectrophotometer.

### 2.3. Hydrogel preparation

Solutions of Scl-$CM_{300}$ (2.0% w/v) were prepared by solubilizing Scl-$CM_{300}$ (0.1 g) in 5 ml of distilled water. The mixtures were kept under stirring at 60°C for 30 minutes to allow a complete solubilization of the polymer. The polymeric solutions were then left to cool down at room temperature (19-20 °C), to obtain the formation of the corresponding physical hydrogels.

Hydrogels loaded with drugs were prepared following the same procedure described above. Specifically, fluconazole, diclofenac sodium salt, and betamethasone phosphate sodium salt were selected as model molecules for the preparation of the medicated physical hydrogels of Scl-$CM_{300}$. Each drug was mixed with the polymeric solution before the gel formation at 60°C in the range of concentration from 0.1 up to 0.5% w/v.

### 2.4. Rheological characterization

Rheological experiments were carried out with a Haake RheoStress 300 Rotational Rheometer (Germany) equipped with a Haake DC10 thermostat. Flow curves were recorded with a share stress in the range of 0.01–100 Pa at 37.0±0.1°C. Physical hydrogels of Scl-$CM_{300}$ (2% w/v) with and without drugs were placed on a cone-plate geometry (angle of 1°) in order to completely cover the surface. In addition, frequency sweep tests were carried out on the same samples in the range of 0.01 up to 10 Hz. Mechanical spectra were recorded within the linear viscoelastic region measuring hydrogels response at a strain amplitude of 1%.

### 2.5. Release studies with Franz diffusion cell

Release studies were carried out from hydrogels loaded with fluconazole, diclofenac sodium salt and betamethasone phosphate sodium salt (0.25% w/v) using a vertical Franz cell (Olejnik, Goscianska, & Nowak, 2012).

The cylindrical donor chamber (cross-section area 0.5 $cm^2$) was loaded with a weighted amount (100 mg) of the drug-carrying hydrogel, gel thickness $L_g$ = 2 mm.

The donor chamber was separated by the receptor one with a dialysis membrane (cellophane membrane, Visking tubing, cut-off 12,000-14,000 Da) having an area of 0.5 $cm^2$ and thickness $L_m$ = 48 μm.

The receptor chamber was filled with 4.1 ml of phosphate buffer pH 7.4 under constant stirring (50 rpm). pH 7.4 was chosen for this study because of the dependence of diclofenac solubility from pH (Pobudkowska & Domanska, 2014). At pH 7.4 we have the maximum solubility of diclofenac, therefore even if back-diffusion of the release medium towards the donor compartment occurred during the study, no drug precipitation is expected within the gel.

Release experiments were carried out keeping the diffusion cell in a water bath at 37.0±0.1°C for 24 h. Aliquots of 250 μl were withdrawn at fixed time intervals and replaced with equal volumes of fresh buffer.

The release rate of diclofenac from Scl-$CM_{300}$-based hydrogels was also studied at room temperature (20 ± 1°C) following the same experimental set-up.

In addition, diffusion profiles of 0.25% w/v aqueous solutions of the three investigated drugs (0.1 ml, solvent thickness in the donor chamber $L_s = L_g$ = 2 mm) were used as blanks.

Diffusion profiles of 0.25% w/v aqueous solutions of theophylline were also used as blanks to investigate the dependence of the drug diffusion coefficient in the dialysis membrane on the drug molecular weight.

All the drugs were quantified by HPLC analysis carried out with a Perkin-Elmer apparatus equipped with a Perkin Elmer Series 200 LC pump and a series 235 Diode Array Detector, using a Merck Hibar LiChrocart (250-4, 5 μm) RP-18 column. The three drugs were determined according to already reported analytical methods, with some modifications. Diclofenac was analyzed using a mixture consisting of methanol and 0.01 M phosphoric acid (80:20, v:v), as the mobile phase, with a flow rate 0.7 ml/min and measuring the drug at 215 nm (Corrente et al., 2012). Fluconazole was analyzed using a mobile phase consisting of methanol, water and acetic acid (50:48:2, v:v:v), with a flow rate of 0.9 ml/min and monitoring the drug at 260 nm (Moraes et al., 1999). Betamethasone was instead detected using a mobile phase made of methanol and 0.01 M phosphoric acid (60:40, v:v), with a flow rate 0.8 ml/min and detecting the drug at 215 nm (Gonzalo-Lumbreras, Santos-Montes, Garcia-Moreno, & Izquierdo-Hornillos, 1997).

All the experiments were repeated in triplicate, and the results reported as mean value ± standard deviation.

### 2.6. Mathematical models of permeation experiments in a vertical Franz cell

We present the time-dependent one-dimensional Fickian and non-Fickian transport models adopted to describe drug permeation in a Franz vertical cell, both accounting for the presence of the cellophane (dialysis) membrane and finite volume of the receptor chamber.

Both transport models are numerically solved by Finite Element Method (FEM) using Comsol 3.5 Multiphysics. The Convection-Diffusion Package in Transient Analysis has been used. The linear solver adopted is UMFPACK, with relative tolerance $10^{-3}$ and absolute tolerance $10^{-6}$. The Time Stepping Method adopted is BDF with a Strict policy for Time steps taken by the solver. Lagrangian quadratic elements are chosen. The number of finite elements is $2 \cdot 10^4$ with a non-uniform mesh. Maximum-minimum element sizes $2.5 \cdot 10^{-3}$-$2.5 \cdot 10^{-7}$ in dimensionless units (total length of the domain in dimensionless units 1.024). Smaller elements are located in the membrane domain and close to the boundaries gel/membrane and membrane/receptor chamber to guarantee the convergence of the numerical scheme and accurate resolution of concentration gradients.

#### 2.6.1. Fickian diffusion model

Drug release from Scl-$CM_{300}$ networks can be described as a purely one-dimensional Fickian diffusion process (along the vertical coordinate z spanning the donor chamber), assuming that no drug/hydrogel matrix interaction and no matrix erosion of the fully swollen hydrogel occurr during the release experiments.

A purely Fickian transport model can be adopted to describe blank experimental release data as well as release data from Scl-$CM_{300}$ hydrogels for molecules that exhibit a typical Fickian behavior, i.e. $M_t/M_\infty \sim t^{1/2}$ at short-intermediate time scales.

Let us indicate with $C_g$, $D_g$, $C_m$, and $D_m$ the drug concentrations and the effective diffusion coefficients in the hydrogel and the dialysis membrane, respectively. $C_0$ indicates the initial drug concentration in the hydrogel (thickness $L_g$ = 2 mm, volume $V_g$ = 0.1 $cm^3$). The dialysis membrane used in the study has a thickness $L_m$ = 48 μm and a volume $V_m$ = 2.4 $mm^3$.

Let $C_{res}$ be the drug concentration in the perfectly mixed receptor chamber of volume $V_{res}$ = 4.1 ml.

By introducing the dimensionless time and space variables $\tau$, $\zeta$, $\alpha_m$, $\beta$ and the diffusivity ratio $\gamma_g$

$$\tau = tD_m/L_g^2,\ \zeta = z/L_g,\ \alpha_m = L_m/L_g,\ \beta = V_g/V_{res},\ \gamma_g = D_g/D_m \quad (1)$$

the transport equations and the boundary/initial conditions can be written as:

$$\frac{\partial C_g}{\partial \tau} = \gamma_g \frac{\partial^2 C_g}{\partial \zeta^2} \ \ for\ \ 0 < \zeta < 1,\ \ \frac{\partial C_g}{\partial \zeta} = 0 \ \ at\ \ \zeta = 0,\ \ C_g(0,\zeta) = C_0 \quad (2)$$

$$\frac{\partial C_m}{\partial \tau} = \frac{\partial^2 C_m}{\partial \zeta^2} \ \ for\ \ 1 < \zeta < 1 + \alpha_m,\ \ C_m = C_g \ \ at\ \ \zeta = 1 \quad (3)$$

$$\gamma_g \frac{\partial C_g}{\partial \zeta} = \frac{\partial C_m}{\partial \zeta} \ \ at\ \ \zeta = 1, C_m = C_{res} \ \ at\ \ \zeta = 1 + \alpha_m,\ C_m(0,\zeta) = 0 \quad (4)$$

$$\frac{dC_{res}}{d\tau} = -\beta \frac{\partial C_m}{\partial \zeta} \ \ at\ \ \zeta = 1 + \alpha_m,\ C_{res}(0) = 0 \quad (5)$$

We assume no mass-transfer resistance at the membrane-receptor chamber interface and unitary partition coefficients at the membrane-receptor chamber interface as well as at the gel membrane interface. The balance equation for $C_{res}$, Eq. (5), and the boundary condition $C_m = C_{res}$ at $\zeta = 1 + \alpha_m$ account for the finite volume of the receptor chamber.

By solving the transport equations Eqs. (2)–(5) for $C_g$, $C_m$, and $C_{res}$, the drug-release curve can be computed as follows

$$\frac{M_\tau}{M_\infty} = \frac{V_{res}C_{res}(\tau)}{V_{res}C_{res}^\infty},\ M_\infty = V_{res}\frac{\beta C_0}{1+\beta(1+\alpha_m)} = \frac{V_g C_0}{1+\beta(1+\alpha_m)} \quad (6)$$

where $M_\infty < V_g C_0$ because of the finite volume of the receptor chamber. The same set of transport equations can be used to describe the blanks, representing the drug release studies from the aqueous solutions without the hydrogel. This is possible by simply replacing $C_g$ (drug concentration in the gel) with $C_s$ (drug concentration in the aqueous solution placed in the donor chamber) and considering the diffusivity ratio $\gamma_s = D_s/D_m$ instead of $\gamma_g = D_g/D_m$, where $D_s$ represents the drug diffusivity in the solvent solution.

The Wilke-Chang correlation (Hayduk & Laudie, 1974) was used to estimate $D_s$ for each model drug

$$D_s^{drug}\left[cm^2/s\right] = 7.4\times10^{-8}\frac{\sqrt{{}_BMW_B}T}{\eta_B V_{drug}^{0.6}} \quad (7)$$

where B indicates the solvent (water, $\psi_B = 2.26$) and $V_{drug}$ is the LeBas drug molar volume usually obtained from a group contribution approach, considering the contributions of individual atoms, functional groups and cycles composing each molecule (Hayduk & Laudie, 1974).

From the blanks, we estimate the effective diffusion coefficient of the different model drugs in the dialysis membrane $D_m$, by best fitting the only unknown parameter $\gamma_s$.

Hence, from the release data from Scl-$CM_{300}$ hydrogel, we estimate the effective diffusion coefficient of each model drug $D_g$ in the hydrogel by best fitting the only unknown parameter $\gamma_g = D_g/D_m$.

This model fits well blank experimental release data as well as release data from Scl-$CM_{300}$ hydrogel for molecules that exhibit a typical Fickian behavior, i.e. $M_\tau/M_\infty \sim \tau^{1/2}$ at short-intermediate time scales.

### 2.6.2. Drug/hydrogel interaction model

A second mathematical model was introduced to describe possible interactions between a model drug and the hydrogel matrix and their effects on the drug release kinetics. This model can be used to explain the apparent "anomalous" non-Fickian behavior $M_\tau/M_\infty \sim \tau^n$ characterized by an exponent n »1/2 that can be observed at short-intermediate time scales in the presence of solute/polymeric matrix interactions (for a fully swollen gel). In this case, a two-phases kinetic model, originally proposed by Adrover (Adrover, Giona, Grassi, Lapasin & Pricl, 1996) for drug release from water swollen scleroglucan matrices, is adopted to describe the system. Specifically, it is possible to define a fraction $\varepsilon$ of the drug molecules that is capable of interacting with the polymeric network, which can be separated from the other drug molecules that are simply dissolved in the water phase of the hydrogel, where they are free to diffuse with an effective diffusion coefficient $D_g$.

A similar approach has been adopted by Singh et al., modeling drug release from hydrogels via a diffusion transport coupled with a sorption/desorption mechanism (Singh, Lumpkin, & Rosenblatt, 1994). The "two-phases" model adopted in the present work actually describes the adsorption/desorption mechanism in terms of a linear transfer rate from the adsorbed "bounded" phase to the desorbed "free" (or gel-solvent) phase and vice versa.

Let us then indicate $C_b$ and $C_g$ as the drug concentrations in the bounded and free (gel-solvent) phases, respectively. By assuming a reversible reaction and a linear transfer rate from the bounded to the free phase $-r_{b\to g} = K_{bg}C_b$ as well as a linear transfer rate from the free to the bounded phase $-r_{g\to b} = K_{gb}C_g$, the dynamic equations describing the phenomenon can be written as

$$\frac{\partial C_g}{\partial\tau} = \gamma_g\frac{\partial^2 C_g}{\partial\zeta^2} + \phi^2\gamma_g\left(C_b - C_g/K_{eq}\right) \quad \text{for} \quad 0\le\zeta\le1 \quad (8)$$

$$\frac{\partial C_b}{\partial\tau} = -\phi^2\gamma_g\left(C_b - C_g/K_{eq}\right) \quad \text{for} \quad 0\le\zeta\le1 \quad (9)$$

$$\frac{\partial C_g}{\partial\zeta} = 0 \;\; at \;\; \zeta = 0, \;\; C_g = C_m \;\; at \;\; \zeta = 1 \quad (10)$$

$$C_g(0,\zeta) = (1-\varepsilon)C_0, \;\; C_b(0,\zeta) = \varepsilon C_0 \quad (11)$$

where $K_{eq} = K_{gb}/K_{bg}$ is the equilibrium constant (depending on the temperature of the experiment) and $\varphi^2 = \frac{K_{bg}L_g^2}{D_g}$ is a dimensionless parameter, equivalent to a square Thiele modulus, representing the ratio between the characteristic diffusion time $L_g^2/D_g$ in the free (gel-solvent) phase and the characteristic time for the reversible transfer from the bounded to the free phase $1/K_{bg}$. No drug diffusion occurs in the bounded phase. Balance equations for $C_m$ and $C_{res}$, as well as the boundary conditions for $C_g$ and $C_m$ remain unchanged with respect to the purely Fickian diffusion model, see Eqs. (3-5) in Section 2.6.1.

In this case, the total amount of drug released up to an infinite time reads as

$$\lim_{\tau\to\infty}M_\tau = \frac{V_g C_0}{1+\beta\left(1+\alpha_m+K_{eq}^{-1}\right)} \quad (12)$$

that can be significantly smaller than $M_\infty$ (see Eq. (6)), depending on the value of $K_{eq}$, because for any finite value of $K_{eq}$, part of the drug, namely the total amount $\frac{V_g C_0\beta K_{eq}^{-1}}{1+\beta\left(1+\alpha_m+K_{eq}^{-1}\right)}$, get trapped in the bounded phase and never released.

The initial partition coefficient $\varepsilon$ depends on the initial temperature of the gel sample. If the gel sample is kept at constant ambient temperature $T_0$ prior of the experiment and then, at time t=0, placed in the donor chamber in contact with the solvent solution in the receptor chamber kept at constant temperature $T = 37.0\pm0.1$°C (temperature of the water bath), the initial partition coefficient reads as

$$\varepsilon = \frac{1}{1+K_{eq}(T_0)} \quad (13)$$

The gel sample, initially at temperature $T_0$, rapidly warms up (1–3 minutes) to the water bath temperature $T$ and the release process takes place at constant temperature $T$.

The equilibrium constant $K_{eq}(T_0)$ at the initial temperature $T_0$, and therefore the initial partition coefficient $\varepsilon$, can be estimated from an independent release experiment performed at temperature $T_0$ of the water bath, by experimentally estimating $\lim_{\tau\to\infty}M_\tau$ at $T = T_0$ and therefore $K_{eq}(T_0)$ from Eq. (12) and $\varepsilon$ from Eq. (13).

### 2.7. Primary skin irritation experiments

Three healthy male New Zealand White rabbits were purchased from Charles River (Calco Lecco, Italy) and acclimated to the laboratory for a week. The rabbits were individually housed and received a standard diet and tap water *ad libitum*. Laboratory animal care guidelines (EEC Directive of 1986; 86/609/EEC) were followed. The back of the animals was clipped free of their fur with an electric clipper 24 h before application of the samples. Clipped rabbit skin was divided into four sites of same area (30 × 30 mm). Scl, Scl-$CM_{300}$-based hydrogels were spread on two of the four different locations (500 mg/site), whereas the other two ones were kept free from any material application and used as a visual control. The treated and the control areas were covered with a gauze, and the back of the rabbit was wrapped with a non-occlusive bandage. After the treatment, the animals were returned to their cages. Bandages and the test hydrogels were removed after 4 h and rabbits were examined for skin irritation 1 hour later. Observation of the different sites was repeated at 24, 48 and 72 h. The reaction, defined as erythema or edema, was evaluated according to the score of the skin reactions already reported. The score of primary irritation (SPI) was calculated for each rabbit as the difference between the sum of the scores of erythema and edema at 24, 48 and 72 h in the treated sites and the control areas. These values were also divided by the number of observations. The primary skin irritation index (PII) was calculated as the arithmetical mean of the SPI values of the three animals. The evaluation of PII was performed according to the categories reported in the literature (Draize, Woodard & Calvery, 1944).

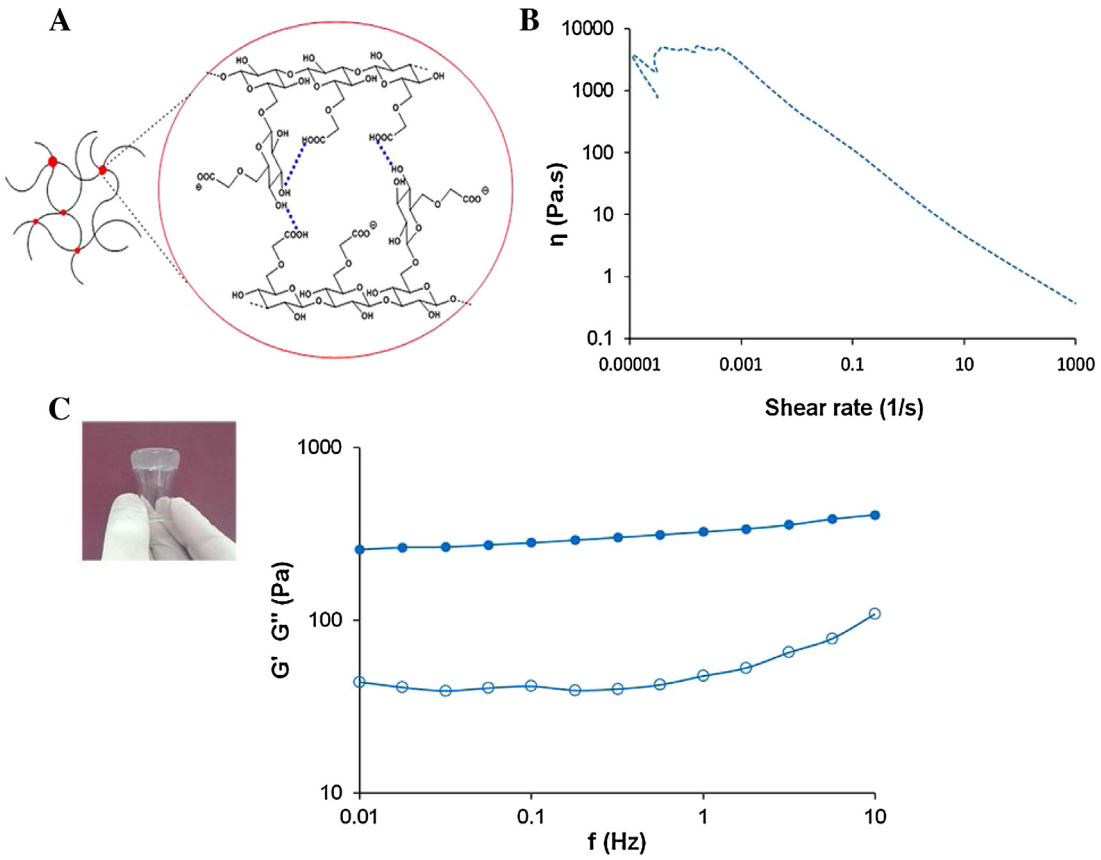


**Fig. 1.** Rheological characterization of Scl-$CM_{300}$ physical hydrogels. A) Schematic representation of hydrogen bond formation among carboxyl and hydroxyl groups. B) Flow curve showing the pseudoplastic behavior of the polymer at 37.0 ± 0.1°C. C) Representative picture of Scl-$CM_{300}$ physical hydrogel and the corresponding frequency sweep test carried out in the range of 0.01–10 Hz. Full circles represent the elastic modulus G' and empty circles the viscous modulus G".

## 3. Results and discussion

### 3.1. Physical hydrogel preparation and characterization

Scleroglucan carboxymethyl (Scl-$CM_{300}$) with a high degree of derivatization was obtained following a previously established protocol (Corrente et al., 2012). FT-IR spectra of the polymer prior and after ion exchange were recorded to evaluate the conversion of Scl in its carboxymethyl derivative. As expected, elution through DOWEX resin caused the complete conversion of the polymer to the free acid derivative and a consequent increase in the intensity of the corresponding stretching band at 1725 $cm^{-1}$ could be observed (Fig. S2). In fact, a shift in the equilibrium from the carboxylate group (-$COO^-$) to the carboxylic group (-COOH) is evident from the overlapping of the FT-IR spectra. Specifically, the stretching of the carbonyl group shifts from 1590 $cm^{-1}$ (before ionic exchange) to 1725 $cm^{-1}$ (after ionic exchange), thus indicating a higher presence of carboxylic groups in the protonated form. The total amount of carboxylic groups added to the polymer backbone was quantified through potentiometer titration and resulted in being 300 ± 10.

The high number of carboxymethyl functional groups introduced on the Scl backbone promote interaction among the polymeric chains, making possible the formation of physical hydrogels without the addition of any salt. Specifically, the carboxylic groups introduced in the backbone of the polysaccharide can form hydrogen bonds and ion-dipole interactions, responsible for the physical gel formation (Fig. 1A). Hydrogels were formed at the concentration of 2.0% w/v in the presence and absence of drugs. This concentration was chosen as the optimal one because of the homogeneous consistency of the hydrogels suitable for topical application.

The flow curve of the plain hydrogel (without drugs) has been carried out to study the rheological properties of the system at different shear rates (Fig. 1B). Scl-$CM_{300}$ at 2.0% w/v showed a *shear-thinning* behavior that is typical of a pseudoplastic macromolecular system. It is noteworthy that the viscosity behavior of Scl-CM at a high degree of derivatization resembles the flow properties of native scleroglucan at the same concentration (Corrente et al., 2012). The preservation of the pseudoplastic flow behavior after derivatization is an essential feature allowing the use of this system as a topical formulation, which can be applied to the skin or to the mucosae.

Frequency sweep tests carried out in the viscoelastic region showed values of the elastic modulus G' higher than the viscous modulus G" over the range of frequencies tested (Fig. 1C), indicating the formation of a physical hydrogel. The value of G' slightly changes throughout the test showing the typical behavior of a weak gel, for which the value of G' is influenced by the frequency of the applied deformation.

### 3.2. Rheological characterization of drug loaded Scl-$CM_{300}$ physical hydrogels

A previous report (Corrente et al., 2012) proposing Scl-$CM_{300}$ hydrogels as drug carriers for oral drug administration, showed that a reduction in the pH value can increase the hydrogel strength (higher values of the G' elastic modulus) and reduce the swelling capacity of the matrix.

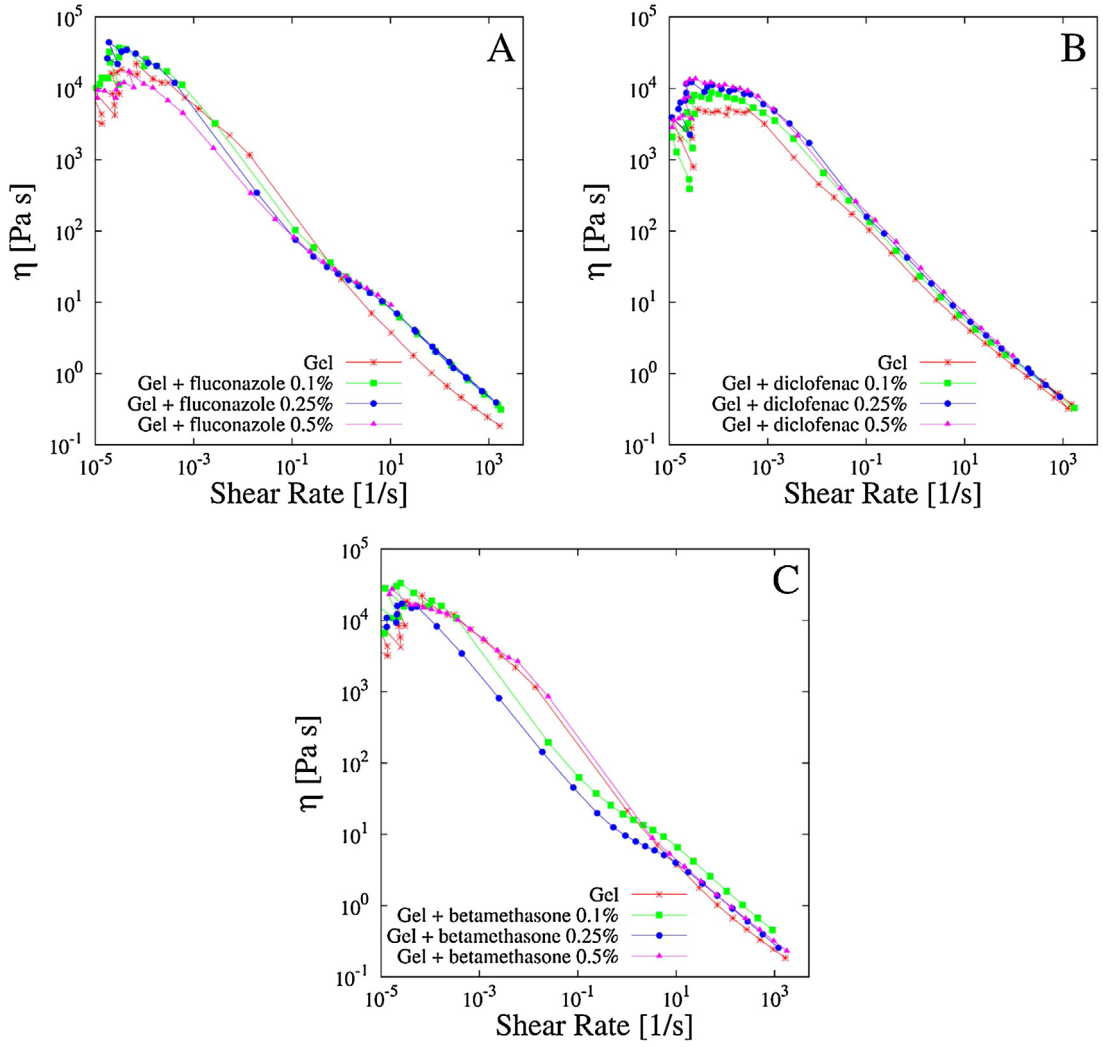


**Fig. 2.** Comparison of flow curves of Scl-$CM_{300}$ physical hydrogels loaded with different concentration (from 0.1% w/v up to 0.5% w/v) of A) fluconazole, B) diclofenac and C) betamethasone. Flow curves were recorded at 37.0 ± 0.1°C.

The focus of our investigation was to determine whether the presence of a loaded drug could affect the rheological properties of Scl-$CM_{300}$ hydrogels as drug carriers for topical administration. To this end, three different therapeutic molecules, such as fluconazole, diclofenac, and betamethasone phosphate were included in the polymeric solution of Scl-$CM_{300}$ 2.0% w/v before hydrogel formation. Different concentrations of the three drugs were tested varying from 0.1% w/v up to 0.5% w/v.

Irrespective of the drug considered and its amount, the corresponding physical hydrogels showed *shear-thinning* behavior similar to the plain system, with almost no significant effects on the viscosity values (see Fig. 2).

Results of frequency sweep tests for the hydrogels loaded with the selected drugs (0.25% w/v) showed different behaviors according to the type of molecule loaded in the polymeric network (see Fig. 3).

Fluconazole did not influence the hydrogel properties over the whole range of frequencies investigated, and only a small decrease in the G" values was observed respect to the hydrogel without the drug. Mechanical spectra of Scl-$CM_{300}$ hydrogel loaded with betamethasone showed a reduction of both G' and G" when compared to the plain hydrogel, indicating that the drug partially interferes with the formation of the polymeric network, thus resulting in a softer hydrogel.

On the contrary, the presence of diclofenac induced a significant increase of both G' and G", thus indicating the formation of a stronger gel (Fig. 3C). It is possible to assume that the presence of a carboxylic group in the diclofenac molecule leads to additional hydrogen bonding interactions affecting the final rheological properties of the physical hydrogel.

Based on these results it may be expected a different ability of the Scl-$CM_{300}$ network to modulate the release of the three selected molecules. In fact, besides the molecular weight and the chemical structure of the investigated drugs, the strength of the drug-polymer interactions is an additional factor, which may affect the molecular mobility of the incorporated model drug, playing a critical role in controlling the release rate from the polymer matrix.

For this reason, these findings were further investigated through *in-vitro* release tests.

### 3.3. Release studies

#### 3.3.1. Analysis of release data from blanks

Fig. 4 shows the release profiles of the three model drugs in aqueous solution (blank systems, points with error bars) and the comparison with the Fickian model described in Section 2.6.1 (continuous lines).

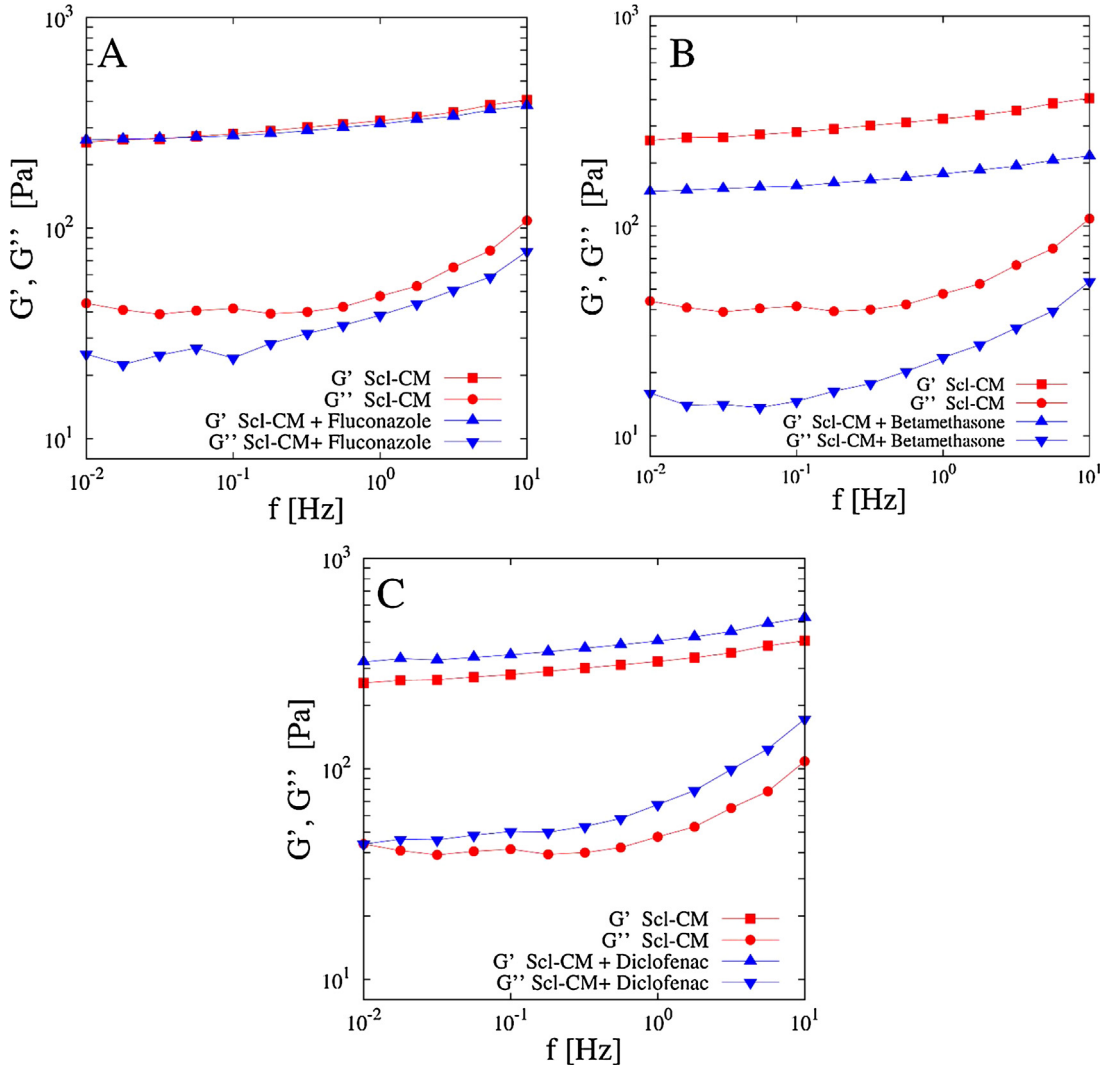


**Fig. 3.** Frequency sweep tests carried out in the range of 0.01–10 Hz for plain Scl-$CM_{300}$ hydrogel (red square and circular points for G' and G", respectively) and loaded with different model drugs (upper and lower triangular points for G' and G", respectively). A) fluconazole; B) betamethasone; C) diclofenac.

It can be observed that diclofenac and fluconazole exhibit similar blank release curves since they are characterized by very close values of the LeBas volume. A slower release is obtained for betamethasone due to the significantly larger value of its LeBas volume.

Model curves were obtained, for each model drug, by estimating $D_s$ from the Wilke-Chang correlation Eq. (7) and by best fitting the ratio $\gamma_s = D_s/D_m$ in the Fickian transport model (see Table 1).

The values of $\gamma_s$ are in the order of $10^1$ for all the model drugs, thus implying that the effective diffusion coefficient in the dialysis membrane is one order of magnitude smaller than the diffusivity in water solution. Therefore the dialysis cellophane membrane, even if extremely thin ($L_m$=48 μm), offers a significant resistance to drug transport from the donor to the receptor compartment and its presence should be necessarily taken into account in the transport model (Ng, Rouse, Sanderson & Eccleston, 2010). This is in agreement with other drug release studies from Scleroglucan hydrogels making use of the same cellophane membrane (Visking tubing, cut-off 12,000-14,000 Da) in two or three compartments diffusion cells (Coviello, Grassi, Lapasin, Marino, & Alhaique, 2003).

This observation is further supported by the analysis of blank release data from a 0.25% w/v aqueous solutions of theophylline (TPH, see Fig. S3), usually adopted as a model drug and characterized by both a low MW and a small LeBas volume.

For TPH, the value of the water diffusivity $D_s = 8.39 \times 10^{-6}$ $cm^2$/sestimated from the Wilke-Chang correlation, is in perfect agreement with experimental literature data $D_s = 8.2 \times 10^{-6}$ $cm^2/s$ at 37.0°C (Grassi, Colombo, Lapasin & Pricl, 2001; Coviello et al., 2003) and the best fit value of the diffusivity ratio is $\gamma_s = 16 \pm 0.2$.

Fig. 4B shows the effective diffusion coefficient in the dialysis membrane $D_m$ as a function of the molecular weight for all the model drugs analyzed, highlighting how $D_m$ is a linear decreasing function of the molecular weight over the whole range of MW analyzed.

### 3.3.2. *Analysis of release data from Scl-$CM_{300}$ hydrogels*

Fig. 5 shows experimental release data of the three model drugs under investigation from Scl-$CM_{300}$ hydrogels at 37.0°C.

Continuous black lines a-b represent the short-intermediate time-scale Fickian behavior $M_t/M_\infty \sim t^{1/2}$ (in agreement with the release data of fluconazole and betamethasone) while curve c represents the "anomalous" non-Fickian behavior $M_t/M_\infty \sim t^n$ with n=1.2 »1/2, in agreement with diclofenac release profile (Fig. 5). Drug-polymer interactions are here responsible for the time-lag observed in the early-stage release curve of diclofenac that is a typical feature of non-Fickian transport. Similar features have been observed in drug release experiments from sclerox and cross-linked

**Table 1**
LeBas molar volumes, diffusion coefficients in water solution, diffusivity ratio $\gamma$ and effective diffusion coefficient in the dialysis membrane and in Scl-CM$_{300}$ hydrogel at 37.0 ± 0.1°C for different model drugs.

| | $V_{LB}\ [mol/cm^3]$ | $D_s\ [cm^2/s]$ | $\gamma_s = D_s/D_m$ | $D_m\ [cm^2/s]$ | $\gamma_g$ | $D_g\ [cm^2/s]$ |
|---|---|---|---|---|---|---|
| Theophylline | 170.2 | $8.39 \cdot 10^{-6}$ | 16.0 ± 0.2 | $5.24 \pm 0.06 \cdot 10^{-7}$ | n.e. | n.e. |
| Diclofenac | 294.8 | $6.05 \cdot 10^{-6}$ | 14.1 ± 0.2 | $4.29 \pm 0.06 \cdot 10^{-7}$ | 14.1 ± 0.2 | $6.05 \cdot 10^{-6}$ |
| Fluconazole | 307.6 | $5.89 \cdot 10^{-6}$ | 14.0 ± 0.2 | $4.20 \pm 0.06 \cdot 10^{-7}$ | 14.0 ± 0.2 | $5.89 \cdot 10^{-6}$ |
| Betamethasone | 471.2 | $4.56 \cdot 10^{-6}$ | 19.4 ± 0.2 | $2.35 \pm 0.02 \cdot 10^{-7}$ | 11.5 ± 0.2 | $2.70 \cdot 10^{-6}$ |

n.e. not evaluated.

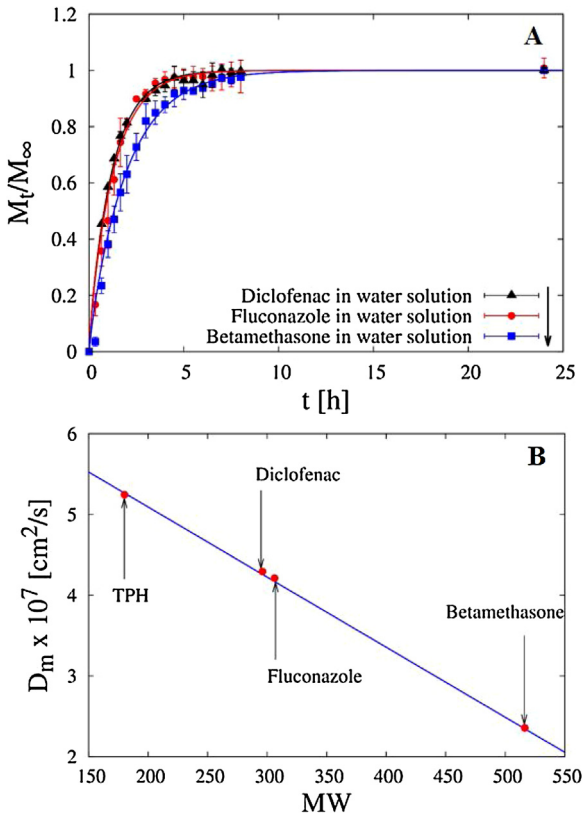


**Fig. 4.** A) Experimental release data from 0.1 ml of aqueous solutions (0.25% w/v) (blanks, points with error bars) containing different model drugs and the comparison with the Fickian transport model described in section 2.6.1 (continuous lines). Best fit values of the diffusivity ratio $\gamma_s = D_s/D_m$ are reported in Table 1. The arrow indicates increasing values of the LeBas volume. B) $D_m$ *vs MW* for different model drugs, including TPH.

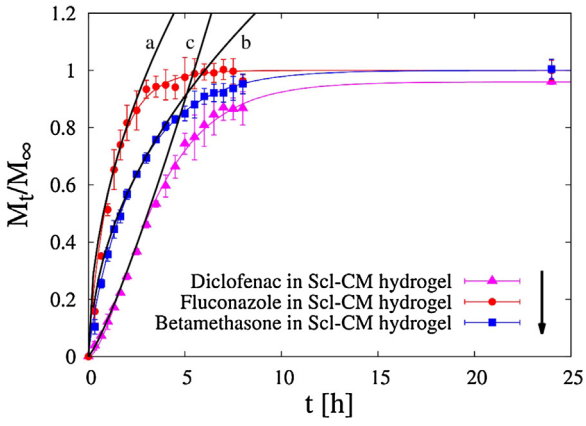


**Fig. 5.** Experimental release data from Scl-CM$_{300}$ hydrogel containing different model drugs and the comparison with the Fickian short-intermediate time-scale behavior $M_t/M_\infty \sim t^{1/2}$ (curves a-b) and the non-Fickian behavior $M_t/M_\infty \sim t^n$ with n=1.2 »1/2 (curve c). The arrow indicates increasing values of LeBas molar volumes.

sclerox hydrogels (Coviello, Grassi, Rambone, & Alhaique, 2001). These results confirmed the trend observed in the frequency sweep tests where diclofenac was the only tested drug capable of increasing the values of G' and G" due to the formation of drug-polymer hydrogen bonding interactions. The same interactions are here responsible for the observed anomalous release.

Specifically, diclofenac is released at a significantly slower rate than fluconazole and betamethasone, despite the fact that its LeBas molar volume is similar or significantly smaller than the ones reported for fluconazole and betamethasone. Moreover, not the whole amount of drug initially loaded is actually released after 24 h. For these reasons, a Fickian transport model was adopted for fluconazole and betamethasone (Section 2.6.1), whereas the non-Fickian solute transport model (Section 2.6.2) taking into account drug/hydrogel interactions, was introduced to describe diclofenac release curves.

The half-life time $t^{1/2}$ for drug molecules non interacting with the hydrogel matrix are $t^{1/2}$=45.6 min for fluconazole (MW=306) and $t^{1/2}$=96 min for betamethasone (MW=516). Therefore by almost doubling the molecular weight of the loaded drug, also the half-life time doubles.

Henceforth the hydrogel Scl-CM$_{300}$ appears to be suitable for drug delivery as the release is strongly dependent on the dimensions of the model drug and therefore the delivery can be tailored in function of the steric hindrance of the entrapped molecule.

Similar release features have been observed by Coviello et al., 2005b for Scl/Borax hydrogels, which they proposed as suitable hydrogels for a sustained drug delivery.

Coviello et al., 2005b observed a Fickian behaviour for the release curves of TPH (MW=180), Vit. B12 (MW=1355) and myoglobin (MW=17800) from Scl/Borax hydrogel in distilled water and showed how half-lives for Vit. B12 (about ten times bigger than TPH in terms of MW) and myoglobin (about one hundred times bigger than TPH) were respectively about two and five times bigger than the TPH half-life.

Therefore, the hydrogel of Scl-CM$_{300}$ appears to be more sensitive to the drug molecular weight than Scl/Borax hydrogel.

### 3.3.3. *Release data modeling*

Fig. 6A shows fluconazole release data from an aqueous solution and from the hydrogel in excellent agreement with the Fickian transport model with $\gamma_s = \gamma_g$, since release data from the hydrogel and from the aqueous solution are almost coincident. It is therefore a case of an ideal topical release, as this formulation does not offer additional resistance to fluconazole release with respect to an aqueous solution.

Fig. 6B shows betamethasone release data from aqueous solution and hydrogel in excellent agreement with the Fickian transport model with $\gamma_s = 19.4$ and $\gamma_g = 11.5$. Therefore, the Scl-CM$_{300}$ formulation offers a small additional resistance to betamethasone transport (larger LeBas molar volume) since $D_g = \left(\gamma_g/\gamma_s\right) D_s \approx 0.59 D_s$. For a direct comparison between $D_g$ and $D_s$ for different model drugs see Table 1.

Fig. 6C shows diclofenac release data from aqueous solution and hydrogel at 37.0 ± 0.1°C, together with the release data

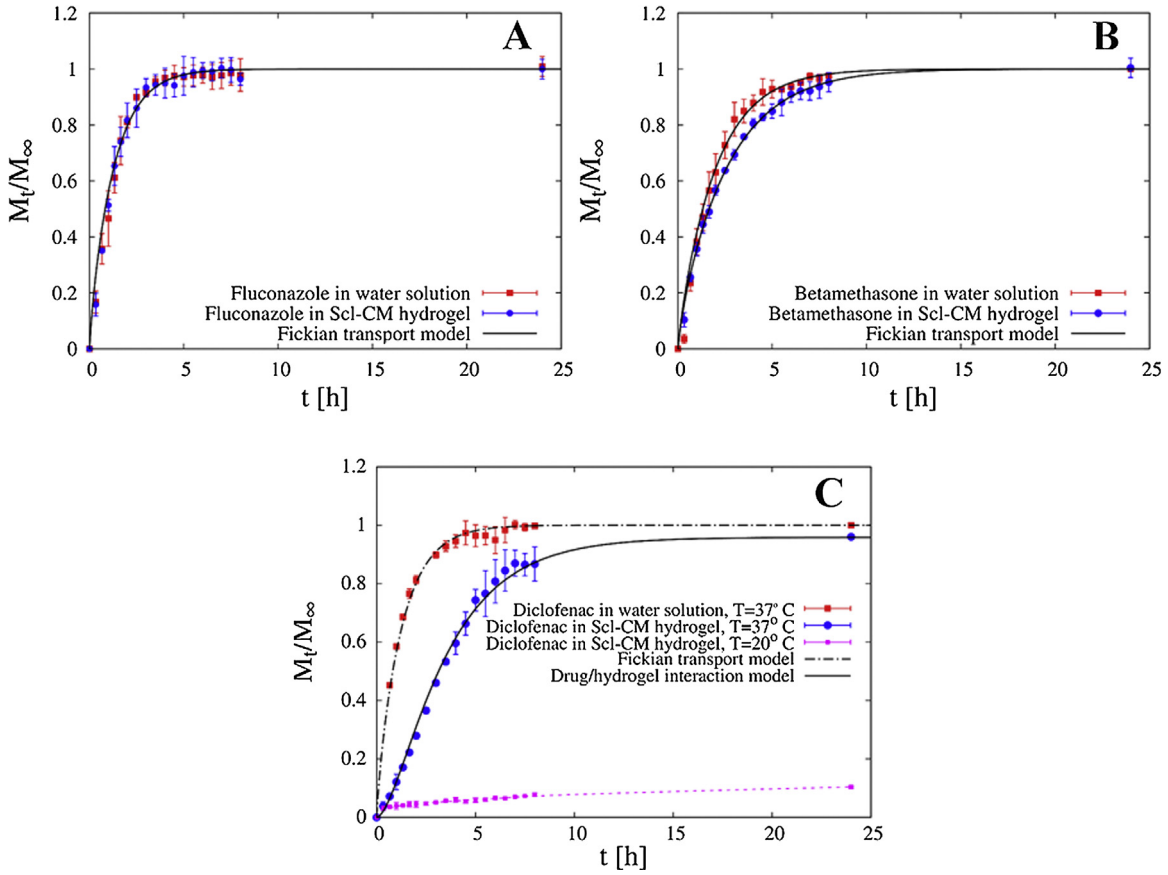


**Fig. 6.** Experimental release data of A) fluconazole from water solution and from Scl-$CM_{300}$ hydrogel and the comparison with the Fickian transport model with $\gamma_s = \gamma_g$; B) betamethasone from water solution and from Scl-$CM_{300}$ hydrogel and the comparison with the Fickian transport model with $\gamma_s = 19.4$ and $\gamma_g = 11.5$; C) diclofenac from water solution (at 37.0°C) and from Scl-$CM_{300}$ hydrogel at 37.0°C and 20°C. Broken dot-line curve represents the Fickian transport model for blank with $\gamma_s = 14.1$. Continuous line represents the non-Fickian drug/matrix interaction model with $\gamma_g = \gamma_s = 14.1$ and $\varphi^2 = 0.74 \pm 0.02$.

from hydrogel at room temperature 20°C. The release curve from Scl-$CM_{300}$ hydrogel is significantly slower than that from water solution although the diclofenac molecule exhibits the smallest LeBas volume among the three model drugs analyzed.

Rheological results support the idea of a chemical interaction between diclofenac and the hydrogel matrix.

Release data at room temperature are a direct evidence not only for the interaction between diclofenac and Scl-$CM_{300}$, but they also suggest that a very large amount of drug is bounded to the polymer matrix and is unable to diffuse out from the hydrogel. In fact, only 10% of the drug is released from the hydrogel after 24 h.

As discussed in Section 2.6.2, from the asymptotic value $\lim_{t\to\infty} M_t/M_\infty\,(20^\circ C) = 0.11 \pm 0.02$ and from Eqs. (12-13) we estimate $K_{eq}\,(20^\circ C) = 2.9 \cdot 10^{-3}$ and the initial partition coefficient $\varepsilon = 0.001$ for the release experiment at the working temperature of 37.0°C.

The three other parameters entering the non-Fickian transport model are $\gamma_g$, $K_{eq}\,(37^\circ C)$ and $\varphi^2$. From the asymptotic value $\lim_{t\to\infty} M_t/M_\infty\,(37^\circ C) = 0.96 \pm 0.03$ and from Eqs. (12) we estimate $K_{eq}\,(37^\circ C = 0.57)$. For $\gamma_g$ we set $\gamma_g = \gamma_s = 14.1$ because of the small LeBas volume of the drug molecule. The only best fit parameter is the square Thiele modulus $\varphi^2$.

Fig. 6C shows the excellent agreement between the release data from the hydrogel and the non-Fickian transport model with $\varphi^2 = 0.74 \pm 0.02$.

The best fit value of $\varphi^2$, order of unity, indicates that the characteristic time for the irreversible transfer from the bounded to the free-solvent phase is of the same order as the characteristic diffusion time, thus explaining the significant slowing down of the experimental release curve.

The data obtained proved that Scl-$CM_{300}$-based hydrogels are useful for a sustained release of diclofenac, provided that the percentage of drug released after 5 h is less than 80%.

### 3.4. Primary skin irritation experiments

Primary skin irritation experiments were carried out on rabbits, to assess possible use of Scl-$CM_{300}$-based hydrogels in topical formulations. Individual skin irritation scores, calculated as described in Section 2.7, were always equal to 0. No signs of erythema or edema were observed in the animals up to 72 h after the application of the samples. According to these data, the primary skin irritation index (PII) of the tested materials was negligible, highlighting that Scl-$CM_{300}$ possesses adequate properties for application as a modified drug delivery system in topical formulations.

## 4. Conclusions

High-carboxymethylated scleroglucan can form physical hydrogels with negligible primary skin irritation index and adequate rheological properties even in the presence of different therapeutic drugs such as fluconazole, diclofenac sodium salt, and betamethasone phosphate sodium.

The shear thinning behavior of the system was not affected by loading these molecules within the polymeric network. A slightly weaker hydrogel was obtained with betamethasone. On the contrary, the carboxylic group of diclofenac made it able to interact

with Scl-$CM_{300}$, thus strengthening the mechanical properties of the corresponding physical gel.

These findings are supported by experimental drug release studies carried out on drug-loaded Scl-$CM_{300}$ hydrogels and further confirmed by mathematical modeling of the release profiles. In fact, while betamethasone and fluconazole were released according to a Fickian transport model, model analysis applied to diclofenac explained the non-Fickian feature of its release profile.

The estimated values of effective drug diffusion coefficients in the hydrogel for betamethasone and fluconazole, compared to those in an aqueous solution, led us to propose Scl-$CM_{300}$ as an excellent formulation for fast topical release. The slower release rate observed for diclofenac, due to drug-polymer interactions, made Scl-$CM_{300}$ useful for a sustained topical release of this drug.

## Appendix A. Supplementary data

Supplementary data associated with this article can be found, in the online version, at http://dx.doi.org/10.1016/j.carbpol.2017.07.008.

## References


Adrover, A., Giona, M., Grassi, M., Lapasin, R., & Pricl, S. (1996). Controlled release of theophylline from water-swollen scleroglucan matrices. *Journal of Membrane Science*, *113*, 7–20.

Arnstein, P. M. (2012). Evolution of Topical NSAIDs in the Guidelines for Treatment of Osteoarthritis in Elderly Patients. *Drugs & Aging*, *29*, 523–531.

Caló, E., & Khutoryanskiy, V. V. (2015). Biomedical applications of hydrogels: A review of patents and commercial products. *European Polymer Journal*, *65*, 252–267.

Cerreto, A., Corrente, F., Botta, B., Pacelli, S., Paolicelli, P., Mannina, L., & Casadei, M. A. (2013). NMR investigation of carboxymethyl scleroglucan. *International Journal of Polymer Analysis and Characterization*, *18*, 587–595.

Corrente, F., Matricardi, P., Paolicelli, P., Tita, B., Vitali, F., & Casadei, M. A. (2009). Physical Carboxymethylscleroglucan/Calcium ion hydrogels as modified drug delivery systems in topical formulations. *Molecules*, *14*, 2684–2698.

Corrente, F., Paolicelli, P., Matricardi, P., Tita, B., Vitali, F., & Casadei, M. A. (2012). Novel pH-sensitive physical hydrogels of carboxymethyl scleroglucan. *Journal of Pharmaceutical Sciences*, *101*, 256–267.

Corrente, F., Abu Amara, H. M., Pacelli, S., Paolicelli, P., & Casadei, M. A. (2013). Novel injectable and in situ cross-linkable hydrogels of dextran methacrylate and scleroglucan derivatives: preparation and characterization. *Carbohydrate Polymers*, *92*, 1033–1039.

Coviello, T., Grassi, M., Rambone, G., & Alhaique, F. (2001). A crosslinked system from Scleroglucan derivative: preparation and characterization. *Biomaterials*, *22*, 1899–1909.

Coviello, T., Grassi, M., Lapasin, R., Marino, A., & Alhaique, F. (2003). Scleroglucan/borax: characterization of a novel hydrogel system suitable for drug delivery. *Biomaterials*, *24*, 2789–2798.

Coviello, T., Palleschi, A., Grassi, M., Matricardi, P., Bocchinfuso, G., & Alhaique, F. (2005). Scleroglucan: a versatile polysaccharide for modified drug delivery. *Molecules*, *10*, 6–33.

Coviello, T., Grassi, M., Palleschi, A., Bocchinfuso, G., Coluzzi, G., Banishoeib, F., & Alhaique, F. (2005). A new scleroglucan/borax hydrogel: swelling and drug release studies. *International Journal of Pharmaceutics*, *289*, 97–107.

Draize, J. H., Woodard, G., & Calvery, H. O. (1944). Methods for the study of irritation and toxicity of substances applied topically to the skin and mucous membrane. *Journal of Pharmacology and Experimental Therapapeutics*, *82*, 377–390.

Gonzalo-Lumbreras, R., Santos-Montes, A., Garcia-Moreno, E., & Izquierdo-Hornillos, R. (1997). High-Performance Liquid Chromatographic Separation of Corticoid Alcohols and Their Derivatives: A Hydrolysis Study Including Application to Pharmaceuticals. *Journal of Chromatographic Science*, *35*, 439–445.

Grassi, M., Colombo, I., Lapasin, R., & Pricl, S. (2001). Experimental determination of the theophylline diffusion coefficient in swollen sodium-alginate membranes. *Journal of Controlled Release*, *76*, 93–105.

Guo, B., Stokke, B. T., & Elgsaeter, A. (1996). Swelling of Sclerolucan gels in binary DMSO water solvents. *Colloids and Surfaces A: Physicochemical and Engineering Aspects*, *112*, 185–191.

Hayduk, W., & Laudie, H. (1974). Prediction of diffusion coefficients for nonelectrolytes in dilute aqueous solutions. *AIChE Journal*, *20*, 611–615. \

Hoare, T. R., & Kohane, D. S. (2008). Hydrogels in drug delivery. *Progress and challenges. Polymer*, *49*, 1993–2007.

Ioannis, G., Harvey, L. M., & McNeil, B. (2005). Scleroglucan. In *Biopolymers Online*. Wiley-VCH Verlag GmbH & Co. KGaA. http://dx.doi.org/10.1002/3527600035.bpol6002

Moraes, L. A., Lerner, F. E., Moraes, M. E., Moraes, M. O., Corso, G., & De Nucci, G. (1999). Fluconazole Bioequivalence Study: Quantification by Tandem Mass Spectrometry. *Therapeutic Drug Monitoring*, *21*, 200–207.

Ng, S. F., Rouse, J., Sanderson, D., & Eccleston, G. (2010). A comparative study of transmembrane diffusion and permeation of ibuprofen across synthetic membranes using Franz diffusion cells. *Pharmaceutics*, *2*, 209–223.

Olejnik, A., Goscianska, J., & Nowak, I. (2012). Active compounds release from semisolid dosage forms. *Journal of Pharmaceutical Sciences*, *101*(11), 4032–4045.

Palleschi, A., Bocchinfuso, G., Coviello, T., & Alhaique, F. (2005). Molecular dynamics investigations of the polysaccharide scleroglucan: first study on the triple helix structure. *Carbohydrate Research*, *340*, 2154–2162.

Pobudkowska, A., & Domanska, U. (2014). Study of pH-dependent drugs solubility in water. *Chemical Industry & Chemical Engineering Quarterly*, *20*, 115–126.

Singh, M., Lumpkin, J. A., & Rosenblatt, J. (1994). Mathematical modeling of drug release from hydrogel matrices via a diffusion coupled with desorption mechanism. *Journal of Controlled Release*, *32*, 17–25.

Touitou, E. (2002). Drug delivery across the skin. *Expert Opinion on Biological Therapy*, *2*, 723–733.

Trookman, N. S., & Rizer, R. L. (2011). Randomized Controlled Trial of Desonlde Hydrogel 0.05% versus Desonide Ointment 0.05% in the Treatment of Mild-to-moderate Atopic Dermatitis. *Journal of Clinical and Aesthetic Dermatology*, *4*, 34–38.

Viñarta, S. C., François, N. J., Daraio, M. E., Figueroa, L. I. C., & Fariña, J. I. (2007). Sclerotium rolfsii scleroglucan: The promising behavior of a natural polysaccharide as a drug delivery vehicle: suspension stabilizer and emulsifier. *International Journal of Biological Macromolecules*, *41*, 314–323.

## Supporting Information

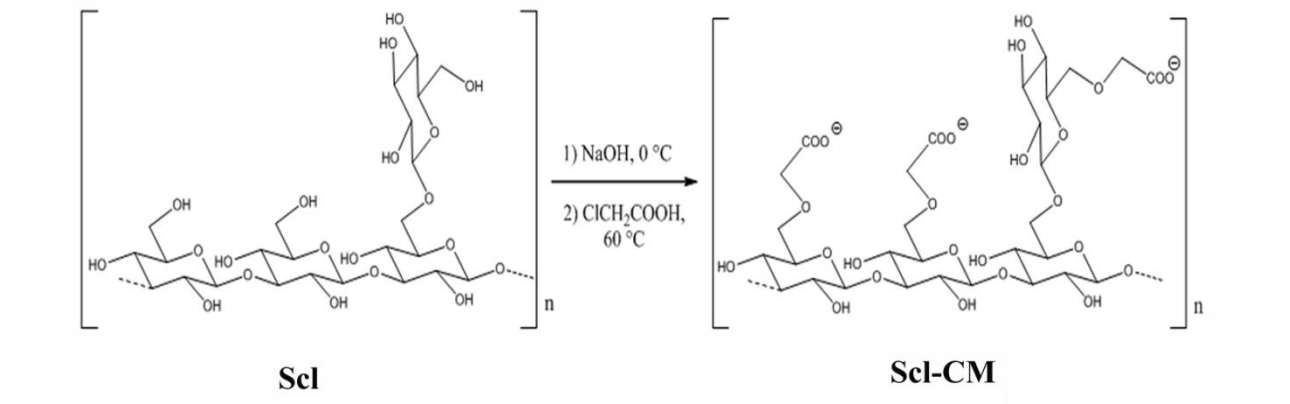


**Figure S1. Scheme of the reaction followed to obtain a high carboxymethyl derivate of scleroglucan.**

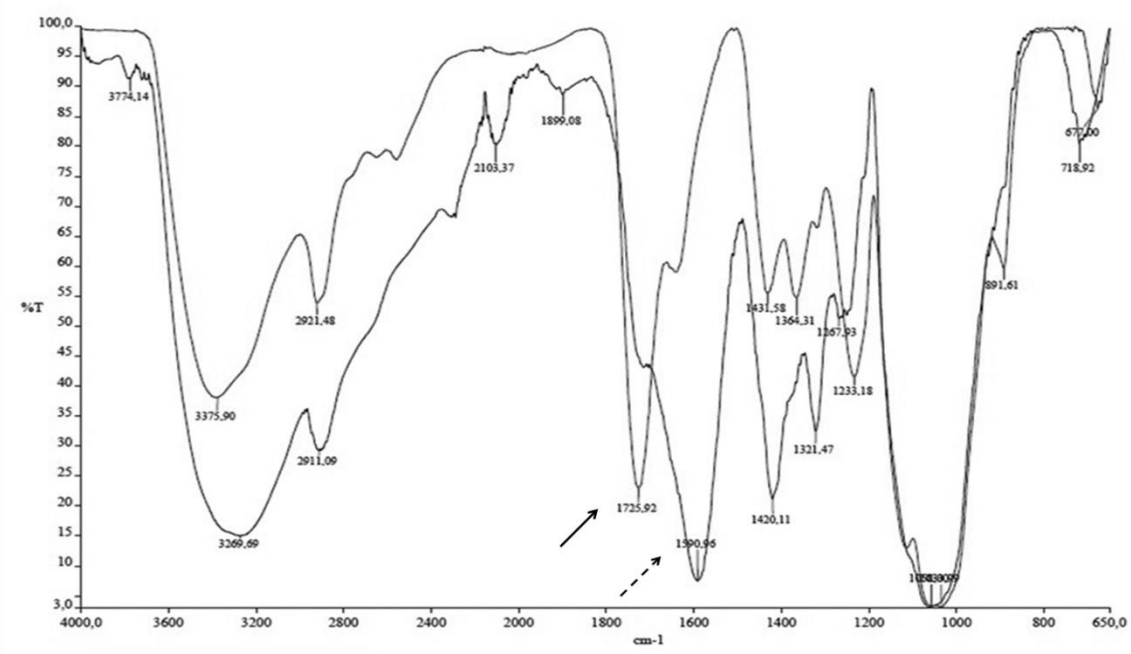


**Figure S2. FT-IR spectra of Scl-CM before and after ionical exchange. A shift in the equilibrium from the carboxylate group (-$COO^-$) to the carboxylic group (-COOH) is evident from the overlapping of the two spectra. Specifically, the stretching of the carbonyl group shifts from 1590 $cm^{-1}$ before ionical exchange (dotted arrow) to 1725 $cm^{-1}$ (bold arrow), indicating a higher presence of carboxylic groups in the protonated form. In fact, the intensity of this band changes according to the protonation degree of the carboxylic groups. As expetcted, it increases markedly after polymer elution through an ion-exchange DOWEX resin, which causes the complete protonation of all the carboxylic groups of Scl-CM.**

The derivatization of the polymer was also previously demonstrated by monodimensional and bidimensional $^{1}$H-NMR analysis carried out on lower derivatized Scl-CM. The NMR analysis clearly showed the presence of carboxymethyl groups and the site of derivatization. In fact, it was demonstrated that, on low derivatized Scl-CM, the carboxymethyl groups were introduced on the primary hydroxyl groups of the lateral glucose (A. Cerreto, F. Corrente, B. Botta, S. Pacelli, P. Paolicelli, L. Mannina, M.A. Casadei. NMR Characterization of Carboxymethyl Scleroglucan. International Journal of Polymer Analysis and Characterization, 2013, 18(8), 587-595.

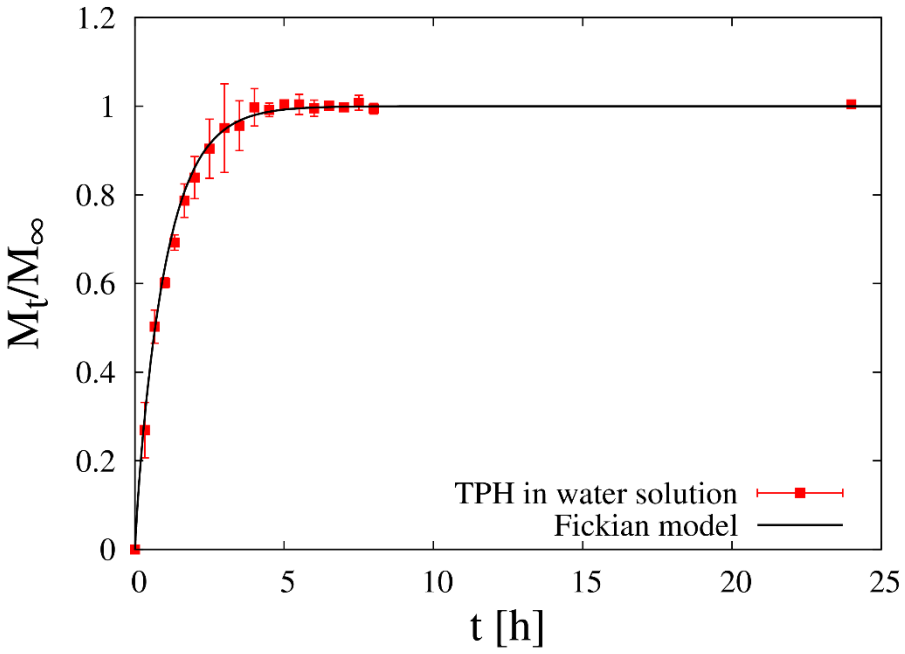


**Figure S3. Experimental release data from 0.1 ml of aqueous solutions (0.25% w/v), (points with error bars), containing TPH and the comparison with the Fickian transport model described in section 2.6.1 (continuous lines). Best-fit values of the diffusivity ratio is $\gamma_s = 16.0 \pm 0.2$.**

European Polymer Journal 104 (2018) 184–193

Contents lists available at ScienceDirect

European Polymer Journal

journal homepage: www.elsevier.com/locate/europolj

Macromolecular Nanotechnology

# Design of a tunable nanocomposite double network hydrogel based on gellan gum for drug delivery applications

Settimio Pacelli[a,b,*], Patrizia Paolicelli[b], Michele Avitabile[b], Gabriele Varani[c], Laura Di Muzio[b], Stefania Cesa[b], Jacopo Tirillò[c], Cecilia Bartuli[c], Martina Nardoni[b], Stefania Petralito[b], Alessandra Adrover[c], Maria Antonietta Casadei[b]

[a] BioIntel Research Laboratory, Department of Chemical and Petroleum Engineering, Bioengineering Graduate Program, School of Engineering, University of Kansas, 66045 Lawrence, USA
[b] Department of Drug Chemistry and Technologies, Sapienza University of Rome, P.le Aldo Moro 5, 00185 Rome, Italy
[c] Department of Chemical, Material and Environmental Engineering, Sapienza University of Rome, Via Eudossiana 18, 00184 Rome, Italy

ARTICLE INFO

*Keywords:*
Sustained release
Toughness
Elasticity
Laponite
Interpenetrated network
Gellan gum

ABSTRACT

The design of an efficient drug delivery platform relies on the fabrication of a suitable polymeric network that can modulate the release of therapeutic molecules. In this study, we aimed to reach this goal by fabricating a novel nanocomposite double network (nDN) hydrogel, which contains the synthetic clay Laponite as the nanofiller necessary to influence the mechanical, physical and releasing properties of the designed carrier. Laponite concentration was varied from 0.5% up to 1.5% w/v to modulate the mechanical and swelling behavior of a hydrogel made of a methacrylate derivate of gellan gum (GG-MA), which served as the first brittle network of the nDN system. Additionally, polyethylene glycol dimethacrylate (PEG-DMA) was chosen as the second soft and elastic network. The inclusion of the clay at a concentration as low as 0.5% w/v positively influenced the single network (SN) hydrogel properties by increasing the stiffness and reducing the swelling ratio of the GG-MA hydrogels. The presence of Laponite® affected the amount of PEG-DMA diffused within the SN of GG-MA. The resulting stretchable and tough nDN system presented a higher swelling ratio in deionized water, and elasticity when compared to the DN hydrogels without any Laponite. Finally, the nDN system showed increased drug adsorption and displayed a better control in modulating the release kinetics of the model drug ofloxacin. Overall, these findings suggest the possible use of the designed nDN system as a novel drug delivery platform for the sustained release of therapeutic molecules.

## 1. Introduction

A suitable polymeric carrier for drug delivery applications possesses the ability to effectively promote the sustained release of a therapeutic molecule over an extended time [1,2]. Achieving this goal allows precise control over the pharmacological activity of a drug and helps to maintain its plasmatic concentration within the therapeutic window [3,4]. Among the available carriers, polymeric hydrogels represent ideal candidates for the design of sustained drug release platforms [5,6]. Their high value relies on the tunable properties, such as swelling, porosity, mechanical stability and responsiveness to physical stimuli. All these factors can be precisely optimized to modulate the loading efficiency and the drug release kinetic [7].

One common strategy to design a polymeric hydrogel for drug delivery consists of the crosslinking of a single network (SN) made of natural or synthetic polymers [8]. However, SN hydrogels often do not possess the requirements to be used as carriers for drug delivery applications. One of the major issues commonly reported with SN hydrogels is the lack of control during the process of crosslinking [9]. This problem leads to the synthesis of a heterogeneous structure, which negatively affects the ability of the hydrogel to modulate the release of a loaded drug. Similarly, SN hydrogels possess poor mechanical properties mainly due to their inhomogeneous brittle network, which easily breaks after the application of small forces. All of these limitations have restricted the applicability of SN hydrogels as carriers for the sustained release of therapeutic molecules [10].

A more promising approach consists of polymeric interpenetrating networks. This route of synthesis combines in a unique platform two different networks to obtain a synergistic effect in terms of physical and mechanical properties [11,12]. A well-explored example of an

* Corresponding author at: BioIntel Research Laboratory, Department of Chemical and Petroleum Engineering, School of Engineering, University of Kansas, 66045 Lawrence, USA. Department of Drug Chemistry and Technologies, Sapienza University of Rome, P.le Aldo Moro 5, 00185 Rome, Italy.
*E-mail addresses:* settimio.pacelli@uniroma1.it, sepace@ku.edu (S. Pacelli).

https://doi.org/10.1016/j.eurpolymj.2018.04.034
Received 2 February 2018; Received in revised form 19 March 2018; Accepted 23 April 2018
Available online 24 April 2018
0014-3057/ 

interpenetrated network is represented by double network hydrogels (DN) [13,14]. One of the most interesting features about DN hydrogels is their excellent mechanical properties including high toughness and resistance to failure along with their high water content [15]. These advantages make them better candidates for the design of novel drug delivery platforms compared to SN hydrogels [16]. A DN hydrogel consists of a first network made of a brittle and polyelectrolyte polymer while the second network presents a soft and elastic behavior [17]. Starting from this original approach, researchers have widely investigated other alternative and innovative designs including but not limited to void DN [18], anisotropic DN [14], microgel-reinforced DN [19], and nanocomposite DN (nDN) systems [20,21]. The last alternative consists of the inclusion of inorganic nanomaterials to generate a nanocomposite material with tunable physical and mechanical properties. For instance, the nanomaterial can impact the equilibrium of swelling, the mechanical properties and the ability of the DN system to retain and control the release of a loaded drug [22]. A large variety of nanomaterials has been tested as nanofillers in both synthetic and natural DN systems. These include polymeric nanoparticles [21], graphene oxide [23,24], carbon nanotubes [25], and inorganic material including nanosilicate-based nanofillers [26]. Among the last group, Laponite is an interesting example of a synthetic nanosilicate that can be introduced to modulate the physical, mechanical and release properties of DN hydrogels [20]. Laponite presents a layered structure (~25 nm diameter, ~1 nm thickness) and anionic charges on the surface that can establish electrostatic interactions both with polymers and drugs [27]. The extent of these interactions can vary based on the concentration of Laponite used and the type of polymers combined in the DN systems [28]. For these reasons, here in this work, we propose the use of Laponite as a nanofiller to modulate the properties of a novel nDN system as a carrier for therapeutic drugs. Specifically, we will investigate the effect of the synthetic clay on the physical, mechanical and release properties of a DN hydrogel made of gellan gum methacrylate (GG-MA) and polyethylene glycol dimethacryate (PEG-DMA). GG-MA will serve as the first brittle poly-anionic network and PEG-DMA will be tested as the second soft and elastic material. The combination of GG-MA and the synthetic polymer PEG-DMA enables the formation of a highly asymmetric structure, which is typically found in DN network hydrogels. Overall the findings gathered from this work will serve to verify whether the inclusion of Laponite can represent a useful strategy to design the next generation of nDN hydrogels for the sustained release of drugs.

## 2. Materials and methods

### 2.1. Materials

Low acetyl gellan gum (GG) Mn $1 \times 10^6$ Da, diethyl ether, anhydrous dimethyl sulfoxide (DMSO), chloroform ($CHCl_3$), triethylamine (TEA), methacrylic anhydride (MA), 4-dimethylamino pyridine (4-DMAP), Irgacure 2959 (2-hydroxy-4-(2-hydroxy-ethoxy)-2-methyl propiophenone), ofloxacin, citric acid, methanol, acetonitrile, N-methyl-pyrrolidone, potassium bromide (KBr), and deuterium oxide ($D_2O$) were purchased from Sigma Aldrich. Polyethylene glycol (PEG) Mn 4000 Da was obtained from Farmalabor. Aluminum oxide was purchased from Merck. Potassium dihydrogen phosphate ($KH_2PO_4$) and sodium phosphate dibasic ($Na_2HPO_4$) were obtained from Carlo Erba Reagents.

Laponite® XLG (low heavy metal and microbiological content) was a gift from Rockwood. Dialysis tubes (cut off 12–14 kDa) were purchased from Medicell international.

### 2.2. Synthesis and characterization of gellan gum methacrylate (GG-MA)

GG was functionalized with methacrylic groups following an established protocol [29]. Briefly, GG (1.0 g) was solubilized in anhydrous DMSO (65 mL) for 5 h at 60.0 ± 0.1 °C. Then, MA (0.5 mL), 4-DMAP (40 mg), and TEA (0.5 mL) were added to the polymeric solution, and the mixture was allowed to react under magnetic stirring for 24 h at room temperature. Extensive dialysis against deionized water was used to purify the methacrylic derivate GG-MA. Once purified, the polymer was freeze-dried and stored in a desiccator for further characterization. Fourier-transform infrared (FT-IR) spectroscopy and proton nuclear magnetic resonance ($^1$H NMR) in $D_2O$ were used to evaluate and quantify the presence of methacrylic functional groups. FT-IR spectra were recorded with a Perkin Elmer Paragon 1000 in the interval 4000–400 $cm^{-1}$ using KBr pellets (resolution of 1 $cm^{-1}$). A Bruker AC-400 was used to record $^1$H NMR spectra of GG-MA. The following Eq. (1) was applied to quantify the degree of derivatization (DD), which defines the percentage of modified hydroxyl groups per repeating unit of gellan gum [30]:

$$Degree\ of\ derivatization\ (DD) = \frac{\frac{I\ CH_3\ (methacryate)\ /\ 3}{I\ CH_3\ (rhamnose)\ /\ 3}}{n\ OH} x100 \quad (1)$$

Specifically, n OH represents the number of hydroxyl groups in each repetitive unit of gellan gum. $ICH_3$ (methacrylate) indicates the integral of the methyl peak at 1.98 ppm, and I $CH_3$ (rhamnose) represents the integral of the methyl peak at 1.32 ppm.

### 2.3. Synthesis and characterization of polyethylene glycol dimethacrylate (PEG-DMA)

PEG 4 kDa was modified with methacrylic groups following an established protocol [29]. Briefly, a large excess of methacrylic anhydride (4 mL) and PEG (10 g) were mixed in a capped scintillation vial (80 mL). A CEM discover (Milan, Italy) microwave reactor was used to carry out the reaction. The functionalization was obtained setting the temperature at 100 °C and using a microwave power of 100 W for 10 min. The polymeric solution was cooled down after the reaction, followed by the precipitation of the polymer using diethyl ether (10 mL). Finally, to remove the excess of methacrylic acid, the polymer was solubilized in $CHCl_3$ and filtrated over alumina. The organic solvent was removed under reduced pressure, and the dried polymer was solubilized in water. Finally, PEG-DMA was frozen and freeze-dried. FT-IR and $^1$H NMR spectroscopy were used to characterize the polymer functionalization with methacrylic groups.

### 2.4. Single network hydrogels formation

SN hydrogels consisting of GG-MA or GG-MA in combination with Laponite were obtained following the following procedure. As the first step, a stock solution of GG-MA (5% w/v) was prepared in deionized water and stored in the dark prior to the gel formation. Similarly, Laponite suspensions (1, 2 and 3% w/v) were obtained by dispersing the clay in deionized water before being included in the polymer solution of GG-MA.

Nanocomposite SN hydrogels (nSN) made of GG-MA and Laponite were fabricated by mixing an equal volume of the GG-MA stock solution and different Laponite suspensions to obtain SN hydrogels with a variable content of clay ranging from 0.5 up to 1.5% w/v. SN systems without Laponite were prepared by replacing the nanosilicate with an equal volume of deionized water. The final concentration of GG-MA (2.5% w/v) was kept constant in all of the systems prepared.

The photoinitiator Irgacure 2959 (0.15% w/v) was added to all of the polymeric mixtures before the UV irradiation (G.R.E. 125 W Helios Italquartz). The hydrogels were obtained by irradiating the polymeric mixtures for 10 min. Once formed, the photochemical hydrogels were stored at 4 °C for 24 h to ensure the complete crosslinking of the methacrylic groups of GG-MA.

### 2.5. Nanocomposite double network (nDN) hydrogel synthesis

DN and nDN hydrogels were synthesized following an established protocol [31]. The SN and nSN systems were fabricated as described in Section 2.3 with a cylindrical geometry (1.4 mm × 0.5 mm). Samples were soaked in aqueous solutions (20 mL) containing PEG-DMA (10 and 20% w/v) and the photoinitiator Irgacure 2959 (0.15% w/v). PEG-DMA was allowed to diffuse in the SN hydrogels for different times (24, 48 and 72 h) at room temperature. The samples were kept in the dark to avoid the photopolymerization of PEG-DMA. Then, the samples were removed from the PEG-DMA solutions, thoroughly washed with deionized water, and UV irradiated for 10 and 30 min to obtain the corresponding DN and nDN systems.

### 2.6. Determination of the content of PEG-DMA diffused within the SN hydrogels

The content of PEG-DMA diffused within the SN and nSN hydrogels was determined by weighing the residual amount of PEG-DMA after the step of diffusion. To this end, the diffusion process was stopped at specific time intervals (1, 3, 5, 8 24, 48 and 72 h) and three different samples for each time point were collected, frozen and freeze-dried to determine the weight of polymer still present in the bulk. The difference between the initial amount of PEG-DMA and that recovered in the bulk corresponds to the content of PEG-DMA diffused within the SN and nSN hydrogels.

### 2.7. Rheological studies

Rheological studies were conducted with a rotational rheometer (Haake Rheo Stress 300, Germany), which was equipped with a Haake DC10 thermostat. All the SN, nSN, DN and nDN hydrogels were investigated through oscillatory analyses using a serrated plate-plate geometry with a diameter of 35 mm. Frequency sweeps were recorded in the linear viscoelastic region using a range of frequencies varying from 0.01 to 10 Hz. All of the samples were analyzed at 1% of strain, which was chosen based on preliminary stress-sweep studies carried out in the range of 0.01–100% of strain. Oscillatory stress-sweep were also performed in the range of stress ranging from 10 Pa to 1000 Pa to determine the maximum values of yield stress and yield strain of the different systems. All the experiments were conducted at least in triplicate at the temperature of 25.0 ± 0.1 °C.

### 2.8. Compression and elongation studies

The compressive modulus of SN, nSN, DN, and nDN hydrogels was determined using a ZWICK-ROELL-Z010 compressing-traction machine, and tested under unconfined uniaxial compression with a 1 kN load cell. Both SN and DN hydrogels with and without Laponite were fabricated with a cubic geometry having a length of 1 cm. The samples have been compressed at the rate of 20 mm/min up to the point of breakage. The compressive modulus has been calculated considering the slope of the stress-strain curve in the range of 5–15% of strain. In addition, elongation studies were performed only on DN and nDN samples. The hydrogels having a rectangular shape (0.7 mm of thickness) have been fixed at the extremities to the same machine used for the compression studies. The samples have been elongated at the rate of 5 mm/min till the point of breakage. This test was necessary to determine the maximum percentage of elongation ε, the maximum yield stress σ, and the elastic modulus E, which was derived from the stress-strain curve as explained above. All the experiments were conducted in triplicate at room temperature.

### 2.9. Physical characterization of the nSN and nDN hydrogels

Freeze-dried SN and DN hydrogels were weighed and soaked in deionized water at 37.0 ± 0.1 °C. The equilibrium of swelling was evaluated by weighing the swollen hydrogel at different time points, and the swelling ratio (%) was calculated using the following Eq. (2):

$$Swelling\ ratio = Ws/Wd \tag{2}$$

where $W_s$ and $W_d$ the weights of the swollen and the freeze-dried hydrogels, respectively.

In addition, the porosity of SN, nSN, DN and nDN hydrogels was evaluated by scanning electron microscopy (SEM, FEI Versa 3D Dual Beam). Hydrogel were frozen at −60 °C and immediately freeze-dried for 2 days. The freeze-dried samples were cross-sectioned to visualize the internal structure. Samples were mounted on a holder with double-sided conductive carbon tape and sputter-coated with gold for 10 min (35 nm thickness). SEM images were obtained at an acceleration voltage ranging from 1 to 10 kV with an in-lens detector.

### 2.10. Release model of ofloxacin from double network (DN)

Cylindrical DN and nDN hydrogels were soaked for 24 h in a solution of ofloxacin (0.15 mg/mL) in phosphate buffered solution (PBS, pH 7.4) at room temperature. Then, the samples were washed to remove the excess of drug adsorbed on the surface of the gels and freeze-dried. The freeze-dried samples were immersed in 10 mL PBS (pH 7.4) at 37.0 ± 0.1 °C and kept under magnetic stirring. Volumes of 1 mL of PBS were withdrawn at specified time intervals and replaced with fresh buffer to maintain the volume constant. The concentration of drug was determined using a Perkin Elmer HPLC equipped with a C-18 LiChroCART® 250–4 LiChrospher® 60 RP-select B (5 μm) column and a 235 diod-array detector. The mobile phase was composed of citric acid 0.4 M, acetonitrile, and methanol (2:1:1, v:v:v) [33]. The analysis was carried out with a flow rate of 0.5 mL/min. Ofloxacin was detected at a wavelength of 280 and quantified using a calibration plot in PBS (pH 7.4) in the range of 1.5–15 μg/mL.

In modeling the release process of ofloxacin, we have to take into account that the freeze-dried cylindrical hydrogel (initial dimensions $R_0 = 0.5$ cm and $H_0 = 0.7$ cm) when immersed in PBS solution, rapidly swells. The swelling process is virtually instantaneous or, in any case, significantly faster than the release time scale. This affects (increases) the actual dimensions of the DN cylinder (sample) releasing ofloxacin.

Let $R_s$ and $H_s$ be the radius and the height of the swollen cylinder. By assuming a homogeneous swelling, i.e., a constant aspect ratio pre- and after- swelling, and that the volume increment is due only to the adsorbed water, the volume balance reads as Eq. (3)

$$\begin{aligned} Volume_{DN_{swollen}} &= \pi R_s^2 H_s = \pi R_s^3 \frac{H_0}{R_0} = \pi R_0^2 H_0 + \frac{W_s^{\infty} - W_d}{\rho_{H2O}} \\ &= Volume_{DN_{Dry}} + Volume_{absorbed_{H2O}} \end{aligned} \tag{3}$$

where $W_s^{\infty}$ and$W_d$ are the fully swollen and dry weights of the DN cylinder and $\rho_{H2O}$ is the water density at 37.0 ± 0.1 °C. Eq. (3) allows us to calculate the swollen dimensions $R_s$ and $H_s$ of the swollen DN.

The release of ofloxacin can be described by a drug-matrix interaction model. The drug in the fully swollen DN cylinder is initially partitioned into two phases: one linked to the polymer and one free to diffuse in the swollen hydrogel. Let $C_g$ and $C_b$ be the concentrations in the free (gel-solvent) and bounded phases, respectively. By assuming a reversible adsorption/desorption process and a linear transfer rate from the bounded to the free phase $-r_{b\to g} = k_{bg} C_b$ as well as a linear transfer rate from the free to the bounded phase , the dynamic equations and boundary conditions describing the release process are reported in the Eq. (4)

$$\frac{\partial C_g}{\partial t} = D_d^g \left( \frac{1}{r} \frac{\partial}{\partial r} \left( r \frac{\partial C_g}{\partial r} \right) + \frac{\partial^2 C_g}{\partial z^2} \right) + k_{bg} \left( C_b - \frac{C_g}{K_{eq}} \right), \frac{\partial C_b}{\partial t} = -k_{bg} \left( C_b - \frac{C_g}{K_{eq}} \right) \tag{4}$$

$$\frac{\partial C_g}{\partial r} = 0 \; at \; r = 0, \; C_g(r, 0) = C_g(r, H_s) = C_g(R_s, z) = C_{res}(t) \tag{5}$$

where $D_d^g$ is the diffusivity of ofloxacin in the DN swollen hydrogel, $K_{eq} = \frac{k_{bg}}{k_{gb}}$ is the equilibrium constant and $C_{res}(t)$ is the drug concentration in the acceptor reservoir. By assuming a perfectly mixed acceptor compartment (volume $V_{res} = 10$mL) and negligible mass transfer resistance at the hydrogel/solvent interface, the (uniform) drug concentration in the reservoir $C_{res}(t)$ can be evaluated at each time instant from the global mass balance taking into account the withdrawals at time instants $t_j, \; j = 1, ..,N$ Eq. (6)

$$V_{res} C_{res}(t) = V_g C_o - \int C_g(r, z, t) dV - \int C_b(r, z, t) dV - \sum_{j=1}^{N_t} V_p C_j^p(t_j) \tag{6}$$

where $V_g$ represents the volume of the swollen DN, $V_p = 1$mL the volume of the withdrawal, $C_j^p$ the concentration of the $j_{th}$ withdrawal and $N_t$ is the number of withdrawals occurred up to time $t$. $C_0$ is the initial drug concentration, distributed between the bounded and free phases as follows $C_g(0) = (1-\varepsilon)C_0, \; C_b(0) = \varepsilon C_0$, and the initial partitioning coefficient $\varepsilon$ is related to the equilibrium constant $\varepsilon = 1/(1 + K_{eq})$ if we assume that, as soon as the cylinder sample is fully swollen, the drug is distributed between the two phases according to the equilibrium concentrations $C_b = C_g/K_{eq}$.

The value of the equilibrium constant $K_{eq}$ can be estimated from experimental data $C_j^p(t_j), j = 1, ..,N$ by considering that, after sufficiently long time, when the release curve $M_t = V_{res} C_{res}(t) + \sum_{j=1}^{N_t} V_p C_j^p(t_j)$ (representing the amount of drug released up to time $t$) saturates towards an asymptotic value $M_\infty = V_{res} C_{res}^\infty(t) + \sum_{j=1}^{N} V_p C_j^p(t_j)$, the concentration in the donor compartment $C_{res}^\infty$ equals the concentration in the free phase $C_g^\infty$ in equilibrium with the concentration in the bounded phase $C_b^\infty = C_g^\infty/K_{eq}$, therefore obtaining from Eq. (6) the following expression for $C_{res}^\infty$ and $M_\infty$ Eq. (7):

$$C_{res}^\infty = \frac{V_g C_0 - V_p \sum_{j=1}^{N} C_j^p}{V_{res} + V_g(1 + K_{eq}^{-1})}, \; \frac{M_\infty}{M_0} = 1 - \frac{C_{res}^\infty}{C_0}(1 + K_{eq}^{-1}), \; M_0 = V_g C_0 \tag{7}$$

From the experimental point of view the value of $C_{res}^\infty$ is the concentration of the last withdrawal (for sufficiently long experiments) $C_{res}^\infty = C_N^p$, the asymptotic value of the release curve $C_{res}^\infty$ is simply evaluated as $M_\infty = V_{res} C_N^p + \sum_{i=1}^{N-1} V_p C_j^p$ and therefore the value of the equilibrium constant $K_{eq}$ can be evaluated from Eq. (7).

The smaller is the equilibrium constant, the larger is the amount of drug asymptotically trapped in the bounded phase $M_{trapped} = V_g C_b^\infty = V_g C_g^\infty/K_{eq} = V_g C_{res}^\infty/K_{eq}$, the smaller the asymptotic value $M_\infty$.

It is extremely important in modeling the release process to take into account the withdrawals, especially when the sample volume $V_p$ is above 5% of the reservoir volume $V_{res}$. Each withdrawal subtracts a non-negligible amount of drug in the acceptor compartment, lowering the concentration $C_{res}$, thus allowing further drug release from the hydrogel. While the equilibrium constant $K_{eq}$ is directly evaluated from experimental data, the two other parameters $k_{bg}$ and $D_d^g$ must be computed by a best fit of release curve.

### 2.11. Cell culture

Human umbilical vein endothelial cells (HUVECs) were purchased from Lonza, and cultured in endothelial basal medium (EGM-2 BulletKit, Lonza) supplemented with vascular endothelial growth factor (VEGF) and basal fibroblast growth factor (bFGF). HUVECs P3-P6 were cultured at 5% of $CO_2$ at 37 °C. HUVECs were seeded in a 48-well plate at the cell density of 20,000 cells/well and allowed to reach confluency in 24 h. The volume of media used in each well was 0.2 mL. Then, freeze-dried DN and nDN hydrogels, (2 pieces/well), previously punched in cylindrical shapes (2.5 × 4.0 mm) and steam sterilized, were placed in the wells and left floating in the media for 48 h. As a positive control group, cells were left untreated.

An MTS assay (Promega) was carried out according to the manufacturer's protocol. Briefly, 20 μL of reagent was added to each well and allowed to incubate for 3 h at 37 °C. Absorbance values were measured at 490 nm and normalized based on the values obtained from the control group. Five different samples for each group were tested, and the results were reported as a mean ± standard deviation. Additionally, cells were treated with calcein and ethidium bromide to stain alive and dead cells, respectively. The process of staining was based on previously established protocol [32].

### 2.12. Statistical analysis

Statistical analysis of mechanical testing, cell viability, and swelling data was carried out using one-way analysis of variance (ANOVA) to determine the significant difference existing among the different groups. All statistical analyses were carried out with GraphPad Prism Software 6. A p-value $<0.05$ indicates statistical significance, which was displayed as $^{*} = p < 0.05$, $^{**} = p < 0.01$, $^{***} = p < 0.001$.

## 3. Results and discussion

### 3.1. Synthesis and characterization of SN hydrogels

The first part of the work was focused on the design of SN hydrogels of GG-MA with tunable physical and mechanical properties as a preliminary step for the fabrication of a novel nDN system for drug delivery applications. To achieve this goal, Laponite was selected as nanomaterial to modulate the mechanical stiffness and swelling degree of the SN hydrogels. Both factors can influence the extent of diffusion of a second polymer within the first network, which is necessary to create a DN structure with tunable swelling, porosity, and elasticity. Controlling these properties can be beneficial to synthesize a drug delivery platform that possesses both excellent mechanical properties and ability to control the loading and release kinetic of therapeutic drugs.

Gellan gum was functionalized with methacrylic groups as reported in our previous study using an established protocol [29]. This naturally derived polysaccharide possesses hydroxyl groups in its repetitive unit that can be easily modified with methacrylic groups to create photocrosslinkable hydrogels of GG-MA. These hydrogels were selected as the first brittle network, which possesses a tightly interconnected structure and can swell when in contact with a buffered aqueous solution due to the polyelectrolyte nature of gellan gum. Successful methacrylation was verified by FT-IR and $^1$H NMR spectroscopy (Fig. S1A and B). The degree of methacrylation of GG-MA (4 ± 1%), time of irradiation (30 min) and the polymer concentration (2.5% w/v) were kept constant for the preparation of the SN hydrogels as established in our previous work [29]. On the contrary, the concentration of Laponite was varied from 0.5% w/v to 1.5% w/v to evaluate the influence of the synthetic clay on the SN hydrogel properties (Fig. 1A). Higher concentrations of Laponite (2.0 and 2.5% w/v) were tested, but the viscosity of the mixture was too high to ensure a homogeneous distribution of the clay and the formation of a reproducible SN hydrogel after UV photocrosslinking. As expected, the storage modulus G', which is indicative of the degree of crosslinking within the network, was lower in the SN systems without any Laponite [33]. The inclusion of the clay positively affected the mechanical stability of the GG-MA network determining an increase in the G' values measured at 1 Hz from 1402 ± 293 Pa to 2959 ± 569 Pa as observed in the system containing Lap 1.5% w/v (Fig. 1B). This effect can be explained by the possible electrostatic interactions between the clay and the polymeric chains as reported in other similar studies using both natural and synthetic polymers [32,34,35]. The presence of these interactions is responsible for the reinforcement observed in the SN network of GG-MA as suggested by the decrease in the values of tan δ

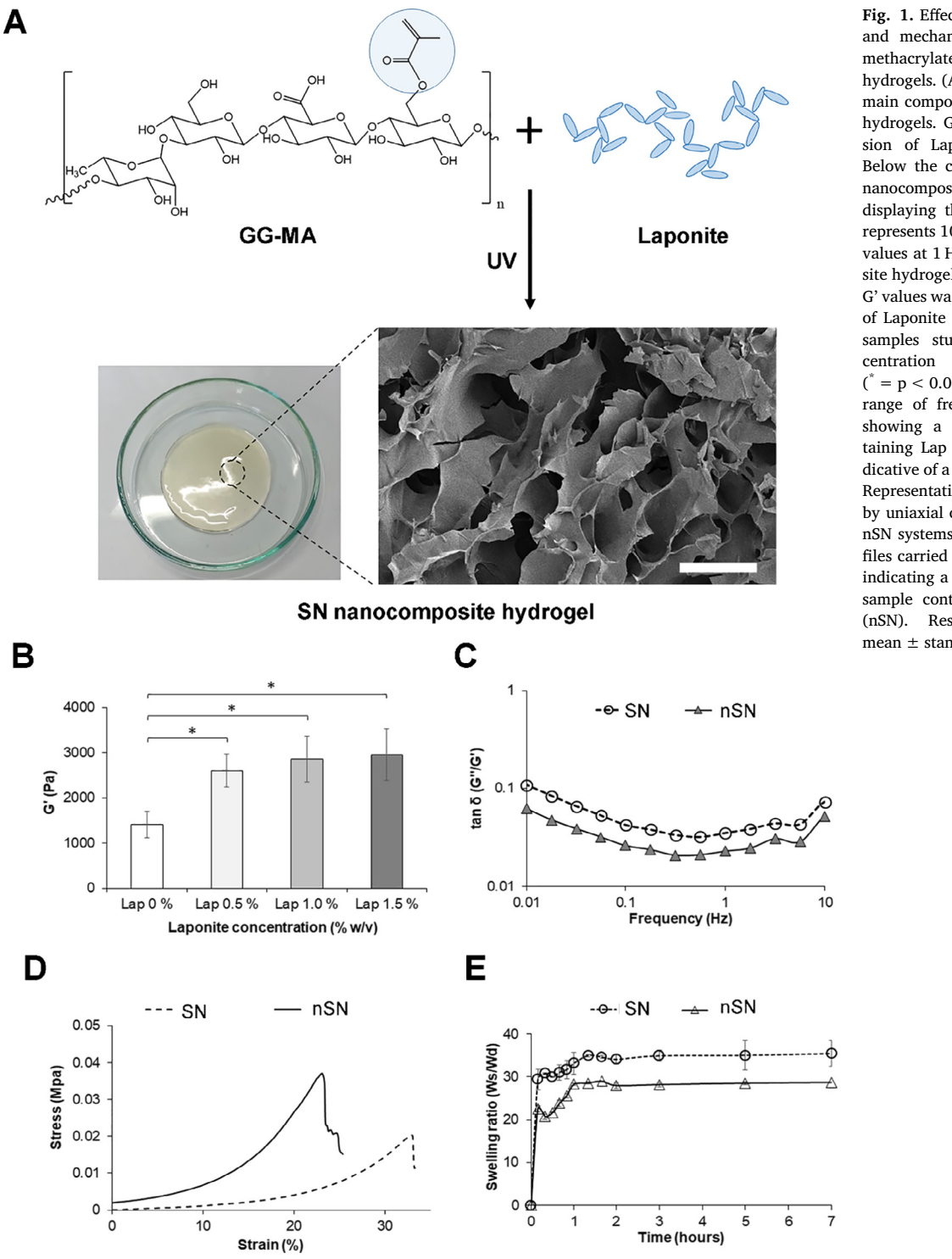


**Fig. 1.** Effect of Laponite on the physical and mechanical properties of gellan-gum methacrylate (GG-MA) single network (SN) hydrogels. (A) Schematic is representing the main components of the SN nanocomposite hydrogels. GG-MA is mixed with a suspension of Laponite before UV irradiation. Below the corresponding image of the SN nanocomposite hydrogel and SEM image displaying the internal porosity. Scale bar represents 100 μm. (B) Storage modulus (G') values at 1 Hz for the different nanocomposite hydrogels. No significant increase in the G' values was observed for the concentration of Laponite higher than 0.5% w/v. All the samples studied contain the same concentration of GG-MA (2.5% w/v) ($^{*}$ = $p < 0.05$). (C) Tan δ profiles in the range of frequencies from 0.01 to 10 Hz showing a decrease for the system containing Lap 0.5% w/v (nSN), which is indicative of a higher crosslinked network. (D) Representative stress-strain curves obtained by uniaxial compression for the SN and the nSN systems. (E) Swelling equilibrium profiles carried out in deionized water at 37 °C indicating a lower degree of swelling in the sample containing Laponite at 0.5% w/v (nSN). Results are reported as the mean ± standard deviation (n = 3).

(G"/G') in the group containing 0.5% w/v of clay (Fig. 1C). A decrease of this value is indicative of a highly crosslinked network which can also sustain higher stress values prior to breakage with an increase of the yield stress from 543.6 ± 3.0 Pa to 717.1 ± 1.0 Pa (Fig. S2A). However, higher concentrations of Laponite did not further decrease the tan δ values detected in the range of frequencies from 0.01 to 10 Hz (Fig. S2B). For this reason, 0.5% w/v was selected as the optimal amount of clay necessary to formulate the nanocomposite single network hydrogel (nSN). A similar increment in the stiffness was observed in the compression studies, although both SN and nSN systems showed the typical behavior of brittle networks displaying failure at low values of strain (20–30% of strain) (Fig. 1D).

Aside from the effect on the mechanical properties, it was critical to evaluate whether the inclusion of this concentration of clay was able to alter the swelling degree of the GG-MA SN hydrogels. The equilibrium of swelling was reached in both systems with and without Laponite after 2 h of soaking the freeze-dried hydrogels in deionized water. However, the inclusion of Laponite at 0.5% w/v reduced the swelling ratio of the network in deionized water after 7 h from 35.4 ± 2.9 to 28.7 ± 0.2, likely due to physical interactions between the polymeric chains and Laponite (Fig. 1E). No change in the swelling ratio was observed for both systems with and without Laponite at 0.5% w/v after

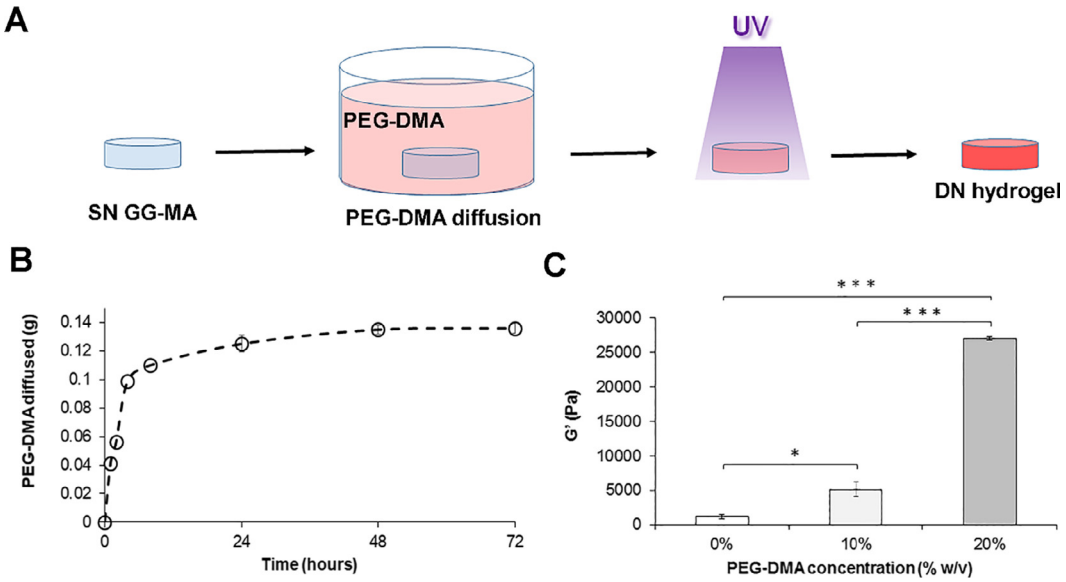


**Fig. 2.** Optimization of the parameters for the fabrication of the DN hydrogels. (A) Schematic is representing the main steps necessary to prepare the DN hydrogels. The photochemical SN hydrogels with or without Laponite were soaked in a solution of PEG-DMA (Mw 4000 Da) for 72 h followed by irradiation with UV to form DN hydrogels and the DN nanocomposite system. (B) Profile of diffusion of PEG-DMA into SN hydrogel overtime. (C) Effect of the PEG-DMA concentration on the G' values at 1 Hz of the corresponding DN hydrogels. An increase in the stiffness was observed as the concentration of PEG-DMA was increased.

24 and 48 h (Fig. S2C). Moreover, the Laponite did not cause any significant change in the internal porosity of the SN hydrogel (Fig. S2D), which was mainly influenced by the GG-MA properties such as the polymer concentration and the degree of methacrylation.

Overall, these results confirmed the successful design of two distinct SN hydrogels that possess tunable mechanical and physical properties, and we further investigated how these changes induced by the synthetic clay impacted the properties of the corresponding DN hydrogels.

### 3.2. Optimization of the parameters necessary to fabricate the DN hydrogels

DN hydrogels were synthesized using PEG-DMA as the second polymer following the procedure described in the schematic reported in Fig. 2A. PEG-DMA Mw 4 kDa was selected based on a previous study where we investigated the effect of the molecular weight of PEG-DMA on the mechanical properties of DN hydrogels using gellan gum hydrogels crosslinked with calcium ions as the first network [31]. PEG-DMA concentration was optimized to evaluate its influence on the DN hydrogel properties considering that the concentration of the second polymer should be 10 or 20 times higher than the amount of polymer used to fabricate the SN hydrogel [15]. The optimization was carried out by testing different concentrations of PEG-DMA. The polymer was allowed to diffuse within the SN of GG-MA monitoring the diffusion process up to 72 h. The equilibrium of diffusion was reached after 48 h (Fig. 2B). The increase in the concentration of PEG-DMA resulted in the formation of DN hydrogels with higher values of storage modulus G' at 1 Hz (Fig. 2C). Precisely, doubling the concentration of PEG-DMA from 10 to 20% w/v increased the values of G' from 5878 ± 1056 Pa to 27165 ± 205 Pa. Higher concentration than 20% w/v were not tested as the polymer started polymerizing forming a gel before its diffusion within the SN of GG-MA. For these reasons, a concentration of 20% w/v of PEG-DMA 4 kDa was used to prepare both DN hydrogels without Laponite and with the clay (nDN system). The time of irradiation of the second network was set at 10 min as no change in the mechanical properties was observed for longer time of irradiation (data not shown).

As next step of our investigation, it was important to verify whether the different content of PEG-DMA and the presence of Laponite embedded in the first network affected the mechanical and physical properties of the DN hydrogels. Moreover, we evaluated how these modifications contributed to modulate the release capabilities of the nDN system compared to the DN network without the synthetic clay.

### 3.3. Effect of Laponite on the mechanical properties of the nDN system

The design of a drug delivery system requires the fabrication of a carrier, which should possess enough mechanical stability to sustain large deformation without breaking. SN hydrogels do not possess this requirement, as they are generally too brittle due to their inhomogeneous interconnected structure. To overcome this issue, the DN strategy enables the fabrication of hydrogels with high toughness as reported in many other studies. Specifically, a DN hydrogel presents a first brittle network that can break into small clusters to efficiently disperse the energy around the damaged area, while the soft and elastic second network can extend to sustain large deformation [36].

Both types of DN hydrogels investigated in this work showed a significant increase in the maximum yield strain and yield stress when compared to the brittle and fragile SN hydrogels as discussed previously (Fig. 3A). Specifically, the DN hydrogel without Laponite (DN) showed the highest value of maximum stress corresponding to 0.62 ± 0.09 MPa, failure at 49.15 ± 1.48% of strain and a compressive Young's Modulus (E) of 0.19 ± 0.09 MPa. The nDN system displayed similar behavior under compression, although both the maximum stress (0.49 ± 0.07 MPa) and E values (0.12 ± 0.04 MPa) were lower with respect to the DN system without Laponite suggesting the presence of a more elastic matrix in the case of the nDN hydrogel. A similar trend was observed when comparing the stress–strain curves obtained from the elongation tests (Fig. 3B). The DN system displayed higher E values (0.395 ± 0.035 MPa) and larger elongation ε (70.5 ± 0.9%) (Fig. 3C and D). Similarly, the maximum stress in elongation σ varied from 0.35 ± 0.01 MPa for the DN hydrogel to 0.11 ± 0.05 MPa for the nDN, respectively (Fig. 3E).

Overall, these findings can be explained by the different content of PEG-DMA present in the two DN systems. A lower amount of PEG-DMA was retained after diffusion in the nDN hydrogel (Fig. 3F). The difference could be attributed to the reduced ability of the nSN hydrogels to swell when in contact with water as discussed above. The same decrease in the swelling ratio has been reported for other nanocomposite systems containing Laponite in poly (N-isopropyl acrylamide)

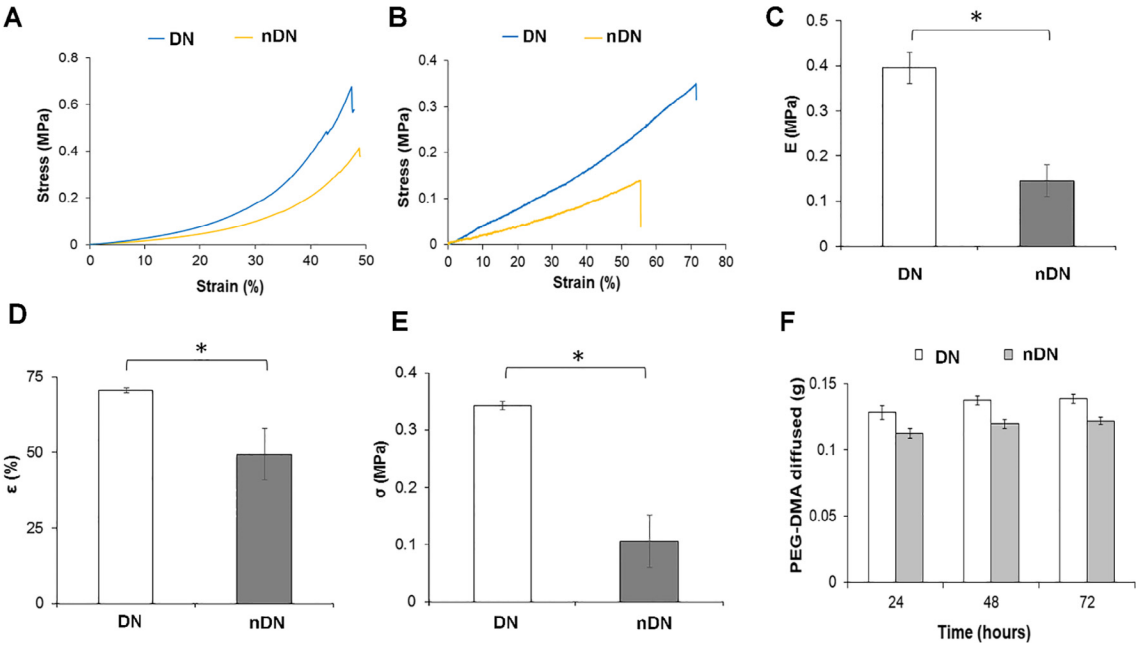


**Fig. 3.** Influence of Laponite on the mechanical properties of the DN hydrogels. (A) Representative stress-strain curves obtained by uniaxial compression. (B) Stress-strain profiles obtained by elongation of the DN systems up to the point of breakage. The nDN system containing Laponite (0.5% w/v) presents a lower elongation and maximum strain. (C) Young's Modulus E calculated from the extensions curves in the interval from 0 to 20% of strain. (D) Percentage of elongation (ε) calculated from the extensions curves for the DN and nDN systems. (E) Maximum strain values (σ) at the point of breakage for the two DN samples. The DN nanocomposite hydrogel possesses lower E, ε and σ values compared to the DN sample without Laponite. (F) Amount of PEG-DMA diffused within the SN with and without Laponite overtime. A higher quantity of PEG-DMA was present in the nDN system in all three times point investigated (n = 3). Results are reported as mean ± standard deviation (n = 3) ($^{*}$ = $p < 0.05$).

PNIPAAm hydrogels [37].

The decreased ability of the nSN matrix to swell and uptake PEG-DMA is the main factor contributing to the lower mechanical properties of the nDN system. Thus, the higher concentration of PEG-DMA within the first network of GG-MA without Laponite is the reason why a larger stiffness (higher Young's Modulus) was observed for the DN system when compared to the nDN hydrogel. On the contrary, the Laponite did not seem to directly influence the DN hydrogel's mechanical properties, which were unaffected by the presence of the clay. A possible explanation is that Laponite remained confined within the cluster of the first network after the preparation of the SN.

### 3.4. Physical characterization of the nDN hydrogels and release studies

Besides the analysis of the mechanical properties, we further investigated the differences between the DN and the nDN system in terms of physical properties. Both systems were freeze-dried, designed as cylinders with dimensions $R_0 = 0.5$cm and $H_0 = 0.7$cm and soaked in deionized water to test whether the different content in PEG-DMA was able to affect the chain flexibility and the equilibrium of swelling. The presence of the second network reduced the swelling degree compared to the SN hydrogels, and this trend was similar to our previous findings using gellan gum physical hydrogels as a first network [31]. Both the DN and nDN hydrogels were able to reach the equilibrium of swelling after 1 h. A larger swelling ratio was detected for the nDN system with an increase from 7.33 ± 1.06 for DN to 10.47 ± 0.23 for nDN after 7 h (Fig. 4A). Same results were observed by studying the swelling after 24 and 48 h in deionized water (Fig. S3A). However, a reduction in the swelling values was observed for the nDN system in PBS when compared to deionized water. This behavior can be explained by the different ionic strength in the two media. Specifically, the higher concentration of $Na^+$ counterions of the phosphate buffer can shield both negative charges of Laponite as well as the carboxylate groups of GG-MA. This effect can lead to an aggregation of the Laponite nanoplatelets and a lower swelling degree of the matrix (Fig. S3A-B).

The difference in swelling is consistent with the results discussed in Section 3.3. The nDN system is more elastic and less rigid due to the lower content of PEG-DMA, which enabled a larger flexibility of the GG-MA polymeric chains within the DN system. This hypothesis was confirmed by SEM analysis of the two DN hydrogels. The DN sample displayed a more packed structure probably due to the higher content of PEG-DMA, (Fig. 4B). Moreover, the higher swelling in the nDN hydrogel is probably due to the inclusion of Laponite as reported for other nanocomposite system using the synthetic DN network made of PNIPAAm and polyacrylic acid [40].

By evaluating, from swelling experiment, the amount of absorbed water, we observed that both DN and nDN hydrogels absorbed almost the same amount of water after 1 h, about $W_{absorbed\ water} = W(1h) - W^0 = 340\text{mg} \pm 2\text{mg}$. This is consistent with the swelling ratio shown in Fig. 4A because the initial dimensions (before swelling) of the cylindrical DN and nDN hydrogels are the same, but the initial weight of nDN hydrogels $W^0_{nDN} = 38$mg is significantly smaller than that of DN hydrogels $W^0_{DN} = 62$mg. The amount of absorbed water led us to estimate the hydrogel dimensions after almost complete swelling and this is an important information for a correct modeling of release experiments. For both systems, the swollen hydrogel dimensions, estimated from Eq. (1), are $R_s = 0.57$cm and $H_s = 0.8$cm (Fig. 4C).

For release experiments, both systems were preliminary loaded with the model drug ofloxacin, which was allowed to diffuse within the matrices after the DN fabrication to avoid the exposure of the drug to the UV light. The nDN system showed a higher loading efficiency when compared to the DN hydrogel. Specifically, the content of drug permeated was 0.423 ± 0.002 mg for the DN system and 0.491 ± 0.028 mg in the nDN hydrogel, respectively. This difference can be attributed to the inclusion of Laponite which can establish ion-dipole interactions with the polar drug ofloxacin as reported in our previous work [33].

DN and nDN hydrogels, once loaded with the model drug, were

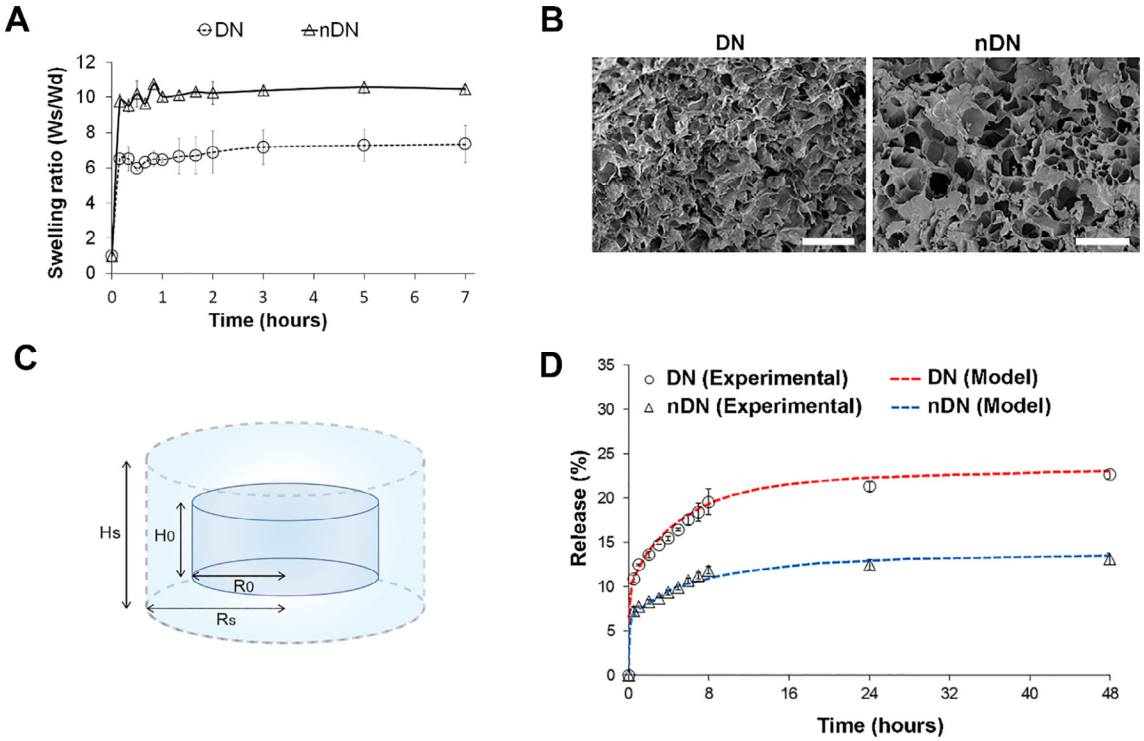


**Fig. 4.** Influence of Laponite on the physical and release properties of the DN and nDN systems (A) Swelling equilibrium profiles carried out in deionized water at 37 °C indicating a higher degree of swelling in the DN nanocomposite hydrogels (Laponite 0.5% w/v). Results are reported as the mean ± standard deviation (n = 3). (B) Cross-sections SEM images showing a different porosity between the two types of DN hydrogels. A higher porosity can be observed in the nDN system. Scale bar = 100 and 300 μm for the DN and nDN system, respectively. (C) The schematic is representing the DN geometry model used to calculate the diffusivity, the constant of equilibrium, and the kinetic constant of ofloxacin. (D) Release profiles of ofloxacin obtained in PBS (pH 7.4) at 37 °C. The experimental data were fitted against the profiles obtained from the mathematical model.

washed, freeze-dried and then immersed in the buffer solution kept under magnetic stirring. Release data are shown in Fig. 4D as $M_t/M_0$ *vs* t. By preliminary focusing on the asymptotic (long scale) behavior, we observed that both systems retained the majority of the drug within the hydrogel matrix after 48 h suggesting a strong interaction between the drug and the polymeric matrix. The nDN system displayed the lower value of $M_\infty/M_0$ probably due to an additional retention effect induced by presence of the synthetic clay.

We adopted the two phases drug/matrix interaction model described in Section 2.10 for interpreting release data for both systems and estimate the drug diffusion coefficient$D_d^g$.

We preliminary estimated the equilibrium constant$K_{eq}$, thus obtaining (from Eq. (7) $K_{eq} = 0.0176$ for DN and $K_{eq} = 0.00905$ for nDN hydrogel. As discussed in Section 2.10, the smaller the equilibrium constant, the larger the amount of drug asymptotically trapped in the bounded phase, the smaller the asymptotic value $M_\infty$. The other two model parameters $D_d^g$ and $k_{bg}$ for both systems were estimated from a best fit of the experimental release curve and reported in Table 1. The excellent agreement between experimental release data and model predictions is shown for both DN and nDN systems (Fig. 4D).

Best fit values for $D_d^g$in nDN hydrogels highlighted that the release of ofloxacin in the presence of laponite is characterized by a higher diffusivity value (consistent with the larger porosity of the nDN hydrogel) and a lower value of $k_{bg}$. Therefore, the drug is more closely bounded to the polymer matrix in the nDN. For both systems, the best fit values of $D_d^g$ and $k_{bg}$ imply that the characteristic time for matrix-to-gel transfer $1/k_{bg}$ is extremely smaller than the characteristic time for drug diffusion $H_s^2/D_d^g$ in the gel/solvent phase. Therefore, the polymeric matrix plays the role of a drug reservoir, thus releasing the drug from the bounded to the gel phase as soon as the drug diffuses out from the hydrogel.

Overall, these data suggest that the inclusion of Laponite within a DN network can be an appealing strategy to decrease the release rate and control the amount of drug released over time. The designed nDN platform plays the role of a drug reservoir and can be used to achieve a sustained release of a therapeutic molecule with better control than the corresponding SN hydrogels of GG-MA as reported in our previous studies [33].

**Table 1**
Values of physical parameters from the best fitting of experimental data.

| | DN | nDN |
|---|---|---|
| $D_d^g\left(\frac{m^2}{s}\right)$ | $4 \cdot 10^{-9}$ | $9 \cdot 10^{-9}$ |
| $K_{eq}$ | 0.0176 | 0.00905 |
| $k_{bg}\,(s^{-1})$ | 10.1 | 1.2 |

### 3.5. Biocompatibility studies

Finally, we assessed the biocompatibility of the novel nDN carrier by investigating the toxicity induced by the presence of Laponite. HUVECs were chosen as the model cell line due to their tendency to display oxidative stress in the presence of radical species [38]. A reduction in cell viability was detected in the nDN group with a decrease from 100 ± 2.6% to 81.4 ± 2.9%. However, this change in cell viability can be considered negligible according to the international guidelines on biological evaluation of cytotoxicity (ISO 10993-5), which defines a material cytotoxic for reduction higher than 30% (Fig. 5A) [39,40]. Moreover, all the systems investigated did not induce any visible change in the morphology of the HUVECs when compared to the control group, which was left untreated (Fig. 5B).

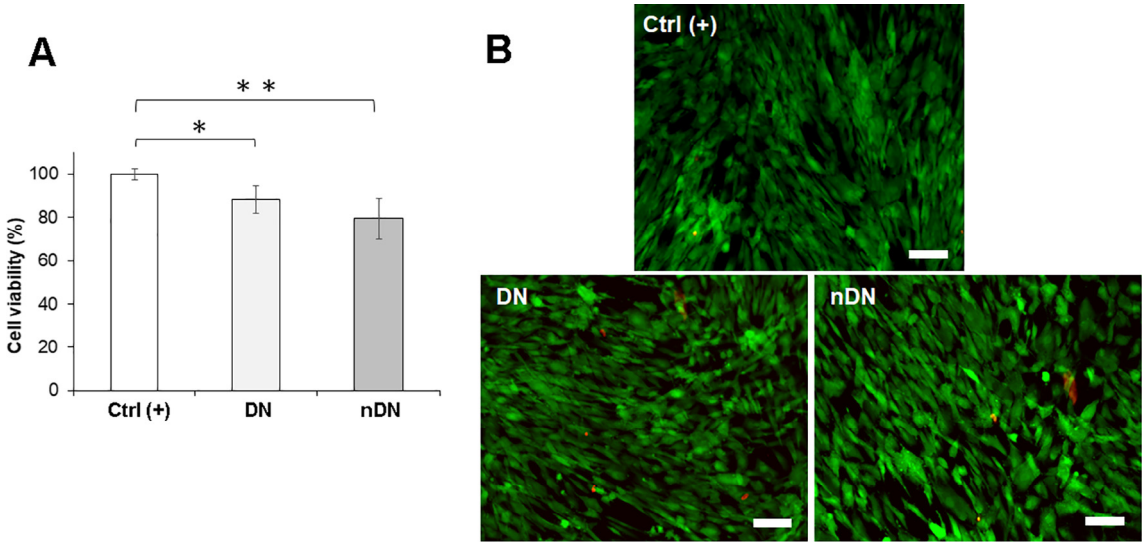


**Fig. 5.** Biocompatibility evaluation of DN and nDN hydrogels. (A) MTS assay results indicating the HUVECs viability after being exposed for 48 h to the DN hydrogels with and without Laponite (n = 5). Results are normalized with the Ctrl (+) consisting of cells without any gel treatment ($^{*}$ = $p < 0.05$ and $^{**}$ = $p < 0.01$). (B) Fluorescence images are indicating the presence of HUVECs stained with calcein (green) and ethidium bromide (red) after being exposed for 48 h to the DN hydrogels. The majority of the cells were alive and stained green with no change in morphology when compared to the Ctrl (+) group. Scale bars = 100 μm. (For interpretation of the references to colour in this figure legend, the reader is referred to the web version of this article.)

## 4. Conclusions

A novel nDN has been successfully designed and characterized as a carrier for the sustained release of therapeutic molecules. The swelling and release properties of the nDN system have been modulated by introducing Laponite as a nanofiller within the first network of GG-MA. Specifically, Laponite was able to increase the stiffness, while reducing the swelling ability of the SN hydrogel. This effect limited the diffusion of PEG-DMA necessary to produce the second polymeric network. The presence of Laponite did not directly influence the mechanical properties of the DN, which were mainly affected by the PEG-DMA content within the first network. On the contrary, Laponite induced a higher loading efficiency of the model drug ofloxacin and reduced its kinetic constant of diffusion. Finally, the formulation is not cytotoxic as demonstrated by the promising results obtained from the MTS and live and dead assays carried out on HUVECs.

Overall, these findings indicate the suitability of this novel nDN system as a carrier of drugs to deliver small doses of therapeutic molecules over time. For instance, this type of polymeric carrier could find application as a patch for the treatment of chronic infections where a local and sustained release of an antibiotic is commonly required.

## Acknowledgments

This work was financially supported by the Italian Ministry of Education, Universities, and Research (MIUR).

## Conflicts of interest

There are no conflicts to declare.

## Appendix A. Supplementary material

Supplementary data associated with this article can be found, in the online version, at https://doi.org/10.1016/j.eurpolymj.2018.04.034.

## References

[1] F. Wu, T. Jin, Polymer-based sustained-release dosage forms for protein drugs, challenges, and recent advances, AAPS PharmSciTech 9 (4) (2008) 1218–1229.
[2] S.B. Tiwari, J. DiNunzio, A. Rajabi-Siahboomi, Drug-polymer matrices for extended release, in: C.G. Wilson, P.J. Crowley (Eds.), Controlled Release in Oral Drug Delivery, Springer, US, Boston, MA, 2011, pp. 131–159.
[3] T.M. Allen, P.R. Cullis, Drug delivery systems: entering the mainstream, Science 303 (5665) (2004) 1818–1822.
[4] S. Pundir, A. Badola, D. Sharma, Sustained release matrix technology and recent advance in matrix drug delivery system: a review, Int. J. Drug Res. Tech. 3 (1) (2017) 12–20.
[5] S. Pacelli, F. Acosta, A.R. Chakravarti, S.G. Samanta, J. Whitlow, S. Modaresi, R.P.H. Ahmed, J. Rajasingh, A. Paul, Nanodiamond-based injectable hydrogel for sustained growth factor release: Preparation, characterization and in vitro analysis, Acta Biomater. 58 (2017) 479–491.
[6] S.J. Buwalda, T. Vermonden, W.E. Hennink, Hydrogels for therapeutic delivery: current developments and future directions, Biomacromolecules 18 (2) (2017) 316–330.
[7] C.C. Lin, A.T. Metters, Hydrogels in controlled release formulations: network design and mathematical modeling, Adv. Drug Delivery Rev. 58 (12–13) (2006) 1379–1408.
[8] T.R. Hoare, D.S. Kohane, Hydrogels in drug delivery: Progress and challenges, Polymer 49 (8) (2008) 1993–2007.
[9] E.M. Ahmed, Hydrogel: Preparation, characterization, and applications: A review, J. Adv. Res. 6 (2) (2015) 105–121.
[10] J. Elisseeff, Hydrogels: Structure starts to gel, Nat. Mater. 7 (4) (2008) 271–273.
[11] E.S. Dragan, Design and applications of interpenetrating polymer network hydrogels, Chem. Eng. J. 243 (2014) 572–590.
[12] P. Matricardi, C. Di Meo, T. Coviello, W.E. Hennink, F. Alhaique, Interpenetrating polymer networks polysaccharide hydrogels for drug delivery and tissue engineering, Adv. Drug Selivery Rev. 65 (9) (2013) 1172–1187.
[13] T. Nonoyama, J.P. Gong, Double-network hydrogel and its potential biomedical application: A review, Proceedings of the Institution of Mechanical Engineers. Part H, J. Eng. Med. 229 (12) (2015) 853–863.
[14] Y. Hagiwara, A. Putra, A. Kakugo, H. Furukawa, J.P. Gong, Ligament-like tough double-network hydrogel based on bacterial cellulose, Cellulose 17 (1) (2010) 93–101.
[15] T. Matsuda, T. Nakajima, Y. Fukuda, W. Hong, T. Sakai, T. Kurokawa, U.-I. Chung, J.P. Gong, Yielding criteria of double network hydrogels, Macromolecules 49 (5) (2016) 1865–1872.
[16] M.A. Haque, T. Kurokawa, J.P. Gong, Super tough double network hydrogels and their application as biomaterials, Polymer 53 (9) (2012) 1805–1822.
[17] Q. Chen, H. Chen, L. Zhu, J. Zheng, Engineering of tough double network hydrogels, Macromol. Chem. Phys. 217 (9) (2016) 1022–1036.
[18] T. Nakajima, H. Furukawa, Y. Tanaka, T. Kurokawa, J.P. Gong, Effect of void structure on the toughness of double network hydrogels, J. Polym. Sci., Part B: Polym. Phys. 49 (17) (2011) 1246–1254.
[19] H. Shin, B.D. Olsen, A. Khademhosseini, Gellan gum microgel-reinforced cell-laden gelatin hydrogels, J. Mater. Chem. B, Mater. Biol. Med. 2 (17) (2014) 2508–2516.
[20] J. Lin, S. Xu, X. Shi, S. Feng, J. Wang, Synthesis and properties of a novel double network nanocomposite hydrogel, Polym. Adv. Technol. 20 (7) (2009) 645–649.
[21] R. Fei, J.T. George, J. Park, M.A. Grunlan, Thermoresponsive nanocomposite double network hydrogels, Soft Matter 8 (2) (2012) 481–487.
[22] J. Tu, Z. Cao, Y. Jing, C. Fan, C. Zhang, L. Liao, L. Liu, Halloysite nanotube nanocomposite hydrogels with tunable mechanical properties and drug release behavior,

Compos. Sci. Technol. 85 (2013) 126–130.
[23] P. Zhu, M. Hu, Y. Deng, C. Wang, One-pot fabrication of a novel agar-polyacrylamide/graphene oxide nanocomposite double network hydrogel with high mechanical properties, Adv. Eng. Mater. 18 (10) (2016) 1799–1807.
[24] P. Huang, W. Chen, L. Yan, An inorganic-organic double network hydrogel of graphene and polymer, Nanoscale 5 (13) (2013) 6034–6039.
[25] W. Dong, C. Huang, Y. Wang, Y. Sun, P. Ma, M. Chen, Superior mechanical properties of double-network hydrogels reinforced by carbon nanotubes without organic modification, Int. J. Mol. Sci. 14 (11) (2013) 22380–22394.
[26] G. Gao, Y. Xiao, Q. Wang, J. Fu, Synergistic toughening of nanocomposite double network hydrogels by physical adsorption and chemical bonding of polymer chains to inorganic nanospheres and nanorods: a comparative study, RSC Adv. 6 (44) (2016) 37974–37981.
[27] L.Z. Zhao, C.H. Zhou, J. Wang, D.S. Tong, W.H. Yu, H. Wang, Recent advances in clay mineral-containing nanocomposite hydrogels, Soft Matter 11 (48) (2015) 9229–9246.
[28] X. Fei, J. Lin, J. Wang, J. Lin, X. Shi, S. Xu, Synthesis and mechanical strength of a novel double network nanocomposite hydrogel with core-shell structure, Polym. Adv. Technol. 23 (4) (2012) 736–741.
[29] S. Pacelli, P. Paolicelli, I. Dreesen, S. Kobayashi, A. Vitalone, M.A. Casadei, Injectable and photocross-linkable gels based on gellan gum methacrylate: A new tool for biomedical application, Int. J. Biol. Macromol. 72 (2015) 1335–1342.
[30] D.F. Coutinho, S.V. Sant, H. Shin, J.T. Oliveira, M.E. Gomes, N.M. Neves, A. Khademhosseini, R.L. Reis, Modified gellan gum hydrogels with tunable physical and mechanical properties, Biomaterials 31 (29) (2010) 7494–7502.
[31] S. Pacelli, P. Paolicelli, F. Pepi, S. Garzoli, A. Polini, B. Tita, A. Vitalone, M.A. Casadei, Gellan gum and polyethylene glycol dimethacrylate double network hydrogels with improved mechanical properties, J. Polym. Res. 21 (5) (2014) 409.
[32] R. Waters, S. Pacelli, R. Maloney, I. Medhi, R.P.H. Ahmed, A. Paul, Stem cell secretome-rich nanoclay hydrogel: a dual action therapy for cardiovascular regeneration, Nanoscale 8 (14) (2016) 7371–7376.
[33] S. Pacelli, P. Paolicelli, G. Moretti, S. Petralito, S. Di Giacomo, A. Vitalone, M.A. Casadei, Gellan gum methacrylate and laponite as an innovative nanocomposite hydrogel for biomedical applications, Eur. Polym. J. 77 (2016) 114–123.
[34] C. Lian, Z. Lin, T. Wang, W. Sun, X. Liu, Z. Tong, Self-reinforcement of PNIPAm–laponite nanocomposite gels investigated by atom force microscopy nanoindentation, Macromolecules 45 (17) (2012) 7220–7227.
[35] J. Du, J. Zhu, R. Wu, S. Xu, Y. Tan, J. Wang, A facile approach to prepare strong poly(acrylic acid)/LAPONITE[registered sign] ionic nanocomposite hydrogels at high clay concentrations, RSC Adv. 5 (74) (2015) 60152–60160.
[36] Q. Chen, H. Chen, L. Zhu, J. Zheng, Fundamentals of double network hydrogels, J. Mater. Chem. B 3 (18) (2015) 3654–3676.
[37] Z.X. Zhao, Z. Li, Q.B. Xia, E. Bajalis, H.X. Xi, Y.S. Lin, Swelling/deswelling kinetics of PNIPAAm hydrogels synthesized by microwave irradiation, Chem. Eng. J. 142 (3) (2008) 263–270.
[38] H. Lum, K.A. Roebuck, Oxidant stress and endothelial cell dysfunction, Am. J. Physiol. Cell Physiol. 280 (4) (2001) C719–C741.
[39] M. Bauer, S. Schroeder, L. Tauhardt, K. Kempe, U.S. Schubert, D. Fischer, In vitro hemocompatibility and cytotoxicity study of poly(2-methyl-2-oxazoline) for biomedical applications, J. Polym. Sci., Part A: Polym. Chem. 51 (8) (2013) 1816–1821.
[40] I. Iso, 10993–5: 2009 Biological Evaluation of Medical Devices-Part 5: Tests for in Vitro Cytotoxicity, International Organization for Standardization, Geneva, 2009.

## Supplementary Information

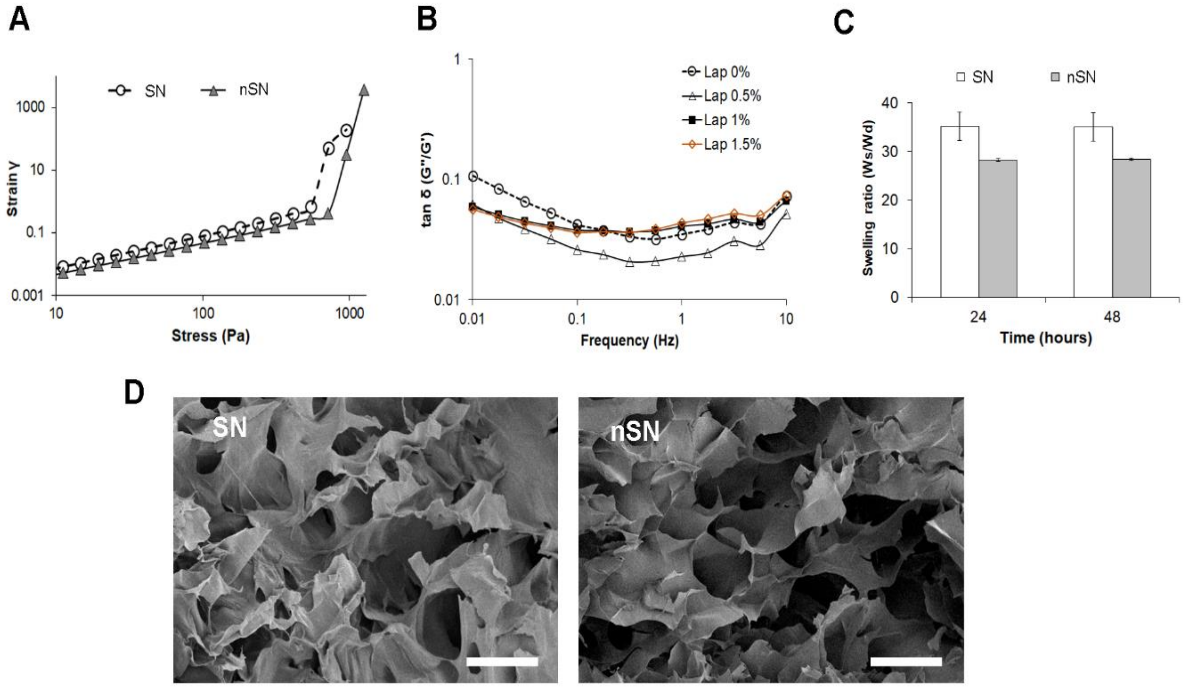


**Figure S1. A) Stress sweep carried out at 1 Hz, showing a higher yield strain for the SN hydrogel containing Laponite at 0.5% w/v. B) Tan δ profiles in the range of frequencies from 0.01 to 10 Hz, showing a constant value of tan δ for the formulations containing Laponite at the concentration of 1% and 1.5 % values. C) Swelling values of GG-MA SN and nSN hydrogels in distilled water at 24 and 48 h. D) SEM images displaying the porosity of GG-MA SN and nSN hydrogels. Scale bars = 100 μm.**

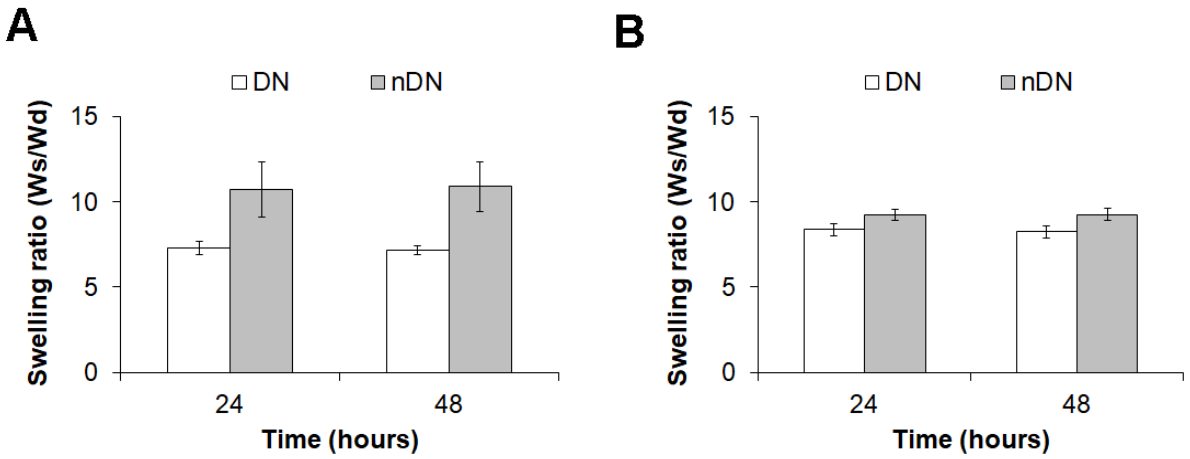


**Figure S2. Swelling values of DN and nDN hydrogels at 24 and 48 hours obtained at 37.0 ± 0.1 °C in A) distilled water and B) phosphate buffer (PBS) pH= 7.4. Results are reported as the mean ± standard deviation (n=3).**

International Journal of Pharmaceutics 547 (2018) 226–234

Contents lists available at ScienceDirect

International Journal of Pharmaceutics

journal homepage: www.elsevier.com/locate/ijpharm

# Effect of glycerol on the physical and mechanical properties of thin gellan gum films for oral drug delivery

Patrizia Paolicelli[a,*], Stefania Petralito[a], Gabriele Varani[b], Martina Nardoni[a], Settimio Pacelli[c], Laura Di Muzio[a], Jacopo Tirillò[b], Cecilia Bartuli[b], Stefania Cesa[a], Maria Antonietta Casadei[a], Alessandra Adrover[b]

[a] Department of Drug Chemistry and Technologies, "Sapienza" University of Rome, Piazzale Aldo Moro 5, 00185 Rome, Italy
[b] Department of Chemical, Material and Environmental Engineering, "Sapienza" University of Rome, Via Eudossiana 18, 00184 Rome, Italy
[c] BioIntel Research Laboratory, Department of Chemical and Petroleum Engineering, School of Engineering, University of Kansas, Lawrence 66045 USA

ARTICLE INFO

*Keywords:*
Thin films
Gellan gum
Glycerol
Buccal delivery
Fluconazole

ABSTRACT

In this work, deacylated gellan gum and the plasticizer glycerol were used as primary components for the preparation of thin films intended for the oral delivery of therapeutic molecules. The samples were prepared by a solvent casting method and characterized for their thickness, tensile properties, swelling ability, mucoadhesion capacity and uniform drug distribution. The amount of glycerol was varied from 20% to 75% w/w in order to obtain films with tunable mechanical properties and high drug loading efficiency. The addition of glycerol was able to positively influence the mechanical characteristics of gellan gum thin film overcoming the brittleness caused by the rigid interconnection among the polymeric chains. Plasticized gellan gum films containing 50% w/w of glycerol showed optimal mechanical resistance and mucoadhesion capacity, which were adversely affected by the inclusion of higher concentrations of glycerol. On the contrary, only high amounts of the plasticizer (≥70% w/w) enabled a homogeneous distribution of the model drug fluconazole within the polymeric matrix. Overall, these results indicate that gellan gum-based thin films can be potentially used for buccal drug delivery upon precise selection of the appropriate concentration of glycerol used as a plasticizer.

## 1. Introduction

The design of efficient films as carriers for drug delivery requires a proper selection of the polymer and excipients used for their fabrication. These essential components affect the ability of the films to swell, degrade and modulate the release of the therapeutic molecule included in the formulation (Borges et al., 2015; Karki et al., 2016). Similarly, the type of polymer can influence the mechanical properties of the produced film, which should be elastic and resistant enough to be handled and applied at the target site without causing any discomfort.

A large variety of film-forming polymers have been investigated over the last decade with particular attention towards natural polymers. For instance, gellan gum (GG), an anionic and linear biopolymer produced by *Pseudomonas elodea,* presents a set of unique properties that make this polysaccharide a valid option for the fabrication of films. Specifically, gellan gum has attracted much attention in both academic and industrial research because of its gelling, texturizing, thickening, emulsifying, suspending, stabilizing and film-forming properties (Prajapati et al., 2013; Osmalek et al., 2014). GG films have been tested as protective coatings to preserve the integrity of food (Leóna and Rojas, 2007; Yang and Paulson, 2000; Yang et al., 2010; Wei et al., 2017), as well as biocompatible and biodegradable materials in wound healing (Lee et al., 2010; Ismail et al., 2014) and bone regeneration (Chang et al., 2010). The unique properties of GG films could also justify their use as carriers for drug delivery, although only one study has investigated so far their potential as therapeutic dosage forms (Sanzgiri et al., 1993). The limited applicability of gellan gum in this research field could be attributed to the technological challenges commonly observed when designing polymeric thin films for drug delivery.

For example, both the reduced size and thickness as well as the large number of excipients used in the film formulation can severely limit the loading levels capacity of the dosage form (Perumal et al., 2008a). Similarly, uncontrolled crystallization of drug upon fabrication or storage is frequently evidenced in this type of delivery systems, especially when a high dose of the active molecule is included. High concentration of a drug can promote the formation of fractal-shaped aggregates randomly distributed within the matrix. The presence of these aggregates,

* Corresponding author.
*E-mail address:* patrizia.paolicelli@uniroma1.it (P. Paolicelli).

https://doi.org/10.1016/j.ijpharm.2018.05.046
Received 14 March 2018; Received in revised form 17 May 2018; Accepted 18 May 2018
Available online 19 May 2018
0378-5173/ 

commonly observed with lipophilic molecules, can adversely affect the uniformity of the resulting film (Perumal et al., 2008b; Qi et al., 2013; Ng et al., 2013).

The process of fractal patterns formation is often related to diffusion-controlled growth processes. Particularly, if an active pharmaceutical ingredient is not freely soluble in the polymer matrix and is present at a supersaturated concentration, then it may phase-separate from the polymer and subsequently crystallize. Such effects potentially cause inhomogeneous drug distribution within drug-loaded films affecting the uniformity of the system as well as drug release kinetics and the physical stability during storage.

Casting, solidification processing, and drying conditions, as well as the right drug-polymer-plasticizer combinations, can impact the homogeneous distribution of the drug in the final dry product (Kestur and Taylor, 2010). Therefore, from a pharmaceutical perspective, the stability of the film and the investigation of strategies aimed to avoid drug nucleation and crystal growth as well as the inhomogeneous distribution of the therapeutic molecule within the matrix deserve special attention as these aspects are of critical importance for the development of commercially viable formulations (Shamma and Elkasabgy, 2016; Zhao et al., 2015; Gaisford et al., 2009).

To this end, process conditions and bulk materials characteristics, such as the viscosity of the polymeric systems before drying as well as the drying conditions, need to be carefully investigated as they can help preventing the inhomogeneous drug distribution in the final dry product.

All these critical aspects have been considered and investigated in this work. Film casting method was used as a preliminary screening technique to determine the optimum ratio of drug, polymer, and plasticizer required to overcome limited diffusion aggregation phenomena during fabrication and storage. Fluconazole (F) and glycerol (Gly) were used as BCS (Biopharmaceutics Classification System) I model drug and plasticizer, respectively. The manufacturing process was optimized considering several critical parameters such as the rheological properties of the starting polymeric solutions, the presence of air bubbles and the residual water content. The physical appearance, thickness, mechanical and release properties of the resulting films were thoroughly investigated.

## 2. Materials and Methods

### 2.1. Materials

Fluconazole, gellan gum (GG, Gelrite® Mn $1 \times 10^6$ Da), type II mucin from porcine stomach and glycerol were purchased from Sigma-Aldrich. Cellulose membrane (cut-off 12,000–14,000 Da) were obtained from Medicell International. Methanol, glacial acetic acid, bidistilled water, potassium dihydrogen phosphate, di-sodium hydrogen phosphate dehydrate, sodium chloride and hydrochloric acid were supplied by Carlo Erba Reagents. Hydroxypropyl-β-cyclodextrins (HP-β-CD) was purchased from Roquette.

### 2.2. Preparation of polymeric films

Films were produced by casting polymeric solutions (6 mL) containing a constant concentration of GG (2% w/v) and different amounts of glycerol, ranging from 0.5% to 6% w/v. In specific, the following GG:Gly weight ratios were investigated: 1:0; 1:0.25; 1:0.5; 1:1; 1:1.5; 1:2; 1:2.5 and 1:3 (w/w). The films were prepared by dissolving GG and glycerol in double distilled water at 60 °C, for 5 h under mild magnetic stirring to avoid air bubble incorporation. Then, the polymeric mixtures were poured onto leveled silicone plates (diameter 5.6 cm), and oven-dried at the constant temperature of 40 ± 2 °C for 15 h. The same procedure was followed to prepare fluconazole-loaded thin films. In this case, 6 mL of a 9.25 mM fluconazole solution in water was used to dissolve the GG:Gly mixture, in the chosen ratio, before the drying process.

All the samples were labeled as $OTF_X$, where x indicates the amount of Gly used for the film preparation respect to GG. Instead, the label $OTF_{XF}$ was used to indicate films also containing fluconazole. Other samples were prepared including HP-β-CD in the formulation and labeled as $OTF_{CD}$. In this case, the selected cyclodextrin (equimolar to fluconazole) was included in the polymeric solution before casting.

### 2.3. Rheological studies

Rheological experiments were carried out with a Haake Rheo Stress 300 Rotational Rheometer equipped with a Haake DC10 thermostat. Flow curves of all the polymeric solutions were obtained with a cone-plate geometry in the range of 0.01–1000 Pa, working at 60.0 ± 0.1 °C. Temperature sweep analyses in the range of 60.0–30.0 °C were also carried out to investigate the effect of temperature on the viscoelastic properties of the polymer-plasticizer mixtures. All the experiments were carried out at least in triplicate.

### 2.4. Thickness measurements

The thickness of the dry films was measured using a Mitutoyo Digimatic Micrometer, characterized by an instrument error ± 2 µm. Measurements were taken at least in three different points of each film.

### 2.5. Thermogravimetric analysis

Thermogravimetric analyses (TGA) were carried out using a Q600 TGA (TA Instruments). Samples (30 mg) were put in open aluminum pans and submitted to three heating/cooling cycles in the temperature range from 25° to 120 °C under a nitrogen atmosphere (5 mL/min). Thermograms were recorded at the constant heating rate of 5 °C/min.

### 2.6. Differential scanning calorimetry

Calorimetric measurements were carried out using a DSC131 (Setaram) differential scanning calorimeter. Samples (5 mg) of free fluconazole and fluconazole-loaded OTF were weighed (~5 mg) in sealed aluminum pans and heated from 25° to 170 °C at the constant heating rate of 5 °C/min. Dry nitrogen with a flow rate of 20 mL/min was purged through the cell during the measurements. An empty aluminum pan was used as a reference.

### 2.7. Tensile tests

Tensile tests were performed with a ZWICK-ROELL-Z010 mechanical testing machine, using a normal load of 1 kN and a strain rate of 1 mm/min. Ten samples of suitable dimensions were cut from each film, mounted between the machine grips and tested to fracture. Samples were obtained cutting films in three different directions (angle 0°, 45°, 90°) to verify the material isotropy. Stress-strain diagrams were recorded, and Young's modulus, strain, and stress at break were acquired. The analyses were repeated eight times and the results were reported as mean values ± standard deviation.

### 2.8. Swelling studies

Films were cut into square pieces (2 × 2 cm), weighed and immersed in simulated saliva (phosphate buffer, pH 6.7, containing NaCl) at 37.0 ± 0.1 °C. At pre-established time points, wet films were drained to remove excess water and weighed. The water-uptake capacity (Q) was expressed as:

$$Q = \frac{W_{s(t)} - W_0}{W_0} \quad (1)$$

where $W_{s(t)}$ and $W_0$ are the weights of the swollen film at time $t$ and the dry film, respectively.

Alternatively, the Q value was calculated according to the following equation:

$$Q = \frac{W_{s(t)} - W_d}{W_d} \quad (2)$$

where $W_{s(t)}$ and $W_d$ are respectively, the weight of the swollen film after 2 h in simulated saliva and the weight of the sample recovered at the end of the swelling study and dried to a constant value.

Finally, to quantify the amount of glycerol lost, portions of the investigated films were kept for 2 h in simulated saliva at 37.0 ± 0.1 °C. Then, they were removed from the medium and oven-dried at 70 °C to constant weight, to calculate the amount of glycerol leached out of the films.

Each test was repeated in triplicate and the results reported as mean values ± standard deviation.

### 2.9. Mucoadhesion tests

The mucoadhesive properties of GG:Gly films were evaluated *in vitro*, measuring the force required for detaching the films from a mucin tablet. The measurements were carried according to an already reported method, based on an in-house pulley system apparatus (Gupta et al., 1993). Briefly, a mucin tablet (diameter 12.5 mm, thickness 1.34 mm) was stuck onto a holder connected to one arm of the pulley system, whereas, round-shaped portions of the films (diameter 12.5 mm) were firmly fixed at the base of the apparatus. Then, the mucin tablets, previously wetted with simulated saliva (pH 6.7), were put on top of the film samples and left in contact for 30 s, before carrying out the test. The mucoadhesive property of the film was measured by adding water to a container connected to the second arm of the pulley system until the film was separated from the tablet. The weight of water needed to separate the film from the mucin tablet was recorded and introduced into the following equation to calculate the detachment force.

$$N = V\rho g \quad (3)$$

where $V$ is the volume of added water, $\rho$ is the density of water and $g$ is standard acceleration of gravity.

### 2.10. Drug content uniformity

The drug content uniformity within the films was assessed on $OTF_{2.5F}$ and $OTF_{3F}$ samples. Each fluconazole-loaded film was divided into three parts. Each section of the film was weighed, and then it was accurately extracted with distilled water for three times. The fluconazole concentration in the extraction solutions was evaluated by HPLC analysis, carried out with a Perkin-Elmer system made of a Series 200 LC pump, a 235 Diode Array Detector, a Total-Chrom data processor and equipped with an RP-18 (250–4.5 μm) Merck Hibar LiChrocart column. The analyses were carried out under isocratic conditions, using a mobile phase composed of methanol, bidistilled water and glacial acetic acid mixture in a proportion of 50:48:2 (v:v:v). The flow rate of the mobile phase was 0.8 mL/min, and the drug was monitored at λ = 260 nm. Under these conditions, the retention time of fluconazole was about 6 min. All experiments were carried out in triplicate, and the results were reported as mean values ± standard deviation.

### 2.11. In vitro release studies

Dissolution tests were carried out in a conventional USP type II paddle apparatus. Round-shaped samples of fluconazole-loaded OTF (surface area 98.5 $cm^2$) were placed in different parts of the vessel: a) taped on the side wall; b) taped on the bottom; c) anchored to the bottom with a wire mesh. All the release studies were carried out in 500 mL of simulated saliva (pH 6.7) at 37.0 ± 0.1 °C with a rotation rate of 50 rpm. Aliquots of the release medium (2 mL) were taken at defined time points from 1 to 30 min and immediately replenished with the same volume of fresh simulated saliva. Fluconazole concentrations were assessed by HPLC analysis as reported in the previous section. Tests were repeated in triplicate, and the results were expressed as mean values ± standard deviation.

### 2.12. Statistical analysis

Quantitative variables are presented as the mean ± standard deviation (SD), and statistics were performed using one-way analysis of variance (ANOVA) by Tukey's multiple comparison post hoc tests. All statistical analyses were performed with Prism 6 (GraphPad Software). $^{*} = p < 0.05$, $^{**} = p < 0.01$, $^{***} = p < 0.001$.

## 3. Results and discussion

### 3.1. Preparation of GG:Gly thin films

Deacylated gellan gum can be used to form films with defined dimensions and shape by casting its aqueous solutions on round-shaped silicon molds. The solvent casting technique involves the initial deposition of a liquid polymeric film on the surface of a solid support followed by the evaporation of the solvent with the conversion of the viscous polymeric solution into a solid film. In this work, silicon supports were selected to promote film detachment at the end of the drying process. The quality and characteristics of the final product are critically dependent on several physical properties of the initial polymeric solution, as well as the manufacturing conditions, such as the rate of solvent evaporation (Siemann, 2005; Huang et al., 2015; Krampe et al., 2016). For this reason, the first part of the work was focused on the characterization of the flow behavior and the temperature-induced modifications of the starting gellan gum solutions during casting and evaporation. These properties can influence the entrapment of air bubbles and the uniform distribution of drugs within the medicated films, which represents the most relevant and desired characteristic of a single-dose formulation designed for a pharmaceutical application.

Fig. 1A shows the viscosity curves of gellan gum obtained at 60 °C for three different polymer concentrations (2.0, 2.5, 3.0% w/v). As expected, all the solutions tested displayed a shear thinning behavior and can be considered as non-Newtonian fluids.

Based on the polymer concentration used, the viscosities of the investigated systems ranged from 1 to 100 Pa·s at 60 °C and shear rate of $10^{-2}\,s^{-1}$. Gellan gum solutions with a concentration of 2.5 and 3% w/v were not suitable for the formation of thin films as they could not be cast homogeneously on the silicon molds probably as a consequence of their high viscosity. In fact, according to Guilbert et al. (1995), the application of a spreader is usually needed to cast high viscous polymer solutions. Therefore, to avoid casting defects within the dried products, 2% w/v gellan gum was selected as the optimal polymer concentration for the film preparation, as it could be freely and homogeneously spread and leveled in the silicon molds. However, after the drying process, gellan gum solutions at 2% w/v formed very brittle films, which were difficult to remove from the silicone molds used for the casting process. Our findings are similar to other reports describing the fabrication of gellan gum films for food application (Yang and Paulson, 2000). A possible reason behind their poor mechanical properties is the formation of strong interactions among the polymeric chains after the step of solvent evaporation, which determines a high level of structural rigidity. For this reason, different amounts of glycerol ranging from 0.5% to 6% w/v were added to 2% w/v gellan gum solutions. Glycerol was selected based on the results reported by Yang and Paulson (2000), who evaluated the effect of different plasticizers on the mechanical properties of gellan gum films, observing that glycerol-plasticized films were more stretchable and transparent than PEG 400, sorbitol, propylene glycol or ethylene glycol-plasticized films.

Glycerol can influence both the viscosity of the film-forming

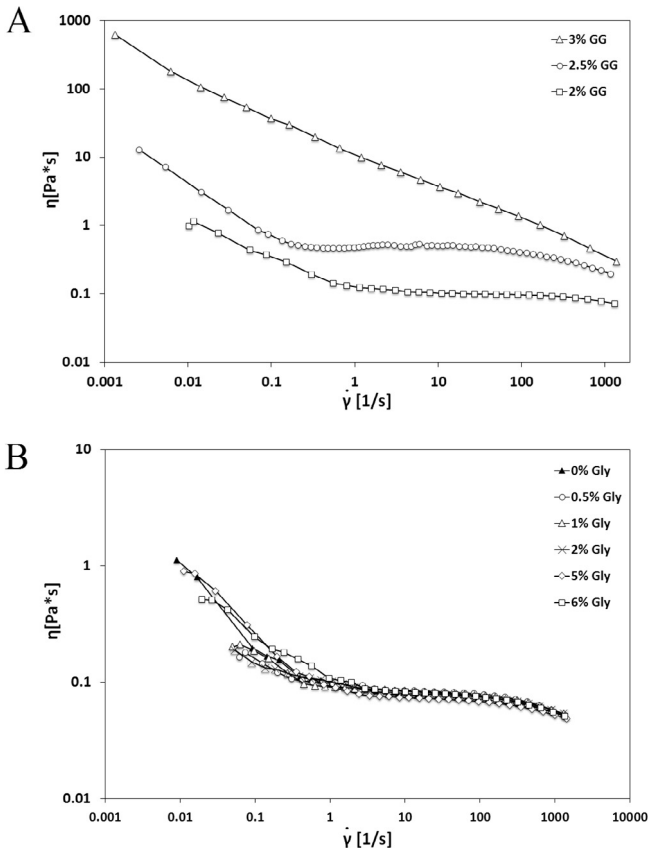


**Fig. 1.** Rheological analysis. Flow curves of GG solutions at 60 °C evaluating: A) effect of polymer concentration on the solution viscosity and B) effect of glycerol concentration on GG (2% w/v) viscosity.

solutions and the corresponding film formation process. For instance, the addition of the plasticizer to GG solutions may lead to a decrease in the intermolecular forces along the macromolecular chains due to its ability to form polymer-plasticizer hydrogen bonds. Therefore, preliminary experiments were carried out to study the effect of glycerol concentration on the viscosity of 2% w/v gellan gum solutions. Flow curves of gellan gum-glycerol mixtures at a different polymer to glycerol ratio were recorded and the results reported in Fig. 1B. It can be observed that irrespective of the amount of plasticizer used, all the investigated mixtures showed almost the same rheological properties in the range of shear stress from 0.01 to 1000 Pa.

Besides investigating the flow behavior of gellan gum/glycerol mixtures, the effect of the plasticizer on the gelation process of the polymer was also studied. To this end, the value of the storage and loss moduli (G′ and G″) were monitored through temperature sweep measurements from 60 to 37 °C to observe the relationship between the gelation temperature and the plasticizer concentration. The gelation point was established at the cross-over between G′ and G″, which is indicative of a transition from sol to gel. The GG solutions exhibit a rapid decrease in molecular mobility with a parallel increase in viscosity as the gelation temperature of the system was approached. The results reported in Table 1 show that the gelation temperature slightly shifted toward higher temperature when glycerol was added to GG solutions with almost no differences for the different polymer-plasticizer combinations analyzed. The increase of the gelation temperature can be attributed to the interaction of the plasticizer with GG (Sakellariou and Row, 1995). At 60 °C the precursor systems behave like solutions, as the loss modulus, G″ is higher than the corresponding storage modulus G′. Therefore, this casting temperature was selected considering the behavior of the viscoelastic and flow properties of gellan gum/glycerol mixtures with temperature. 60 °C resulted a good

**Table 1**
Effect of glycerol concentration on the gelation temperature of 2% (w/v) gellan gum solutions.

| Glycerol (%, w/v) | Gelation temperature (°C) |
|---|---|
| 0 | 49.4 ± 1.5 |
| 0.5 | 52.1 ± 0.4 |
| 1 | 50.8 ± 1.0 |
| 2 | 52.4 ± 0.2 |
| 5 | 51.6 ± 1.1 |
| 6 | 52.5 ± 0.8 |

compromise for optimal casting of the polymeric mixtures and for the formation of homogeneous films. At this temperature, they show sufficiently low viscosity and have a liquid-like behavior, which enable homogeneous pouring of the mixtures onto the silicon support avoiding air bubbles incorporation. Higher temperatures were tested, but they did not give any substantial advantage over the main properties of the final formulations.

During the preliminary step of film formation, all the GG:Gly mixtures are not in a gel state, subsequently, the high surface area along with the reduced thickness of the liquid film allow the rapid cooling of the samples, which is the main cause for the observed sol-gel transition. This event is defined by the inversion of the G′ and G″ moduli in the temperature sweeps graphs.

After the casting step, all the gels were dehydrated at the constant temperature of 40 °C until polymeric films were obtained and easily peeled off from the molds. Clear and transparent films were obtained and easily removed from the supports. Samples were dried for 15 h at the constant temperature of 40 °C. TGA was used to monitor residual water content in the plasticized films during the drying step. Under the adopted operating conditions, the residual water content in the final plasticized film was in the range of 10.0–14.5%, as observed from the thermogravimetric curves reported in Fig. 2. Prolonging any further the drying process brought to excessive dehydration of the films, which resulted in poor mechanical properties, even in high-plasticized systems. In fact, besides glycerol, also the presence of water molecules within the constrained polymeric networks increases the macromolecular mobility and effectively reduces the system rigidity.

Films with mean thickness values varying from 25.8 ± 2.8 to 157.7 ± 6.6 μm were obtained with almost a linear increase dependent on the amount of glycerol included (Table 2). All the systems prepared can be classified as ultra-thin films, according to a generally accepted classification, which defines as ultra-thin films for buccal delivery all polymeric systems having a thickness comprised in the range of 50–150 μm (Karki et al., 2016). The film thickness is a major factor

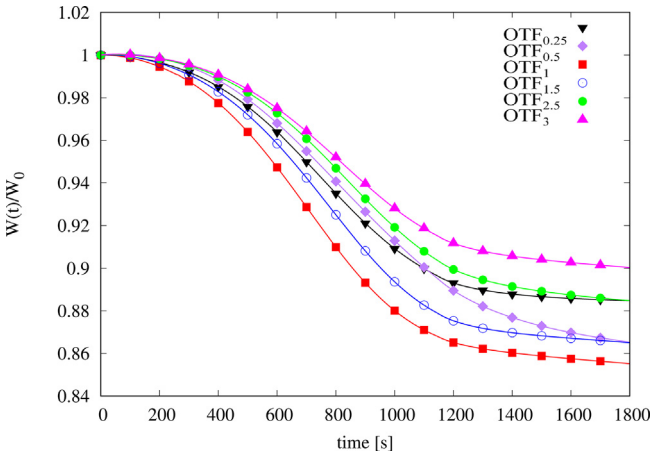


**Fig. 2.** TGA analysis. Thermogravimetric curves of OTF containing different amounts (% w/w) of the plasticizer glycerol.

**Table 2**
Composition of the starting polymeric solutions. Composition and thickness of the final films.

| Sample | Starting solutions | | Final films | | | |
|---|---|---|---|---|---|---|
| | Gellan gum (%, w/v) | Glycerol (%, w/v) | Weight ratio GG:Gly | Glycerol (%, w/w) | Total mass (mg) | Thickness (μm) |
| $OTF_0$ | 2 | 0 | 1:0 | 0 | 120 | 25.8 ± 2.8 |
| $OTF_{0.25}$ | 2 | 0.5 | 1:0.25 | 20 | 150 | 45.5 ± 7.7 |
| $OTF_{0.5}$ | 2 | 1 | 1:0.5 | 33 | 180 | 57.5 ± 4.9 |
| $OTF_1$ | 2 | 2 | 1:1 | 50 | 240 | 76.9 ± 6.3 |
| $OTF_{1.5}$ | 2 | 3 | 1:1.5 | 60 | 300 | 93.9 ± 4.8 |
| $OTF_2$ | 2 | 4 | 1:2 | 67 | 360 | 96.4 ± 7.7 |
| $OTF_{2.5}$ | 2 | 5 | 1:2.5 | 71 | 420 | 142.5 ± 10.6 |
| $OTF_3$ | 2 | 6 | 1:3 | 75 | 480 | 157.7 ± 6.6 |

outlining the specific application of the designed film. However, no requirement for this parameter is reported in the European Pharmacopoeia, which classifies thin films only on the basis of the release rate of the drug (European Pharmacopoeia Commission, Oromucosal Preparations, 2014).

### 3.2. Mechanical properties of GG:Gly thin films

The mechanical properties of the final films were influenced by the amount of glycerol included in the formulation. An increase in the weight fraction of the plasticizer determined an improvement in film flexibility as shown by the progressive reduction of Young's modulus (E) and the increase in the percentage of deformation at the breakpoint (Fig. 3A). Samples containing 20% w/w of plasticizer ($OTF_{0.25}$) were stiff with an E value of around 1600 MPa, whereas more elastic OTFs were formed by including a higher concentration of glycerol in the final formulation. Specifically, the addition of at least 33% w/w of the plasticizer ($OTF_{0.5}$) caused a significant decrease in the E value of one order of magnitude. It is likely that large quantities of glycerol, higher than 33% w/w, may reduce the strong interactions between GG and the plasticizer observed in the samples $OTF_{0.25}$ and $OTF_{0.5}$. In these formulations, it may be present a "cross-linker" effect, which decreases the free volume and the molecular mobility of the polymer, thus reducing the flexibility of the films. On the contrary, incorporation of at least 50% w/w of glycerol within these systems, as in $OTF_1$ sample, is likely to replace some of the gellan–gellan hydrogen bonds with glycerol-gellan hydrogen bonds, increasing the intermolecular separation among the polymeric chains leading to an increase in their mobility (Yang and Paulson, 2000).

To further confirm this hypothesis, tensile tests were carried out on

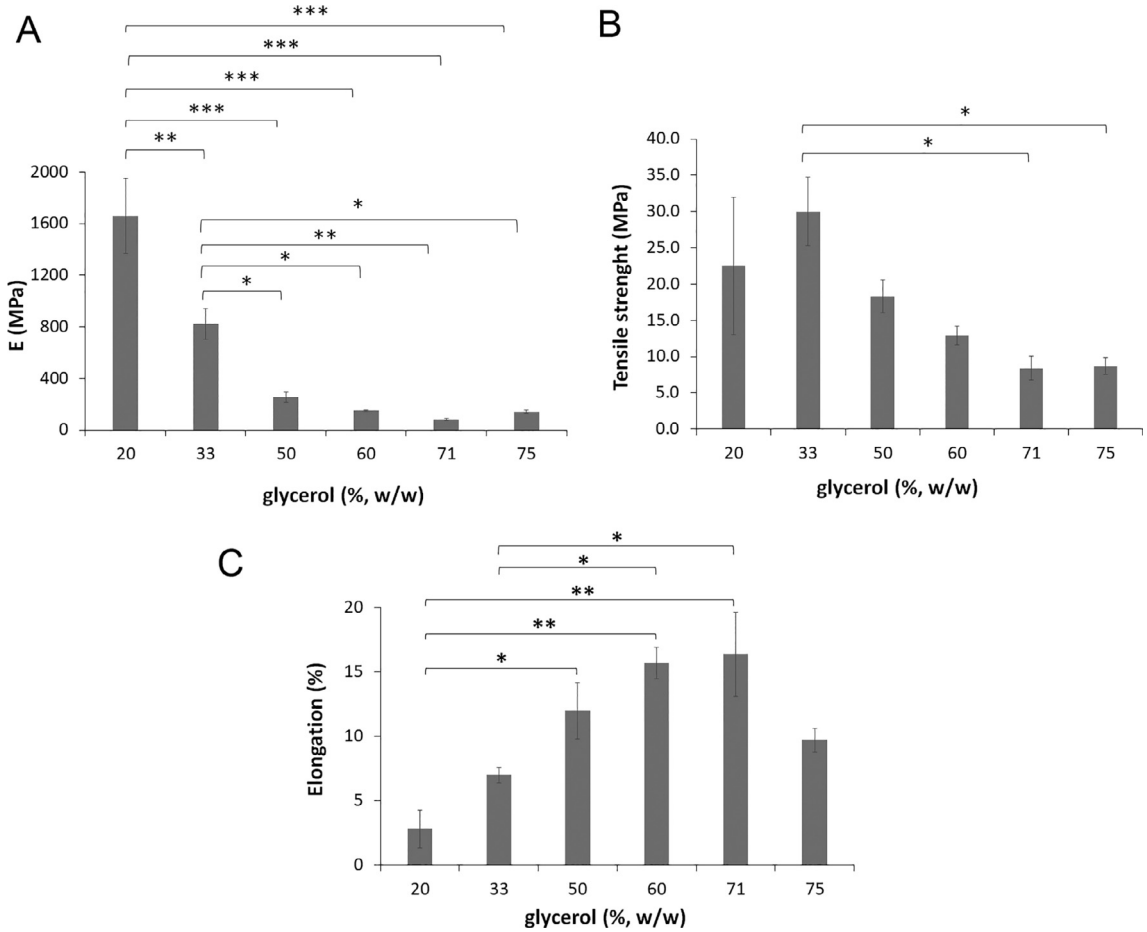


**Fig. 3.** Tensile properties. Mechanical properties of gellan-based OTF containing different amount of the plasticizer glycerol: A) Young's modulus (E); B) tensile strength; and C) elongation at break.

each OTF sample. The films were cut and tested in three different directions to evaluate whether the polymeric chains were oriented in a specific direction. No difference was detected in the analyzed samples, suggesting that the films were completely isotropic regarding tensile properties (data not shown). The $OTF_{0.5}$ samples displayed the higher tensile stress value 30.0 ± 4.7 MPa, and a reduction in the mechanical strength was observed as the concentration of glycerol was increased (Fig. 3B).

Aside from modulating the elasticity, glycerol concentration was able to influence the film's elongation property. Films containing the lower content of glycerol (< 33% w/v) showed the lowest percentage of elongation (2.8 ± 1.5% $OTF_{0.25}$ and $OTF_{0.5}$ 7.0 ± 0.6%), which was statistical significant (Fig. 3C). This result can be explained by the higher rigidity of $OTF_{0.25}$ and $OTF_{0.5}$ formulations when compared to the more flexible film samples containing a larger amount of glycerol.

### 3.3. Swelling studies

All the OTFs were studied for their swelling ability. In a first attempt, the swelling degree of the thin films was calculated as the ratio between the weight of the swelled and the starting dry film. The obtained results are reported in Fig. 1S of Supplementary Material. It can be observed that all the systems reached the equilibrium of swelling in simulated saliva (pH 6.7) within 30 min. Moreover, results in Fig. 1S show a progressive reduction of the equilibrium Q values as the amount of glycerol in the films was increased. However, considering the small dimension of glycerol and its high solubility in water, it was subsequently evaluated whether a loss of the plasticizer may have occurred during the swelling study. Although the OTFs prepared in this work did not undergo any degradation process in the time frame of the swelling study (the formulation resulted completely stable without signs of degradation for at least 48 h), glycerol could diffuse toward the swelling medium enabling water penetration within the polymeric film. Based on this hypothesis, it was evaluated the rate of glycerol loss from the OTFs. Films were let to swell in simulated saliva, then, at regular time intervals, the films were removed from the swelling medium, weighed and dried to constant weight. It was found that the plasticizer diffused out the films almost completely within 20 min of contact with simulated saliva. Importantly, the weight of the dried samples almost corresponded to the value expected for a film made only of gellan gum (Fig. 2S). Therefore, an alternative equation (Eq. (2) in Materials and Methods section) was elaborated to take into account the loss of plasticizer in the swelling medium and properly evaluate the equilibrium of swelling.

An opposite trend in the swelling capacity of the different OTFs was observed in this case (Fig. 4). Precisely, the amount of water taken up by the films at equilibrium increased with the percentage of glycerol originally present in the polymeric system. Based on these data, plasticized OTFs should be evaluated considering that a loss of the plasticizer may occur within time, with a possible effect on the swelling rate and the release of any drug loaded within the film. The diffusion of the plasticizer has been ignored up to now and the swelling behaviour of polymeric films is always calculated according to Eq. (1). This approach can be valid only when a low amount of plasticer (< 10% w/w) is included in the formulation. In all the other cases, the possible loss of the plasticizer has to be taken into consideration to correctly evaluate the behaviour of the film, when in contact with biological fluids, as well as all the properties that depend on the amount of water penetrated within the polymeric network.

### 3.4. Evaluation of the mucoadhesive properties of GG:Gly thin films

The mucoadhesive properties of GG:Gly films were evaluated *in vitro* measuring the force required for detaching the films from a mucin tablet. The obtained results are reported in Table 3.

A progressive reduction of the force required for detaching the OTFs

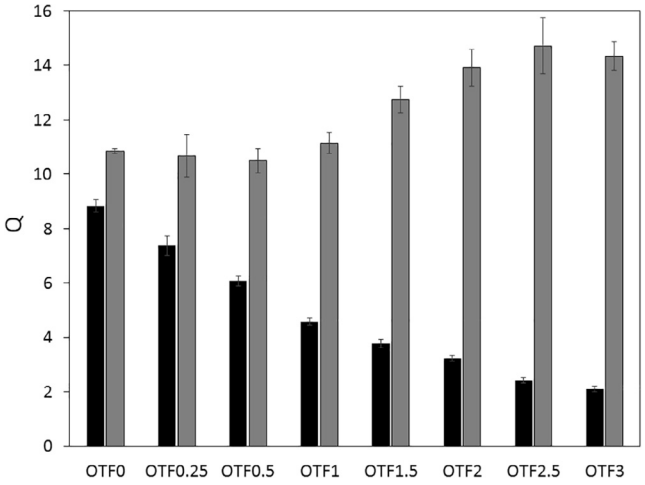


**Fig. 4.** Swelling studies. Effect of glycerol content on the swelling capacity of gellan gum-based OTFs. The black bars indicated the swelling degree (Q) calculated, according to Eq. (1) as the weight ratio between the water content ($W_s$-$W_0$) and the weight of the films before swelling ($W_0$). $W_s$ is the weight of the swollen film after 2 h in simulated saliva at 37.0 ± 0.1 °C. The grey bars indicates instead the swelling capacity (Q) calculated according to Eq. (2), which takes into account the loss of glycerol from the films. In this case, the swelling capacity was obtained by the difference between $W_0$ and the weight of the residual film ($W_d$) recovered after 2 h in simulated saliva at 37.0 ± 0.1 °C and dried to constant weight.

**Table 3**
Mucoadhesive properties of GG:Gly thin films.

| Sample | Weight ratio GG:Gly | Force (N) |
|---|---|---|
| $OTF_{0.25}$ | 1:0.25 | 0.71 ± 0.03 |
| $OTF_{0.5}$ | 1:0.5 | 0.58 ± 0.01 |
| $OTF_1$ | 1:1 | 0.13 ± 0.01 |
| $OTF_{1.5}$ | 1:1.5 | 0.14 ± 0.01 |
| $OTF_{2.5}$ | 1:2.5 | 0.05 ± 0.01 |
| $OTF_3$ | 1:3 | 0.03 ± 0.01 |

from mucin was observed when higher amounts of glycerol were included in the formulation. In particular, a marked drop in the mucoadhesive properties of the films was measured for $OTF_1$ containing equal amounts of GG and glycerol. In fact, changing the amount of glycerol from 33% w/w ($OTF_{0.5}$) to 50% w/w ($OTF_1$) caused a decrease of the mucoadhesive force from 0.58 to 0.13 N. A further reduction was measured in samples $OTF_{2.5}$ and $OTF_3$ containing 71 and 75% w/w of glycerol respectively. It is likely that the excess of plasticizer prevented the polymer from interpenetrating and interacting with mucin, thus negatively affecting the mucoadhesive properties of the final formulation.

Overall, these results suggest that an optimal amount of glycerol should be used in the fabrication of GG-based thin films for mucosal delivery because it affects differently two important features of the formulation, namely the mechanical and the mucoadhesive properties. Films containing 50% w/w of glycerol resulted to be a good compromise between mechanical resistance and mucoadhesive ability.

### 3.5. Drug-loaded films

Glycerol-plasticized films were loaded with a BCS I model drug, namely fluconazole. Although fluconazole is slightly soluble in water (Dash and Elmquist, 2001), uniform distribution of the drug within GG films was critically dependent on the amount of glycerol used. In fact, films containing a concentration of the plasticizer lower than 70% w/w resulted in the separation of white aggregates within the polymeric matrix, probably due to phenomena of limited diffusion aggregation of

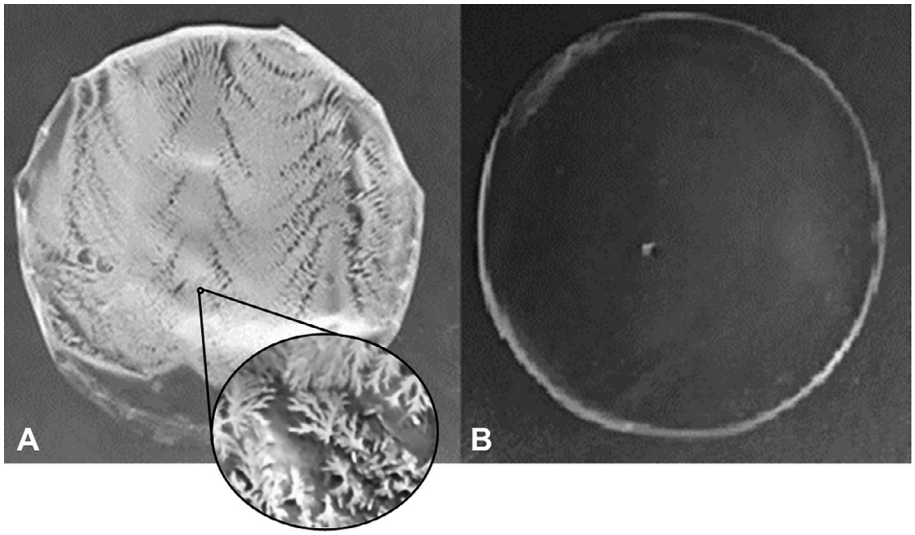


**Fig. 5.** Morphological analysis of OTFs. Photographs of (A) low-plasticized gellan based OTF containing 50% w/w of glycerol and (B) high-plasticized films containing 70% w/w of glycerol. The presence of crystals of fluconazole is well visible in the low plasticized OTFs.

the drug molecules. Specifically, this issue occurred when 0.64 mg/cm$^2$ of fluconazole was included in the formulation. (Fig. 5).

After the drying process, all the systems showed an initial homogeneous appearance with no aggregates, as evidenced by visual observation and confirmed by DSC analysis. Particularly, no melting peaks of fluconazole were observed in the corresponding thermograms (data not shown). However, films containing an amount of glycerol ≤50% w/w displayed the presence of some aggregates of fluconazole within few days after the preparation. It was observed that fluconazole aggregation depends on the glycerol concentration within the films. In fact, a faster appearance of drug aggregates was observed in films with a low weight fraction of the plasticizer, maybe because of the different ability of fluconazole to diffuse within the differently plasticized systems. Low mobility of the drug may cause segregation of fluconazole within drug-rich regions of the film where local concentration may exceed its saturation limit, thus causing and promoting its nucleation and crystallization. This process is in accordance with the hypothesis that branch-structured dendritic crystallization is a result of phase separation from supersaturated states (Seif et al., 2015; Alhijjaj et al., 2015). In contrast, a more homogeneous drug distribution could be achieved when a high amount of the plasticizer was added to the formulation. According to the effect of glycerol on the tensile properties of GG films, it is likely that the inclusion of glycerol reduced the intermolecular interaction among gellan gum chains generating a less tight matrix where fluconazole could be distributed more uniformly (Fig. 6).

The presence of drug aggregates was confirmed by DSC analysis. The thermograms reported in Fig. 7 show the presence of an endothermic peak, which can be attributed to drug crystallization within

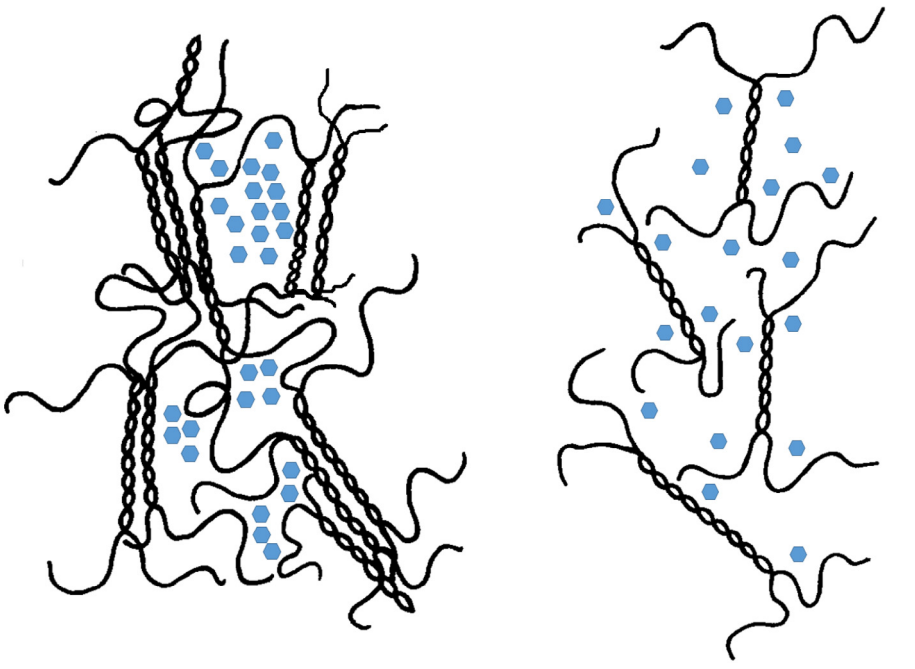


**Fig. 6.** Schematization of drug loaded OTFs. Different drug distribution in low and high plasticized gellan based OTFs. The lines represents the polymer chains, while the hexagons represents the drug molecules.

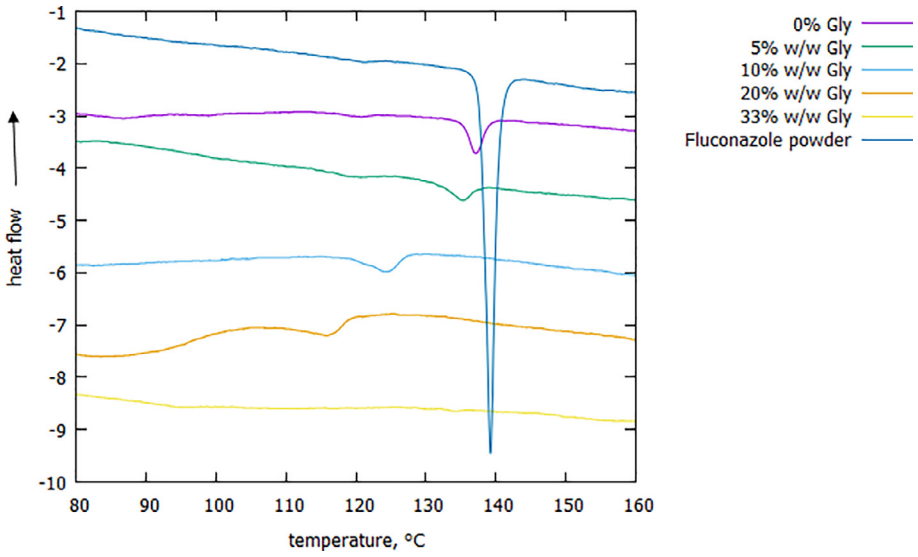


**Fig. 7.** DSC analysis. Thermograms of free fluconazole and drug-loaded OTFs containing different amounts of glycerol. The arrow indicates exothermic processes.

the polymeric matrix. It can also be observed a shift of the melting temperature of fluconazole toward lower values and the progressive broadening of the peak with increasing glycerol concentrations. This effect can be induced by the residual presence of the plasticizer within the crystal lattice, which introduces defects in the structure during the crystallization process. The formation of fluconazole crystals was evidenced by thermal analysis for concentrations of glycerol lower than 50% w/w. On the contrary, no endothermic peak of fluconazole could be observed in films containing 50% w/w of plasticizer (sample $OTF_{1F}$), although white aggregates were well visible within the films.

It is likely that the inclusion of glycerol within fluconazole lattice first reduces the degree of crystallinity of the drug, and then it converts the solid into a completely amorphous structure. Similar results were already reported for felodipine loaded thin films (Kestur and Taylor, 2010).

An alternative explanation may also be proposed for this behavior. Specifically, taking into account the relatively large amount of glycerol employed in the $OTF_1$ sample, the disappearance of the melting peak of fluconazole in the DSC thermogram may be due to the dissolution of the drug in the excess of plasticizer present in the film. In fact, dissolution of fluconazole in glycerol may occur during the heating phase, since the drug solubility in the plasticizer may increase with higher temperatures leading to an absence of a melting peak for fluconazole (Kestur and Taylor, 2010).

To test this hypothesis, we loaded an equimolar amount of fluconazole and HP-β-CD within glycerol-free films. No sign of drug crystallization was observed in this formulation ($OTF_{CD}$), suggesting that the solubility of the drug in glycerol may not be the correct hypothesis. Specifically, the presence of HP-β-CD may produce a preferential localization of fluconazole in its internal cavity during the OTF formation. This effect may prevent appreciable degrees of supersaturation, with minimal interference in the arrangement of the polymeric chains in the dried film. In fact, only a quite low amount of HP-β-CD (76 mg, 0.055 mmol) was used in the formulation. Thus, the observed effect is more likely due to an altered disposition of the drug in the final film caused by cyclodextrin, rather than to a modified interaction between gellan gum chains.

Based on these results, high amounts of plasticizer need to be used in the formulation of fluconazole-loaded GG-based OTFs to have a stable and homogeneous molecular dispersion of the drug within the polymeric matrix. In specific, at least 70% w/w of glycerol need to be present in the final formulation to avoid any drug aggregation within the thin film. Therefore, not less than 5% w/v of glycerol needs to be combined with 2% w/v GG in the starting polymeric solution when fluconazole is included in the formulation.

Based on these results, thin films containing a 71 or 75% w/w of glycerol were loaded with fluconazole ($OTF_{2.5F}$ and $OTF_{3F}$ samples) and selected for further investigation. These samples were characterized by residual water content and tensile properties to evaluate the effect of fluconazole on the main properties of the OTFs and investigate their possible use as drug delivery systems. The residual water content and the correlated tensile properties were not significantly affected by the presence of fluconazole within the films, which showed water content, tensile strength, Young' modulus and elongation values at break similar to those measured for the plain formulation (data not shown).

### 3.6. Release studies

After evaluation of the uniform distribution of fluconazole within $OTF_{2.5F}$ and $OTF_{3F}$ films, these samples were studied for the release profile of the drug in simulated saliva (pH 6.7) at 37.0 ± 0.1 °C using a USP type II apparatus. The results showed almost no difference between films containing 71 or 75% w/w of glycerol (Fig. 8). In both cases, fluconazole was completely released from the film within 15 min, in agreement with the results of the swelling studies, which evidenced similar Q values for $OTF_{2.5}$ and $OTF_3$.

Release studies were also carried out on films containing HP-β-CD (sample $OTF_{CD}$). Results reported in Fig. 8 show a slightly different behavior between samples $OTF_{3F}$ and $OTF_{CD}$. Both systems quantitatively released fluconazole within 10 min in simulated saliva (pH 6.7) at 37.0 ± 0.1 °C. However, it can be observed that films containing HP-β-CD show a different and slower release profile compared with sample $OTF_{3F}$. This result may suggest that, besides the appearance of the sample $OTF_{3F}$, where no signs of drug crystallization were visually observed, some fluconazole crystallites may have been formed within the film. On the contrary, the inclusion of HP-β-CD affected drug organization within the polymeric network and contributed to maintain the drug dispersed and molecularly separated, avoiding drug nucleation and allowing slower diffusion of fluconazole from the films. Therefore, it may be expected that drug aggregation and its consequent phase separation may occur even in GG-based OTF plasticized with a high weight fraction of glycerol. In fact, considering that the diffusion-limited aggregation is a kinetic-based phenomenon, aging of the films may lead to drug crystallization within the polymeric network. These results further corroborated the hypothesis that the inclusion of cyclodextrins may have altered fluconazole distribution within the polymeric network.

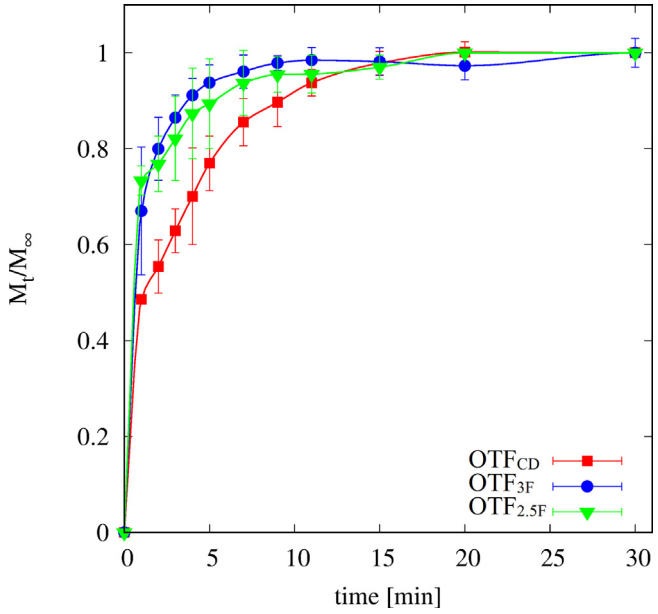


**Fig. 8.** Release studies. Release profile of fluconazole from $OTF_{2.5F}$, $OTF_{3F}$ and $OTF_{CD}$ in simulated saliva (pH 6.7) at 37.0 ± 0.1 °C.

## 4. Conclusions

In this work, the potential of gellan gum thin films for drug delivery was investigated. The addition of a plasticizer was required to improve the poor mechanical properties of the polymer formulated as a thin film. It was observed that, while the low amounts of the plasticizer glycerol (≤50% w/w) were sufficient to increase the resistance and strength before rupture of the films, they resulted to be completely inadequate for drug delivery applications. In fact, much higher percentages of glycerol (≥70% w/w) were needed to homogeneously include the model drug fluconazole within the polymeric matrix avoiding drug nucleation and crystallization phenomena. However, the inclusion of high amounts of glycerol in the formulation impaired some important properties of the films as drug delivery vehicles, as they interfere with the ability of GG of interacting with mucin, and negatively influence the mucoadhesive properties of the films. Therefore, besides the interesting characteristics of GG for the development of thin films with potential application in the field of drug delivery, further approaches need to be investigated for the optimal inclusion of drugs within this polymeric network.

An interesting strategy may be represented by the use of a functional excipient, such as cyclodextrins, which should help maintaining low amount of plasticizer avoiding problems related to drug solubility and crystallization.

## Acknowledgements

The authors wish to thank Dr. Elisabetta Veca from ENEA, Italian National Agency for New Technologies, Energy, and Sustainable Economic Development, Rome (Italy) for TGA analysis.

## Appendix A. Supplementary data

Supplementary data associated with this article can be found, in the online version, at http://dx.doi.org/10.1016/j.ijpharm.2018.05.046.

## References

Alhijjaj, M., Bouman, J., Wellner, N., Belton, P., Qi, S., 2015. Creating drug solubilization compartments via phase separation in multicomponent buccal patches prepared by direct hot melt extrusion – injection molding. Mol. Pharm. 12, 4349–4362.
Borges, A.F., Silva, C., Coelho, J.F., Simões, S., 2015. Oral films: current status and future perspectives I — Galenical development and quality attributes. J. Controlled Release 206, 1–19.
Chang, S.J., Kuo, S.M., Liu, W.T., Niu, C.C.G., Lee, M.W., Wu, C.S., 2010. Gellan gum films for effective guided bone regeneration. J. Med. Biol. Eng. 30, 99–103.
European Pharmacopoeia Commission, 2014. Oromucosal Preparations. European Pharmacopoeia, eigth ed. European Directorate for the Quality of Medicines (EDQM), Strasbourg.
Dash, A.K., Elmquist, W.F., 2001. In: Brittain, H.G. (Ed.), Fluconazole. Analytical Profiles of Drug Substances and Excipients, pp. 85–88.
Gaisford, S., Verma, A., Saunders, M., Royall, P.G., 2009. Monitoring crystallisation of drugs from fast-dissolving oral films with isothermal calorimetry. Int. J. Pharm. 380, 105–111.
Guilbert, S., Gontard, N., Cuq, B., 1995. Technology and applications of edible protective films. Packag. Technol. Sci. 8, 339–346.
Gupta, A., Garg, S., Khar, R.K., 1993. Measurement of bioadhesion strength of mucoadhesive buccal tablet: design of an in vitro assembly. Ind. Drugs 30, 152–155.
Huang, Y.C., Wang, T.Z., Liu, T.J., Tiu, C., 2015. Operating window of solution casting. II. Non-Newtonian fluids. J. Appl. Polym. Sci. 132, 41411.
Ismail, N.A., Mohamad, S.F., Ibrahim, M.A., Mat Amin, K.A., 2014. Evaluation of gellan gum film containing virgin coconut oil for transparent dressing materials. Adv. Biomater. 2014, 1–12.
Karki, S., Kim, H., Na, S.J., Shin, D., Jo, K., Lee, J., 2016. Thin films as an emerging platform for drug delivery. Asian J. Pharm. Sci. 11, 559–574.
Kestur, U.S., Taylor, L.S., 2010. Role of polymer chemistry in influencing crystal growth rates from amorphous felodipine. Cryst. Eng. Comm. 12, 2390–2397.
Krampe, R., Visser, J.C., Frijlink, H.W., Breitkreutz, J., Woerdenbag, H.J., Preis, M., 2016. Oromucosal film preparations: points to consider for patient centricity and manufacturing processes. Expert Opin. Drug Delivery 13, 493–506.
Lee, M.W., Chen, H.J., Tsao, S.W., 2010. Preparation, characterization and biological properties of gellan gum films with 1-ethyl-3-(3-dimethylaminopropyl) carbodiimide cross-linker. Carbohydr. Polym. 82, 920–926.
Leóna, P.G., Rojas, A.M., 2007. Gellan gum films as carriers of l-(+)-ascorbic acid. Food Res. Int. 40, 565–575.
Ng, Y.C., Yang, Z., McAuley, W.J., Qi, S., 2013. Stabilisation of amorphous drugs under high humidity using pharmaceutical thin films. Eur. J. Pharm. Biopharm. 84, 555–565.
Osmalek, T., Froelich, A., Tasarek, S., 2014. Application of gellan gum in pharmacy and medicine. Int. J. Pharm. 466, 328–340.
Perumal, V.A., Govender, T., Lutchman, D., Mackraj, I., 2008a. Investigating a new approach to film casting for enhanced drug content uniformity in polymeric films. Drug Dev. Ind. Pharm. 34, 1036–1047.
Perumal, V.A., Lutchman, D., Mackraj, I., Govender, T., 2008b. Formulation of monolayered films with drug and polymers of opposing solubilities. Int. J. Pharm. 358, 184–191.
Prajapati, V.D., Jani, G.K., Zala, B.S., Khutliwala, T.A., 2013. An insight into the emerging exopolysaccharide gellan gum as a novel polymer. Carbohydr. Polym. 93, 670–678.
Qi, S., Moffat, J.G., Yang, Z., 2013. Early stage phase separation in pharmaceutical solid dispersion thin films under high humidity: improved spatial understanding using probe-based thermal and spectroscopic nanocharacterization methods. Mol. Pharm. 10, 918–930.
Sakellariou, P., Row, R.C., 1995. Interactions in cellulose derivative films for oral drug delivery. Prog. Polym. Sci. 20, 889–942.
Sanzgiri, Y.D., Maschi, S., Crescenzi, V., Callegaro, L., Topp, E.M., Stella, V.J., 1993. Gellan-based systems for ophthalmic sustained delivery of methylprednisolone. J. Controlled Release 26, 195–201.
Seif, S., Franzen, L., Windbergs, M., 2015. Overcoming drug crystallization in electrospun fibers–Elucidating key parameters and developing strategies for drug delivery. Int. J. Pharm. 478, 390–397.
Shamma, R., Elkasabgy, N., 2016. Design of freeze-dried Soluplus/polyvinyl alcohol-based film for the oral delivery of an insoluble drug for the pediatric use. Drug Delivery 23, 489–499.
Siemann, U., 2005. Solvent cast technology – a versatile tool for thin film production. Progr. Colloid Polym. Sci. 130, 1–14.
Wei, Y.C., Cheng, C.H., Ho, Y.C., Tsai, M.L., Mi, F.L., 2017. Active gellan gum/purple sweet potato composite films capable of monitoring pH variations. Food Hydrocolloids 69, 491–502.
Yang, L., Paulson, A.T., 2000. Mechanical and water vapour barrier properties of edible gellan films. Food Res. Int. 33, 563–570.
Yang, L., Paulson, A.T., Nickerson, M.T., 2010. Mechanical and physical properties of calcium-treated gellan films. Food Res. Int. 43, 1439–1443.
Zhao, Y., Quan, P., Fang, L., 2015. Preparation of an oral thin film containing meclizine hydrochloride: in vitro and in vivo evaluation. Int. J. Pharm. 496, 314–322.

## Supporting Information

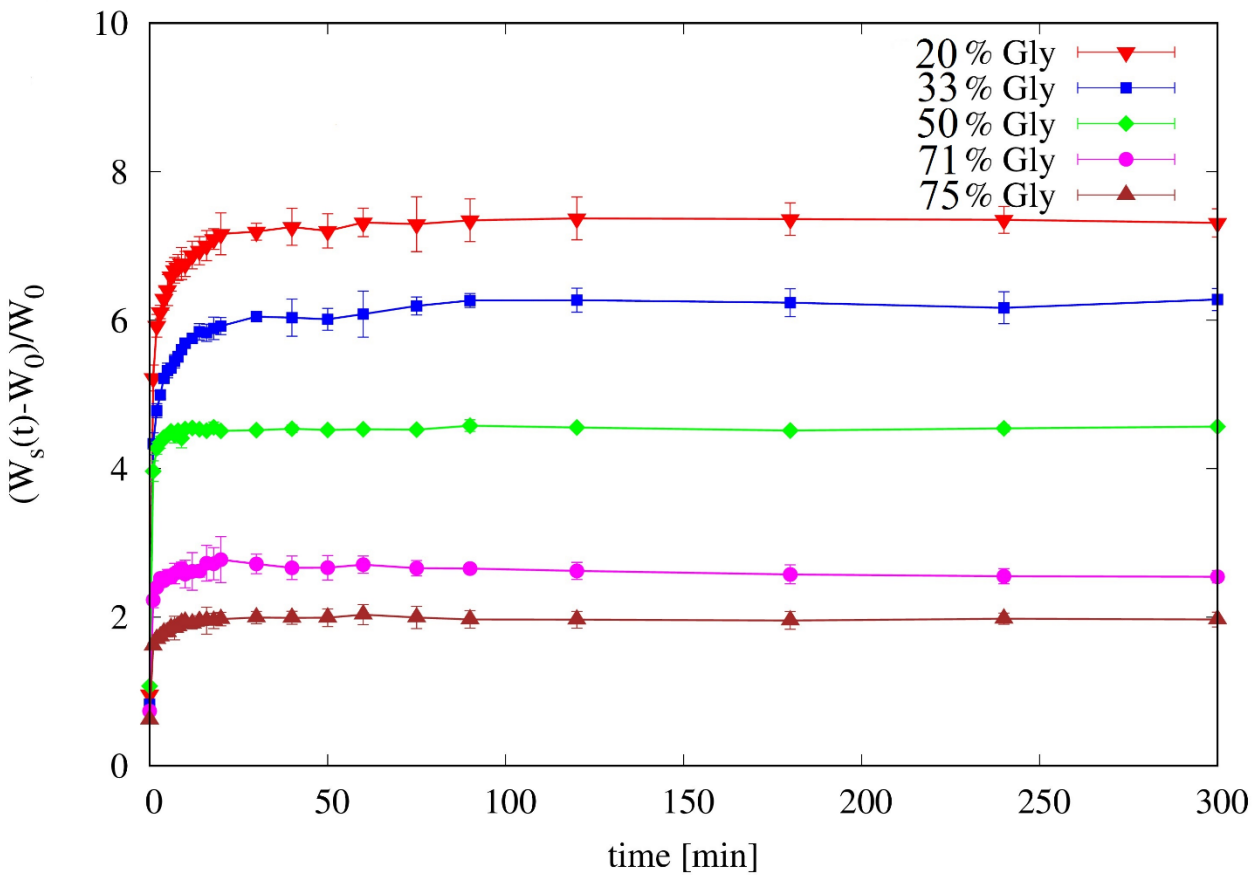


**Figure S1. Dynamic swelling study. Evaluation of the variation of the swelling capacity over time for the gellan gum-based OTFs, containing different amount of the plasticizer glycerol.**

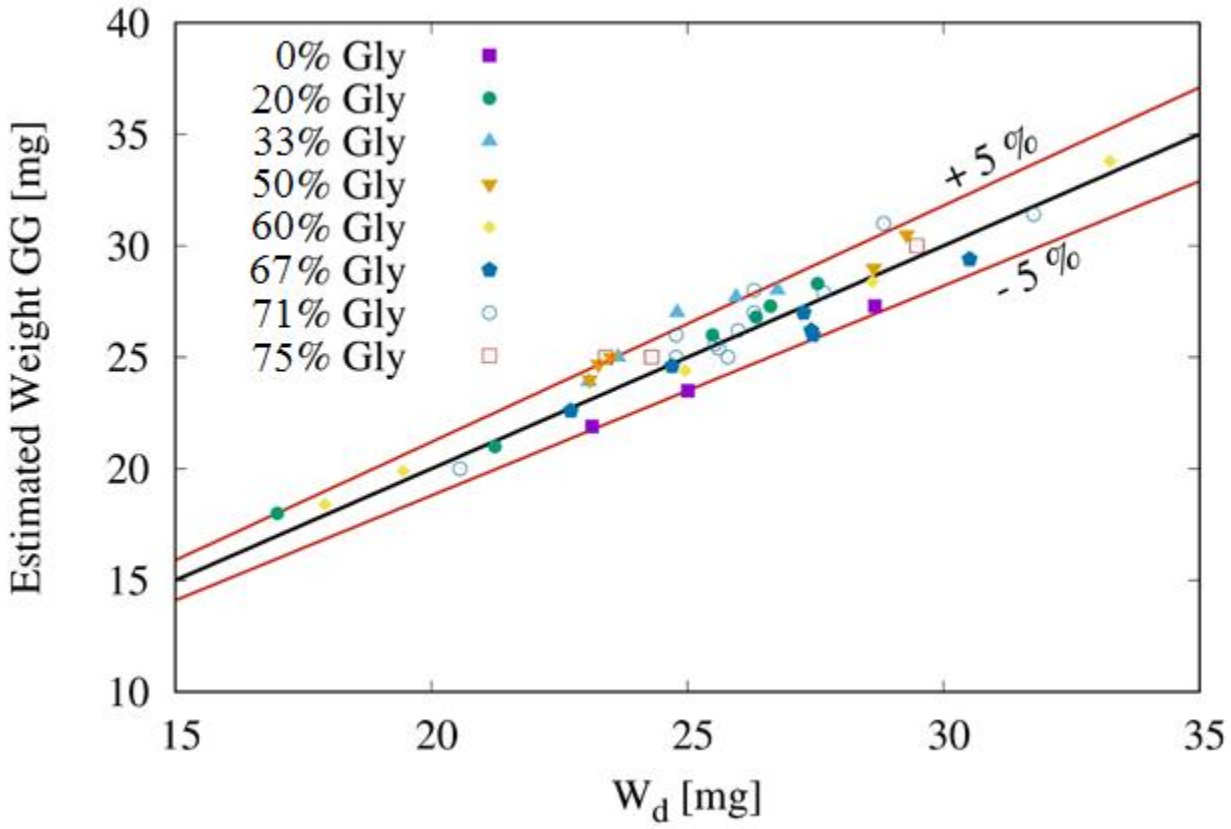


**Figure S2. Composition of OTFs. Analysis of the composition of the OTFs recovered after 2 h in simulated saliva (pH= 6.7) at 37.0±0.1 °C and dried to constant weight.**

## Publications:

1. Petralito, S.; Paolicelli, P.; **Nardoni, M.**; Apollonio, F.; Liberti, M.; Merla, C.; Pinto, R.; Casadei, M.A.; Annesini, M.C. *Magnetoliposomes: Envisioning new strategies for water decontamination*. CHEMICAL ENGINEERING TRANSACTIONS. **2016**, 47; ISBN 978-88-95608-38-9; ISSN 2283-9216.

2. Paolicelli, P.; Petralito, S.; **Nardoni, M.**; Varani, G.; Pacelli, S.; Adrover, A; Casadei, M.A. *Thin film technology: new opportunity for buccal controlled delivery*. MITO. A journey through liposomes and polysaccharides, 29-30 November. CONTROLLED RELEASE SOCIETY SEZIONE ITALIANA. **2016**, 1, 46, ISBN: 9788894140415.

3. Petralito, S.; Paolicelli, P.; Apollonio, F.; Liberti, M.; **Nardoni, M.**; Varani, G.; Pacelli, S.; Adrover, A.; Casadei, M.A. *Emerging trends in liposome design*. MITO. A journey through liposomes and polysaccharides, 29-30 November. CONTROLLED RELEASE SOCIETY SEZIONE ITALIANA. **2016**, 1, 47, ISBN: 9788894140415.

4. Paolicelli, P.; Varani, G.; Pacelli, S.; Ogliani, E.; **Nardoni, M.**; Petralito, S.; Adrover, A.; Casadei, M.A. *Design and characterization of a biocompatible physical hydrogel based on scleroglucan for topical drug delivery*. CARBOHYDRATE POLYMERS. **2017**, 174, 960-969, ISSN: 0144-8617.

5. **Nardoni, M.**; Della Valle, E.; Liberti, M.; Relucenti, M.; Casadei, M.A.; Paolicelli, P.; Apollonio, F.; Petralito, S. *Can pulsed electromagnetic fields trigger on-demand drug release from high-Tm magnetoliposomes?* NANOMATERIALS. **2018**, 8(4), 196, doi:10.3390/nano8040196.

6. Paolicelli, P.; Petralito, S.; Varani, G.; **Nardoni, M.**; Di Muzio, L.; Pacelli, S.; Tirillò, J.; Bartuli, C.; Cesa, S.; Casadei, M.A.; Adrover, A. *Eeffect of glycerol on the physical and mechanical properties of thin gellan gum films for oral drug delivery*. INTERNATIONAL

JOURNAL OF PHARMACEUTICS. **2018**, 547(1-2), 226-234, https://doi.org/10.1016/j.ijpharm.2018.05.046.

7. Pacelli, S.; Paolicelli, P.; Avitabile, M.; Varani, G.; Di Muzio, L.; Cesa, S.; Tirillò, J.; Bartuli, C.; **Nardoni, M.**; Petralito, S.; Adrover, A.; Casadei, M.A. *Design of a tunable nanocomposite double network hydrogel based on gellan gum for drug delivery applications*. EUROPEAN POLYMER JOURNAL. **2018**, 104, 184-193, https://doi.org/10.1016/j.eurpolymj.2018.04.034.

8. Di Sotto, A.; Paolicelli, P.; **Nardoni, M.**; Abete, L.; Garzoli, S.; Di Giacomo, S.; Mazzanti, G.; Casadei, M.A.; Petralito, S. *SPC liposomes as possible delivery systems for improving bioavailability of the natural sesquiterpene β-caryophyllene: lamellarity and drug-loading as key features for a rational drug delivery design*. PHARMACEUTICS, ISSN 1999-4923. **2018**, Accepted for Publication.

## Proceedings:

1. Varani, G.; Adrover, A.; **Nardoni, M.**; Pacelli, S.; Paolicelli, P.; Petralito, S.; Casadei, M.A. *Manufacturing and characterization of polymeric thin films for buccal delivery of drugs*. 10th World Meeting on Pharmaceutics, Biopharmaceutics and Pharmaceutical Technology, Glasgow, Vol. 10, p. 37, from 4th to 7th April 2016.

2. **Nardoni, M.**; Pacelli, S.; Paolicelli, P.; Petralito, S.; Casadei, M.A. *From surface to core modification: development of gel-in-liposome hybrid systems*. Nanomedicine Viterbo 2016, from 21st to 23rd September 2016.

3. **Nardoni, M.**; Della Valle, E.; Liberti, M.; Relucenti, M.; Matassa, R.; Setti, S.; Cadossi, R.; Casadei, M.A.; Paolicelli, P.; Apollonio, F.; Petralito, S. *Effect of pulsed electromagnetic fields (PEMFs) on magnetoliposomes*. 11th World Meeting on

Pharmaceutics, Biopharmaceutics and Pharmaceutical Technology, Granada, Vol. 11, from 19th to 22nd March 2018.

4. Merla, C.; Attal-Tretout, B.; **Nardoni, M.**; Ghorbel, A.; Petralito, S.; Apollonio, F.; Liberti, M.; Schermann, M.; Mir, L.M. *A wide-field CARS Setup for spectroscopy under lectropulsation of biological media*. BioEM2018, Piran, Portoroz, Slovenia, from 24th to 29th June 2018.
5. **Nardoni, M.**; Paolicelli, P.; Di Muzio, L.; Pacelli, S.; Casadei, M.A.; Petralito, S. *Gelation of liposomal internal core for improved drug delivery*. Controlled Release Society Annual Meeting & Exposition, New York, from 22nd to 24th July 2018.

6. **Nardoni, M.**; Della Valle, E.; Liberti, M.; Relucenti, M.; Di Muzio, L.; Paolicelli, P.; Apollonio, F.; Casadei, M.A.; Petralito, S. *Controllable release from high-transition temperature magnetoliposomes by magneto-mechanical actuation*. Controlled Release Society Annual Meeting & Exposition, New York, from 22nd to 24th July 2018.

7. Caramazza, L.; **Nardoni, M.**; De Angelis, A.; Paolicelli, P.; Petralito, S.; Liberti, M.; Apollonio, F. *Feasibility of drug delivery mediated by ultra-short and intense pulsed electric fields*. V Convegno ICEMB – INTERAZIONI TRA CAMPI ELETTROMAGNETICI E BIOSISTEMI, Salerno, from 28th to 30th November 2018.

8. Petralito, S.; Paolicelli, P.; **Nardoni, M.**; Abete, L.; Garzoli, S.; Di Giacomo, S.; Mazzanti, G.; Trilli, J.; Casadei, M.A.; Di Sotto, A. *SPC liposomes as possible delivery systems for improving bioavailability of the natural sesquiterpene β-caryophyllene.* 3rd EUROPEAN CONFERENCE, Bringing science into pharmaceutical practice, Bologna, from 25th to 26th March 2019.